Electroreduction of carbon monoxide on copper electrodes

Bertheussen, Erlend

Publication date:
2018

Document Version
Publisher's PDF, also known as Version of record

DTU Physics
Department of Physics

Electroreduction of carbon monoxide on copper electrodes

a PhD dissertation by

Erlend Bertheussen

Supervisor: Professor Ib Chorkendorff
Co-supervisor: Senior Lecturer Ifan E.L. Stephens

Section for Surface Physics and Catalysis
Department of Physics
Technical University of Denmark

January 2018

Preface

This thesis is submitted as partial fulfilment of the PhD degree in physics at the Technical University of Denmark (DTU). The work presented herein was performed at the Section for Surface Physics and Catalysis (SurfCat), which is part of the Deparment of Physics, between February 2015 and January 2018. The project was performed under the supervision of Prof. Ib Chorkendorff and Senior Lecturer Ifan E.L. Stephens (Ifan recently moved to Imperial College London, but held a position as Associate Professor at DTU Physics during the main part of my PhD). SurfCat is funded by a grant (9455) from the VILLUM FONDEN through the VILLUM Center for the Science of Sustainable Fuels and Chemicals.

Firstly, I would like to express my gratitude to the supervisors for giving me the possibility to carry out this project, and for their support and discussion throughout my PhD. Doing research in the highly skilled and inspiring environment that they have created and maintained has helped me develop a lot. I would also like to thank all my current and previous colleagues for creating such an inclusive and positive work environment. I have learned a lot from three years of scientific and social interactions, and it has been great fun spending all this time with them. A particular word of gratitude goes to the SurfCat members that I have had the privilege of working closely with, and who have helped me along the way; Amado Velazquez-Palenzuela, Arnau Verdaguer-Casadevall, Daniel B. Trimarco, Claudie Roy, Younes Abghoui, Thomas Vagn Hogg, Anna Winiwarter, Albert K. Engstfeld, Søren B. Scott, Stefano Mezzavilla, Brian Seger, Zarko P. Jovanov,

Ana Sofia Varela, Jacqueline McAnulty, Brian P. Knudsen, Kenneth Nielsen and Robert Jensen. In addition, Thomas, Claudie, Albert, Anna, Stefano, Viktor Colic, Sungeun Yang, Søren and Ifan all made highly appreciated efforts in helping me improve this thesis towards a finished document. I am also thankful to the external collaborators Davide Ravasio, Joseph H. Montoya, Sebastian Meier, Jens K. Nørskov, Anne Hector, Casper Hoeck and Kasper Enemark-Rasmussen for playing important roles in making the various projects successful.

I would like to thank all the members of the Jaramillo group at Stanford University, where I spent 3 months during my PhD. The inclusive environment they have created made me feel welcome, and I thoroughly enjoyed my time there. I learned a lot from the impressive science they perform, and their different approaches. Special thanks go to to Lei Wang, Stephanie A. Nitopi, Alan T. Landers, John C. Lin, Drew Higgins and Chris Hahn in particular for help, collaboration and supervision during my time there.

Finally, I thank my family, in particular my parents, for their interest and backing, both during my time at DTU and at any other stage of my life. Although they do not live that close, I feel their strong support. I am also grateful to all my friends, both those that I have made during my PhD, and the ones going way back, for making my life fun and enjoyable. Last, but not in any way least, I would like to thank my girlfriend, Morlin. Her support and understanding for the sometimes unpredictable nature of life as a PhD student has been invaluable, in particular during the last months. Even more importantly, thanks for sharing all those small and big moments with me, and for making the world a better place.

Kongens Lyngby, January 31 2018

Erlend Bertheussen

Abstract

Electrochemical CO_2 reduction is receiving increasing attention as a means for (i) storage of renewable electricity and (ii) recycling of CO_2 into valuable chemicals and fuels. Cu is the only monometallic catalyst that can facilitate formation of $>2e^-$ products with moderate selectivity and high activity. However, a mixture of products are formed and low energy efficiency is achieved for formation of $>2e^-$ products. As a result, improvements are needed before the technology can be commercialised. One approach is electroreduction of CO, for which previous studies report high oxygenate selectivity at low overpotentials on nanostructured catalysts. Since CO is as an intermediate in $>2e^-$ product formation, any insight obtained for CO reduction will aid our understanding of CO_2 reduction. In this thesis, I have studied CO reduction on nanostructured and polycrystalline Cu electrodes.

Due to the mixture of products formed during CO reduction, thorough product analysis is important in order to obtain all the information possible about the reaction. We benchmarked the performance of two techniques used for liquid product analysis; static headspace-gas chromatography (HS-GC) and NMR spectroscopy. CO reduction is often carried out in alkaline electrolyte, since this leads to enhanced C_{2+} product selectivity and suppressed H_2 evolution. The high pH can, however, also lead to undesired reactions occurring with the liquid products from CO reduction. It turns out that acetaldehyde and propionaldehyde are unstable in alkaline electrolytes, leading to polymerisation and precipitation. As a result, these aldehydes, in particular acetaldehyde, are difficult to detect using NMR

spectroscopy. HS-GC, on the other hand, can quantify aldehydes with high sensitivity.

Using HS-GC for liquid product analysis allowed us to detect acetaldehyde as an additional, previously overlooked product from CO reduction on oxide-derived Cu. Using a combination of experiments and DFT calculations, we determined that acetaldehyde is an intermediate in the reduction of CO to ethanol. This has been previously observed for polycrystalline Cu, confirming that ethanol formation occurs through a similar pathway on planar and nanostructured electrodes. We identified a single intermediate in the further conversion of acetaldehyde to ethanol, which represents a thermodynamically uphill step. The free energy of this intermediate is thus likely to determine whether ethanol production is favoured or not.

Although nanostructured Cu electrodes are promising for CO reduction to $>2e^-$ products, a robust benchmark for the activity of Cu in this potential region is yet to be reported. Polycrystalline foils represent a robust benchmark for CO_2 reduction, which led us to study CO reduction on polycrystalline Cu. We measured relatively high selectivity and activity between -0.40 and -0.59 V vs. RHE, with similar total CO reduction activity to that of nanostructured Cu, when normalised by ECSA. This suggests that nanostructuring mainly results in a change in product distribution, and might not influence the intrinsic activity of Cu to a significant extent.

Significant deactivation could be observed for polycrystalline Cu during CO reduction. We mainly attributed this to poisoning by Si from the glass cell. However, surface restructuring has been proposed in the literature as a possible reason for activity and selectivity changes during CO_2 and CO reduction. Phenomena occurring under reaction conditions are difficult to evaluate using *ex-situ* characterisation. This led us to perform *operando* characterisation of Cu during CO reduction using synchrotron techniques. In the results reported in this thesis, we used grazing incidence X-ray diffraction to study the average surface and near-surface structure of polycrystalline Cu films under reaction conditions. We have obtained preliminary data this far that demonstrate the possibility to apply this technique under CO reduction conditions. I also present results where certain regions of the spectra are tracked real-time as the reaction conditions are changed.

Resumé

Elektrokemisk CO_2-reduktion er en lovende process for (i) lagring af elektricitet fra bæredygtige kilder og (ii) omdannelse af CO_2 til værdifulde kemikalier. Cu er det eneste rene metal som kan drive reduktion af CO_2 til $>2e^-$-produkter med høj aktivitet. Der vil imidlertid blive dannet en blanding af flere forskellige produkter. Samtidig foregår produktion af $>2e^-$-produkter med lav energieffektivitet. Dermed kræves forbedringer inden denne teknologi kan blive kommercialiseret. En tilgang til dette er CO reduktion, hvor studier af nanostrukturerede elektroder har rapporteret høj selektivitet til oxygenerede forbindelser. CO er også et mellemprodukt i dannelsen af $>2e^-$-produkter fra CO_2, hvorfor indsigt opnået for CO reduktion også vil være relevant for CO2 reduktion. I den sammenhæng har jeg i løbet af mine ph.d.-studier hovedsageligt fokuseret på nanostrukturerede og polykrystallinske Cu-elektroder for CO-reduktion.

Da en blanding af mange forskellige produkter bliver dannet, er en grundig produktanalyse essensiel, for ikke at tabe vigtig information om reaktionen. I den sammenhæng benchmarkede vi hvordan to forskellige teknikker, *static headspace-gas chromatography* (HS-GC) og NMR-spektroskopi, præsterede for analyse af væskeprodukter. CO-reduktion bliver ofte udført i basisk elektrolyt, siden dette giver højere selektivitet til C_{2+}-produkter, såvel som lavere udvikling af H_2. Den høje pH kan derimod også føre til uønskede spontane reaktioner imellem de forskellige væskeprodukter i opløsningen. Det viser sig, at acetaldehyd og propionaldehyd er ustabile i basisk opløsning, hvor de polymeriserer og fælder ud. Dette fører til at

aldehyderne er svære at detektere med NMR-spektroskopi. HS-GC, på den anden side, kan måle disse produkter med høj følsomhed.

Ved brug af HS-GC til analyse af væskeprodukter, kunne vi detektere acetaldehyd, et produkt der tidligere var overset, fra CO-reduktion på nanostrukturerede Cu-elektroder. Ved at kombinere eksperimenter og DFT-beregninger, fandt vi ud af at acetaldehyd er et mellomprodukt for CO-reduktion til ethanol. Denne observation er tidligere blevet gjort for polykrystallinsk Cu, hvilket bekræfter at ethanoldannelse går igennem en lignende reaktionsmekanisme på nanostrukturerede og polykrystallinske elektroder. Vi identificerede også kun et enkelt mellemprodukt imellem acetaldehyd og ethanol, der repræsenterer en termodynamisk barriere. Energien til dette mellemprodukt ser ud til at bestemme om ethanolproduktion er favorabelt.

Selv om lovende resultater er blevet rapporteret for CO-reduktion på nanostrukturerede Cu-elektroder, er denne reaktion stadig ikke blevet benchmarket for Cu-katalysatorer. For CO_2-reduktion er polykrystallinske elektroder blevet brugt til at måle robuste benchmarks. Derfor ville vi bruge disse elektroder til at opnå det samme for CO-reduktion. Vi målte relativ høj aktivitet og selektivitet for denne reaktion imellem -0.40 og -0.59 V. Vi observerede en lignende total CO-reduktionsaktivitet som for nanostruktureret Cu når det elektrokemiske overfladeareal (ECSA) er taget med i betragtning. Dette antyder at nanostrukturering hovedsagelig giver ændret produktfordeling, men at det ikke påvirker den egentlige aktivitet i betydelig grad.

En betydelig deaktivering kunne observeres for CO-reduktion på polykrystallinsk Cu. Vi tilskrev hovedsagelig dette til forgiftningen af elektroden med Si fra glasset i cellen. Restrukturering af overfladen er imidlertid nævnt i literaturen som en mulig årsag til ændringer i aktivitet og selektivitet under CO_2- og CO-reduktion. Karakterisering af sådanne fænomener er svært ved brug af *ex-situ*-metoder. Derfor udførte vi *operando*-karakterisering af polykrystallinske Cu-elektroder under CO-reduktion med synkrotronbaserede teknikker. I denne afhandling, beskriver jeg resultater fra røntgendiffraktionsmålinger, hvor vi studerede den gemmensnitlige struktur af de øverste atomlag på overfladen af vores elektroder. Vi fik specielt interessante data da vi holdt øje med en lille del af diffraktionsspektrummet med høj tidsopløsning.

Contents

List of Figures

List of Tables

Acronyms

1-PrOH 1-Propanol.

AcO$^-$ Acetate.

C_1 Single-carbon.

C_{2+} Multi-carbon.

CE Counter electrode.

CV Cyclic voltammetry.

DFT Density functional theory.

ECSA Electrochemically active surface area.

EtCHO Propionaldehyde.

EtOH Ethanol.

FID Flame ionisation detector.

GC Gas chromatography/gas chromatograph.

GDE Gas diffusion electrode.

GDP Gross domestic product.

GIXRD Grazing incidence X-ray diffraction.

HDI Human development index.

HS-GC Static headspace-gas chromatography.

MeCHO Acetaldehyde.

MeOH Methanol.

MS Mass spectrometry.

NMR Nuclear magnetic resonance.

OCV Open-circuit voltage.

OD Cu Oxide derived Cu.

PV Photovoltaics.

PVD Physical vapour deposition.

RE Reference electrode.

SEM Scanning electron microscopy.

TCD Temperature conductivity detector.

WE Working electrode.

XPS X-ray photoelectron spectroscopy.

XRD X-ray diffraction.

List of publications

Appended articles

Paper I

Acetaldehyde as an intermediate in the electroreduction of carbon monoxide on oxide-derived copper

Erlend Bertheussen, Arnau Verdaguer-Casadevall, Davide Ravasio, Joseph H. Montoya, Daniel B. Trimarco, Claudie Roy, Sebastian Meier, Jürgen Wendland, Jens K. Nørskov, Ifan E.L. Stephens, Ib Chorkendorff.

Angewandte Chemie International Edition, 2016, volume **55**, pages 1450-1454.

Paper II

Quantification of liquid products from the electroreduction of CO_2 and CO using static headspace-gas chromatography and nuclear magnetic resonance spectroscopy

Erlend Bertheussen, Younes Abghoui, Zarko P. Jovanov, Ana-Sofia Varela, Ifan E.L. Stephens, Ib Chorkendorff.

Catalysis Today, 2017, volume **288**, pages 54-62.

Paper III
Electroreduction of CO on polycrystalline copper at low overpotentials
Erlend Bertheussen, Thomas V. Hogg, Albert K. Engstfeld, Younes Abghoui, Ib Chorkendorff, Ifan E.L. Stephens.
Submitted, 2018.

Paper IV
Electroreduction of CO_2 on copper electrodes
Erlend Bertheussen, Stephanie A. Nitopi, Søren B. Scott, Albert K. Engstfeld, Xinyan Liu, Karen Chan, Christopher Hahn, Jens K. Nørskov, Thomas F. Jaramillo, Ifan E.L. Stephens, Ib Chorkendorff.
In preparation, 2018.

Other articles – not appended

Paper V
Electrochemical carbon monoxide reduction on polycrystalline copper: Establishing selectivity trends for multi-carbon and oxygenate products as function of potential, pressure and pH
Lei Wang, Stephanie A. Nitopi, Erlend Bertheussen, Marat Orazov, Carlos G Morales-Guio, Christopher Hahn, Thomas F. Jaramillo
Submitted, 2018

1 Introduction

This chapter serves as a general introduction for the work presented later in this thesis. The first section comprises an overview of the motivation for the work that I have carried out. Subsequently, I introduce the concept of electrochemical CO_2 conversion, and discuss some economic perspectives that are relevant to this technology.

1.1 Global warming and sustainable development

The world is facing an energy problem. Increasing population and a rise in energy consumption per capita is leading to a significant increase in global energy demand. Currently, the energy consumed globally is mainly produced using fossil fuels. However, due to our large-scale emission of carbon dioxide (CO_2) and other greenhouse gases, we are currently experiencing significant global warming and resulting climate change. Thus, we cannot rely on the fossil fuels that have built the modern world for much longer. In this section, I present the background for these issues, and possible solutions to help mitigate it.

1.1.1 Fossil fuels – from a blessing to a curse

The industrial revolution that started at the end of the 18th century lay the foundation for the modern society. The invention of the coal fired steam machine started a transition from relying on manual labour to harvesting the large amounts of energy contained in fossil fuels. Since then, a cornerstone of our society has been cheap and readily available energy, from

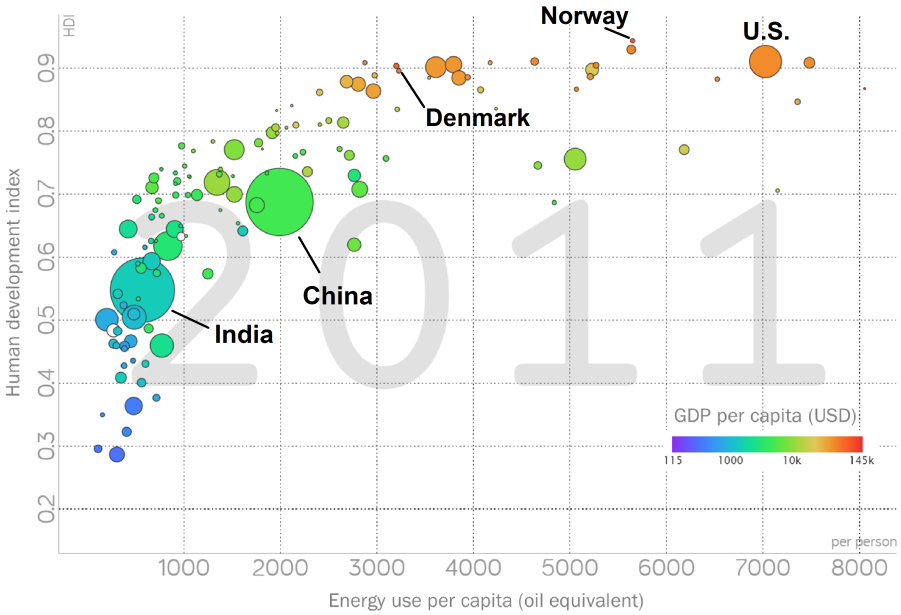

Figure 1.1: Human development index (HDI) for individual countries as a function of energy consumption per capita. Gross domestic products are indicated by the colour scheme, where more red-ish colour means higher GDP and more blue-ish means lower GDP. The size of an individual circle indicates the population of a given country. Figure produced using Gapminder Tools.

coal, petroleum and natural gas. The energy content in a barrel of oil corresponds to approximately 25 000 man-hours, or 12 man-years, of labour.[1] Denmark consumed approximately 10 barrels of oil per capita in 2016.[2] This means that in a non-industrial world, our oil consumption is equivalent to 120 people working year-round to provide enough energy for each Danish citizen, an illustration of the significance of the fossil fuels for the modern industrialised society.

For the parts of the world that have been able/allowed to take part in this development, great prosperity has been the result. There is a strong correlation between the energy consumption of a certain country and its human development index (HDI). In Figure 1.1, this is displayed graphically, where the y-axis shows the HDI and the colour code shows the gross domestic product (GDP) per capita. GDP is a measure of the total value produced in a year in a given country, while HDI is a complex measure taking into account factors such as life expectancy and degree of education in

the population. Data for a number of countries are shown, with each circle representing an individual country (the size of the circle reflects the population of the country). It can clearly be seen that countries positioned at higher HDI in the figure also exhibit higher GDP per capita. Interestingly, both these measures seem to correlate well with the energy use per capita, shown on the x-axis of Figure 1.1. It turns out that a country with low HDI has to significantly increase its energy consumption in order to achieve better conditions for its population. A good example of this is China, that has more than tripled its energy consumtion the last decades in order to improve the HDI of their population.[3] The correlation between energy use and HDI breaks at some point, however, and plateaus. For instance, the HDI of Denmark, Norway and the United States is similar, although they exhibit widely different energy consumption per capita.

The increased availability of energy has had a huge impact on people's lives. At the same time, along with a significant increase in world population,[4] an increased energy consumption per capita has led to a drastic rise in the global energy demand the last decades.[5–7] We still rely heavily on fossil fuels, with 86% of the global energy consumption in 2016 coming from oil, natural gas and coal.[5] Meanwhile, renewables comprise only 10%. We could, in theory, continue to rely on fossil resources for a long time, as the known oil and gas reserves are large enough to satisfy the global energy demand for the forseeable future.[5,7]

However, there are significant issues related to our dependence on fossil fuels. For instance, these resources are distributed very unevenly around the world,[8] which can lead to challenging political situations. Importantly, it is also becoming increasingly clear that we are facing significant negative consequences from the CO_2 released from combustion of fossil energy carriers. CO_2 has been identified as a powerful greenhouse gas, meaning that when present in the atmosphere, it absorbs and reemits infrared radiation from the earth, significantly increasing the surface temperature. We are absolutely dependent on the greenhouse effect for the earth to be inhabitable. If it did not exist, the average surface temperature of the earth would be around -18 °C, instead of the ~15 °C we currently experience.[9] However, the concentration of greenhouse gases in the atmosphere has increased drastically since the beginning of the industrial revolution. In Figure 1.2a, the atmospheric concentration of CO_2, methane (CH_4) and nitrous oxide

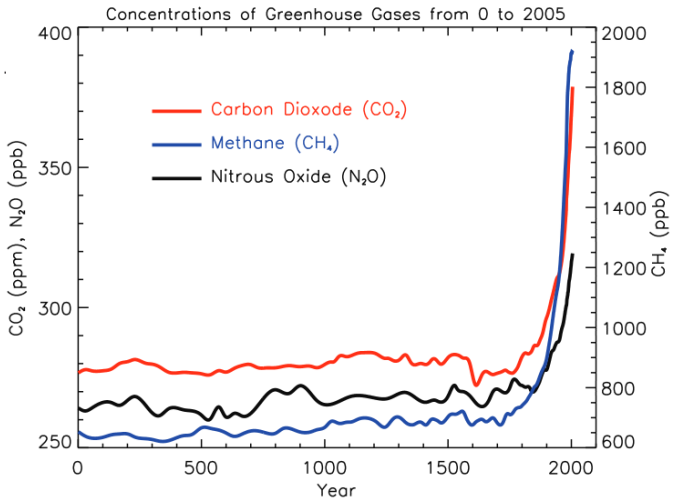

Figure 1.2: Atmospheric concentrations of carbon dioxide, methane and nitrous oxide, the three most important greenhouse gases, from year 0 to 2005. Reprinted from the 2007 IPCC assessment report.[12]

(N_2O), is shown from year 0 to 2005. Only minor fluctuations took place until the beginning of the industrial revolution, where an exponential increase started for all of them. This has resulted in a rising average global temperature that can be correlated to the sum of human activities, of which greenhouse gas emissions is by far the most significant factor.[10,11]

In general, warming of the earth by a few degrees might not sound that dramatic. However, this corresponds to an enormous increase in the total amount of energy contained within the complex system that is the global climate. The Intergovernmental Panel on Climate Change summarises the main influence of this change on regional weather as an increased probability for extreme weather events.[10] This manifests itself in increased occurrence of warm and wet extreme events in particular.

As a result of the negative consequences of accumulating CO_2 in the atmosphere, significant international efforts have been started, aiming to reach a common, global policy for reducing the emission of greenhouse gases, culminating in the Paris agreement of 2015.[14] Virtually every nation in the world signed it, agreeing to take actions in order to reach certain emission goals. Meeting the goals would involve leaving large amounts of the global fossil fuel reserves unburnt.[15] If reached, this is likely to limit the total global warming to less than 2°C compared to the pre-industrial era.[16] Cu-

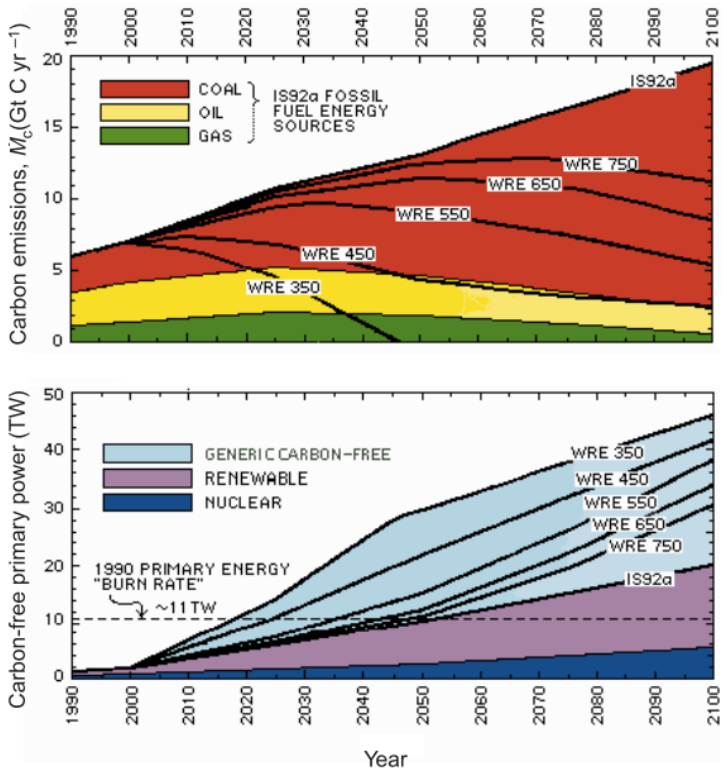

Figure 1.3: Energy implications for stabilisation of atmospheric CO_2 concentration at various values. The curves represent paths that need to be followed to stabilise the CO_2 concentration at the ppm value specified by the number after 'WRA'. Top: Annual global carbon emissions. Bottom: Annual global production of carbon-free power. Reprinted with permission from Hoffert et al.[13] Copyright © 1998, Springer Nature.

mulative CO_2 emissions are useful concepts in order to model how we need to act to reach this goal.[17–19] In an important work in that regard, Hoffert et al. studied the decreases in CO_2 emissions needed throughout the 21st century for stabilisation of the atmospheric concentration at different levels. The results are reproduced in Figure 1.3. In the top panel, the annual emission needed to stabilise the atmospheric CO_2 concentration at different values is shown. Note that when this study was published in 1998, limiting the accumulation of CO_2 to 350 ppm was still possible, albeit unrealistic. The current global mean CO_2 concentration is ~404 ppm,[20] which means that in the 20 years since the publication of this study, the most optimistic scenario is already out of sight. The 450 ppm scenario is now unrealistic,

while stabilisation at 550 ppm would require immediate action to significantly reduce annual CO_2 emissions compared to the current level by the end of the century. The carbon-free primary power needed to reach each of the scenarios is shown in the bottom panel. Evidently, significantly increased carbon-free energy production is needed in order to stabilise the atmospheric CO_2 concentration at an acceptable level.

1.1.2 Toward a sustainable future

In the Paris agreement of 2015, virtually every nation in the world has committed to reduce greenhouse gas emissions.[14] Meanwhile, the global energy demand is projected to increase significantly throughout the rest of this century, due to effects such as social and economic development.[21] Simultaneously, which has to be facilitated by a significantly increased shared of renewables in the global energy production.[13] Thus, developing new and improving existing technologies for sustainable energy production is critical, and arguably represents the most important challenge of the 21st century.

The competition from fossil fuels is tough. Their exceptionally high energy density,[22] makes for highly efficient production, and a resulting low cost per energy unit obtained. Furthermore, since the energy is contained in chemical bonds, they can be stored with little to no energy loss. In particular oil and coal, that are in the liquid and solid state, can simply be stored like they are produced, with no energy loss. Natural gas needs to be compressed, giving slightly lower storage efficiency.

However, there are significant economic incentives for investing in renewable energy sources. It is clear that a future where no measures are taken to mitigate the climate change will result in serious economic losses.[23,24] Based on different scenarios of global temperature rise, reductions in average global income as high as 23% by the end of this century have been estimated, with all regions heavily affected.[24] In addition, the market for renewable energy technologies is bound to increase in the coming decades as almost every nation is committed to taking measures to mitigate greenhouse gas emissions.[14] The private sector is also taking part in the transition, adapting their long-term strategies in order to be in a position to benefit from the sustainable technological development that is bound to occur.[23]

As a result of the increasing investments, renewable energy sources such as solar and wind power have undergone significant development, and are

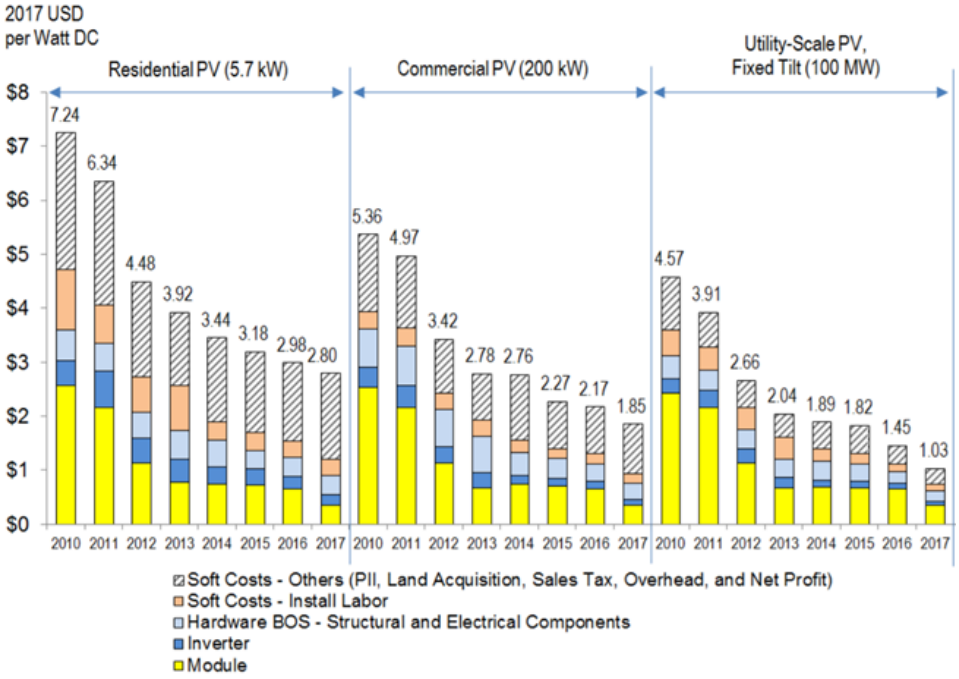

Figure 1.4: Cost of electricity from photovoltaic systems on three different output scales 2010-2017. Reprinted from Fu et al.[25]

becoming increasingly competitive.[26,27] Solar power is the renewable energy source with the largest potential globally. In fact, the sun irradiates Earth's surface with enough energy in one hour to satisfy a year of global energy demand.[7] The key is to find an efficient and cost-effective way to harvest this energy. Photovoltaics (PV), the direct conversion of photons to electricity, is a promising method in that regard. Like any other new technology, the initial cost was high. Due to low efficiency and high system costs, the price of electricity produced from PV was uncompetitive for a long time. However, the technology has experienced a relatively steep learning curve, gradually lowering the price of electricity towards that achieved from fossil-based systems. In Figure 1.4, the cost of electricity from PV systems on different scales in the US since 2010 is displayed, exhibiting a rapid decrease in all cases.

Wind power can be a particularly good alternative for countries with a low mean insolation, for which Denmark is an excellent example. However, the technology is universally applicable and can be installed most places.

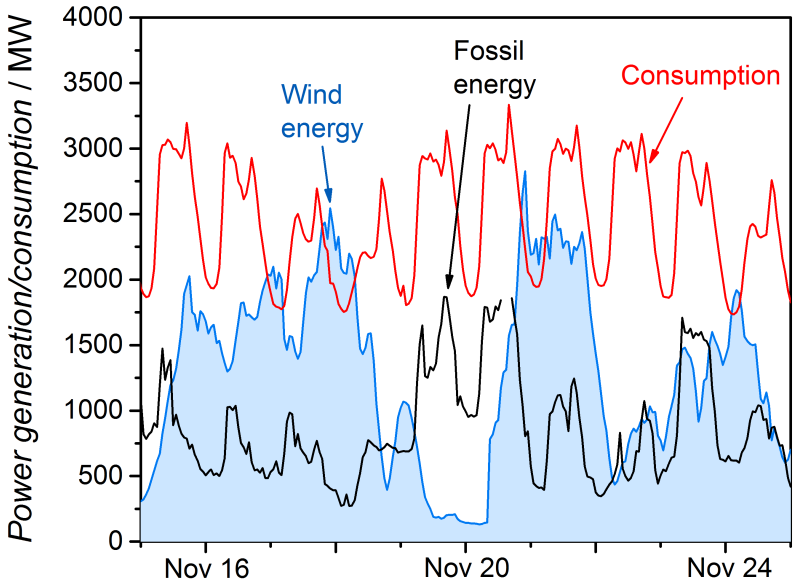

Figure 1.5: Electricity production from fossil fuels (black) and wind power (red), and electricity consumption (red) in Western Denmark during a period of 10 days in November 2017. Data for this plot were retrieved from energidataservice.dk.

The Wind Energy Technology Office of the U.S. Department of Energy estimated in 2016 that recently lowered installation costs will make electricity from wind energy competitive on the U.S. market in a short-term perspective.[27]

Overall, it seems likely that renewable energy production will increase significantly throughout the next decades, giving hope that we can reduce the impact of climate change originating from human activities. This does, however, lead to new challenges. Importantly, PV and wind power, two of the renewable energy technologies with the largest global potential, both deliver fluctuating output. Figure 1.5 shows the electricity consumption in Western Denmark in November 2017, together with electricity production from fossil fuels and wind power. The consumption fluctuates with every day/night cycle. The wind power electricity output also fluctuates, but evidently not in synchronisation with the demand. This leads to certain situations where wind energy can supply more than the entire electricity demand by itself. In other periods, little or no wind power is produced. Currently, these irregularities can be compensated for by increasing/decreasing the electricity production from fossil fuel power plants, and/or by trading

electricity with neighbouring countries. When the share of wind power in the energy system is significantly increased, however, these measures are no longer sufficient to smoothen out discrepancies between production and demand. As a result, energy storage technologies are needed to provide a stable electricity supply in the future.[26,28]

1.2 The need for energy storage

Our current energy system relies heavily on fossil resources for energy storage, as described previously. Such fuels exhibit high energy density,[22] which leads to efficient storage and transportation of large amounts of energy. Renewable sources, on the other hand, produce electricity, which cannot be stored as readily. With the increased electrification of the energy system from the larger implementation of renewable energy sources, electricity storage is needed. Batteries are relatively efficient for short-term storage of low to intermediate amounts of energy.[29,30] For long term storage and large-scale purposes, on the other hand, different solutions are necessary.

1.2.1 What about carbon?

At the same time, electricity production and energy storage is not the only sector where fossil fuels currently play an important role. A large number of chemicals and materials used both commercially and industrially are derived from petroleum.[31] Examples include materials such as plastic, as well as chemicals such as hydrogen, ammonia, methanol. Novel technologies for producing these chemicals without releasing large amounts of CO_2 are needed.[32] A promising short-term solution could be to keep using fossil fuels for production of important chemicals and materials, and subsequently capture the CO_2 emitted and store it by pumping it into underground formations.[33,34] This would be technologically relatively straightforward, and has the potential to be implemented relatively quickly.[33] There are, however, uncertainties involved. Importantly, it is not clear whether leakage of CO_2 with time can be completely avoided from the underground storage.[1,7,33] With the immense amount of CO_2 that needs to be stored (tens of billions of tons per year), even very small leak rates could be enough for the emitted flux to outcompete the benefits of carrying out the storage in the first place.[7] Furthermore, energy would be needed to pump the CO_2

into the reservoirs, lowering the economic viability of the process.

An alternative approach that is receiving increasing attention is the storage of electricity in chemicals. This could both meet the demand for energy storage technologies and alternative means of chemical production. H_2 is one example of a possible sustainable energy carrier. It is currently a chemical of high demand, produced mainly through steam reforming of natural gas and other fossil fuels.[35] One of its main industrial uses is for production of chemicals, with ammonia as an important example. It is used as a fertilizer, and is thus crucial to feed a global population that is projected to keep growing throughout this century.[36] A potentially carbon-neutral technology for H_2 production is the splitting of water into H_2 and O_2 by electrolysis.

However, many industrially and commercially important chemicals need building blocks containing carbon. This could be provided by recycling the captured CO_2 and converting it into valuable products. The CO_2 would then be a building block for producing the chemicals currently derived from fossil fuels. In Figure 1.6, an overview of a possible energy landscape for a future without fossil fuels is shown. The abundant precursors CO_2, N_2 and H_2O can be converted into fuels, chemicals and materials through thermal or electrochemical processes, using renewable electricity. Importantly, the combustion of any fuels in this scheme will be carbon-neutral, since the CO_2 is already captured from the atmosphere. If captured CO_2 is instead converted to chemicals and materials not intended for combustion, this would be carbon-negative process, a highly desirable concept to reverse the current accumulation of CO_2 in the atmosphere. One example of a chemical that could play an important in a future energy landscape like the one shown in Figure 1.6 is methanol. If produced selectively and efficiently, it could substitute fossil fuels without major modificantions to the current infrastructure. Furthermore, it can be converted to different chemicals.[1]

Thermal processes have existed for the production of many of the desired chemicals for decades. Examples include the vital production of ammonia for fertilisers, as well as methanol synthesis.[37–39] Therefore, these processes have great advantages in terms of technological maturity and efficiency. However, they occur under high temperatures and pressures. Methanol synthesis, as an example, occurs at ~250 °C and 50-100 bar.[39] As a result, this way of producing chemicals is highly centralised in order to keep the

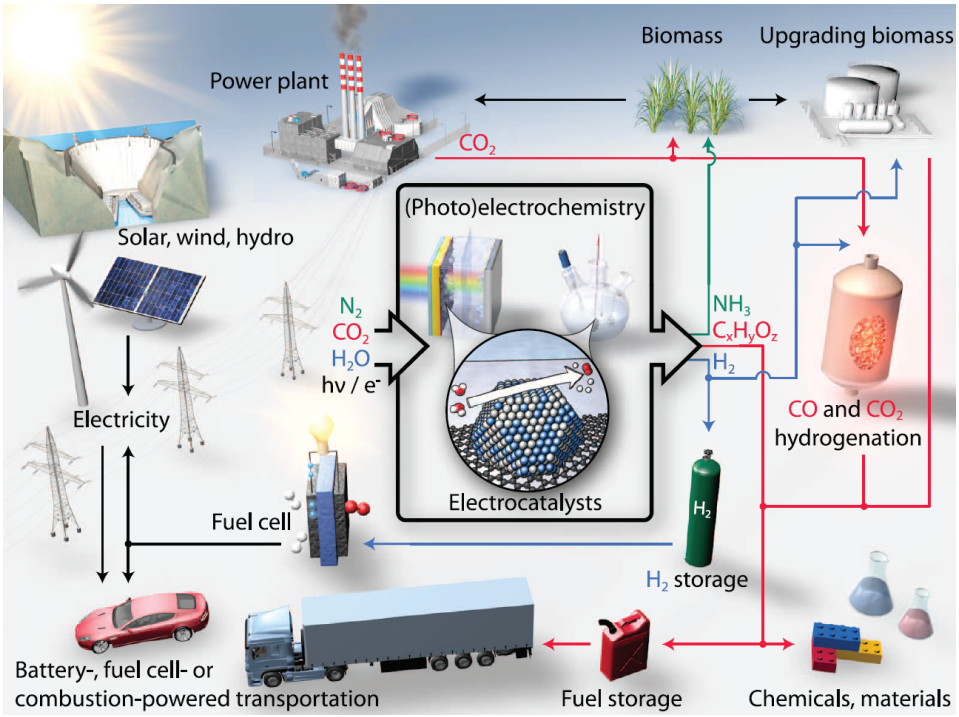

Figure 1.6: A proposed future energy landscape where all processes are carbon-neutral or carbon-negative. From Seh et al.[32] Reprinted with permission from AAAS.

cost of production down, with subsequent transport to the point of consumption. Electrochemical processes are emerging as alternatives. They often exhibit a lack of technological maturity, and resulting high cost and low efficiency of production. However, they also give important advantages. As the market penetration of renewable energy sources rises, the overall energy system is experiencing increasing electrification. Furthermore, renewable electricity generation is typically more delocalised than the fossil fuel-based production, where several smaller units are needed to produce the same amount of energy as fossil fuel power plants. Electrochemical systems exhibit high scalability and can, in principle, be operated at ambient temperature and pressure, giving a high degree of compatibility with renewable energy sources.

Due to the scale of the challenge that is making our society independent from fossil fuels, however, any technology for conversion of CO_2 and the other precursors for important chemicals will be needed. Furthermore, it

is likely that CO_2 storage, which was discussed at the beginning of this section, will provide an important alternative that allows us to keep making important chemicals from fossil fuels, without accumulation of CO_2 in the atmosphere. This can be implemented on a relatively short time scale, which is important to limit the accumulative CO_2 emissions. However, the remainder of this thesis will focus on electrochemical reduction of CO_2, as one piece in the puzzle.

1.2.2 Economic viability of electrochemical CO_2 conversion

Before diving into the science of electrochemical CO_2 reduction, it is instructive to discuss various economic aspects of the technology. In the following, I will briefly give some perspective about important factors influencing the commercial viability of the process. Note that the efficiency and selectivity of the conversion process will be discussed further in the following chapter, and left out for now. Note also that this section is based partly on a review article I am participating in writing, that is in preparation.[40]

The cost of production of chemicals from CO_2 reduction is directly influenced by the cost of the electricity used. Thus, cheaper electricity will help making the technology more competitive. As discussed previously, electricity from renewable sources such as wind power and PV has become significantly cheaper over the last decades, and cost is expected to continue dropping. An interesting concept in that regard is peak, or excess energy production. When the share of renewables in the total power system increases, electricity production is likely to exceed demand at times of high production. Developing means of storing energy during periods of peak production is one of the important motivating factors for CO_2 reduction. The cost of electricity will decrease significantly in such a situation, since it is based on supply and demand. Thus, the production cost for chemicals in periods of high production will be lowered, if only taking the price of electricity into account.

It is, however, important to keep in mind the influence of the capital cost of a CO_2 reduction system on the resulting cost of any chemicals produced this way. If running the reaction only during peak production of electricity, the system will be idle for a significant fraction of its potential operating time, significantly increasing the influence of the capital investment. This will be particularly true in the early stages of commercial implementation,

Table 1.1: Value and size of market for selected CO_2 reduction products. *These are values for natural gas, of which methane is the main constituent. Table prepared by Søren B. Scott, as part of a review article currently in preparation.[40]

Product	**Market price / USD tC^{-1}**	**Global production / MtC $year^{-1}$**
Formic acid (HCOOH)	3800	0.19
Methanol (CH_3OH)	750	24
Methane (CH_4)	160*	1700*
Acetaldehyde (CH_3CHO)	1840	0.69
Ethanol (C_2H_5OH)	1030	38
Ethylene (C_2H_4)	1400	120

when the capital cost will be at its highest. As has been the case for various novel technologies, such as photovoltaics, technological and practical advances will gradually lead to cheaper materials and installation. At the early stages of commercialisation, though, it is likely that a CO_2 reduction system will have to run constantly at its most efficient operating conditions in order to optimise the cost-competitiveness of the products.

Another important factor determining the economic viability of CO_2 reduction is the value of the compounds produced. It directly determines which products are economically feasible to make assuming a certain production cost. In Table 1.1, the market value and size of some relevant products are shown. They are both key factors to evaluate the role of these chemicals in the market. Any chemicals produced can be listed in three different categories; (i) fine chemicals, meaning chemicals with high value, but small market, (ii) bulk chemicals, meaning chemicals with intermediate to high value and a relatively large market and (iii) fuels.

This is best illustrated with specific examples; formic acid is a valuable product, and thus attractive to produce.[41] However, its marked is small, limiting the potential for large-scale production. If the market is flooded with product, the price will drop significantly, and the incentive for producing it disappears. C_2H_4, on the other hand, exhibits both a relatively high value and a large market. Thus, significant production will be possible before being limited by the market size. As mentioned above, it is

also one of the compounds produced with the highest selectivity from CO_2 reduction on polycrystalline Cu, giving the potential for further selectivity improvements. Finally, it is a gaseous product, meaning that it does not have to be manually separated from the large number of liquid products in the electrolyte. If produced together with other hydrocarbons, processes exist for separation of those.[42]

The case of chemicals that can be used as fuels warrants further discussion. Please note here that a certain compound might fall under category (i) or (ii) as a chemical, and still exhibit high flammability, making it suitable for use as a fuel. Thus, an important consideration for the prospect of producing sustainable fuels from CO_2 reduction, is the competition from fossil fuels. Taking C_2H_5OH as an example, it has a market price of ~1000 USD tC^{-1}. However, this is what it is worth as a chemical. If it were to be used as a fuel, the price would have to be pushed down towards that of fossil fuels. An example of low cost of fossil fuels is CH_4, the main constituent of natural gas. It can be produced very efficiently, as reflected in its low market value of 160 USD tC^{-1}, as shown in Table 1.1.

As a result of the strong competition from fossil resources, production of fuels from CO_2 reduction is currently challenging to make economically feasible. Initially, only chemicals that can be produced with high efficiency and activity, i.e. mainly the $2e^-$ products $HCOO^-$ and CO, or specialty chemicals with particularly high value, are likely to be able to compete with existing solutions. However, as commercial systems are installed and the technology developed further, together with a further decrease in the cost of renewable electricity, the cost of chemical production from CO_2 reduction is likely to go down. If this is the case, production of commodity chemicals of intermediate value can become competitive, an important step for large-scale implementation. The final step, cost-competitive fuel production, lies further ahead, after significant development of the technology. However, if this can be realised, a door to large-scale implementation is opened. Fuels exhibit particularly large markets, as shown for the case of methane in Table 1.1

When aiming to produce fuels, energy density is an important metric. In Figure 1.7, the volumetric and gravimetric energy densities (or energy density and specific energy, respectively) of various energy carriers are shown, together with thermodynamic upper limits for lithium-ion and lithium-air

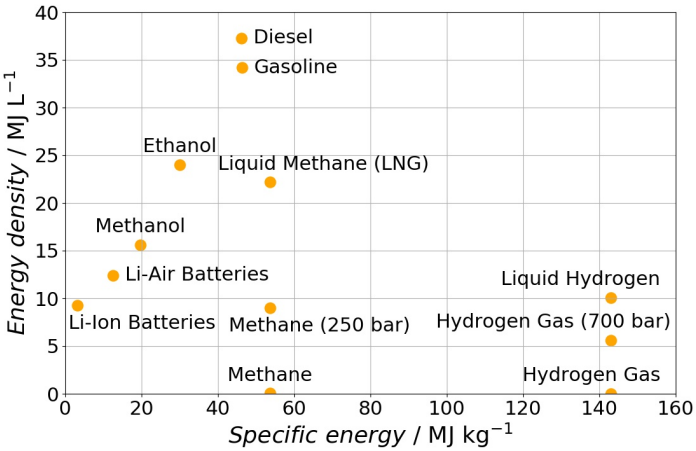

Figure 1.7: Energy densities of various chemicals and storage technologies. Data for chemicals are calculated using tabulated thermodynamic data.[22] The data for batteries are upper thermodynamic limits, and were obtained from Gallagher et al.[43] The plot is created using openly available Python code made by Scott Dial.[44]

batteries.[43] While batteries represent an excellent energy storage technology for many purposes due to their high energy transfer efficiency, the low energy density is a significant limitation for other purposes. H_2 was previously mentioned as a promising chemical energy carrier. While exhibiting very high specific energy, even H_2 in its liquid state has relatively low energy density, leading to bulky storage. Diesel and gasoline, on the other hand, exhibit excellent energy density. This is another reason for their high competitiveness. Amongst the products relevant to CO_2 reduction, alcohols show relatively high energy density, with ethanol more so than methanol.

Throughout this section I have presented various economic and technical aspects regarding which products would be preferred from CO_2 reduction. However, as I will demonstrate in the following chapter, we do not currently understand CO_2 reduction well enough to control the selectivity towards individual products. Thus, these considerations are important to keep in mind, but we cannot yet use them to pick which products to make. Even if a certain product is not currently commercially useful, however, any insight into how selectivity can be steered in different directions is highly valuable at this stage. Therefore, understanding trends in selectivity will be a main

focus for the remainder of this thesis. I will make comments on the commercial relevance of various products presented throughout, but this will not be my main focus.

2

Electrocatalysis and CO_2 reduction

In the previous chapter, I presented the motivation for performing CO_2 reduction, and various economical and commercial aspects that are important to keep in mind when developing the technology. However, the field is still pretty young, and more understanding is needed. In this chapter, I give an overview of the current state of the field, and point out particular areas that could benefit from more attention.

The chapter is partly based on a review article that is currently in preparation,[40] where I made significant contributions in the preparation of the first draft. I am the shared first author with Stephanie A. Nitopi, a PhD student of the Jaramillo group at Stanford University. The paper is a collaborative effort between several members of my group and the Jaramillo and Nørskov groups of Stanford University. Details can be found at the end of this thesis, where the abstract, outline and author details are attached. In addition to Stephanie and me, Albert K. Engstfeld and Søren B. Scott from my group at DTU, and Karen Chan from the Nørskov group at Stanford University, participated in writing the first draft. The other authors participated in the planning and revision of the draft. I wrote the section about nanostructured Cu catalysts, and had a lead role together with Stephanie in revising the sections written by the other authors and merging the separate sections into the final manuscript. For any figures and tables that I have not prepared myself, this is stated in the caption.

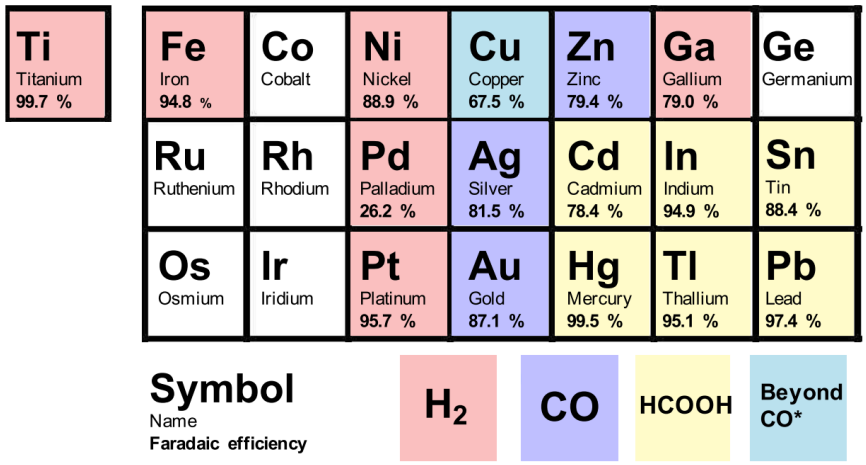

Figure 2.1: Section of the periodic table showing the main CO_2 reduction product from various transition metals. The colour code illustrates the product, while the number at the bottom of each element shows the Faradaic efficiency to that product. The data were collected by Hori et al. for chronopotentiometric CO_2 reduction in 0.1 M $KHCO_3$ at -5 mA cm^{-2}.[45] The figure is reprinted with permission from Bagger et al.[46]. Copyright © 2017, John Wiley and Sons.

2.1 Electrochemical CO_2 reduction on Cu

In pioneering work by Hori et al., CO_2 reduction on various transition metals in aqueous electrolyte was studied. The authors showed that the metals can be grouped after their main product,[45,47] as illustrated in Figure 2.1.[46] It turns out that quite a few of them, such as Pt, Ni and Fe, mainly produce hydrogen (H_2) from water splitting, even in the presence of CO_2. Other metals, including In, Sn and Pb, mainly produce formic acid/formate ($HCOOH/HCOO^-$). Note that while HCOOH and $HCOO^-$ are different compounds, they are both used to refer to the the same CO_2 reduction product. HCOOH is likely to be the compound produced at the electrode. However, because of its low pK_a (3.8[22]), it is deprotonated at neutral or higher pH. Since all experiments discussed in this thesis are conducted at pH ~7 or higher, HCOOH will always be present in the electrolyte in the deprotonated form. As a result, HCOOH is used whenever the intrinsic reaction on the electrode is discussed, whereas $HCOO^-$ is used when discussing product analysis of the bulk electrolyte.Acetic acid and acetate (CH_3COOH/AcO^-), which will be discussed further below, are differenti-

Table 2.1: Known products from CO_2 reduction on polycrystalline Cu, shown together with their equilibrium potentials and the number of electrons used to produce them. Reprinted with permission from Kuhl et al.[48]. Copyright © 2012, Royal Society of Chemistry.

Product	# e⁻	E	Product	# e⁻	E
Formate 	2	−0.02	Acetaldehyde 	10	0.05
Carbon monoxide 	2	−0.10	Ethanol 	12	0.09
Methanol 	6	0.03	Ethylene	12	0.08
Glyoxal 	6	−0.16	Hydroxyacetone 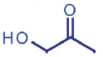	14	0.46
Methane 	8	0.17	Acetone 	16	−0.14
Acetate 	8	−0.26	Allyl alcohol 	16	0.11
Glycolaldehyde 	8	−0.03	Propionaldehyde 	16	0.14
Ethylene glycol 	10	0.20	1-Propanol 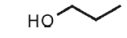	18	0.21

ated in the same manner. The third group of metals are Zn, Ag and Au, which mainly facilitate carbon monoxide (CO) formation. Both formic acid and CO are formed by the transfer of two electrons ($2e^-$ products). Among the metals that were studied by Hori et al., Cu stands out as the only pure metal that can catalyse CO_2 reduction to products where more than two electrons are transferred, such as hydrocarbons and oxygenates. This has made Cu a highly studied material for this reaction.

Building further on these initial results, Kuhl et al. studied CO_2 reduction on polycrystalline Cu in a cell with a large electrode surface area to electrolyte volume ratio.[48] This enabled them to detect liquid products with particularly high sensitivity. As a result, they detected and quantify as many as 16 different CO_2 reduction products, which are listed in Table 2.1.[48] In addition to the CO_2 reduction products, H_2 is produced from water splitting, as a competitive side reaction. The large number of products

shows that Cu has the potential to facilitate the production of a wide range of chemicals from electrochemical reduction of CO_2. However, no individual compound is produced with a Faradaic efficiency above 40%.[45,47,48] A reason for this behaviour is that most of the compounds have equilibrium potentials within ±200 mV of 0 V. Thus, at the potentials where CO_2 reduction takes place, there will be a significant thermodynamic driving force for production of all of them. The low selectivity towards individual products represents a challenge for the aim to commercialise the technology, leading to the need for energy-intensive separation processes.[?,49,50] In addition low selectivity, high overpotentials are required for formation of $>2e^-$ products. Significant CO_2 reduction activity can only be achieved close to or cathodic of -1 V vs. RHE on polycrystalline Cu.[45,48] This leads to energy losses in terms of heat evolution at the electrode/electrolyte interface region.[51]

Still, Cu is the only monometallic electrocatalyst that facilitates significant CO_2 reduction to $>2e^-$ products. As a result, a large number of studies have been trying to explain the behaviour of Cu for this reaction. In particular, understanding why Cu is a unique catalyst for CO_2 reduction to $>2e^-$ products could yield valuable information about how to improve the selectivity towards particular products. Furthermore, gaining insight about the origin for the high overpotentials is important when aiming to design strategies for mitigating them. Computational studies of the thermodynamics of CO_2 reduction using density functional theory (DFT) has been an important tool in understanding the intrinsic behaviour of Cu. In the following, I will discuss some of this work.

2.2 Electrocatalysis and the origin of overpotentials

To understand processes that are occurring on the electrode surface, it is important to know the role of an electrocatalyst. The simple textbook definition of a catalyst is a substance that increases the rate of a reaction, without being consumed itself.[31] Herein, only heterogeneous catalysts are discussed, meaning that the catalyst material is in a different phase than the reactants and products. In this case, the catalyst is solid-phase, while the reactants and products are liquids and/or gases. Electrocatalysis means the catalysis of an electrochemical reaction, which involves charge transfer

between an electrode (the catalyst) and the reactant/intermediates. The reaction rate depends on the potential drop between the surface and reactant, which is directly influenced by the electrode potential. As a result, this easily tunable parameter can be used to control the reaction taking place.[52] In principle, understanding the fundamentals of CO_2 reduction on Cu means gaining insight about how relevant species behave on the electrode surface under applied potentials.

2.2.1 What makes Cu special?

This approach has been used to explain the selectivity of various metals to certain products, and importantly, why Cu is a unique electrocatalyst for CO_2 reduction. Bagger et al. proposed a simple model based on the binding energies of adsorbed CO (CO*) and H (H*), as displayed in Figure 2.2.[46] Their calculations indicated that all metals catalysing H_2 efficiently (indicated in red in Figure 2.2) are able to adsorb H* via underpotential deposition. This means that they have a certain H* coverage at more anodic potentials than the H_2 evolution equilibrium potential, illustrated by their negative binding energies to H*. At the same time, these metals exhibit negative CO* binding energies. Thus, they are in theory able to catalyse the formation of $>2e^-$ products. However, they catalyse H_2 evolution much more efficiently, and CO_2 reduction is outcompeted. Formation of small amounts of $>2e^-$ products, such as methane and methanol, has been reported experimentally for Ni, Fe, Pt and Pd.[45,53].

All other metals studied by Bagger et al. exhibit H* binding energies that are almost zero or positive. As a result, they can facilitate CO_2 reduction without overwhelming competition from H_2 evolution. Metals with weak *CO binding facilitate either CO or HCOOH formation. Which of the two is the main product depends on the H* binding energies, according to the authors. Metals that exhibit *H binding at CO_2 reduction potentials seem to mainly lead to CO production (shown in blue), while those that bind *H even weaker yield HCOOH formation (shown in yellow). Finally, Figure 2.2 shows the unique nature of Cu for further reduction of CO. It is the only metal that does not exhibit H underpotential deposition, while still binding CO. The former allows for CO_2 reduction with significant selectivity, without getting outcompeted by H_2 evolution. Meanwhile, the latter is necessary to facilitate formation of $>2e^-$ products, as metals with weak CO

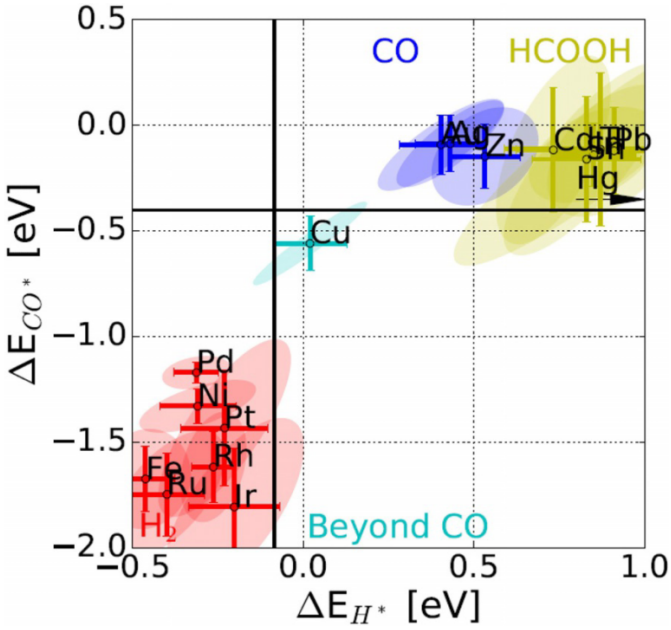

Figure 2.2: *CO and *H binding energies for various transition metals. The colour code describes the main product from CO_2 reduction on the relevant metal, where red illustrates H_2 blue CO, yellow HCOOH and cyan represents $>2e^-$ products. Reprinted with permission from Bagger et al.[46]. Copyright © 2017, John Wiley and Sons.

binding only exhibit production of CO or HCOOH.

2.2.2 The origin of overpotentials

Another important point to address in relation to the behaviour of Cu for CO_2 reduction is the origin of the high overpotentials needed for formation of $>2e^-$ products. In order to explain this, it is instructive to further introduce concepts of catalysis and electrocatalysis. To illustrate these concepts, I will start by how they can be applied to the case of H_2 evolution. Subsequently, I will move on to discuss CO_2 reduction, by using the specific case of methane formation as an example.

$2e^-$ reactions: The case of H_2 evolution/oxidation

The simplest electrocatalytic reactions involve only one intermediate and the transfer of two electrons (e^-) and protons (H^+). H_2 evolution and oxidation

is an example of such a reaction, for which the reversible chemical equation is shown in eq. (2.1)

$$2\,H^+(aq) + 2\,e^- \rightleftharpoons H_2(g) \tag{2.1}$$

The performance of a certain catalyst towards this reaction can be explained by how strongly the intermediate binds to the surface. This binding strength can be measured, or estimated using DFT. In Figure 2.3, free energy diagrams calculated using DFT for H_2 evolution/oxidation on the metals Au, Pt, Ni and Mo are shown.[54] At the thermodynamic equilibrium potential of the reaction (0 V), the reactants and product exhibit the same free energy. Au binds *H weakly, meaning that it is unlikely that the reactants adsorb to the surface in the first place. This is reflected in a thermodynamically strongly uphill reaction step in the free energy diagram for adsorbing H* on Au. Ni and Mo, on the other hand, bind H* strongly. Now, the adsorption of the intermediate represents a downhill step. However, the desorption of the intermediate to form free H_2 is strongly uphill instead, making for poor catalysis. Pt, on the other hand, exhibits an intermediate H* binding strength. As a result, both the adsorption of H* and desorption of H_2 exhibit relatively flat free energy profiles, and catalysis occurs efficiently. This picture is reflected in experimental reports, where Pt appears as an ideal catalyst for this reaction.[55,56]

This concept has been formulated in what is known as the Sabatier principle.[57] It states that an ideal catalyst is one with a binding energy to reaction intermediate(s) that is neither too weak, nor too strong. This is often also called the volcano relationship, a term originating from the volcano-shaped curve that arises if the activity of various catalysts is plotted against their binding strength to intermediate(s), with the top of the volcano at an intermediate binding strength.[54,56,58,59] This principle has been used to design improved electrocatalysts, for instance for O_2 reduction.[60–62]

>2e⁻ reactions: The case of CO_2 reduction to methane

The Sabatier principle can be directly applied for any $2e^-$ reaction with a single intermediate. The picture does, however, become more complex when the electrochemical reaction involves more than one intermediate, i.e. more than 2 H^+/e^- transfers. I will illustrate the reason for this with the case of methane formation (CH_4) from CO_2. This reaction requires the transfer

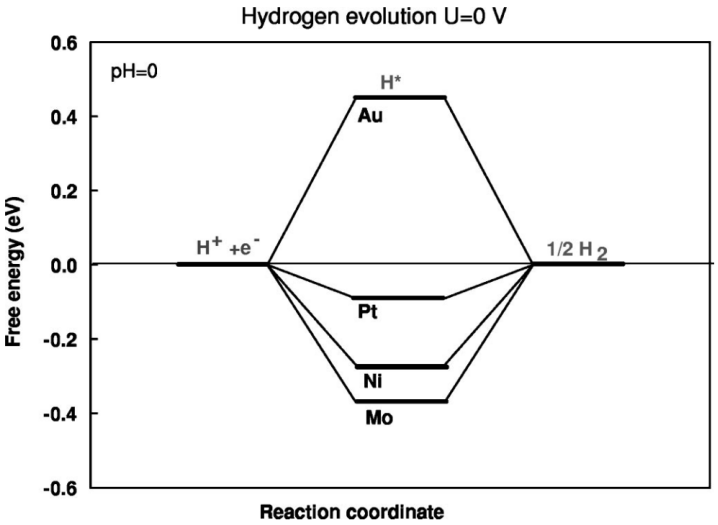

Figure 2.3: Free energy diagram for H_2 evolution/oxidation on Au, Pt, Ni and Mo. Reprinted with permission from Nørskov et al.[54]. Copyright © 2005, The Electrochemical Society.

of 8 H^+/e^-, while many CO_2 reduction products require 10 or more. The chemical equation for CO_2 reduction to CH_4 is shown in eq. (2.2).

$$CO_2(g) + 8\,H^+(aq) + 8\,e^- \longrightarrow CH_4(g) + 2\,H_2O(l) \tag{2.2}$$

A free energy diagram for this reaction on C, is displayed in Figure 2.4, calculated using DFT. The black steps represent the pathway at 0 V. Note that the equilibrium potential for this reaction is 0.17 V, as seen in Table 2.1. Thus, 0 V is equivalent to 170 mV of applied overpotential. The surface binds the various intermediates with different strength, leading to some steps being uphill and some downhill at this potential. According to the free energy diagram, a potential of -0.74 V (910 mV overpotential) needs to be applied before the pathway is thermodynamically downhill, as marked in red in the figure.

Now, if following the Sabatier principle, one approach to improve the catalysis could be optimisation of the binding of one of the intermediates. It turns out, however, that on a macroscopic surface, all the different intermediates bind to the surface in a similar way. This means that if a catalyst is developed that binds an intermediate in an ideal manner, another intermediate will be bound too strongly or too weakly. Thus, the

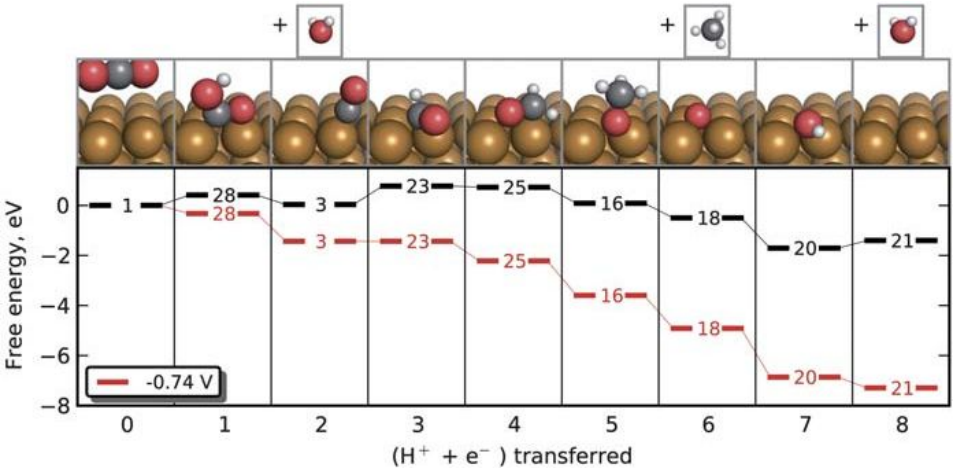

Figure 2.4: Free energy diagram for CH_4 formation from CO_2 reduction on Cu. The black pathway represents a potential of 0 V, while the red represents -0.74 V. Reprinted with permission from Peterson et al.[63]. Copyright © 2010, Royal Society of Chemistry.

steps that are thermodynamically uphill in Figure 2.4 will remain uphill on another catalyst with different binding strength. This concept is called scaling relations, and is a well-known limitation for electrocatalysis of complex reactions.[32,64–66] In Figure 2.5, the binding energies of the various intermediates in methane formation on different metals is shown, underlining the effect of scaling relations. It can be seen that the various intermediates bind with different free energy. Nevertheless, replacing the catalyst with a metal that binds one intermediate stronger clearly also leads to stronger binding to the others.

Overcoming scaling relations could be key to developing new CO_2 reduction electrocatalysts with improved energy efficiency.[32] Various strategies have been proposed to achieve this, such as three-dimensional binding, achieved through alloying/doping[65,67] or confinement,[68], or the addition of promoters/ligands to the electrolyte.[64]

2.2.3 Which Cu facets are the most active for CO_2 reduction?

The scaling relations discussed in the previous section represent a theoretical lower limit for the overpotential that needs to be applied to drive

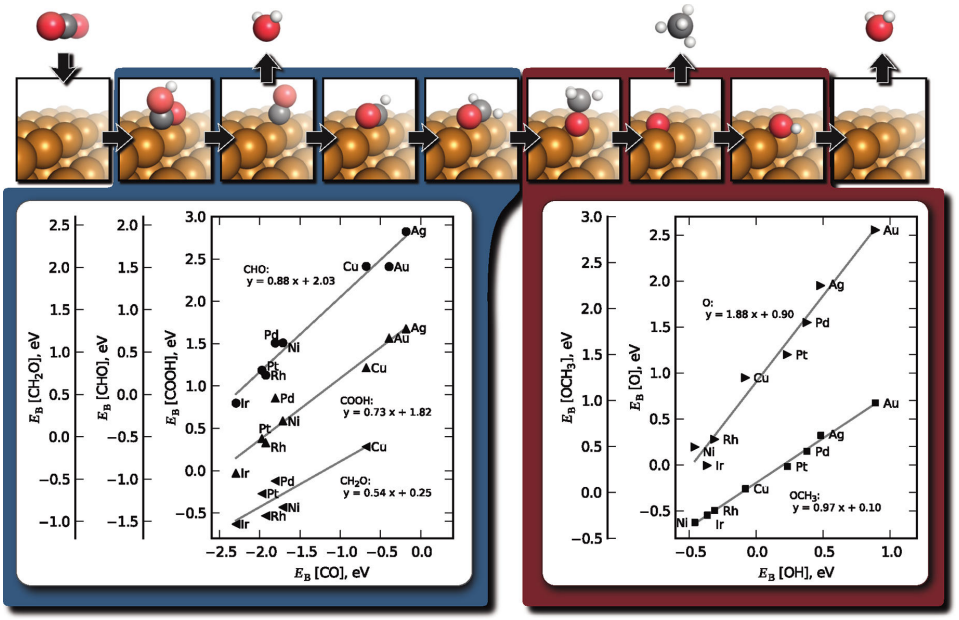

Figure 2.5: The binding energy of various metals to the intermediates in CO_2 reduction to CH_4, illustrating the scaling relations. Reprinted with permission from Peterson and Nørskov[64]. Copyright © 2012, American Chemical Society.

CO_2 reduction. However, the binding energies of the intermediates for a certain reaction is necessary to avoid even worse performance. Durand et al. used DFT calculations to determine that Cu(211) exhibits lower theoretical overpotential for both methane and CO formation than Cu(111) and Cu(100).[69] This indicates that undercoordinated sites perform better for this reaction than terraces. Liu et al. used DFT to calculate barriers between different intermediates for CO reduction, and microkinetic modelling to calculate the resulting reaction rate. CO was chosen because it is a key intermediate in CO_2 reduction to $>2e^-$ products. The resulting theoretical polarisation curves for Cu(111), Cu(100) and Cu(211) are displayed in Figure 2.6, together with experimental data for CO_2 reduction to $>2e^-$ products on polycrystalline Cu. According to these calculations, there is a difference of several orders of magnitude between the activity of Cu(211) and Cu(100), and an additional several orders of magnitude down to Cu(111). The experimental data exhibit somewhat higher activity than Cu(100), which is reasonable because of the presence of some undercoordinated sites on polycrystalline electrodes.

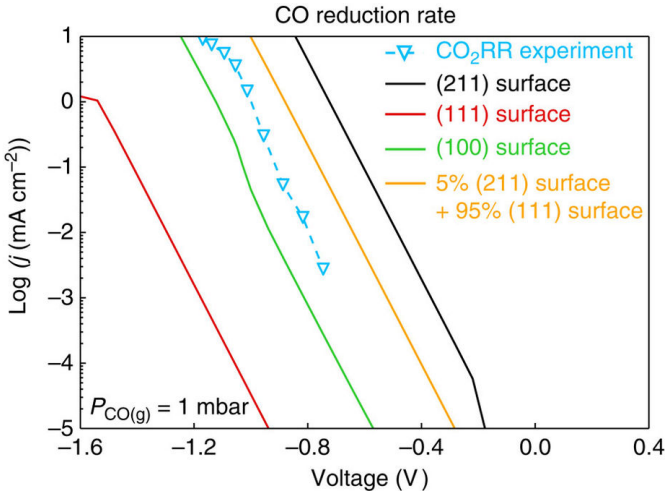

Figure 2.6: Theoretical polarisation curves for CO reduction on Cu(111), Cu(100) and Cu(211) surfaces, as calculated by DFT. The experimental data represent the activity towards $>2e^-$ products from CO_2 reduction on polycrystalline Cu, as reported by Kuhl et al.[53] The figure is reprinted from Liu et al.[70]

Experimental data from Cu single crystals show different results than these DFT calculations. Hori et al. performed CO_2 reduction at a series of Cu single crystals, including planar surfaces and crystals with varying step density.[71,72] They observed some difference in activity between Cu(111) and Cu(100), but little to no difference between Cu(100) and a number of different stepped surfaces. Hahn et al. prepared films that were epitaxially grown in the Cu(111), Cu(100) and Cu(751) directions.[73] All these samples yielded similar activity. One possible explanation for the discrepancy between theory and experiments regarding activity of undercoordinated vs. planar surfaces could be the quality of the electrodes used experimentally. Although single crystals are accurately cut to represent a certain surface orientation, some degree of imperfection is inevitable.[74,75] Based on the DFT calculations, even a small amount of steps can yield significant activity.

Although experiments did not show significant differences in activity between planar and stepped surfaces, some conclusions can be drawn about the product distribution. Many of the stepped surfaces exhibit significantly increased selectivity towards oxygenates.[71–73] Furthermore, certain orientations, such as Cu(100) surfaces with various density of (111) steps, exhibit significant selectivity towards C_{2+} products and suppression of C_1

compounds.[71]

2.3 Nanostructured and bimetallic Cu catalysts

Copper is a promising CO_2 reduction catalyst due to its ability to facilitate production of $>2e^-$ products. However, in its polycrystalline form, major drawbacks such as low energy efficiency and selectivity makes commercial applications unrealistic. Different methods have been applied to improve the performance of Cu electrodes for production of $>2e^-$ compounds. Two approaches that are widely used in the literature are preparing bimetallic catalysts containing Cu, and nanostructuring. In this section, I will start by introducing bimetallic electrodes briefly. Subsequently, I will discuss various efforts involving nanostructured electrodes in more depth.

2.3.1 Bimetallic electrodes with Cu

Preparation of bimetallic electrodes has previously been used to improve the catalysis of other electrochemical reactions, such as O_2 reduction.[60] Various effects, including electronic ligand and strain effects and geometric ensemble effects, can lead to changes in the surface reactivity, and can thus influence catalysis.[76–78] As discussed in the previous section, alloying has also been suggested as one approach to move beyond the limitations of scaling relations.[32,65]

A large number of studies on Cu bimetallic electrodes for CO_2 reduction have been reported. These can be grouped after the main product from the second metal used, which was shown in Figure 2.1: (i) Cu with H_2 producing metals, (ii) Cu with metals producing formic acid and (iii) Cu with CO producing metals. In the following, some relevant examples spanning the three groups will be discussed.

(i) In the first group, bimetallics with the H_2 producing metals Pt, Ni and Fe have been reported.[79–84] These systems appear to mainly lead to increased Faradaic efficiency towards H_2 formation. In a previous study from my group, Varela et al. propose a reason for this behaviour.[83] They studied CO_2 reduction on thin Cu overlayers (~1 monolayer) on Pt single crystals, deposited by underpotential deposition. The high H_2 selectivity could be attributed to the overlayers becoming destabilised under reaction conditions. Due to the high affinity of Pt to CO, which is produced from

CO_2 on Cu, it is energetically favourable for Pt to be exposed on the surface. As a result, the Cu overlayer forms islands during CO_2 reduction, exposing part of the substrate. All the H_2 producing metals exhibit strong CO binding, as shown in Figure 2.2. As a result, surface segregation/exposure of all these metals when in bimetallics with Cu seems likely. Reske et al. showed that Cu could be stabilised in overlayers thicker than 5 nm on Pt.[84] However, for such systems, the effect of the Pt substrate on the surface is weak, and the electrode behaves similarly to bulk Cu.

(ii) Several studies exist reporting CO_2 reduction on the formic acid-producing metals In and Sn.[85–93] In their pure form, these metals exhibit significantly lower H_2 evolution than Cu. This can be explained by their weak H* binding, as shown in Figure 2.2. As a result, preparation of such bimetallics has been used as a strategy to suppress H_2 evolution while aiming to retain the unique CO_2 reduction performance of Cu. These studies did report suppressed H_2 evolution compared to pure Cu. However, CO and/or $HCOO^-$ seemed to be the main CO_2 reduction product from these bimetallics, while the formation of $>2e^-$ products was suppressed.

(iii) Finally, other studies have been carried out on bimetallic systems with Cu and one of the CO producing metals Au, Ag and Zn.[94–104] Most of them reported enhanced CO selectivity compared to pure Cu, as could be expected. However, improved selectivity and/or activity towards $>2e^-$ products was also presented. Ren et al. measured CO_2 reduction on electrodeposited Cu-Zn electrodes.[102] They observed increased ethanol selectivity, and attributed it to a higher partial pressure of CO near Cu sites because of the presence of Zn. This spillover effect will be discussed in further detail in section 2.4. An alternative explanation was proposed by Clark et al.[103] They studied CO_2 reduction on bimetallic Ag foils, and observed improved oxygenate selectivity and activity compared to pure Cu. They observed compressive strain on a Cu overlayer, and reported a weakening of the H* and O* binding energies relative to CO*. If such a situation occurs, it would enhance CO_2 reduction relative to H_2 evolution, and result in a lower degree of hydrogenation due to the lower coverage of H*. This corresponds well with the observed trend. It is possible that spillover from Ag domains still contributed to the results.

Bimetallic electrodes exhibit a certain potential in order to steer selectivity towards specific classes of products. Furthermore, alloying is proposed as

a means to break scaling relations. However, with a few notable exceptions, most bimetallic materials appear to increase selectivity towards H_2 or $2e^-$ products, compared to pure Cu. This suggests that better understanding of Cu electrodes is an important task in designing improved catalysts for the formation of $>2e^-$ products. As a result, the remainder of this thesis will deal with monometallic Cu electrodes.

2.3.2 Nanostructured Cu electrodes

For monometallic catalysts, nanostructuring is one way to modify electrocatalytic performance. An obvious effect is improved activity normalised to the geometric surface area of the electrode (denoted geometric activity throughout the rest of this thesis). This is caused by a n increase in electrochemical surface area (ECSA), and does not necessarily involve changes in the intrinsic activity per surface site. However, a number of other effects can come into play as well. For instance, nanostructuring might promote the presence of certain surface sites, in particular undercoordinated sites. This could change surface reactivity, and thus catalytic performance. Other important effects that can occur for nanostructured electrodes are changes to the local pH close to the surface, and readsorption and further reduction of products.

Nanostructuring has received much attention as an approach to improve CO_2 reduction on Cu electrodes towards commercial viability. These efforts can be divided into two groups after how the nanostructure is achieved: (i) electrodes derived from an oxidised precursor, and (ii) electrodes prepared using other techniques. In the following, these different approaches will be discussed in further detail. In addition, different types of nanostructured electrodes will be compared, both in terms of product distribution and activity.

Oxide-derived Cu electrodes

One of the most widely used methods for preparation of nanostructured Cu is to purposefully oxidise the electrodes and subsequently reduce them. The rapid lattice decompression during reduction leads to an un-relaxed, porous surface structure.[105] The many different materials in this category can be grouped by the method that was used to oxidise them. Kanan and coworkers

reported oxidation through thermal annealing, that has later been used by other groups as well.[105–109] Other approaches to form the initial oxide are anodic treatments,[110–114] plasma oxidation,[115–117] and preparation of Cu_2O films using electrodeposition or hydrothermal synthesis.[118–122]

Many similarities can be found in the CO_2 reduction performance of the different oxide-derived nanostructured Cu (OD Cu) electrodes. At potentials anodic of -0.7 V vs. RHE, this nanostructuring seems to yield improved selectivity towards carbon monoxide, and in some occasions formate ($HCOO^-$), as compared to polycrystalline Cu.[105–107] Polycrystalline Cu is mainly selective towards H_2 evolution in that potential region.[48] Interestingly, many of the OD Cu studies report improved C_{2+} over C_1 product selectivity. In particular, all the studies that quantify the formation of hydrocarbons show little to no methane (CH_4) formation on the OD Cu electrodes. In contrast, many of them report increased Faradaic efficiency towards C_2H_4.[109–117,119–121] Mistry et al. reported a Faradaic efficiency as high as 62% towards C_2H_4 formation from copper foils treated with oxygen plasma.[115]

The improved C_{2+} product selectivity from the OD Cu electrodes could have various explanations, and different hypotheses have been proposed by the authors of the individual studies. Kanan and coworkers identified a large amount of grain boundary surface terminations on their annealed foils.[105] They suggested that this could lead to surface sites with special geometries, exhibiting improved CO_2 reduction activity. Other groups have attributed the behaviour to an increase in local pH.[123–125] The rough surface of these electrodes leads to a depletion of CO_2 and H^+ in the boundary layer, and enhanced local concentrations of OH^-, leading to elevated local pH.[124–126] Several studies have shown that high pH leads to increased C_{2+} product selectivity.[123,126,127] Another hypothesis is related to preferential faceting of the surface. OD Cu electrodes prepared by cycling to anodic potentials in the presence of halide salts exhibit a cubic surface structure.[111,116,117] Cu is an fcc metal, which means that the surface of cubic features is likely to be preferentially oriented in the (100) direction. This surface orientation has previously been shown to promote C_{2+} selectivity from CO_2 reduction compared to other planar single crystals.[72,128] However, it was shown that the cubic structure seems to undergo an evolution to less ordered surface structures during CO_2 reduction,[129] indicating that preferential (100) faceting

is probably not a main influence.

There are some differences between the individual studies reporting CO_2 reduction on OD Cu electrodes. The electrodes derived from anodically oxidised foils and Cu_2O films all lead to improved C_{2+} over C_1 product selectivity, and generally push the product formation of $>2e^-$ products. On the other hand, many of the studies on annealed oxide-derived electrodes report little to no $>2e^-$ product formation. A likely explanation for these differences is the varying ECSA of the electrodes. CO_2 reduction in aqueous electrolytes is extremely sensitive to the mass transport of CO_2 to the electrode surface, because of the low solubility of CO_2 in water.[22] For nanostructured electrodes, CO_2 near the electrode surface is depleted faster due to the higher ECSA per geometric surface area.[124,125] This means that they reach mass transport limitations at less cathodic potentials than their planar counterparts. In fact, the higher a roughness factor an electrode exhibits, the lower an overpotential is needed before mass transport limitations are reached. Annealed OD Cu electrodes generally have higher surface roughness than those prepared using other methods. Hence, they will reach mass transport limitations at lower overpotentials, as evidenced by their increasing Faradaic efficiency towards H_2 evolution at potentials cathodic of -0.6 V. Meanwhile, hydrocarbons first start to form with significant selectivity at potentials cathodic of -0.8 V on polycrystalline Cu. As a result, the annealed OD Cu electrodes exhibit mass transport limitations in the region where hydrocarbons can be produced, which explains their low selectivity towards those compounds.

It can be challenging to accurately compare studies reported by different groups, due to varying approaches to product analysis, different cell geometries and resulting mass-transport conditions, etc. As a result, the variations in product distribution that were discussed in the previous paragraph could appear larger or smaller depending on mass transport of the setup used to measure it. In order to better compare the results from the groups, Lum et al. prepared four different types of OD Cu, spanning most of the preparation methods listed above, and tested them for CO_2 reduction.[124] This ensured that they were all characterised under the same conditions, and thus allowed for more accurate comparison. The roughness factors of the electrodes spanned from 6 to 103, as evaluated by double-layer capacitance measurements (described in detail in section 3.2.5). The electrodes

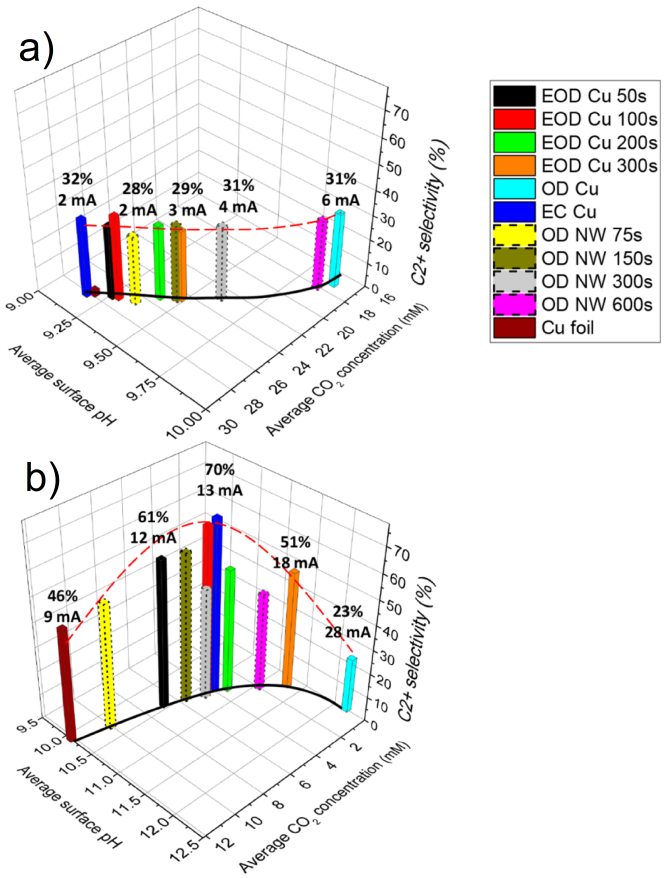

Figure 2.7: C_{2+} product selectivity from CO_2 reduction on various oxide-derived Cu electrodes in 0.1 M KOH at (a) -0.7 V and (b) -1.0 V. Reprinted with permission from Lum et al.[124]. Copyright © 2017, American Chemical Society.

were tested at potentials ranging from -0.7 to -1.0 V, and results from the most anodic and most cathodic potentials Figure 2.7a and b, respectively. At -0.7 V the C_{2+} Faradaic efficiency was similar for the different types of electrodes, indicating that they had not yet reached mass transport limitations. At -1.0 V, however, significant variation was observed. As discussed previously, the annealed OD Cu electrodes (marked with light blue in the figure) were by far the roughest, and exhibited the lowest C_{2+} selectivity. Interestingly, an optimum could be observed for electrodes of intermediate roughness, indicating that a compromise between elevated local pH and depletion of CO_2 near the surface can be found. This study confirms that

local pH effects indeed play an important role in facilitating improved C_{2+} product selectivity. It also supports the hypothesis that varying roughness factor, and thus varying degree of mass transport of CO_2 to the surface at strongly cathodic potential, is a likely explanation for the variability between different studies.

Non-oxide-derived Cu electrodes

In addition to oxide-derived copper, studies describing nanostructured copper electrodes prepared using different methods have been reported. Yang et al. produce a well-defined, mesoporous copper film to study effects from systematically changing pore depth and width.[130] Like for the oxide-derived nanostructured surfaces, they observed increased selectivity towards the C_2 products ethylene and ethane (C_2H_6) independently of pore size. Interestingly, narrow pores led to higher C_2product selectivity than wide pores, attributed by the authors to elevated local pH. This fits well with the explanation given above for oxide-derived electrodes. Furthermore, deeper pores led to increased C_2H_6 formation compared to more shallow ones, while the opposite trend was the case for ethylene. This is likely to be caused by increased readsorption and further reduction of C_2H_4 to C_2H_6 in the long and narrow pores, an explanation also given by the authors. Studies on well-defined nanostructured electrodes like this are helpful for achieving deeper understanding of the reasons behind the influence of nanostructuring on product distribution. Decoupling of the various possible effects is challenging when the surface structure is irregular, which is the case for the OD Cu electrodes.

Several other studies have been carried out on less ordered nanostructured electrodes that are not derived from an oxidised precursor. Techniques applied to produce the nanostructure include electrodeposition,[131–136] and dealloying.[137] Interestingly, all of these studies described similar behaviour to what was reported for oxide-derived Cu, namely enhanced Faradaic efficiency to C_{2+} product formation, in particular in terms of improved C_2H_4 and suppressed CH_4 selectivity. These observations indicate that non-oxide-derived Cu electrodes are intrinsically very similar to oxide-derived ones. It appears that using an oxidised precursor is simply a practical technique for achieving a nanostructured electrode. This provides further support to the hypothesis that enhanced local pH, resulting from lower mass transport to

and from the electrode surface, plays a major role in steering the selectivity towards C_{2+} products.

The role of oxygen

The observation that nanostructured electrodes perform similarly for CO_2 reduction independently of the oxidation state of the precursor material, has other interesting implications. A major controversy is currently taking place in the CO_2 reduction literature concerning the role of subsurface oxygen in Cu electrodes for CO_2 reduction catalysis. The first report (to the best of my knowledge) about intentionally oxidised Cu electrodes for CO_2 reduction was published by Frese in 1991.[138] The author reported significant formation of methanol when performing CO_2 reduction on oxidised electrodes. As mentioned in section 1.2, methanol would be a desirable chemical because of its many possible applications. However, the results were poorly reproducible, and most later works on intentionally oxidised Cu for CO_2 reduction report no methanol formation. In a recent study by Le Duff et al., the influence of having oxygenated species present on the surface of Cu single crystals during CO_2 reduction was investigated.[139] This was achieved by pulsing the potential between CO_2 reduction conditions and less cathodic potentials where hydroxide species would adsorb. As a result, significant formation of oxygenated products was observed. Interestingly, the authors also reported the formation of methanol under these conditions, providing insight about how to steer selectivity towards this important compound.

When carrying out chronoamperometric CO_2 reduction, on the other hand, it is likely that the surface is entirely reduced at the strongly cathodic potentials. Still, several groups argue that surface or subsurface oxygen can be stable under reaction conditions, and that it leads to stronger binding of CO* to the surface.[119,140–147] For instance, Cavalca et al. prepared oxide-derived Cu in an inert atmosphere and carried out CO_2 reduction. Subsequently, they transferred the electrodes in a sealed container to the vacuum of a transmission electron microscope. There, they identified oxygen present in the near-surface region of their electrodes. Although they tried to mitigate contact with air, this is highly challenging to completely avoid. It is known that a native oxide layer is quickly formed on Cu upon contact with air.[148–150] Lum and Ager showed that this process occurs even faster

on nanostructured electrodes, most likely due to the many defects in the Cu lattice.[150] They produced oxidised ^{18}O-enriched OD Cu electrodes and performed CO_2 reduction. Subsequently, they measured the depth profile of ^{18}O and ^{16}O concentrations on these electrodes, and compared the resulting data with normal OD Cu electrodes that had undergone the same treatment. The ^{18}O-enriched samples exhibited $< 1\%$ of the original ^{18}O content after CO_2 reduction, indicating that the initial oxide is removed during reaction.

The quick reoxidation of Cu upon contact with air is a general problem with using *ex-situ* characterisation tools to study the oxidation state of Cu. Still various other reports have suggested that oxygen is present and influences CO_2 reduction performance, based on *ex-situ* measurements.[119,138,146] Other groups have used *in-situ* or *operando* measurements, which are in principle much more suited, to investigate whether oxygen is present and what effects it could have.[115,144,145] Favaro et al. carried out ambient pressure XPS to show that subsurface oxygen is critical for chemisorption of CO_2 to a Cu surface.[144] However, these measurements were carried out in the gas phase with no applied potential. The picture is likely to be widely different at cathodic potentials in an electrolyte. In two other studies, oxidised Cu species were detected under reaction conditions using *operando* X-ray absorption spectroscopy. However, these techniques penetrate deeply into the sample. Even if grazing X-ray incidence angles are used, the minimum penetration depth of the radiation is approximately 1.5-2.0 nm (discussed further in chapters 3 and 7), corresponding to tens of atomic layers. According to DFT calculations, stabilisation of O in the Cu bulk under reaction conditions is plausible, but O is needed within the topmost 2-3 atomic layers to have an electronic effect on the surface chemistry.[70,151]

To summarise, both computational and experimental evidence indicate that near-surface oxygen is not stable under CO_2 reduction conditions.[150,151] The fact that oxide-derived nanostructured electrodes exhibit similar product distribution to non-oxide derived electrodes, as discussed in the previous sections, supports this notion. Still, several groups have reported experimental data indicating that oxygen is present under reaction conditions, which could be caused by artefacts. Importantly, Cu electrodes oxidise quickly upon contact with air, making reliable *ex-situ* characterisation difficult.

Comparison of nanostructured Cu electrodes for CO_2 reduction

In the previous sections, I have been comparing different nanostructured Cu electrodes qualitatively in terms of their product distribution. It is, however, also instructive to compare the different catalyst materials quantitatively. One way to do this is to study the total CO_2 reduction current density they exhibit. In Figure 2.8, the geometric and specific CO_2 reduction activity from a number of studies on nanostructured Cu is shown. Data on polycrystalline Cu is included as well, as a benchmark for the activity of Cu for this reaction. Note that far from all the studies that were discussed previously share enough information to calculate the specific CO_2 reduction activity. This is imperative in order to have a common figure of merit for various materials with widely different structure and ECSA. It is hard to understate the importance of reporting all relevant parameters for future work on nanostructured materials. Proper comparison is vital to evaluate whether novel catalyst materials represent an improvement over known systems. The studies in Figure 2.8 are all carried out in 0.1 M potassium bicarbonate ($KHCO_3$), and capacitance measurements were used for estimation of ECSA. They should thus be directly comparable. They are, however, carried out using different types of reactors and setups with slightly different experimental conditions. This could lead to some variation in the resulting CO_2 reduction performance.

In Figure 2.8a, the geometric CO_2 reduction activity of the various studies is shown. A significant variation in activity can be seen. As expected, planar, polycrystalline foils (studies A and B) exhibit the lowest activity, while the CO_2 reduction current density of the nanostructured electrodes increase with higher ECSA. All the studies reach a plateau at some point when going from low to high overpotentials. This can be attributed to the electrodes reaching mass transport limited catalysis. Two interesting observations can be made in that regard. Firstly, most of the studies plateau at a CO_2 reduction current density of 10-20 mA cm^{-2} . This has been established as the general limiting current for CO_2 reduction on Cu in aqueous electrolytes,[152] a figure that depends on geometric area rather than ECSA. Secondly, the electrodes with higher ECSA reach mass transport limitation at more anodic potentials. This is a direct consequence of the first point, since their larger number of surface sites make them reach the limiting current density at lower overpotentials.

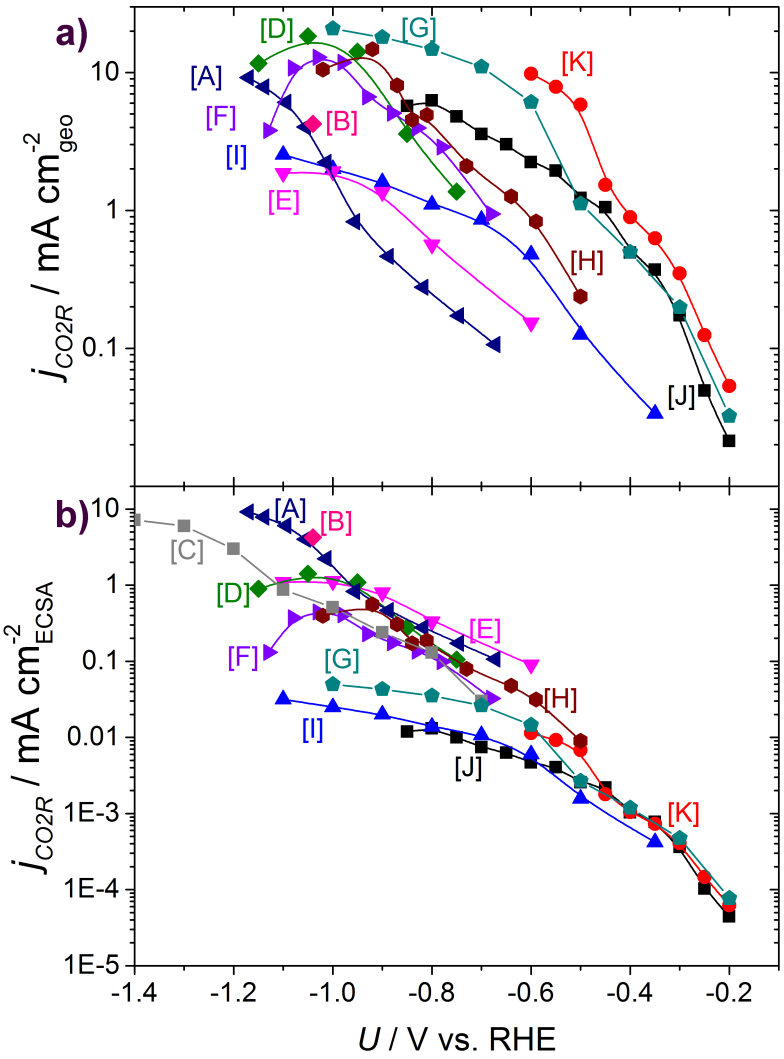

Figure 2.8: Comparison of (a) geometric and (b) specific CO_2 reduction partial current densities for various nanostructured Cu electrodes and polycrystalline Cu. All measurements are carried out in 0.1 M $KHCO_3$ electrolyte. The data are obtained from the following studies: [A] Kuhl et al.[48]; [B] Hori et al.[45]; [C] Yang et al.[130]; [D] Ren et al.[114]; [E] Kwon et al.[113]; [F] Handoko et al.[121]; [G] Raciti et al.[106]; [H] Mistry et al.[115]; [I] Ma et al.[108,109]; [J] Li et al.[105]; [K] Min et al.[107]. Studies [A,B] are polycrystalline copper, [C] is non-oxide derived, nanostructured copper and [D-K] are oxide-derived, nanostructured copper.

Figure 2.8b displays the specific CO_2 reduction activity of the same studies. Normalising the activity to the ECSA of the electrodes gives a different picture. In this case, the various materials exhibit highly comparable CO_2 reduction activity when not under mass transport limitation. This means that all the different surface geometries do not only lead to similar product distribution, as discussed previously, but also similar activity on a per-site basis. Note here that specific activity gives the average activity of the different surface sites. Variation in activity for different site configurations is likely, as discussed in section 2.2. Interestingly, polycrystalline Cu also follows this trend, exhibiting similar specific CO_2 reduction activity as the nanostructured electrodes. This indicates that nanostructuring is mainly a way of altering the product distribution obtained from CO_2 reduction on Cu electrodes, and does not intrinsically alter their activity to a large extent. As a result, different approaches than nanostructuring should be applied to develop catalysts with improved intrinsic activity, such as attempts to break scaling relations.

CO_2 reduction with Cu gas diffusion electrodes

While the intrinsic activity is an important metric for catalyst development purposes, the geometric activity that can be obtained from a system is key for future commercial applications. As discussed previously, the capital cost of installed systems are likely to be an important contributor to the cost of any chemicals produced from CO_2 reduction. This will be particularly truein the initial stages of commercial implementation, before significant development has taken place. Since high production rate from each unit is important in order to drive the cost down, reaching higher geometric activity is an important challenge that needs to be overcome before commercialisation is feasible.

As discussed in the previous section, the low solubility of CO_2 in aqueous media leads to a maximum limiting CO_2 reduction current density of ~20 mA cm^{-2} on Cu electrodes.[152] A promising approach to avoid this limitation is to feed CO_2 in the gas phase instead of dissolving it in the electrolyte, using what is called gas diffusion electrodes (GDE). This is a similar approach to what is used for commercial water electrolysis/H_2 fuel cell systems, where the reactant is fed in the gas phase. What makes CO_2 reduction on Cu complicated is that both gaseous and liquid products are

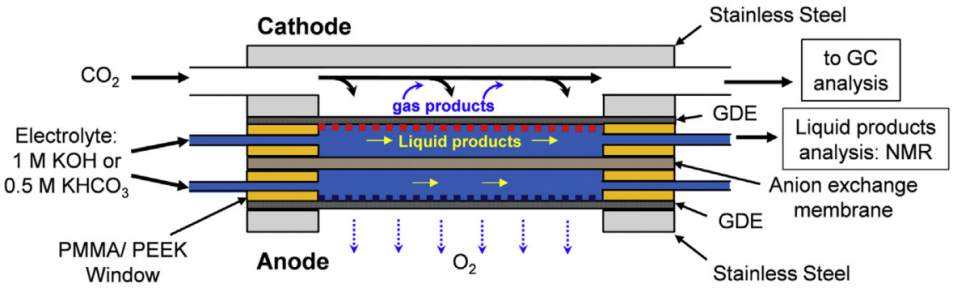

Figure 2.9: Example of cell design used for CO_2 reduction with gas diffusion electrodes. By feeding CO_2 in the gas phase instead of dissolved in the electrolyte. Reprinted with permission from Ma et al.[153] Copyright © 2016, Elsevier B.V.

formed and need to be collected. Ma et al. showed one way to address this in their cell design,[153] which is displayed in Figure 2.9. CO_2 is flowed on one side of the cathode GDE, while there is a liquid electrolyte on the other. Thus, gaseous products will mainly migrate into the gas stream, while liquid products are likely to dissolve in the electrolyte.

Ma et al. used the cell shown in Figure 2.9 to study CO_2 reduction on interconnected Cu nanoparticles. Significantly enhanced geometric activity could be observed, with C_2H_4 partial current densities reaching 160 mA cm^{-2} at ~40 % Faradaic efficiency, and C_2H_5OH current densities reaching 50 mA cm^{-2} at ~20% Faradaic efficiency. Reller et al. showed similar performance for GDE measurements on electrodeposited Cu nanodendrites, reaching 100 mA cm^{-2} C_2H_4current density with a Faradaic efficiency of ~60%.[133] Stability seems to be an issue for these catalysts, though.[133] This is likely to be, at least partly, caused by the high mobility of Cu, causing sintering of the nanostructure.

Initial GDE measurements do seem promising. Geometric current densities of >100 mA cm^{-2} to C_2H_4, a valuable product with a large market, have been reached. However, more work is needed, for instance to improve the stability of the electrodes.[133] Furthermore, the energy efficiency of the Cu electrocatalyst is still not satisfactory, giving large energy losses in terms of release of heat at the electrode that needs to be managed.

2.4 The tandem catalytic approach

In the previous section, I discuss how nanostructuring improves the selectivity of Cu electrodes for CO_2 reduction towards C_{2+} products, particularly C_2H_4 and C_2H_5OH. A main explanation for this seems to be that their structure leads to elevated local pH. However, I also present data showing that the specific activity is similar for all Cu electrodes, ranging from annealed, oxide derived Cu with roughness factor >100, to planar, polycrystalline Cu foils. This means that nanostructuring is not a particularly promising approach for improving the energy efficiency for the formation of $>2e^-$ products.

In order to make CO_2 reduction more cost-competitive, lowering the overpotentials at which the reaction(s) occur(s) is highly desirable. One approach is to split the reaction into more than one step. As described in section 2.2, fewer proton/electron transfers makes it easier to optimise the catalysis. One way to do this in practice is to start with CO_2 reduction to CO in a $2e^-$ reaction, for which the catalysis more straightforward to optimise. Au, which exhibits close to optimal binding energy of the intermediate for this reaction,[154] is the most efficient catalyst for this reaction reported to date.[155] Numerous studies have shown it to catalyse CO_2 reduction to CO with high selectivity, both in the polycrystalline and nanostructured forms.[45,154,156–159] Other materials, such as Ag[160] and transition metal doped nitrogenated carbon[161–163] are also promising catalysts for CO_2 reduction to CO.

Once CO is formed, it can be reduced further in a separate reaction. It has been identified as an intermediate in CO_2 reduction towards $>2e^-$ products,[63,127,164] which means that starting with CO in the gas feed instead of CO_2 steers selectivity in the direction of these products. Furthermore, this reduces the number of e^-/H^+ transfers with 2 per carbon atom in the final product, giving less complex reaction mechanisms with fewer intermediates. As discussed in section 2.2, fewer reactions steps leads to more facile optimisation of the catalysis. The disadvantage of this approach is increasing capital cost if the two reactions are carried out in two different reactors. The magnitude of the gains in energy efficiency and selectivity versus the increase in capital cost will then determine whether it can pay off. Another approach to the same principle is preparing bi-phasic electrodes

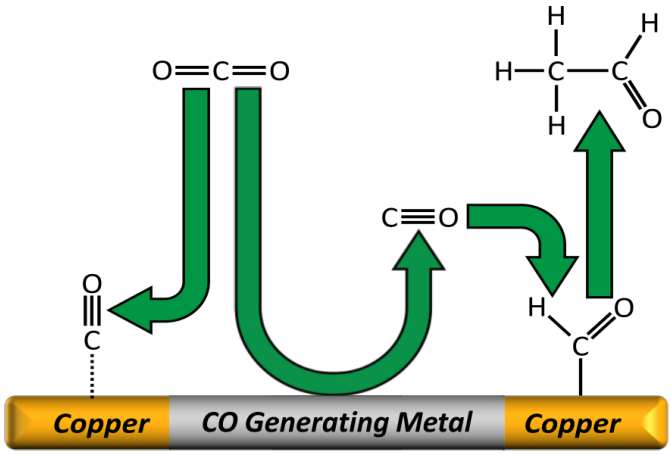

Figure 2.10: Schematic illustrating spillover mechanism on bimetallic electrodes. It has been proposed that Cu combined with a CO generating metal such as Au or Ag can lead to higher $>2e^-$ product selectivity due to an elevated local partial pressure of CO. Reprinted with permission from Clark et al.[103] Copyright © 2017, American Chemical Society.

that have regions of a CO-producing material (typically Au, Ag or Zn) and regions of a catalyst that can reduce CO further (typically Cu), as discussed in section 2.3.1. This would lead to an elevated partial pressure of CO close to the electrode compared to a pure Cu surface, and would thus be likely to facilitate improved energetics towards $>2e^-$ products. A proposed scheme for this is shown in Figure 2.10.

Electroreduction of CO is interesting in a more fundamental perspective as well. Since CO is a common intermediate for CO_2 reduction to all $>2e^-$ products, any insight obtained for this reaction will also be highly relevant for CO_2 reduction catalysis.

2.5 Further reduction of CO

Hori et al. published the first report (to the extent of my knowledge) concerning CO reduction on Cu electrodes.[79] As expected since CO is an intermediate in CO_2 reduction to $>2e^-$ products, the authors observed a similar product distribution to that observed for CO_2 reduction, except with exclusive formation of $>2e^-$ products. In a later study, some of the same authors reported CO reduction on polycrystalline Cu in electrolytes

with different pH.[127] A list of products relevant to CO reduction is shown in Table 2.2. As is the case for CO_2 reduction, the equilibrium potentials for most of the products are within ±200 mV of 0 V. However, the amount of H^+/ e^- transfers required to form a certain product is lower compared to CO_2 reduction, as mentioned above.

As discussed in section 2.3.2, Hori et al. showed that pH has a significant influence on C_{2+} product selectivity.[79,127] In 0.1 M KOH electrolyte, which has a pH of ~13, CH_4 formation is almost completely suppressed while C_2H_4 selectivity is enhanced compared to neutral pH. It appears that while ethylene formation is relatively independent of pH, CH_4 and H_2 evolution decrease with higher pH. A possible reason for this is that the rate-determining step for CH_4 formation represents a concerted H^+ and e^- transfer.[59] Therefore, it is influenced directly by the amount of protons present in the electrolyte, which leads to it being pH independent on an RHE scale.[59,127] For C_2H_4, on the other hand, the rate-determining step is an electron transfer only, making this reaction pH independent on the SHE scale and thus pH dependent on an RHE scale. This shifts it closer to the equilibrium potential at alkaline pH.[59] The possibility to vary electrolyte pH is an advantage for CO reduction, since CO is dissolved approximately like an ideal gas. CO_2, on the other hand, is in equilibrium with carbonic acid (H_2CO_3) and bicarbonate (HCO_3^{2-}) in water, giving a pH close to 7. Thus, CO_2 reduction in aqueous solution gives limited possibility to vary pH, although CO_2 reduction in 1 M KOH has been reported for gas diffusion electrode-type setups, as shown in Figure 2.9.[153]

Adding to the initial findings for CO reduction on polycrystalline Cu, Kanan and coworkers tested their annealed OD Cu electrodes for the same reaction, and showed high selectivity and geometric activity for CO reduction to oxygenates at low overpotentials.[165] At -0.3 V, they observed 57% Faradaic efficiency towards CO reduction, with 43% going to C_2H_5OH and 14% to acetate (CH_3COO^-), as shown in Figure 2.11. They observed a large density of grain boundaries when characterising their electrodes using scanning electron microscopy (SEM), and thus attributed the unprecedented CO reduction performance to special site geometries that could be possibly stabilised by high-energy structures at the grain boundary surface terminations. Similarly high selectivity to oxygenates was obtained in a recent study reporting CO reduction on Cu nanowires.[166]

Table 2.2: Known products from CO reduction on Cu, along with their half-cell reactions and equilibrium potentials. The potentials were calculated using Gibbs free energies of formation obtained from the CRC Handbook of Chemistry and Physics.[22]

Product	**Chemical equation**	***E* / V**
Methanol	$CO + 4\,H^+ + 4\,e^- \longrightarrow CH_3OH$	0.09
Methane	$CO + 6\,H^+ + 6\,e^- \longrightarrow CH_4 + H_2O$	0.26
Acetic acid	$2\,CO + 4\,H^+ + 4\,e^- \longrightarrow CH_3COOH$	0.38
Acetaldehyde	$2\,CO + 6\,H^+ + 6\,e^- \longrightarrow CH_3CHO + H_2O$	0.18
Ethanol	$2\,CO + 8\,H^+ + 8\,e^- \longrightarrow C_2H_5OH + H_2O$	0.19
Ethylene	$2\,CO + 8\,H^+ + 8\,e^- \longrightarrow C_2H_4 + 2\,H_2O$	0.17
Propionaldehyde	$3\,CO + 10\,H^+ + 10\,e^- \longrightarrow C_2H_5CHO + 2\,H_2O$	0.19
1-propanol	$3\,CO + 12\,H^+ + 12\,e^- \longrightarrow C_3H_7OH + 2\,H_2O$	0.20

In follow-up work, Kanan and coworkers prepared Cu nanoparticles with a large amount of grain boundaries.[167] By annealing at different temperatures, they could produce samples with varying grain boundary density. When measuring CO reduction on these samples, the activity towards this reaction could be correlated to the grain boundary density. Also, in a recent study, they used a technique they call *scanning electrochemical cell microscopy* to study CO_2 reduction to CO on Au,[168] another reaction proposed to be promoted by grain boundaries.[156,169] Using this technique, they evaluated the electrochemical activity at specific points on the electrode with micrometer resolution, obtaining results indicating that enhanced CO_2 reduction occurred at grain boundary surface terminations.

The hypothesis that grain boundaries were causing the high performance of OD Cu was studied further in a collaboration between other members of my group and Kanan and coworkers.[170] The authors characterised electrodes prepared under varying conditions using CO temperature programmed desorption. In this technique, CO is adsorbed to the surface at low temperatures. The sample is then heated linearly while a probe connected to a mass spectrometer monitors the amount of CO desorbing from the surface. This way, the binding strength of CO can be probed. The spectra obtained from CO temperature programmed desorption of various Cu samples are shown in Figure 2.12. Panel (a) shows the spectrum obtained from a polycrystalline Cu foil. The peak can be deconvoluted into two main

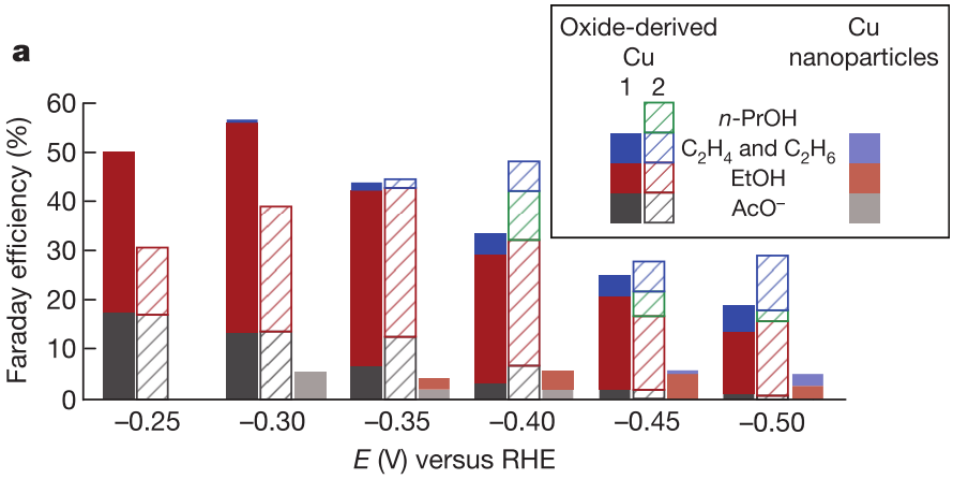

Figure 2.11: Product distribution from CO reduction on annealed OD Cu electrodes in 0.1 M KOH. Reprinted with permission from Li et al.[165] Copyright © 2014, Springer Nature.

features, arising from CO binding to facets and steps, respectively. For the OD Cu electrodes, the positions of these two peaks are marked by stapled lines. For the normal OD Cu electrodes that are prepared by oxidation at 500 °C (shown in panel (b); OD Cu 500), a large peak at stronger CO binding can be observed. Results from microkinetic modelling indicated that this peak originated from a particularly strong binding site, and not from re-adsorption of CO in the porous structure of the sample. Annealing the OD Cu 500 at 200 °C or 350 °C (shown in panel (c) and (d), respectively) led to a decrease in the occurrence of this feature. The same was the case for electrodes prepared by oxidation at 300 °C (panel (e)).

The authors also measured CO reduction on the various electrodes at -0.4 V in 0.1 M KOH (panel (f)). It turned out that the specific CO reduction activity correlated well with the occurrence of the strong binding sites, as quantified through the microkinetic model. Interestingly, polycrystalline Cu foils exhibited little to no CO reduction activity at this potential. Other studies by Hori et al. report significant activity from such electrodes, albeit at higher overpotentials.[79,127] Additionally, I showed in section 2.3.2 that polycrystalline Cu exhibits similar specific CO_2 reduction activity as nanostructured electrodes. Since CO is an intermediate in the reduction of CO_2 to $>2e^-$ products, a similar behaviour could be expected for CO reduction.

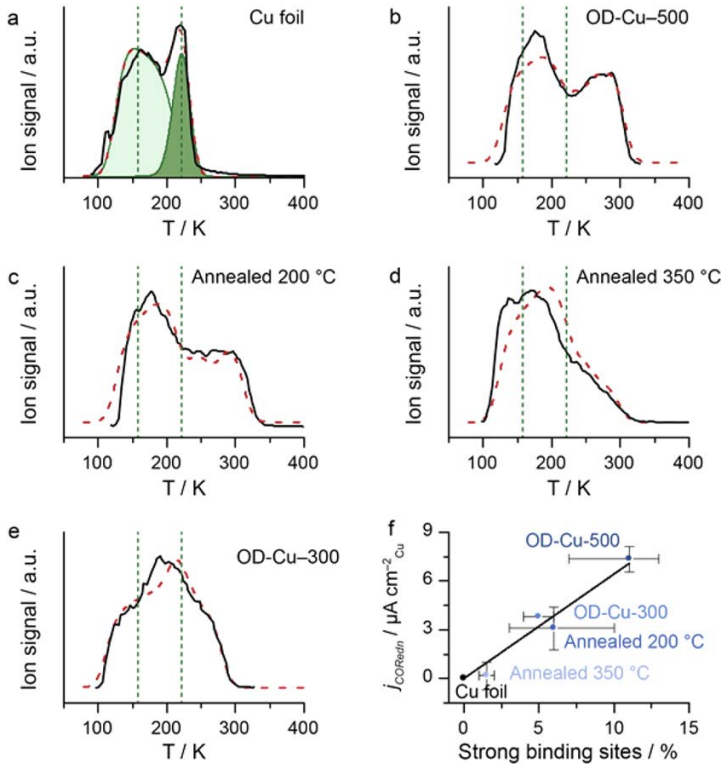

Figure 2.12: CO temperature programmed desorption measureemts of different Cu electrodes. (a) Polycrystalline Cu foil. (b-e) Oxide-derived Cu electrodes prepared with different procedures. (f) Specific CO reduction activity at -0.4 V as a function of the amount of strong-binding sites identified on the various electrodes.Reprinted with permission from Verdaguer-Casadevall et al.[170] Copyright © 2015, American Chemical Society.

According to these measurements, this is not the case.

In general, the findings regarding CO reduction on OD Cu open a range of questions about the behaviour of Cu electrodes as catalysts for CO reduction. These comprise some of the main aims for this thesis, which are specified below.

2.6 Aims for thesis

In the previous section, I described how oxide-derived, nanostructured Cu electrodes exhibit excellent CO reduction selectivity and geometric activity at low overpotentials. Throughout the rest of this thesis, I aim to provide

further insight regarding the following points:

- What are the reasons for the high selectivity towards ethanol for oxide-derived Cu electrodes? (Chapter 5)
- Verdaguer-Casadevall et al. measured little to no CO reduction activity from polycrystalline Cu,[170] while this type of electrode exhibits similar specific activity for CO_2 reduction as nanostructured electrodes. Why is this? (Chapter 6)
- What is the average surface structure of Cu electrodes under CO reduction conditions? (Chapter 7)

Additionally, I will be addressing another important topic:

- What are adequate analytical techniques for quantification of CO reduction products in alkaline electrolyte? (Chapter 4)

3

Experimental Methods

From the next chapter and onwards, I will present four projects that I have carried out throughout my PhD studies. I have utilised a number of experimental techniques for sample preparation, electrochemical measurements, product analysis and sample characterisation. In this chapter, I will give an overview of these methods and how they were used. Note that details regarding important chemicals and materials used for the various projects can be found in appendix A.

3.1 Electrochemical setup

The electrochemical setup is the basis for the CO reduction electrocatalysis measurements discussed later, as well as for sample preparation and characterisation. In this section, I discuss the setup that I used for this and the techniques that I applied.

3.1.1 Two-electrode setup

The simplest electrochemical setup possible is one consisting of two electrodes, a working electrode (WE) and a counter electrode (CE). The WE represents the electrocatalyst material that is being studied, while the CE is an auxiliary electrode; its role is to facilitate the counter-reaction at the same rate as the reaction occurring on the WE. The most important limitation of a two-electrode setup is that no information about the potential on the WE can be obtained, since only the potential difference between the two WE and CE can be monitored. For the work performed in this thesis, a

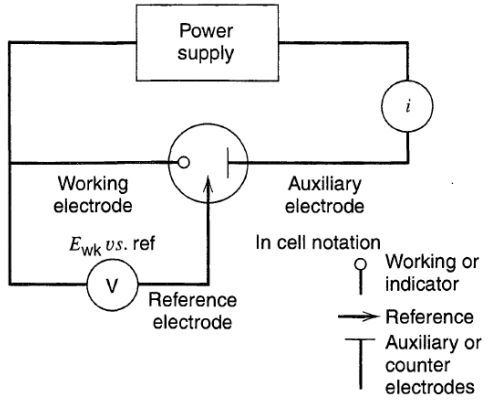

Figure 3.1: Schematic of three-electrode setup. Reprinted from Bard and Faulkner.[172]

two electrode setup was only used for electropolishing (described in further detail in section 3.2.3.

3.1.2 Three-electrode setup

For fundamental electrocatalysis research, it is vital to be able to accurately monitor and control the potential of the WE, since the reaction rate depends directly on the applied potential.[52] In order to achieve this, a three-electrode setup is necessary. A schematic of such a configuration is shown in Figure 3.1. The key component that enables control of the WE potential is the reference electrode (RE). This is an electrode where a well-defined electrochemical reaction occurs, at a stable potential, achieved by buffered or saturated concentrations of the aqueous species involved.[171] Because of its stability, it can be used as a reference point to which the WE potential can be compared. As a result, the current is drawn between the WE and CE, while the potential is measured between the WE and RE.

3.1.3 Potentiostat

A potentiostat is arguably the most important piece of equipment when aiming to perform well-controlled fundamental electrocatalysis measurements. Its main purpose is to facilitate accurate control and monitoring of electrochemical processes occurring in the system, of which the importance was underlined in the previous section. In the three-electrode setup schematic

in Figure 3.1, a power supply, amperometer and voltmeter are included. In practice, all these functions are carried out inside the potentiostat. As mentioned in the previous paragraph, current is drawn between the WE and RE, while the WE potential is monitored by comparing it to the RE. However, in order to keep the WE potential at the desired value, the potential applied between WE and CE needs to be constantly varied accordingly. The potentiostat achieves this by monitoring the WE potential and alternating the cell potential in a feedback loop.[171] For all the work reported in this thesis, a Biologic VMP-2 potentiostat was used, together with the EC-Lab software.

3.1.4 Reference electrode calibration

The RE is an electrode that keeps a stable potential in order to work as a reference point for the WE potential. However, a large number of different reference electrodes exist, that work at different potentials. Therefore, the H_2 /H^+ redox couple shown in eq. (3.1) has been chosen as a universal scale for potentials.

$$2\,H^+ + 2\,e^- \rightleftharpoons H_2 \tag{3.1}$$

The equilibrium potential of this reaction is defined as 0 V at standard conditions, meaning 1 M concentrations of H^+ and 1 bar pressure of H_2. This potential reference point is referred to as the *standard hydrogen electrode* (SHE). The disadvantage of the SHE is that it requires a very precise pH at the electrode. In order to facilitate more versatility, the *reversible hydrogen electrode* (RHE) was developed. Here, the pH of the electrolyte is considered in the reference potential. The relationship between the SHE and RHE is given by eq. (3.2), which can be derived from the Nernst equation.

$$E_{RHE} = E_{SHE} - 0.059 \times \mathrm{pH} \tag{3.2}$$

In order to be able to compare data between groups working with different REs and electrolyte pH, the RE of choice should be calibrated against RHE. This can be done readily by measuring the onset of the H_2 evolution/oxidation reaction on Pt in the same electrolyte that is being used during electrocatalysis experiments, while saturated with 1 bar of H_2. In this thesis, a mercury/mercurous sulfate (Hg/Hg_2SO_4) RE was used for all

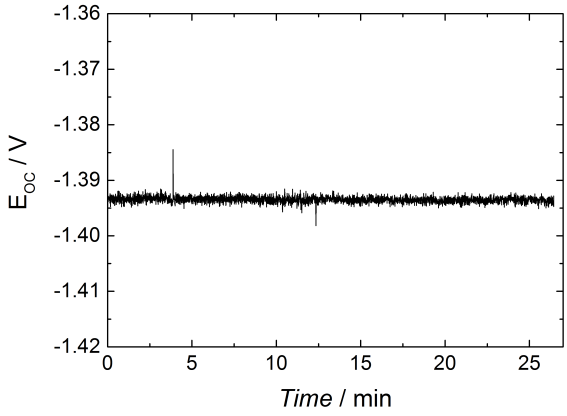

Figure 3.2: Open-circuit voltage measurement on Pt in H_2 -saturated 0.1 M KOH for reference electrode calibration. The calibration value obtained from this particular measurement was 0 V vs. RHE = -1.394 V vs. Hg/Hg_2SO_4, or $U_{RHE} = U_{Hg/HgSO4} + 1.394$ V.

measurements. The chemical equation for the Hg/Hg_2SO_4 redox couple is shown in eq. (3.3).

$$Hg_2SO_4 + 2\,e^- \rightleftharpoons 2\,Hg + {SO_4}^{2-} \tag{3.3}$$

RE calibrations were carried out in a two-compartment glass cell in H_2 saturated 0.1 M KOH, since this was the electrolyte used for all CO reduction measurements included in this thesis. Pt wires were used as WE and CE. The H_2 evolution/oxidation onset potential was found by measuring the open-circuit voltage (OCV) for a certain period of time (>15 min) to check that the potential was stable. An example of such a measurement is shown in Figure 3.2.

3.1.5 Electrochemical techniques

Several different electrochemical techniques were applied throughout this thesis, all facilitated by the potentiostat. In the following, I will present them briefly.

Chronoamperometry

In chronoamperometry, the WE potential is kept constant, while the resulting current is recorded as a function of time. The constant WE potential

is achieved by the potentiostat varying the CE potential accordingly. This technique was used for all CO reduction measurements reported in this thesis.

Chronopotentiometry

Chronopotentiometry means keeping a constant current and recording the resulting potential with time. This means that the potentiostat varies the cell potential so that a constant current can be drawn. This technique was only used for in-situ reduction of the precursor oxide layer on OD Cu electrodes.

Cyclic voltammetry

When performing cyclic voltammetry (CV), the potential is varied linearly between two limits at a certain rate (called *scan rate*). The current response from reactions and adsorption processes occurring on the electrode at the potentials measured is recorded. It is thus a useful technique to probe the current response of an electrode in a certain potential region. In this work, CV was used for evaluating the ECSA of OD Cu electrodes, as well some electrode characterisation during our *operando* measurements that are described later.

Electrochemical impedance spectroscopy

Electrochemical impedance spectroscopy (EIS) was used in this work to evaluate the Ohmic resistance of the system, which mainly arises from the electrolyte.[172] EIS is based on small, periodic perturbations of the electrode-electrolyte interface at a certain frequency.[172] By varying the frequency, different processes will be probed. A simplified model of the interface, called an equivalent circuit, can be used to deconvolute the capacitance measured. A schematic of the equivalent circuit typically used to model electrochemical cells is shown in Figure 3.3.[172] In the figure, C_d is the double-layer capacitance of the interface. Z_f is the general impedance of the system, which is caused by the charge-transfer resistance among other effects. R_Ω is the Ohmic resistance in the system. In the work contained herein, the values of the various components were estimated by fitting the impedance spectrum to the equivalent circuit using the EC-Lab software.

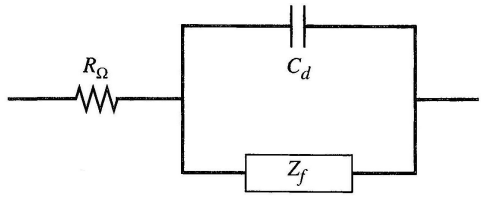

Figure 3.3: Schematic of the equivalent circuit used to model the electrochemical cell. R_Ω represents the Ohmic resistance in the system, mainly arising from the ionic conductivity in the electrolyte. C_d represents the double-layer capacitance, while Z_f is the general impedance of the system. Reprinted from Bard and Faulkner.[172]

Ohmic resistance values were normally in the range of 35 to 45 Ohms in the 0.1 M KOH electrolyte, and were used to compensate the applied potential for the Ohmic drop.

3.2 Preparation for electrochemical experiments

In this section, I describe the various approaches I used for measurement preparation, including cleaning of glassware and electrode preparations. All the electrodes described were installed as WEs. An Au mesh CE was used for all CO reduction measurements performed with this setup. Au was chosen because it is noble, and exhibits relatively high stability at anodic potentials. Furthermore, it does not exhibit significant activity towards CO reduction, because of its weak CO* binding. This gives lower possibility for measuring increased CO reduction activity at the WE because of contamination from the CE.

3.2.1 Cleaning of glassware

All glassware that was used for electrochemical measurements was cleaned regularly using piranha solution (3:1 96% H_2SO_4 and 30% H_2O_2) or aqua regia (3:1 37% HCl and 65% HNO_3). The glassware was immersed in the cleaning solution and stored overnight. Then, thorough rinsing (immersing in water 4-7 times) and sonication/boiling (2-3 times) was performed.

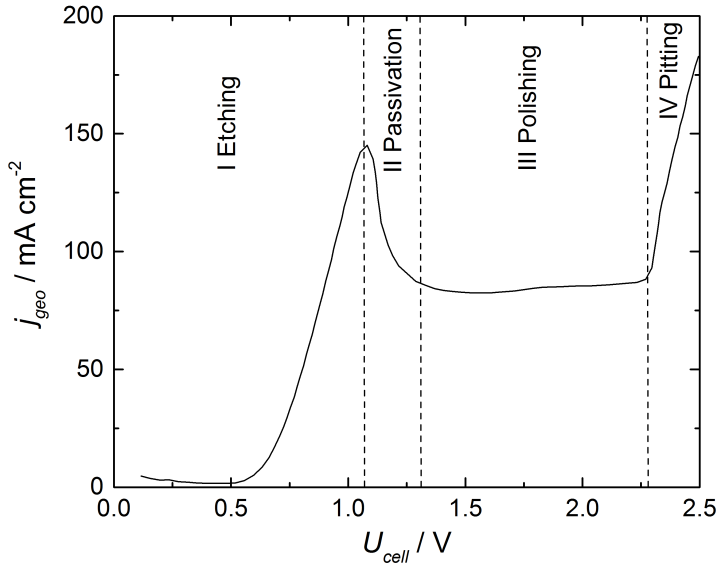

Figure 3.4: Polarisation curve for Cu in 14 M phosphoric acid. Region III represents the potential window where electropolishing takes place. Replotted using data from Van Gils et al.[174]

3.2.2 Polycrystalline Cu electrodes

Two of the projects presented later in this thesis are carried out using polycrystalline Cu foils as either the CO reduction catalyst itself, or a precursor to the final catalyst. The foils were cut into 5×10 pieces from a 100×100 mm sheet and attached to a ~10 cm long piece of Cu wire. Subsequently, all samples were electropolished individually.

3.2.3 Electropolishing of Cu foils

Electropolishing is a common method for pre-treating metals,[173] used in this case to prepare the Cu foil for CO reduction measurements. The technique can serve several purposes, depending on the application. In this case, the most important functions were removal of organic species from the electrode surface and microscopic smoothening. Electropolishing refers to anodic treatment in suitable electrolytes, which are often strong acids with high viscosity. The electrode is selectively etched at edges and tips due to stronger polarization on these features, resulting in an overall smoothing.[173]

A typical example of the current response of Cu in 14 M phosphoric acid is shown in Figure 3.4. Four distinct regions can be seen in this polarisation curve.[173,174] In region I, starting from open-circuit voltage (OCV), anodic surface dissolution occurs. When going anodic, a local maximum in current density can be observed. Then a short region (II) can be seen where the current decreases from the local maximum to a plateau. This relatively long current plateau (region III) is where the actual smoothening occurs. If the WE is strongly anodically polarised, the current increases again and surface roughening through formation of pitholes starts to occur (region IV).

The same conditions were used during electropolishing for all the work contained in this thesis: The Cu foil was placed ~2.5 cm from a Pt wire CE, immersed deeply so that ~2 cm of the Cu wire was electropolished as well. 30% H_3PO_4 was used as electrolyte. The WE was held using a clamp to minimize its movement during treatment. Immobilisation of the electrode is important to maximise the smoothening. Electropolishing was carried out at a cell potential of 2.1 V for 2×90 seconds, rotating the foil 180° halfway through the treatment so that each side was facing the CE once. After this procedure, the electrode appeared shiny, suggesting smoothening on the scale of the wavelength of visible light. In Figure 3.5, an SEM image of an as-received Cu foil (panel a) is compared with one of an electropolished foil (panel b). In the image from the as-received sample, some deep grooves can be observed, most likely originating from the rolling of the foil. Additionally, the surface between the grooves is also relatively uneven. Note that the image from the electropolished foil was measured at higher magnification, which leads to the two images not being completely comparable. Still, smoothening of the surface is evident, and no significantly uneven features can be observed for the electropolished electrode.

3.2.4 Preparation of oxide-derived Cu

As described in chapter 1, oxidation and subsequent reduction of Cu foils has received much attention as an efficient method to produce nanostructured electrodes. The quick reduction and resulting compression of the Cu lattice at room temperatures leads to formation of nanostructures and pores.[105]

One of the projects presented later in this work concerns CO reduction on oxide-derived Cu produced this way. To prepare the electrodes, polycrystalline Cu foils were made and electropolished as described above. They

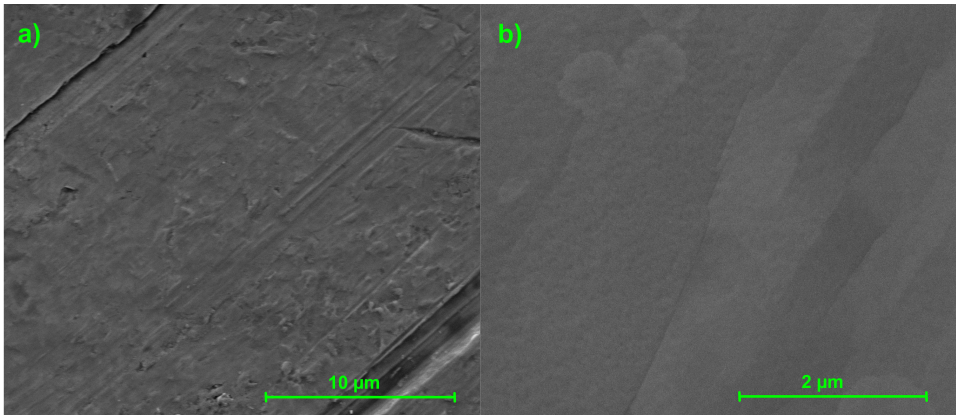

Figure 3.5: SEM images of (a) an as-prepared polycrystalline Cu electrode, and (b) an equivalent electrode after electropolishing. Note the different magnification of the two images. The images were measured by Anna Winiwarter.

were subsequently annealed at 500 °C for ~60 minutes and cooled down naturally to room temperature over several hours. Previous work by Li et al. showed that this procedure leads to the formation of a Cu_2O film with a thickness of approximately 3 µm.[105,165]

After annealing, the oxidised electrodes were mounted in the H-cell used for CO reduction measurements. Electrochemical reduction was carried out chronopotentiometrically at 7 mA cm^{-2} in Ar-saturated 0.1 M KOH, until fully reduced. The polycrystalline foil turns black after annealing, and reddish after reduction, as shown on the pictures in Figure 3.6. An example of an oxide reduction measurement is shown in Figure 3.7. The complete reduction of the oxide layer could be observed by a sharp negative increase in potential and a subsequent stabilisation, due to a change of the electrode process from oxide reduction to H_2 evolution. To avoid reoxidation, CO reduction measurements were started as quickly as possible after the reduction procedure was completed. Note that the electrolyte was purged between reduction of the electrode and starting of CO reduction.

3.2.5 Electrochemically active surface area of oxide-derived Cu

Whenever working with non-planar electrodes, determining the ECSA is important in order to normalise the activity measured to the actual surface

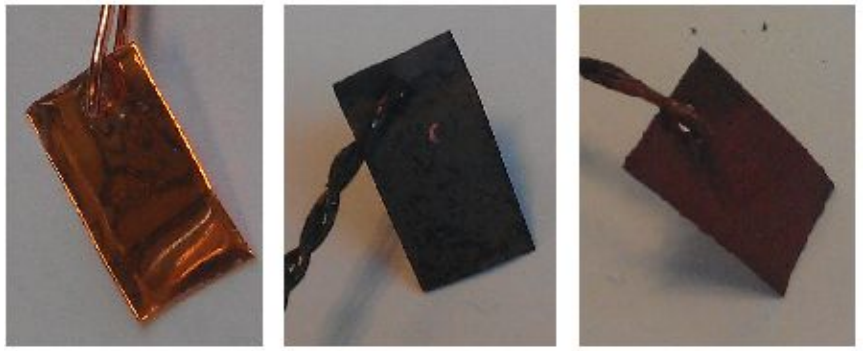

Figure 3.6: Pictures of oxide-derived Cu electrodes in the various stages of preparation. Left: As-prepared Cu foil. Middle: Cu foil after annealing at 500 °C in air for 1 hour. Right: OD Cu electrode after in-situ reduction.

area. By doing this, the intrinsic activity can be evaluated and compared between electrodes with different surface roughness. One approach to determine the ECSA of nanostructured Cu is by measuring the capacitative current in CVs in a region dominated by double-layer charging.[105,165] The double-layer capacitance is proportional to the ECSA. Thus, by comparing the capacitance of the nanostructured electrodes to that of a planar one, the roughness factor of the surface can be found.

In this work, the capacitance is determined by measuring CVs at different scan rates on polycrystalline and OD Cu foils of the same dimensions. The roughness factor of OD Cu can then be found from the ratio of its capacitance to that of polycrystalline Cu. Ar-saturated 0.1 M KOH was used as the electrolyte. Figure 3.8 shows examples of CVs and the resulting plot of capacitative current vs. scan rate for a representative OD Cu (a-b) and electropolished polycrystalline Cu (c-d) electrode. For the OD Cu in the figure, a specific capacitance of 22.7 mF cm^{-2} was observed, while that of the polycrystalline Cu was 264 μF cm^{-2}. This resulted in a roughness factor of 86 for this particular OD Cu electrode. 7 OD Cu electrodes were measured, giving an average roughness factor of 87 ± 10. This value was later used to normalise the CO reduction activity measured on OD Cu electrodes (in chapter 5).

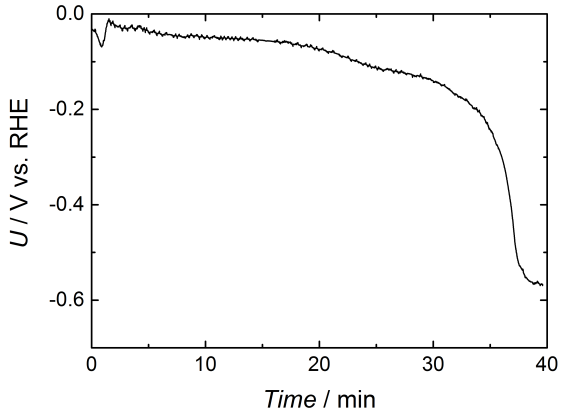

Figure 3.7: Chronopotentiometry trace from in-situ reduction of the OD Cu precursor for a representative electrode. The measurement was performed at -7 mA cm^{-2} in Ar-saturated 0.1 M KOH. The oxide layer is completely reduced when the potential makes a sharp drop and stabilises.

3.2.6 Preparation of polycrystalline Cu films for *operando* measurements

Polycrystalline Cu thin films were used for the operando measurements described in chapter 7. These were prepared by e-beam physical vapour deposition (PVD) onto an n-doped Si(100) substrate. First, a Si wafer was cut into 3×10 mm rectangular samples in a dicing saw. These were ultrasonicated, first in a 6:3:1 mixture of acetone, isopropanol and MilliQ water, and subsequently in pure MilliQ water. After this, the Si substrates were immersed in buffered hydrofluoridic acid in order to remove the native oxide layer, and loaded into the deposition chamber. A 3 nm Cr sticking layer was deposited first to facilitate better contact. Subsequently, a 50 nm Cu layer was deposited on top of this.

3.3 CO reduction setup

Most of the CO reduction measurements shown later in this thesis were conducted as batch experiments with *ex-situ* product analysis. In this section, I will describe the setup used for these measurements, along with important parts. A completely different setup was used when performing CO reduction

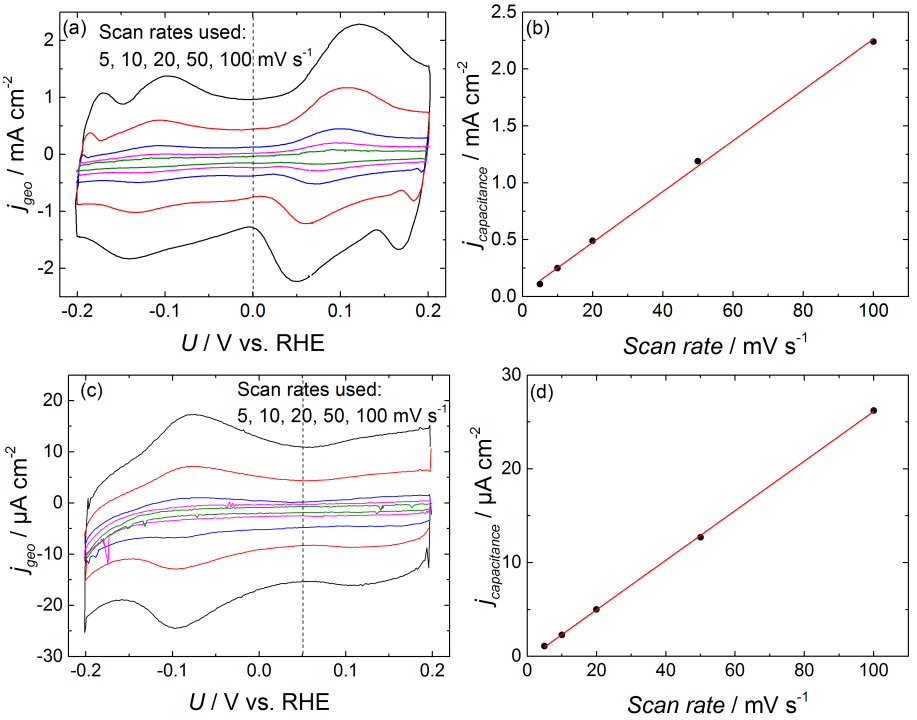

Figure 3.8: Determination of electrochemically active surface area of a representative OD Cu electrode. (a,c) Cyclic voltammograms in Ar-saturated 0.1 M KOH used for determination of the double layer capacitance of oxide-derived Cu and polycrystalline Cu, respectively. The stapled lines represent the potential where the capacitative current was recorded. (b,d) Capacitative current plotted versus scan rate for oxide-derived Cu and polycrystalline Cu, respectively. The capacitance of the electrode can be estimated from the slope of the linear fit. The specific capacitance of this particular OD Cu electrode was 22.7 mF cm^{-2}, while that of the polycrystalline Cu foil was 264 µF cm^{-2}. These values were used to determine a roughness factor for this particular OD Cu electrode of 86.

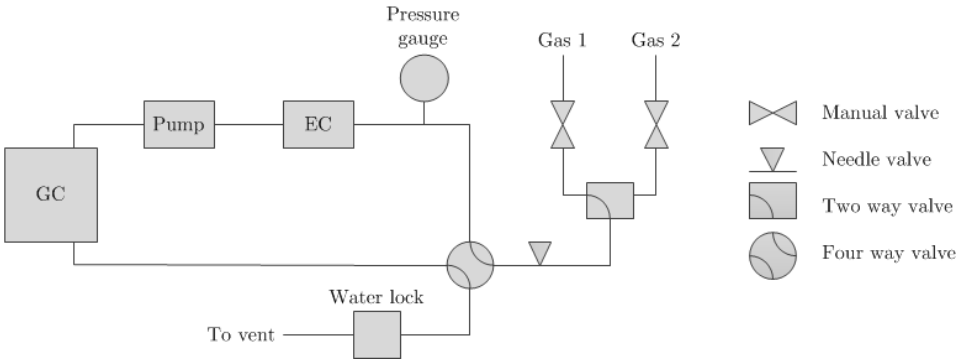

Figure 3.9: Schematic of setup used for CO reduction with *ex-situ* product analysis. The position of the four way valve determines whether the gas line is purged or in a closed loop. Prepared by Daniel B. Trimarco.

with *operando* GIXRD; this will be described in a separate section (3.6).

3.3.1 Setup overview

There are two important parts of the *ex-situ* setup; the gas loop and the electrochemical cell. All experiments carried out with this setup were batch measurements, meaning that both liquid and gaseous products accumulate. A schematic of the setup is shown in Figure 3.9. The liquid products get dissolved in the electrolyte, while the gaseous products leave the cell with the gas stream. Accumulation of these compounds is achieved by circulating the gas in the setup in a closed loop. However, before commencing measurements, the gas line and electrolyte needs to be saturated with the relevant gas, which is most often CO. By using the four way valve that is shown in the schematic, one can switch between flushing the setup and closing the loop. The electrolyte was sparged with the relevant gas for 15 minutes before measurements to ensure that saturation was achieved.

3.3.2 Electrochemical cell

A crucial part of the setup is, of course, the electrochemical cell. It is a custom-made H-cell in Pyrex glass, of which a picture and schematic shown in Figure 3.10. Several design principles need to be taken into account when designing a cell for CO reduction. The electrolyte volume of the WE compartment should be as small as practically possible. A small volume makes

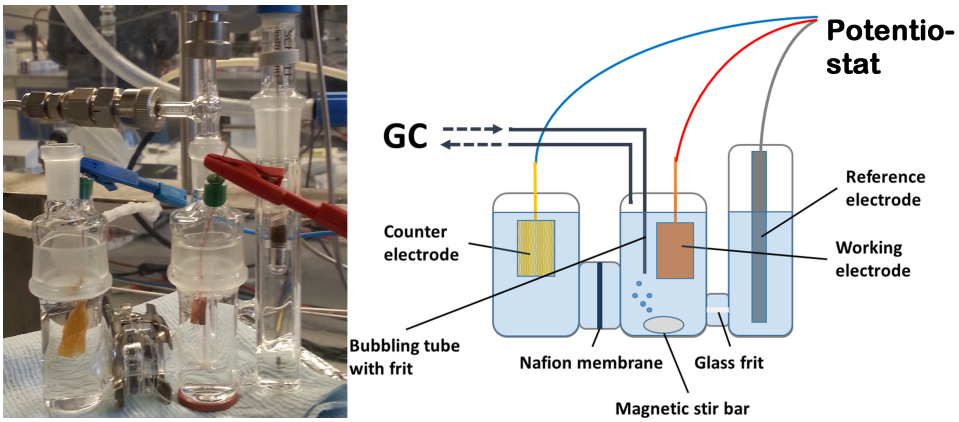

Figure 3.10: Picture (left) and schematic (right) of the electrochemical cell design used for all CO reduction measurements with *ex-situ* product analysis. An Au mesh counter electrode, and a Hg/Hg_2SO_4 reference electrode were used for all measurements. The schematic was prepared by Thomas V. Hogg.

achieving product concentrations above the detection limits of analytical equipment easier. For measurements reported herein, the WE compartment was filled with 12 mL of electrolyte.

Cation conducting membrane

The WE compartment needs to be separated from the CE compartment, both to keep the electrolyte volume at a minimum, but also to prevent diffusion of products to the CE. If products reached the CE, they could get reoxidised due to the positive polarisation of the CE, resulting in quantification errors. In this work, cation conducting membranes (Nafion 117) were used to separate the WE and CE compartments. The membranes were pretreated following a standard procedure.[175] They were cut into pieces that fit the flange of the cell. Then they were boiled or ultrasonicated at 85 °C for ~60 minutes in 3% hydrogen peroxide for cleaning, in a Piranha-cleaned beaker. They were rinsed thoroughly and boiled/sonicated for ~60 min again in 0.1 M sulfuric acid (H_2SO_4) for protonation. After rinsing them thoroughly again, they were boiled/sonicated for ~60 min in 0.1 M $KClO_4$. This step was carried out to saturate them with potassium instead of protons, in order to avoid the potential lowering of electrolyte pH from protons released from the membrane. Finally, the membranes were boiled/sonicated

Table 3.1: Solubility and Henry's law constant for CO_2 and CO. References for the latter were found through a compilation made by Rolf Sander.[177]

Reactant gas	**Solubility / g L^{-1}**	**k_H / M atm^{-1}**
Carbon dioxide	1.50[22]	3.5×10^{-2}[178,179]
Carbon monoxide	2.76×10^{-2}[22]	7.5×10^{-3}[180]

in MilliQ water for for ~20 min 2-3 times.

Gas dispersion

Another important detail with regards to cell design is the gas sparging. The solubility and Henry's law constant of the CO_2 and CO are shown in Table 3.1. Both, and in particular CO, have very low solubility in aqueous solutions.[22] Thus, efficient dissolution of the reactant gas into the electrolyte during electrolysis is important to avoid depletion. A common approach is to use a gas dispersion frit. This distributes the gas into a large number of small bubbles, significantly increasing the overall liquid/gas interface area and thus also the gas dissolution rate.[176] In our case, a bubbling tube is used with a gas dispersion frit at the end, releasing bubbles at the bottom of the cell. This can be seen in the picture and schematic of the cell displayed in figure Figure 3.10.

Leak tightness

Finally, the cell needs to be leak tight, both for liquids and gases. It is important to keep the electrolyte volume constant to achieved a well-defined accumulation of products for the later analysis. The crucial point for liquid leaktightness is the flange connection between the WE and CE compartments, where the cation-conducting membrane is positioned. As mentioned above, a thick version of the Nafion membrane was chosen (Nafion 117, 0.007 inches thick). The thicker membranes appeared to give better sealing of the flange, most likely because they can compress to a larger extent, sealing any defects or uneven regions of the two flange surfaces. A clamp pressing on each side of the flange was used to apply an even pressure on the membrane, as shown in Figure 3.10.

The cell also needs to be gas tight. All CO reduction experiments were carried out as batch measurements, meaning that the reactant gas was cir-

culated in a closed loop at a pressure of 1.1 bar, with gaseous products accumulating. This enables significantly increased detection limits for gas products, compared to measurements conducted with constant flushing of the setup. However, this approach significantly increases the vulnerability towards gas leaks. To mitigate leaks, MilliQ water was sprayed on all the glass fittings and PTFE sealing rings were used to fit the lid to the cell body.

3.4 Product analysis

Because of the many different products that can be formed from CO_2 and CO reduction,[48] thorough product analysis is crucial to get a complete picture of the behaviour of the electrode that is being studied. In this section, I will describe the various techniques that were used for product analysis. I used gas chromatography (GC) for gaseous product analysis, and static headspace-gas chromatography (HS-GC) and nuclear magnetic resonance (NMR) spectroscopy for liquid product analysis.

3.4.1 Gas chromatography

Gas chromatography relies on physical separation of products. A gas sample is transported through a narrow tube, the column, by the means of an inert carrier gas. A capillary column was used in this work, where the walls are covered by a polymer film. The individual constituents are separated as they move through the column, since they exhibit different degrees of interaction with the polymer film. After separation, the individual compounds can be measured with a detector. The interaction strength between a particular compound in the sample and the column, depends on the size of the compound (through van der Waals interactions), its polarity, etc. Compounds that are retained weakly in the column reach the detector first, and vice versa. Thus, a key parameter for identifying CO reduction products using GC is the *retention time*, meaning the time passing between the sample injection and the signal from a specific product in the detector.

An agilent 7890A was used for all gas product analysis. In our setup, the gas cycling loop for CO reduction measurements goes through two 250 µL sample loops, connected to automatic gas sampling valves mounted on the GC. The position of the GC in the overall setup is shown schemati-

cally in figure Figure 3.9. After injection, the two individual gas samples are led through separate columns by an Ar carrier gas, where the individual constituents are separated. An HP-PLOT Q column leads to a flame ionisation detector (FID), while an HP-PLOT Molesieve column leads to a temperature conductivity detector (TCD).

The column temperature has a significant influence on how strongly the products are retained. Increasing the column temperature lowers the retention time, and vice versa. This is a way to tune the separation of the products detected. Increasing the retention improves separation, but leads to longer measurement duration. Thus, a compromise needs to be found that is suitable for the specific set of compounds analysed for a given sample. For all measurements contained herein, the initial column temperature was kept at 35°C for 5 minutes. Subsequently, it was increased to 85 °C at a rate of 10 °C min^{-1} and kept at that temperature for the final 5 minutes.

Flame ionisation detector

In the FID, a hydrogen flame is used to ionise any organic compounds entering into CH^+ species. These are accelerated in an electric field towards a cathode, where a current generated that constitutes the output signal. As a result, FIDs can only detect oxidisable organic compounds, but are highly sensitive towards those. Because the carbon backbone of organic molecules is broken up into single-carbon species, the FID signal for a particular product is proportional to the number of carbon atoms in the molecule and their respective oxidation states.

Temperature conductivity detector

As is evident from the name, a TCD utilises differences in temperature conductivity to create a signal. It consists of two gas channels, one for the sample gas and one for the reference gas. The reference gas in this case is Ar, the carrier gas. A filament burns in each of them, and whenever the gas environment in the sample channel is different from the reference channel, a change in temperature conductivity can be measured, creating the signal. Note that while all products are in principle detectable using a TCD, the sensitivity at which they can be detected can vary significantly. The signal measured for a certain compound depends on the difference between its

thermal conductivity and that of the reference gas. The reason that Ar is used as a carrier gas is related to this. For CO_2 /CO reduction, the TCD is mainly used for detection of H_2, which is a side product from water splitting. All CO_2/CO reduction products are organic, which means that they can be measured using the more sensitive FID. Ar exhibits significantly lower thermal conductivity than H_2 (26.5 and 271 mW m^{-1} K^{-1} at 500 K, respectively[22]). This helps increasing the sensitivity towards H_2, compared to if the more common carrier gas He was used, that has a similar thermal conductivity to H_2.

3.4.2 Static headspace-gas chromatography

A GC can also used to analyse liquid products by direct injection. However, for all measurements in this thesis, the samples are in a 0.1 M KOH matrix. When evaporating the sample, the KOH salt would remain, and could seriously damage the injection port and column. One approach to vaporising the compounds without injecting the liquid sample directly is to heat up an electrolyte sample in a sealed vial. This way, a significant concentration of any volatile products would be created in the headspace gas volume of the vial, mixed with water vapour. This gas mixture can be injected into the GC, avoiding the electrolyte salt. This is the general principle behind the HS-GC technique. The heating and injection process can of course be carried out manually, for example using a water bath of the desired temperature and a gas syringe. However, it is normally carried out in an autosampler in order to achieve as high an accuracy as possible. For all my measurements involving HS-GC, such a specialised sampler was used, connected to a split/splitless inlet on the GC. After injection, the sample was separated in the HP-PLOT Q column and detected in the FID, giving high sensitivity to any volatile organic species present. Examples of HS-GC vials are shown in Figure 3.11. The vials need to be approximately half-filled, allowing for accumulation of any volatile species in the gas headspace above the liquid sample.

However, because HS-GC relies on vaporisation of the sample, non-volatile products cannot be detected. For CO_2/CO reduction, this is particularly applicable to carboxylic acids, that have acidic pK_a and are deprotonated under neutral and alkaline conditions. As a result of the inability to detect non-volatile species, this technique has to be combined with another

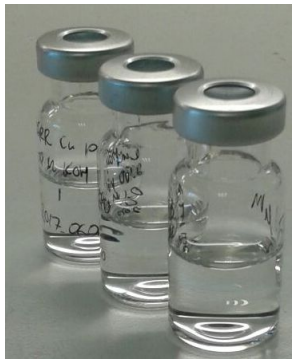

Figure 3.11: Picture of HS-GC sample vials.

that does not exhibit the same limitation. This way, a complete overview of the products contained in the sample can be ensured. Because the amount of each individual compound injected in the GC is directly correlated with its concentration in the sample vial headspace, the sensitivity of the technique to a particular product is heavily influenced by its Henry's law constant, as discussed in further detail in section 4.2. A list of Henry's law constants for all known CO_2 reduction and CO reduction products is shown in Table 3.2.

In this work, a 7694E headspace sampler was used, together with the same 7890A GC described above. The samples were equilibrating at 70 °C for 15 minutes, before a sample of the headspace gas mixture was injected through a split/splitless inlet in splitless mode. 5 mL samples were measured in 10 mL vials, to facilitate sufficient headspace gas volume. Normally, the sample would be heated to 85% of the boiling point of the matrix for maximum sensitivity. However, I observed significant inaccuracy for quantification at this temperature, at least partly caused by leaks from a high pressure build-up of water vapour. At 70 °C, quantification was more accurate.

Different temperature programs were used for the different experimental projects contained in this thesis. These are summarised in Table 3.3.

3.4.3 Gas chromatography-mass spectrometry

For the project concerning oxide-derived Cu described in chapter 5, HS-GC was used in combination with mass spectrometry (MS). MS is a powerful

Table 3.2: Henry's law constants for known liquid products from CO_2 and CO reduction. All products were detected from CO_2 reduction on polycrystalline Cu by Kuhl et al.[48] The Henry's law constants have been retrieved from the references stated, via a complation made by Rolf Sander.[177] *Since the two values for ethylene glycol were widely different, I included them separately.

Product	**k_H / M atm^{-1}**	**References**
Formate ($HCOO^-$)	–	–
Formic acid (HCOOH)	$(9.1\pm3.8) \times 10^3$	[181–183]
Methanol (CH_3OH)	$(2.2\pm0.1) \times 10^2$	[184–187]
Acetate (CH_3COO^-)	–	–
Acetic acid (CH_3COOH)	$(6.3\pm2.7) \times 10^3$	[181–183]
Glyoxal (OCHCHO)	$(3.3\pm0.4) \times 10^5$	[188,189]
Glycolaldehyde ($HOCH_2CHO$)	4.1×10^4	[188]
Ethylene glycol ($(CH_2OH)_2$)	1.7×10^4, 4.0×10^6	[190], [191]*
Acetaldehyde (CH_3CHO)	$(1.4\pm0.2) \times 10^1$	[187–189,192,193]
Ethanol (C_2H_5OH)	$(2.0\pm0.3) \times 10^2$	[184–187,194]
Hydroxyacetone (CH_3COCH_2OH)	7.8×10^3	[195]
Acetone ($(CH_3)_2CO$)	$(2.8\pm0.4) \times 10^1$	[185,187,189,192,193,196–198]
Allyl alcohol (C_3H_5OH)	$(2.8\pm1.4) \times 10^2$	[199–201]
Propionaldehyde (C_2H_5CHO)	1.3×10^1	[189,192]
1-Propanol (C_3H_7OH)	$(1.4\pm0.2) \times 10^2$	[184,185,187]

technique for determining the mass of unknown compounds. This is done by ionising any incoming compound and passing it through a mass analyser, which separates ions by size using electric fields and selects certain masses using a slit.[204] In contrast to the conventional GC detectors FID and/or TCD, the individual separated compounds in the chromatogram can be identified from their mass spectrum, which is often done through comparison with reference spectra. This is particularly helpful for liquid product analysis, since a large number of liquid compounds can potentially be formed from CO_2 reduction,[48] and thus also CO reduction.

Herein, an Agilent 7890B/5977 GC/MS instrument was used for all measurements with this technique. 5 mL of the liquid sample was equilibrated at 70 °C for 5 min in a 20 mL vial, and a 2.5 mL PFTE Tipped Plunger Headspace Syringe (SGE Analytical Science) was used to sample 250 µL of the headspace gas composition in the vial. The products were separated in a Solgel-wax column (Length: 30 m; ID: 0.25 mm; Film: 0.25 µm). The column temperature was kept at 40 °C for 4 minutes, before heated to 250 °C at a rate of 6 °C min^{-1}.

Table 3.3: Overview of the column temperature programs used for HS-GC analysis in the various projects discussed in this thesis.

Project	**$T_{initial}$ / Duration**	**Heating rate**	**T_{final} / Duration**
CO reduction on OD Cu[202] (section 4.2.4 and chapter 5)	130 °C / 35 min	–	–
HS-GC benchmark[203] (section 4.2)	130 °C / 20 min	10 °C min^{-1}	230 °C / 5 min
CO reduction on polycrystalline Cu (chapter 6)	150 °C / 35 min	–	–

3.4.4 Nuclear magnetic resonance spectroscopy

NMR spectroscopy is another powerful method for identifying unknown liquid compounds. In this technique, the spin that certain nuclei exhibit is utilised to probe the chemical environment they experience. Nuclei with a net spin will align upon the application of an external magnetic field. The direction of the spin will then be either parallel or anti-parallel to the field lines. The parallel configuration exhibits lower energy, and is thus more highly populated. If electromagnetic radiation with frequency corresponding exactly to the energy difference between the two spin states is applied, some spins in the parallel state will be excited to the anti-parallel state. This phenomenon is called resonance. If the radiation is stopped, some nuclei will relax and release energy in the form of electromagnetic radiation that can be detected. Importantly, a nucleus in a molecule experiences somewhat varying magnetic fields depending on the other nuclei in its vicinity, due to shielding effects. Thus, nuclei in different chemical compounds can be differentiated from their slight variation in resonance frequency, which allows for identification of the compounds present.[205]

In the present work, ^{1}H NMR spectroscopy was used to identify and quantify products, because of the high natural abundance (99.98%[205]) of

the ^{1}H isotope. The other commonly used isotope for NMR spectroscopy of small organic compounds is ^{13}C, which has a natural abundance of 1.1%,[205] giving significantly lower sensitivity. However, all CO reduction measurements contained herein are carried out in aqueous electrolyte, meaning that the samples contain mainly water. The concentration of liquid products in the electrolyte is normally a few hundred μM or below. Thus, the peak from the protons in the water molecules will give a peak that is several orders of magnitude larger than those from the CO reduction products. To prevent the water peak from overshadowing the products, water suppression is applied.

All NMR spectra were aquired using a Bruker Ascend 400 MHz spectrometer equipped with a Prodigy Cryoprobe. 1D NOESY experiments with pre-saturation were performed for water suppression. 17% D_2O and 500 μM DMSO were added. The former compound is necessary for water suppression, while the latter was used as an internal standard. Exact parameters for data aquisition can be found in [203].

3.5 *Ex-situ* characterisation

Throughout the studies reported in this thesis, scanning electron microscopy (SEM) and X-ray photoelectron spectroscopy (XPS) were used for *ex-situ* characterisation of the electrodes. In the following, I will give a brief introduction to these techniques, and describe how they were applied in this work.

3.5.1 Scanning electron microscopy

SEM is a versatile technique that can be used to study the morphology of conductive surfaces with a resolution down to ~5 nm.[31] In SEM, a focussed electron beam is used to scan the surface and obtain information. In general, intermediate to high-energy electrons can lead to a number of interactions with the surface. SEM utilises either backscattered or secondary electrons. The former are electrons that are elastically scattered off atoms in the sample. Atoms with higher mass give a higher yield of backscattered electrons, and thus a contrast by atomic mass is obtained from this technique.[206] Secondary electrons are weakly bonded electrons from the sample that are excited from the incoming electrons, and then undergo a cascade of inelas-

tic scattering interactions.[31] These electrons sample a larger volume if they enter the surface at an angle than if they enter perpendicularly. As a result, a larger signal is normally obtained from parts of the surface that are not perpendicular to the electron gun. Thus, secondary electrons give contrast by surface morphology.[206] They generally have lower energy than backscattered electrons, which leads to SEM characterisation by secondary electrons being more surface sensitive than backscattered electrons.[31]

In this work, measurements were performed with a FEI Quanta 200 ESEM with a field emission gun at an acceleration voltage of 5-10 kV. Secondary electrons were measured using an Everhart-Thornley detector. A pressure of $< 6 \times 10^{-6}$ mbar was used for all measurements.

3.5.2 X-ray photoelectron spectroscopy

XPS is a useful technique for studying the elemental composition and chemical state of the surface of a solid sample. In the present thesis, it was mainly used to investigate whether foreign metal impurities were present on Cu electrodes after CO reduction.

XPS relies on X-ray radiation to excite electrons from the sample surface.[31] A schematic showing the mechanism is displayed in Figure 3.12. An incoming X-ray photon gets absorbed, and its energy is transferred to a bound electron. This electron (called a photoelectron) is excited and leaves the surface with a certain kinetic energy. The following relation thus exists between the incoming X-ray energy ($h\nu$), the binding energy of the electron in the sample (E_b) and the resulting kinetic energy of the photoelectron (E_k):

$$E_k = h\nu - E_b - \phi \tag{3.4}$$

Here, ϕ is the work function of the electron energy analyser. The binding energy of the electron is specific to the element that it was excited from, and its chemical state. Once an electron from a higher energy level relaxes to fill the hole left by the photoelectron, the energy released can exite an additional electron, in what is referred to as an *Auger process*. The kinetic energy of an Auger electron is element-specific and does not depend on the energy of the incoming X-rays. A schematic of this process is shown on the right side of Figure 3.12.

Examples of XPS spectra measured on Cu electrodes are shown in Figure 6.5 on page 124. In the measurements contained in this thesis, an Al

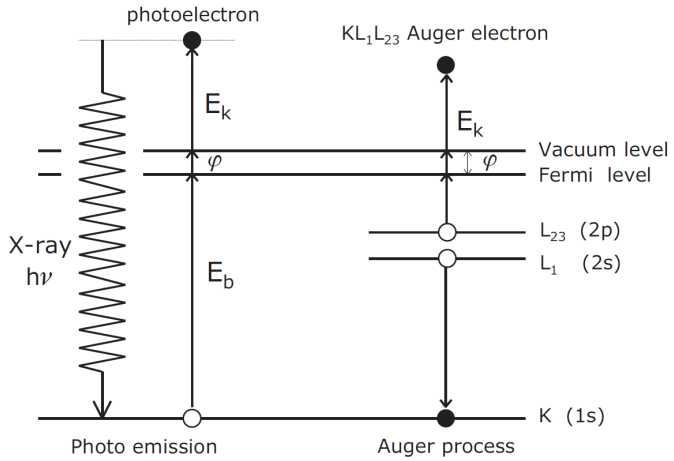

Figure 3.12: Schematic showing the various excitation mechanisms that can occur during X-ray photoelectron spectroscopy. Reprinted with permission from Chorkendorff and Niemantsverdriet.[31] Copyright © 2003, John Wiley and Sons.

Kα source was used to generate X-rays with an energy of 1486.3 eV. The kinetic energies of the photoelectrons were ranging from this value to 136 eV. As a result, the samples were probed at a depth of ~0.5 to 2 nm.[31,207]

In this thesis, measurements were performed using a ThermoScientific Thetaprobe spectrometer. An Ar flood gun was used for charge neutralisation, resulting in a chamber pressure of $\sim 1 \times 10^{-7}$ mbar. Survey spectra were measured with 20 scans in 1 eV steps with 20 ms dwell time. Si 2p scans were measured with 50 scans in 0.1 eV steps with 50 ms dwell time.

Whenever performing *ex-situ* characterisation after electrocatalysis measurements, care must be taken when transferring the electrode from the electrochemical cell to the analysis instrument. In this case, XPS was mainly used to identify metal impurities on the electrode surface after CO reduction. These are deposited at the cathodic operating potentials, but can easily be oxidised off the surface at anodic potentials. The open-circuit potential of Cu is ~0.5 V in CO-saturated 0.1 M KOH. As a result, if an electrode is left in the electrolyte after the CO reduction measurement is stopped, it will quickly drift to this potential, and the impurities might be removed. To prevent this, the electrodes were removed from solution under potential control, meaning that the measurement was first stopped when the electrode was no longer in contact with the solution.

Once removing the electrode from the cell, it is tempting to rinse it

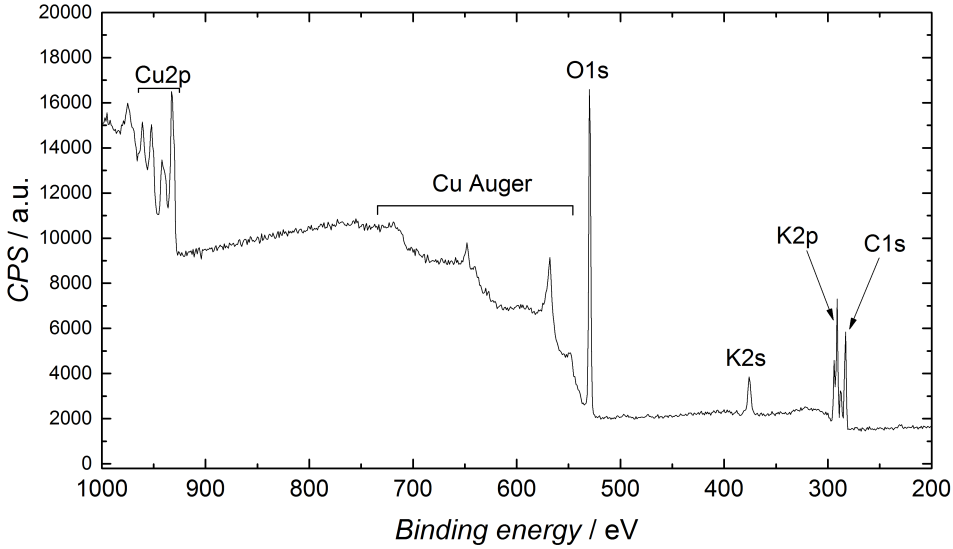

Figure 3.13: Part of an XPS survey spectrum from a polycrystalline Cu electrode that was not rinsed after a CO reduction measurement. Potassium originates from the 0.1 M KOH electrolyte.

in order to remove electrolyte residues. However, O_2-saturated water can easily oxidise metallic impurities off the surface. As a result, two different approaches were used in the work contained in this thesis. Either, the electrodes were not rinsed, but instead dried with lens paper. This was done carefully to avoid the paper touching the part of the surface that would later be used for characterisation. The second approach was to rinse the electrode by briefly (2-3 seconds) immersing it in a beaker with Ar-saturated MilliQ water, hoping that this would avoid significant oxidation. In Figure 3.13, an XPS spectrum from a polycrystalline Cu electrode that was not rinsed after CO reduction is shown. The Cu2p peaks exhibit low intensity, while large potassium peaks can be observed. This shows that KOH from the electrolyte dries and forms a film on the surface. As a result, a lower signal from the electrode itself is obtained. In this work, XPS is mainly used to evaluate whether metal impurities are present on the electrode after CO reduction. Because the presence of KOH on the surface significantly lowered the signal from the Cu electrode, this would also decrease the sensitivity towards metals deposited under reaction conditions. As a result, data shown later are obtained from briefly rinsed samples (Figure 6.5 on page 124).

3.6 *Operando* measurements during CO reduction

In addition to the CO reduction measurements with *ex-situ* product analysis, I have carried out *operando* X-ray diffraction (XRD) on polycrystalline Cu during CO reduction. Carrying out catalyst characterisation under operating conditions leads to additional requirements of the setup, compared to what was described previously.

3.6.1 Synchrotron X-ray radiation

One of the most significant differences between *operando* XRD measurements during electrocatalyis and *ex-situ* analyis is the addition of an aqueous electrolyte. Water interferes with the incoming X-rays, severely reducing the intensity that can be detected from the surface. As a result, synchrotron radiation needs to be used, because of its particularly high flux of X-rays. In a synchrotron, X-rays are generated by changing the direction of high-energy electrons. The resulting X-ray energy can be tuned using a monochromator. For the measurements discussed in this thesis, 17 keV X-rays were used.

3.6.2 Grazing incidence X-ray diffraction

XRD relies on the elastic scattering of X-rays in solid samples. The X-rays penetrate relatively deeply into the material because of their high energy. For a material with an ordered crystal structure, different X-ray photons will thus scatter off different layers of the crystal lattice, leading to constructive or destructive interference at a certain incident angle depending on the interatomic distance. This principle was formulated in Bragg's law, which is expressed in eq. (3.5).

$$n\lambda = 2d\ sin\alpha \tag{3.5}$$

Here, λ is the X-ray wavelength, d is the interatomic distance, α is the incidence angle of the X-rays and n is an integer number, called the reflection order. By scanning through different angles, the crystal structure and interatomic distance can be determined.

At most incidence angles, the X-rays penetrate several hundred nanometres or more into the sample. However, catalysis happens at the surface, and thus only the surface and near-surface structure, or the topmost few nanometres, is relevant. One approach to improve the surface sensitivity is

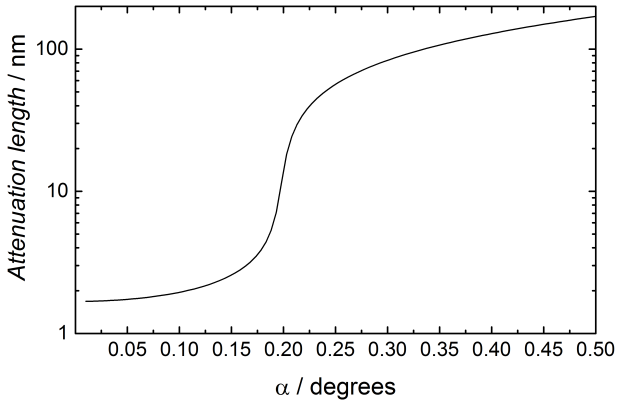

Figure 3.14: Attenuation length of 17 keV X-rays in Cu at various incidence angles (α). The data are calculated using an online tool from the Center for X-ray Optics at the Lawrence Berkeley National Laboratory, based on work by Henke et al.[208] The built-in tabulated value of the online tool was used for the density of Cu.

to measure at very low angles, performing grazing incidence XRD (GIXRD). If measuring at or below the critical angle of total reflection, the penetration depth can be limited to just a few nanometres. In Figure 3.14, the calculated attenuation length in Cu for X-rays of the relevant energy (17 keV) is shown.

3.6.3 *Operando* cell

For *operando* measurements, the cell needs to be optimised after the reqirements from the characterisation technique. In Figure 3.15, a picture and schematic of the cell used for the *operando* XRD described in this thesis is shown. measurements is shown. The orange part of the cell is the X-ray transparent window made of Kapton. Below that, the sample (marked as "working electrode" in schematic) is placed horizontally. The electrolyte volume on top of the WE is small (~30 μL), in order to minimise the path length of the X-ray beam through the electrolyte. As a result of the small volume, the electrolyte needs to be flowed through the cell to avoid fast depletion of CO. Furthermore, the flow mitigates bubble formation inside the electrolyte volume due to the formation of gaseous products at the WE, which might break the electrochemical contact between the electrodes. The CE consists of two Pt wires that are stretched across the top of the cell, parallell to the WE surface. The RE is introduced through a capillary, as

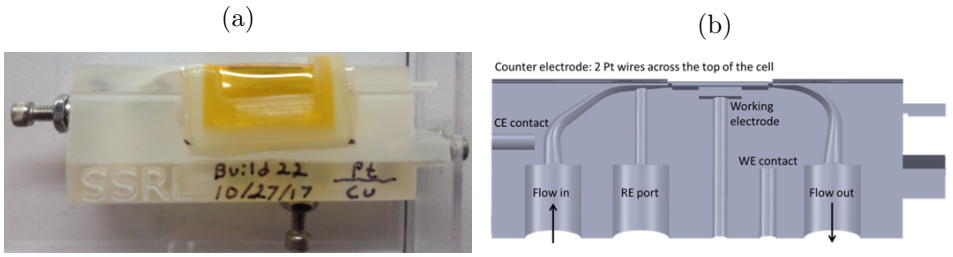

Figure 3.15: Picture and schematic of the cell design used for *operando* GIXRD measurements during CO reduction.

shown in the schematic in Figure 3.15b.

3.6.4 *Operando* setup

In Figure 3.16, a schematic of the full setup is shown. The desired gas (CO or Ar) is flowed through a cell containing MilliQ water, in order to humidify the gas. This prevents significant evaporation when the electrolyte is sparged. The sparging of the electrolyte occurs in a separate cell, equipped with a gas dispersion frit to facilitate more efficient saturation. A gas flow rate of 5-15 mL min^{-1} was used for the present work. The CO gas is then led to the exhaust, while the electrolyte is circulated through the setup at 5-15 mL min^{-1} using an HPLC pump. We used a flow rate of 15 mL min^{-1} initially. However, due to high resistance in the flow path, this led to leaks and pump issues, which made us decrease the flow rate. Another cell filled with Chelex was placed in the electrolyte flow path. Chelex consists of pellets covered with a chelating agent that binds strongly to any metal ions present in solution. This was installed in the setup to minimise the amount of metal impurities present in the electrolyte during CO reduction.

3.6.5 Pilatus detector

A Dectris Pilatus 100K detector was used for all measurements. It can detect the incoming radiation with spatial resolution in two dimensions (487 × 195 pixels). This means that at every diffraction angle, an image is measured. An example of such an image is shown in Figure 3.17. The detector has a size of 84 mm in the 2θ dimension, which is the x-axis of the image. This corresponds to around 5 degrees of the 2θ spectrum. The bright

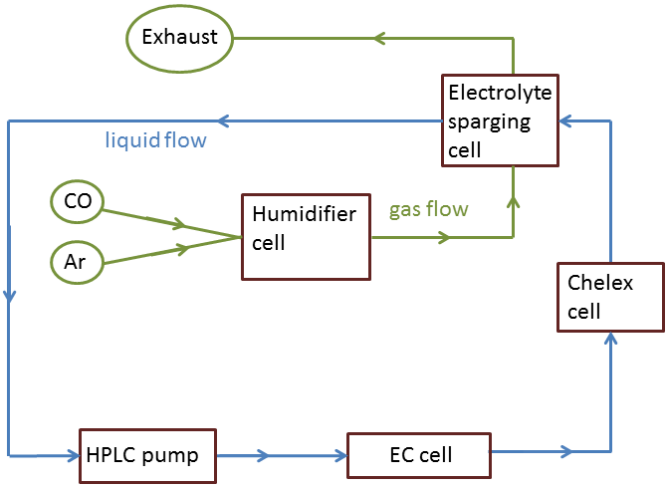

Figure 3.16: Schematic of setup used for sparging and circulation of electrolyte for *operando* GIXRD mreasurements during CO reduction.

line in the middle is part of a diffraction ring, from powder diffraction off the polycrystalline Cu sample. The two dark areas on either end of the 2θ axis are caused by adjustable slits blocking part of the incoming radiation. The spatial resolution of the detector gives a significant advantage when performing two different types of measurements.

2θ scans

For 2θ scans, the detector is moved in order to probe the scattered X-rays over a large 2θ range. Such measurements can also be carried out using detectors without any spatial resolution. However, the signal measured is significantly improved by using the Pilatus detector. The signal can be integrated along the diffraction line, which is the y-axis in Figure 3.17. In addition, every time the detector moves its position to sample the 2θ direction, the diffraction ring will move slightly on the detector. This way, the signal can be integrated over multiple images, leading to further improvements of the sensitivity. 2θ scans measured using this approach are shown in section 7.1. They were carried out by scanning the detector from $2\theta = 10$ to 60 degrees with 250 points. A dwell time of 1 second was applied per point, but including processing between data aquisition, 2-3 seconds were used per point. As a result, each 2θ scan took around 10 minutes.

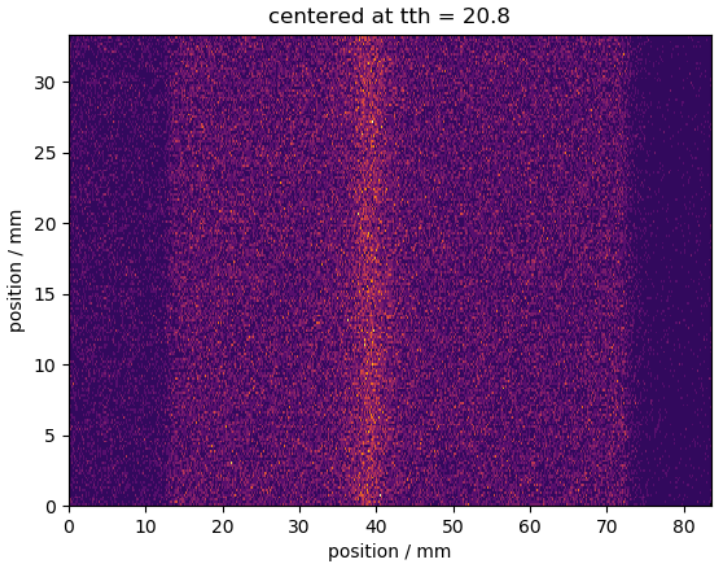

Figure 3.17: Example of an image with spatial resolution captured by the Pilatus X-ray detector. The x-axis in the figure represents the 2θ direction.

Timescans

In addition to the significant improved signal achieved for 2θ scans when using the Pilatus detector, its spatial resolution allows for a different type of measurements. Because it samples ~5 degrees in the 2θ dimension, part of the spectrum can be measured without moving the detector. This allowed for monitoring of certain important diffraction peaks with significantly higher time resolution than the ~10 minutes used for 2θ scans. With a dwell time of 1 second per data point and additional time used for processing, a time resolution of 2-3 seconds could be achieved.

4

Development and benchmark of analytical methods

As many as 16 products have been detected from CO_2 reduction on Cu electrodes,[48] and most of them are also possible to form during CO reduction. As a result, I have spent a significant amount of time during my PhD developing and benchmarking analytical methods suitable for CO reduction. I introduced the principle behind the various techniques in section 3.4. In this chapter, I present calibrations for relevant products and compare the different techniques for liquid product analysis.

The discussion about techniques for liquid product analysis (section 4.2) is mainly based on my two published peer-reviewed papers, which are attached to this thesis (articles 1 and 2 in the list of publications).[202,203] I was the first author of both these studies, and carried out the main part of the experimental work myself. I also had the main responsibility for writing first drafts for both manuscripts. In the first study, we investigated the organic chemistry of acetaldehyde in alkaline electrolytes.[202] Note that I carried out some preliminary measurements for this study during my Master's project.[209] However, all the data shown herein were obtained during my PhD. Davide Ravasio, who was employed at Carlsberg Laboratory at the time, carried out GC-MS measurements to confirm the presence of acetaldehyde, together with Jürgen Wendland. Sebastian Meier, a senior researcher at DTU Chemistry, carried out high-resolution NMR spectroscopy. In the second study, we benchmarked the performance of HS-GC and NMR spectroscopy by measuring on standard solutions containing relevant CO reduction products.[203] Younes Abghoui, who was a visiting PhD student in our group at the time, participated in planning of the study, and he conducted

some preliminary measurements. Zarko P. Jovanov and Ana Sofia Varela were in my group before I started my PhD; they installed and optimised the HS-GC equipment. Ifan E. L. Stephens and Ib Chorkendorff participated in planning the study and analysing the results. All the authors assisted in revision of the manuscript. For any measurements presented that I did not carry out myself, this is specified in the figure caption.

4.1 Gaseous product analysis

As discussed in section 3.4, and shown in the setup schematic in Figure 3.9 on page 60, gaseous products accumulate in a loop that is directly connected to the GC during CO reduction measurements. They can be detected and quantified through automatic injection into the GC, separation in the column and subsequent detection using the FID and/or TCD. However, a number of parameters need to be determined to achieve accurate quantification. First of all, calibration of the individual gaseous products should be carried out. In addition, the internal gas volume of the setup needs to be determined.

4.1.1 Gaseous product calibration

Calibration of gaseous products can be carried out by injection of standard gases containing the relevant compounds. In this work, I used one gas mixture to calibrate for H_2 and another to calibrate for C_1 to C_3 alkanes and alkenes. The two gas mixtures are 5% H_2 in Ar, and approximately 1% CO (CO_2 reduction product), 0.2% CH_4, 0.25% C_2H_4, 0.15% C_2H_6, 0.10% C_3H_6, 0.15% C_3H_8 and 1.00% CO in Ar, respectively. H_2 can only be detected using the TCD. The hydrocarbons can in principle be measured using both the FID and TCD. However, the FID is significantly more sensitive towards the compounds that it can measure. Thus, I have only calibrated hydrocarbons on that detector. A common method for achieving high sensitivity towards CO is using a methaniser, meaning that the CO is catalytically converted to methane right before the FID. CO is included here since it is a CO_2 reduction product, and is calibrated on the FID. Example chromatograms for injection of the two different calibration gas mixtures are shown in figure Figure 4.1. The hydrocarbon gases are separated well in the Q-PLOT column, except for a slight overlap between CO

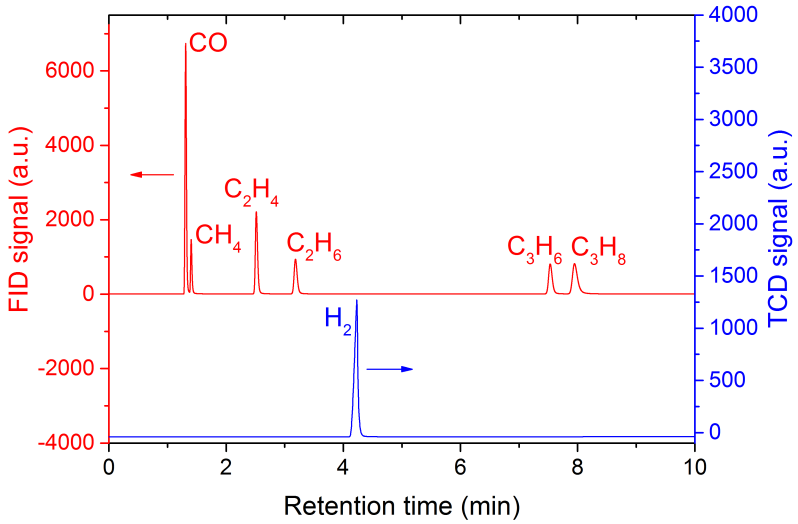

Figure 4.1: Example of injections with standard gas mixtures for GC calibration. Red: FID calibration with a gas mixture containing approximately 1% CO, 0.20% CH_4, 0.25% C_2H_4, 0.15% C_2H_6, 0.10% C_3H_6 and 0.15% C_3H_8 in Ar. Blue: TCD calibration with a gas mixture containing around 5% H_2 in Ar.

and CH_4. The retention times and response for the individual products in a calibration with these gases is shown in Table 4.1.

The peak areas obtained for each compound when normalised to 1% concentration scale with the number of carbon atoms in the molecule. As explained in section 3.4, this is because the incoming molecules are ionised to $C{-}H^+$ ions, and thus each individual carbon atom gives a signal. Since CO is converted to methane these two compounds give a similar response. The TCD is relatively sensitive towards H_2 because of its significantly different thermal conductivity from Ar, the carrier gas. Still, the FID exhibits an order of magnitude higher response or more towards hydrocarbons than the TCD does to H_2. Nevertheless, gas product analysis using GC gives excellent sensitivity. Additionally, as long as care is taken so that the sample pressure is well-defined in the sample loop during injection, the error between individual measurements is below 1%. This versatility and robustness is reflected in GC being the technique-of-choice for *ex-situ* gas product analysis for most groups in the field.[47,48,105,110,210–214]

Table 4.1: Retention time and calibration peak area from GC injections of standard gas mixtures. The signal shown is the peak area from 3-5 individual injections, and the resulting standard deviations were below 1%.

Product	**Retention time / min**	**Conc. in calibr. gas / %**	**Calibration signal / a.u.**	**Signal for 1% / a.u.**
H_2	4.2	5.00	5.62×10^4	1.13×10^4
CO	1.3	1.01	1.33×10^5	1.32×10^5
CH_4	1.4	0.197	2.29×10^4	1.16×10^5
C_2H_4	2.5	0.262	6.07×10^4	2.32×10^5
C_2H_6	3.2	0.151	3.49×10^4	2.31×10^5
C_3H_6	7.5	0.102	3.59×10^4	3.52×10^5
C_3H_8	7.9	0.149	5.20×10^4	3.49×10^5

4.1.2 Setup volume

In order to be able to determine the number of mols produced of a certain gas product, the internal gas volume of the setup needs to be known. The total gas volume,V_{tot}, can be expressed using the ideal gas law, as shown in eq. (4.1).

$$V_{tot} = \frac{n_{tot} RT}{p_{tot}} \tag{4.1}$$

Here, n_{tot} is the total amount of gas in mol, R is the ideal gas constant (0.0831 L bar K^{-1} mol^{-1}), T is the temperature (~298 K) and p_{tot} is the total gas pressure in the system, which was set to 1.1 bar for all measurements. n_{tot}, which is the only unknown, can be estimated by performing H_2 evolution in an Ar-saturated setup. This is achieved by saturating the electrolyte with Ar. n_{tot} is related to the amount of H_2 in the gas volume, n_{H2}, by eq. (4.2).

$$n_{H2} = c_{H2} n_{tot} \tag{4.2}$$

Here, c_{H2} is the volumetric concentration of H_2 in the gas mixture. The concentration of H_2 can be determined through eq. (4.3) by performing GC analysis.

$$c_{H2} = \frac{A_{H2}}{100 K_{1\%H2}} \tag{4.3}$$

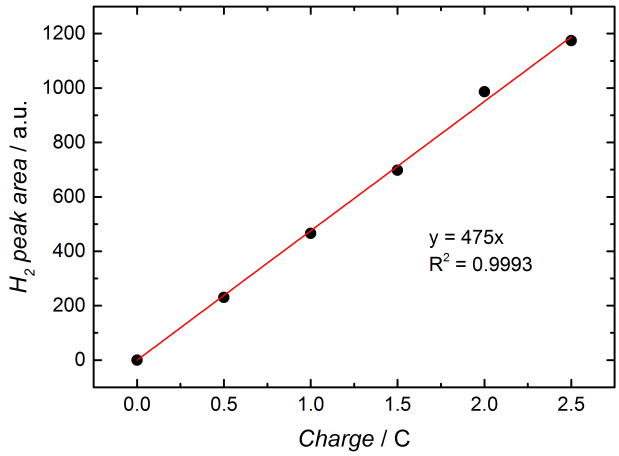

Figure 4.2: H_2 peak area from GC injections as a function of total charge going to H_2 evolution. The slope, α can be used to determine the gas volume of the CO reduction setup through eq. (4.5). In this case, $\alpha = 475$ gives a gas volume of 28 mL.

Here, A_{H2} is the H_2 peak area from the GC measurement, while $K_{1\%H2}$ is the peak area for 1% H_2 obtained from calibration, as shown in Table 4.1.

Now, only n_{H2} in eq. (4.2) needs to be determined before the volume can be calculated. This can be estimated from Faraday's law of electrolysis, as shown in eq. (4.4).

$$n_{H2} = \frac{Q_{H2}}{zF} \tag{4.4}$$

Here, Q_{H2} is the charge going to H_2 formation. Since the system is saturated with Ar, 100% Faradaic efficiency towards this reaction can be assumed, and Q_{H2} is equivalent to the total measurement charge. z is the amount of electrons transferred in mol per mol of product (2 for this reaction). F is the Faraday constant (96485 C mol^{-1}).

Based on the equations above, eq. (4.1) can be expressed as follows:

$$V = \frac{100 K_{1\%H2}\ RT}{p_{tot} z F\ \alpha} \tag{4.5}$$

Here, α is A_{H2}/Q_{H2}, and can be estimated from the slope of the linear fit obtained from performing H_2 evolution with varying charge. An example of such a measurement is shown in Figure 4.2. By inserting $\alpha = 475$ into eq. (4.5), a volume of 28 mL can be found. This includes the gas headspace above the electrolyte in the WE compartment of the cell, which depends

on the electrolyte volume. A well-defined electrolyte volume is therefore important, achieved in this case by using a micropipette.

4.2 Liquid product analysis

From the previous section, it is clear that *ex-situ* analysis of gaseous products can be carried out with high sensitivity and accuracy by using GC if proper procedures are followed. Quantification of liquid products is more challenging, however, due to a number of factors that will be discussed in detail in this section. Notable examples are lower sensitivity, and the potential for spontaneous chemical reactions occurring with the products. Typical techniques used for *ex-situ* liquid product analysis in the literature are nuclear magnetic resonance (NMR) spectroscopy[48,99,105,120,155,215] and high-performance liquid chromatography.[103,110,140,161,216,217] HS-GC is another relevant techniques, which was used together with NMR spectroscopy for all product analysis in this thesis. In this section, I present calibrations of relevant liquid products. One of the main aims is to benchmark the performance of HS-GC and NMR spectroscopy for the relevant products. A quantitative comparison of relevant techniques is useful when choosing which of them to apply for certain scenarios, achieved in this work by determining approximate detection limits. This was done in previous work by Hong et al., but they did not include HS-GC in their study.[218] In addition to the calibration, I discuss acetaldehyde chemistry in alkaline solution, an example of a situation where organic chemistry influences product analysis.

HS-GC is a promising technique for analysis of volatile liquid products, since it is a simple add-on to a conventional GC, making it a minimal investment for labs conducting CO_2 and CO reduction. In this study, we assessed the advantages and disadvantages of HS-GC and NMR spectroscopy by comparing the sensitivity of the two techniques for quantification of liquid products in alkaline electrolyte. The comparison was done by measuring calibration curves for six products relevant to CO reduction: methanol (CH_3OH), acetate (CH_3COO^-), acetaldehyde (CH_3CHO), ethanol (C_2H_5OH), propionaldehyde (C_2H_5CHO) and 1-propanol (C_3H_7OH). 0.1 M KOH was chosen as the sample matrix, since it is a commonly used electrolyte in CO reduction measurements. The calibrations were carried out with the products mixed in pairs, for practical reasons. We tested various

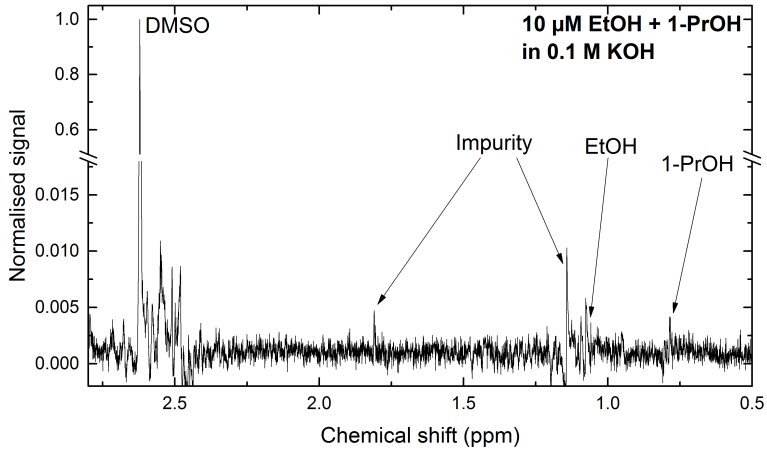

Figure 4.3: NMR spectrum of solution containing 10 µM ethanol and 1-propanol in 0.1 M KOH. Reprinted from Bertheussen et al.[203]

combinations to see if the mixing of products influenced the results, but did not make any observations indicating that this was the case.

The performance of a technique for analysis of a certain product can be quantified by its detection limit, i.e. the lowest concentration where the signal is quantifiable. In this work, we defined the practical detection limit as the concentration where the peak is no longer discernible. An example of this is given in Figure 4.3, for 10 µM C_2H_5OH and C_3H_7OH measured with NMR spectroscopy. At this concentration, the peaks from the two compounds can be identified, but quantification is impossible due to the noise. The concentrations used were ranging from 0.5 to 200 µM, depending on the product. More points were measured at low concentration to improve the resolution close to the detection limits.

4.2.1 Calibration for ethanol and 1-propanol

In Figure 4.4a, an NMR spectrum of a 200 µM ethanol (EtOH) and 1-propanol (1-PrOH) solution in 0.1 M KOH is shown. At this concentration, signals from all the different groups of protons are clearly discernable. The integrated area of a certain NMR peak is directly proportional to the amount of protons that give rise to it. Thus, the intensity of the peak mainly depends on this factor, together with its multiplicity. Low multiplicity gives sharp and narrow peaks, while high multiplicity gives the opposite effect. As a

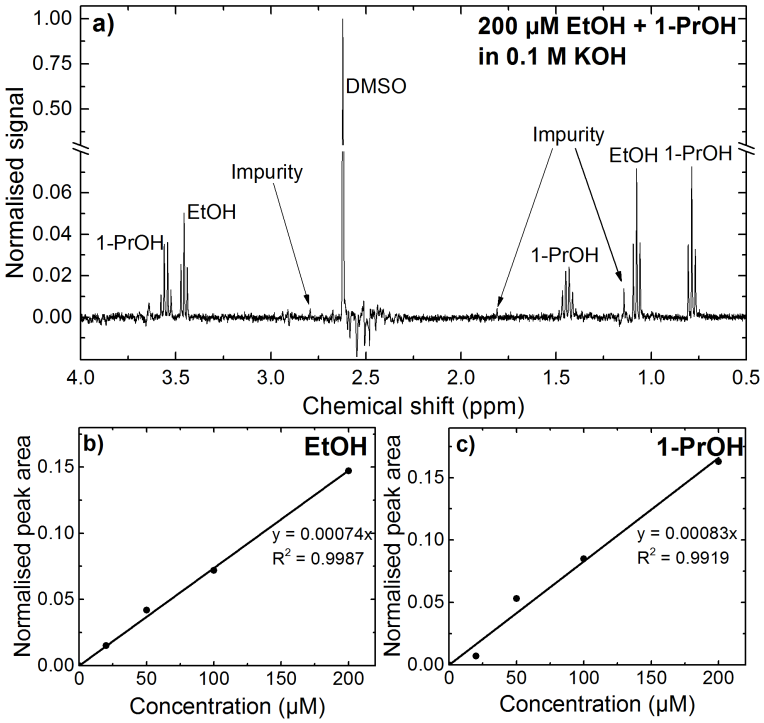

Figure 4.4: NMR spectroscopy calibration data for ethanol (EtOH) and 1-propanol (1-PrOH). (a) NMR spectrum of a solution containing 200 µM EtOH and 1-PrOH in 0.1 M KOH. The y-axis is normalised to the intensity of the DMSO peak. (b) Calibration curve for EtOH, based on integration of the triplet peak at 1.07 ppm. (c) Calibration curve for 1-PrOH, based on integration of the triplet peak at 0.79 ppm. The calibration curves are linear fits of the data points, for which the y-axis intercepts are forced through 0. Reprinted from Bertheussen et al.[203]

result, there is some variation in the peak intensities in Figure 4.4a. The most intense peak gives the lowest detection limit, and was thus chosen for the later analysis; this principle was used throughout the study. Here, the most intense peaks were the triplets from the methyl group of the two molecules, with chemical shifts of 1.07 ppm and 0.79 ppm for EtOH and 1-PrOH, respectively.

Some minor peaks that we could not account for were present in the spectrum in Figure 4.4a, in addition to the peaks from EtOH and 1-PrOH. Identical peaks were could be observed in blank samples, as shown in Figure 4.5. We thus concluded that they were from impurities, most likely trace amounts of organic compounds from polymer equipment such as pipette tips

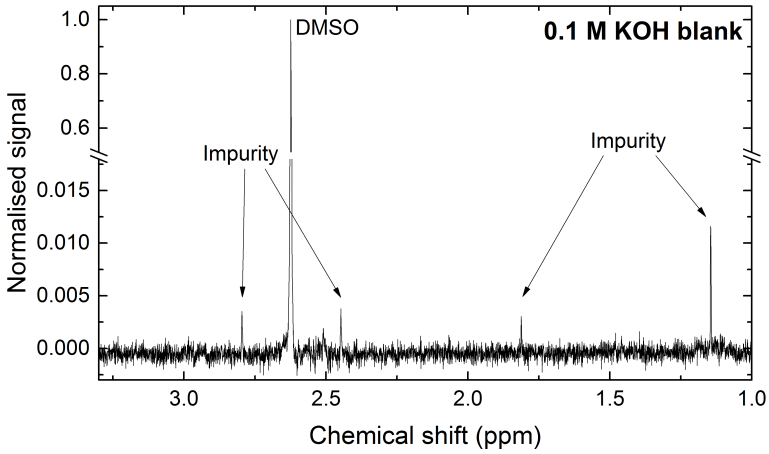

Figure 4.5: NMR spectrum of a blank sample containing only 0.1 M KOH. Reprinted from Bertheussen et al.[203]

and Eppendorf tubes, which were both used for preparing the samples. This underlines the importance of measuring blanks, to avoid mistaking impurities for products. A noisy artefact can be seen around 2.5 ppm chemical shift on most of the spectra presented herein. We identified this as resonance from the water suppression pulse, since a symmetric feature could be observed on the other side of the water peak (not shown).

Figure 4.4b and c show the response of these two compounds when measured by NMR spectroscopy. In both cases, the most intense peak was stemming from the methyl group at the end of the molecules, which involves an equal number of protons and the same multiplicity. As a result, their response is nearly identical. Detection limits of ~10 µM were determined, with a spectrum at this concentration shown in Figure 4.3.

In Figure 4.6, data for HS-GC measurements of the same compounds are shown. In panel (a), a chromatogram from sample containing 200 µM EtOH and 1-PrOH in 0.1 M KOH. Ethanol can be identified at 10 minutes retention time, while 1-propanol gives a peak at 24 minutes. Note that these retention times are highly dependent on the column in use and the temperature profile of the measurement (described in section 3.4.2). A different temperature profile is for instance the reason for the higher retention of ethanol in this study, compared to that observed for measurements presented from a different study later in this chapter (e.g. in Figure 4.11). The complex peaks at retention time 2.5 to 5.0 minutes are caused by hydrocar-

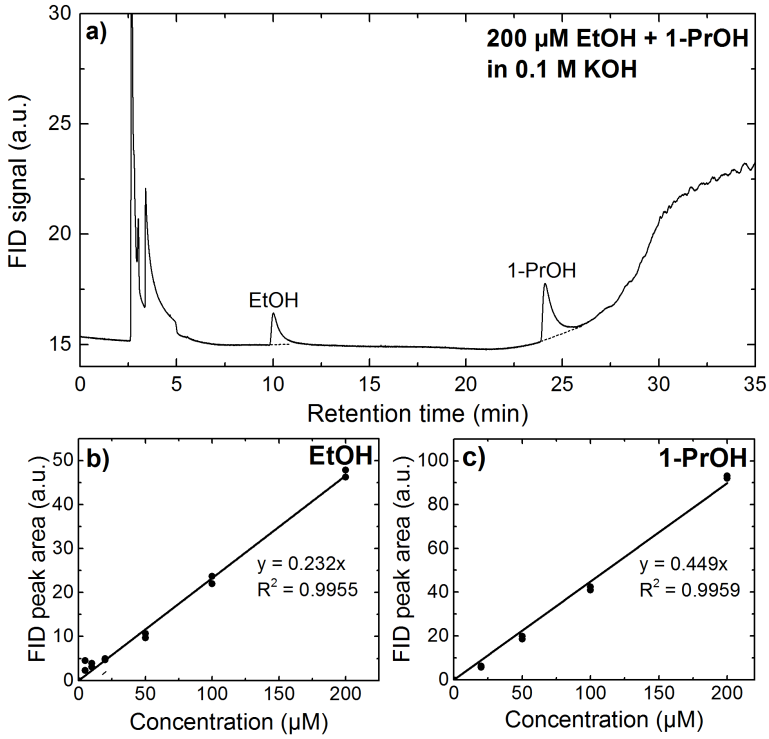

Figure 4.6: HS-GC calibration data for ethanol (EtOH) and 1-propanol (1-PrOH). (a) HS-GC chromatogram of a solution containing 200 µM EtOH and 1-PrOH in 0.1 M KOH. (b) Calibration curve for EtOH, based on integration of the peak at 10.0 min. (c) Calibration curve for 1-PrOH, based on integration of the peak at 24.5. The calibration curves are linear fits of the data points, for which the y-axis intercepts are forced through 0. Reprinted from Bertheussen et al.[203]

bons and CO_2 that dissolve in the samples from the air. The increase in baseline signal is caused by the temperature rising towards the end of the measurement, which results in column bleeding. This means that the active phase of the column starts decomposing, releasing various compounds. The same effect is most likely the reason for the fluctuations in the baseline signal in this region.

From the calibration curves shown in Figure 4.6b and c, it can be seen that the two compounds exhibit different responses. For HS-GC, the response of a certain compound depends mainly on its Henry's law constant and the number of carbons in the molecule backbone. EtOH and 1-PrOH have similar Henry's law constants, as seen from Table 4.2. The reason

Table 4.2: Henry's law constants for liquid prodcucts relevant to CO reduction. The values are obtained from the various references through a compilation made by Rolf Sander.[177] A list of all liquid products reported from CO_2 reduction is shown in Table 3.2 on page 67.

Product	**Chem. formula**	k_H **(M atm^{-1})**	**References**
Methanol	CH_3OH	$(2.2\pm0.1) \times 10^2$	[184–187]
Acetate	CH_3COO^-	–	–
Acetic acid	CH_3COOH	$(6.3\pm2.7) \times 10^3$	[181–183]
Acetaldehyde	CH_3CHO	$(1.4\pm0.2) \times 10^1$	[187–189,192,193]
Ethanol	C_2H_5OH	$(2.0\pm0.3) \times 10^2$	[184–187,194]
Propionaldehyde	C_2H_5CHO	1.3×10^1	[189,192]
1-Propanol	C_3H_7OH	$(1.4\pm0.2) \times 10^2$	[184,185,187]

1-PrOH gives a higher response is that it contains 3 carbon atoms, as opposed to 2 carbons for EtOH. However, the 1-PrOH peak is significantly wider, which actually leads to higher detection limits. This illustrates well that both the response and peak width have an influence on the detection limits. A detection limit of ~5 µM was found for EtOH and and ~10 µM for 1-PrOH. A chromatogram for a 10 µM solution of the two is shown in Figure B.1 on page 176.

When comparing the HS-GC and NMR spectroscopy data, it seems that the two techniques yield similar detection limits for the C_2 and C_3 alcohols in with the current measurement parameters. The obtained detection limits are summarised in Table 4.3 on page 100. It should be noted that for HS-GC, the measurement parameters can be tuned easily to improve the detection limits. Increasing the temperature to which the sample is heated will lead to injection of a higher amount of the volatile product, since the signal directly depends on the concentration of the relevant compound in the gas phase over the liquid sample in the sample vial. Furthermore, the peak width depends on the time the compounds spend in the column. Thus, if the column temperature was increased so that the retention of 1-PrOH was decreased, it would lead to a sharper peak and corresponding improved detection limit. For NMR spectroscopy, increasing the amount of scans per measurement would lead to improved signal-to-noise. This does, however, increase measurement time, while the changes in HS-GC can be done without such a negative consequence.

4.2.2 Calibration for methanol and acetate

An NMR spectrum of a 200 μM solution of methanol (MeOH) and acetate (AcO^-) is shown in Figure 4.7. As opposed to EtOH and 1-PrOH, these two compounds only exhibited one peak, from the methyl group. These peaks were singlets, since no coupling between different protons was occurring, giving optimal peak intensity. This was reflected in detection limits below 5 μM for these compounds, with discernable peaks still present at that concentration. An NMR spectrum of a 5 μM solution of the two compounds is shown in Figure B.2 on page 176, illustrating this. Note that the most intense EtOH and 1-PrOH peaks were also stemming from a methyl group, giving the same integrated signal, but higher detection limits (~10 μM). This demonstrates how the multiplicity of NMR peaks influences detection limits.

The picture was different for these compounds when measured by HS-GC. A chromatogram of a 200 μM MeOH and AcO^- solution in 0.1 M KOH is shown in Figure 4.8. Evidently, AcO^- was not detectable with this technique, since it gets deprotonated and does not exhibit any vapour pressure. The inability to detect compounds with little to no vapour pressure is one of the major disadvantages of HS-GC. It should ideally be coupled with another technique that can detect such products (formate is another example), such as NMR spectroscopy or HPLC. An approach that could possibly be used to measure deprotonated CO_2 and CO reduction products using HS-G,C is acidifying the samples before analysis. However, the Henry's law constant of formic acid and acetic acid is very high, as shown in Table 4.2, meaning that sensitivity will be correspondingly low.

The case of MeOH is not as easily explainable. There was a significant error in its quantification, as evidenced by the large spread at each concentration. The peak was positioned right where the signal from the dissolved gases decreased sharply. It is thus likely that this induced some error in the peak integration, particularly at low concentrations. One way to improve the detection of MeOH could have been to modify the GC parameters in order to tune its retention time relative to the gas peaks. However, this would have made the data unsuitable for comparison with those of the other compounds, and was not performed in the present study. Since the Henry's law constant of MeOH is similar to that of EtOH and 1-PrOH, we would expect its response to be roughly proportional to the number of carbon atoms,

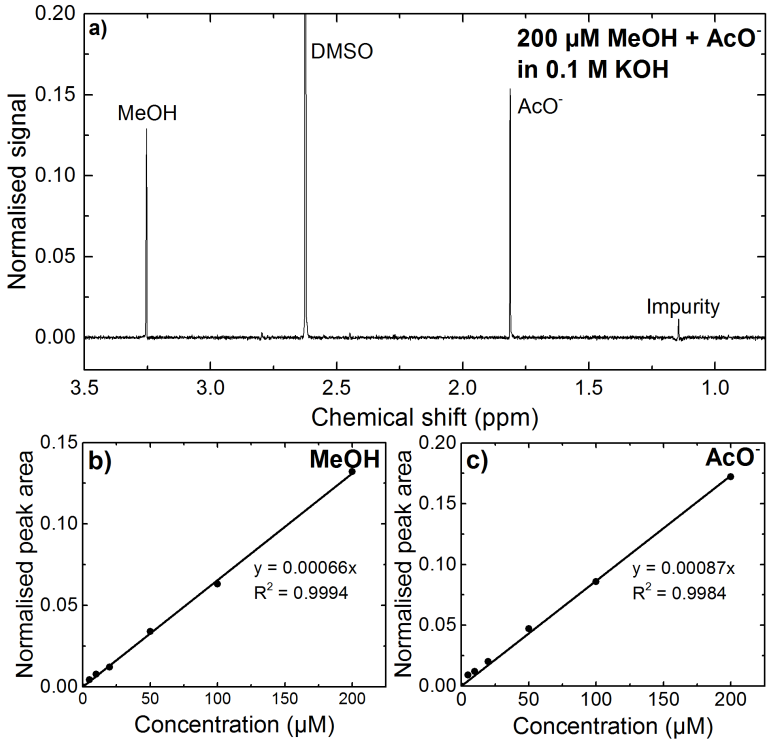

Figure 4.7: NMR spectroscopy calibration data for methanol (MeOH) and acetate (AcO^-). (a) NMR spectrum of a solution containing 200 µM MeOH and AcO^- in 0.1 M KOH. The y-axis is normalised to the intensity of the DMSO peak. (b) Calibration curve for MeOH, based on integration of the peak at 3.25 ppm. (c) Calibration curve for AcO^-, based on integration of the peak at 1.80 ppm. The calibration curves are linear fits of the data points, for which the y-axis intercepts are forced through 0. Reprinted from Bertheussen et al.[203]

meaning half of that of EtOH and a third of that of 1-PrOH. However, it exhibited a significantly higher detection limit of >20 µM. The detection limits measured for the different products are summarised in Table 4.3. A chromatogram of a solution containing 20 µM MeOH is shown Figure B.3 on page 177, illustrating the poor sensitivity towards this compounds using HS-GC.

On a general note, there is no doubt that NMR spectroscopy is a more suitable technique compared for quantifying MeOH and AcO^- than HS-GC. This is a result of the sharp and intense peaks obtained when measured with the former technique, and the insuitability of the latter for these two

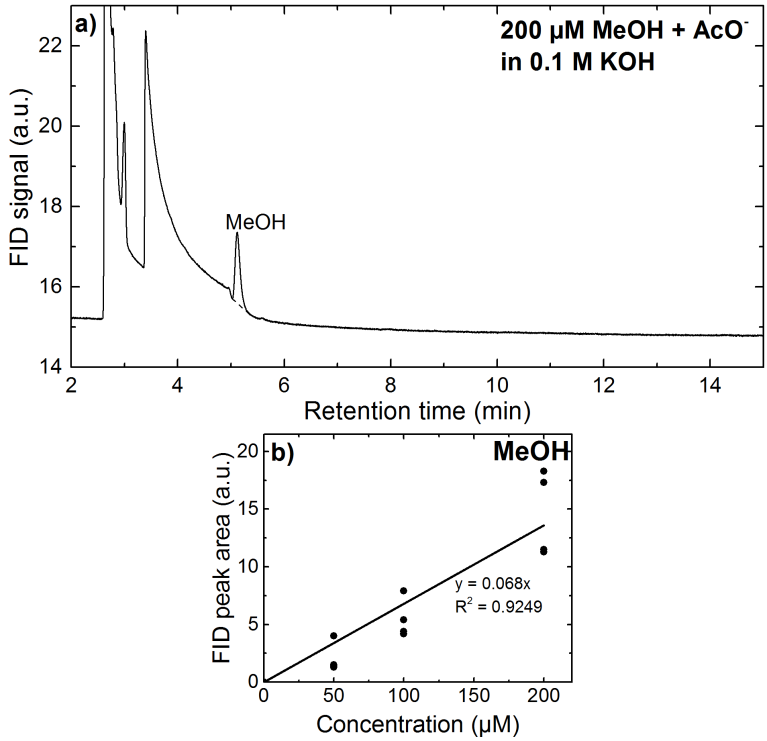

Figure 4.8: HS-GC calibration data for methanol (MeOH) and acetate (AcO^-). (a) HS-GC chromatogram of a solution containing 200 µM MeOH and AcO^- in 0.1 M KOH. (b) Calibration curve for MeOH, based on integration of the peak at 5.1 min. The calibration curve is a linear fit of the data points, for which the y-axis intercept is forced through 0. Reprinted from Bertheussen et al.[203]

compounds. MeOH detection with HS-GC could most likely be improved compared to what is shown here, but would still be inferior to NMR spectroscopy.

4.2.3 Calibration for acetaldehyde and propionaldehyde

In Figure 4.9, a NMR spectrum from a 200 µM solution of acetaldehyde (MeCHO) and propionaldehyde (EtCHO) in 0.1 M KOH is shown. Interestingly, no peaks could be observed for MeCHO at all. EtCHO only gave a minor peak at this concentration, originating from the methyl group. This peak should have exhibited similar response as that from methyl group of EtOH and 1-PrOH, but was significantly lower. The reason for this behaviour will be discussed at length in section 4.2.4. It turns out that acetaldehyde

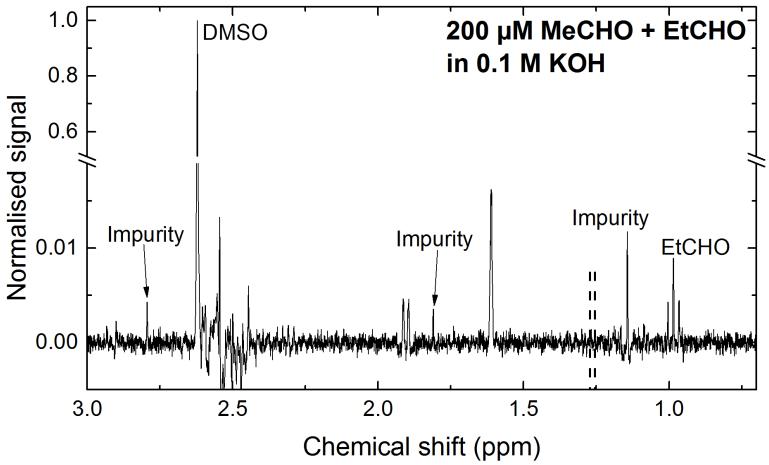

Figure 4.9: NMR spectrum of a solution containing 200 µM acetaldehyde (MeCHO) and propionaldehyde (EtCHO) in 0.1 M KOH. The y-axis is normalised to the intensity of the DMSO peak. Reprinted from Bertheussen et al.[203]

polymerises in alkaline solution, and forms partly insoluble species. As a result, it cannot be detected in an adequate way at any concentration relevant to CO reduction. The data presented in Figure 4.9 indicate that this also occurs for EtCHO, to a somewhat lesser extent. While MeCHO could not be detected at a concentration of 200 µM, EtCHO exhibited a detection limit of ~100 µM. An NMR spectrum of MeCHO and EtCHO at 100 µM is shown in Figure B.4 on page 177.

These two aldehydes gave a widely different response when measured by HS-GC. Figure 4.10a shows a chromatogram measured on a solution containing 200 µM MeCHO and EtCHO in 0.1 M KOH. These compounds both gave a sharp, intense peak, with the peak from EtCHO a little broader than that of MeCHO. In Figure 4.10b and c, the resulting calibration curves are shown. As was the case for 1-PrOH compared to EtOH, EtCHO gave higher response due to the extra carbon atom. However, it exhibited a wider peak due to the long retention time. For these compounds, we measured solutions with as low concentrations as 0.5 µM, but could still observe clearly discernable peaks. A chromatogram of MeCHO at this concentration is shown in Figure B.4 on page 177. It appeared that HS-GC analysis is not significantly affected by the aldehydes polymerising. We hypothesised that the reason for this is that the solution is heated for analysis by HS-GC. This leads to a thermodynamical driving force for conversion of aldehyde polymers into

the higher-entropy state of individual molecules in the gas-phase. However, the fact that the aldehydes undergo transformations in solution gave some more uncertainty for these compounds in our measurements, evidence by the larger spread of the points at a particular concentration compared to EtOH and 1-PrOH.

While NMR spectroscopy is evidently unsuitable for analysis of aldehydes in alkaline solution, HS-GC seems like an ideal technique in this case. Its sensitivity depends directly on the volatility of the compounds in question, and aldehydes exibit by far the highest volatility amongst products relevant for CO reduction, as evidenced by their Henry's law constants listed in Table 4.2. The detection limits achieved by the two techniques are summarised in Table 4.3

4.2.4 Aldehyde chemistry in alkaline electrolyte solutions

When carrying out CO reduction, the liquid products formed will dissolve in the electrolyte. This allows for accumulation of products above the detection limits of the analytical equipment. However, it also means that a mixture of organic compounds is created in the electrolyte, which increases the likelyhood for spontaneous chemical reactions to occur. I first encountered this issue during a project regarding CO reduction on oxide-derived Cu, which is described in detail in chapter 5. In the Figure 4.11, data from product analysis using HS-GC and NMR spectroscopy are compared for a CO reduction sample (data marked in red). In NMR spectra, only C_2H_5OH and CH_3COO^- could be identified as products from CO reduction. When studying the same sample using HS-GC, an additional compound could be observed (Note: acetate cannot be measured with this technique, since it is not volatile). Its retention time indicated that the unknown product could be acetaldehyde (CH_3CHO). This was later confirmed using HS-GC-MS, by comparing the mass spectrum of the peak assigned to CH_3CHO with a database reference spectrum, as shown in figure Figure 4.11b.

To investigate the discrepancy between HS-GC and NMR spectroscopy further, two solutions with known amounts of the three products added to them were measured. The solutions were made from two different precursors, one containing 40% CH_3CHO dissolved in water, and one with ~100% anhydrous CH_3CHO. Interestingly, CH_3CHO was detected in the solution made from the 40% precursor solution using NMR spectroscopy. Meanwhile,

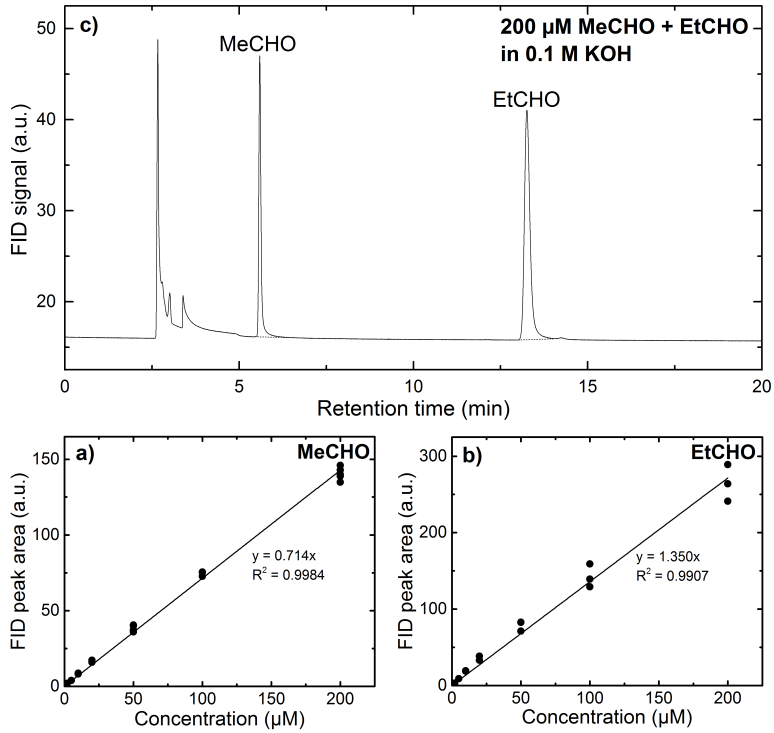

Figure 4.10: HS-GC calibration data for acetaldehyde (MeCHO) and propionaldehyde (EtCHO). (a) NMR spectrum of a solution containing 200 µM MeCHO and EtCHO in 0.1 M KOH. The y-axis is normalised to the intensity of the DMSO peak. (b) Calibration curve for MeCHO, based on integration of the peak at 6.0 min. (c) Calibration curve for EtCHO, based on integration of the peak at 13.5 min. The calibration curves are linear fits of the data points, for which the y-axis intercepts are forced through 0. Reprinted from Bertheussen et al.[203]

the solution made from the ~100% precursor did not exhibit any CH_3CHO lines, similarly to the CO reduction samples.

These observations led to important questions. How could it be that NMR spectroscopy, a technique that is considered highly versatile due to its ability to detect and distinguish all kinds of organic compounds, cannot measure acetaldehyde under certain conditions? Furthermore, why did acetaldehyde appear in NMR spectra in solutions we made from one stock solution, but not the other? We were unfortunately not able to determine what is causing the discrepancy between solutions made from the 40% and the 100% precursor. The most likely reason is that they were obtained from different suppliers (see appendix A). For instance, a stabilising agent

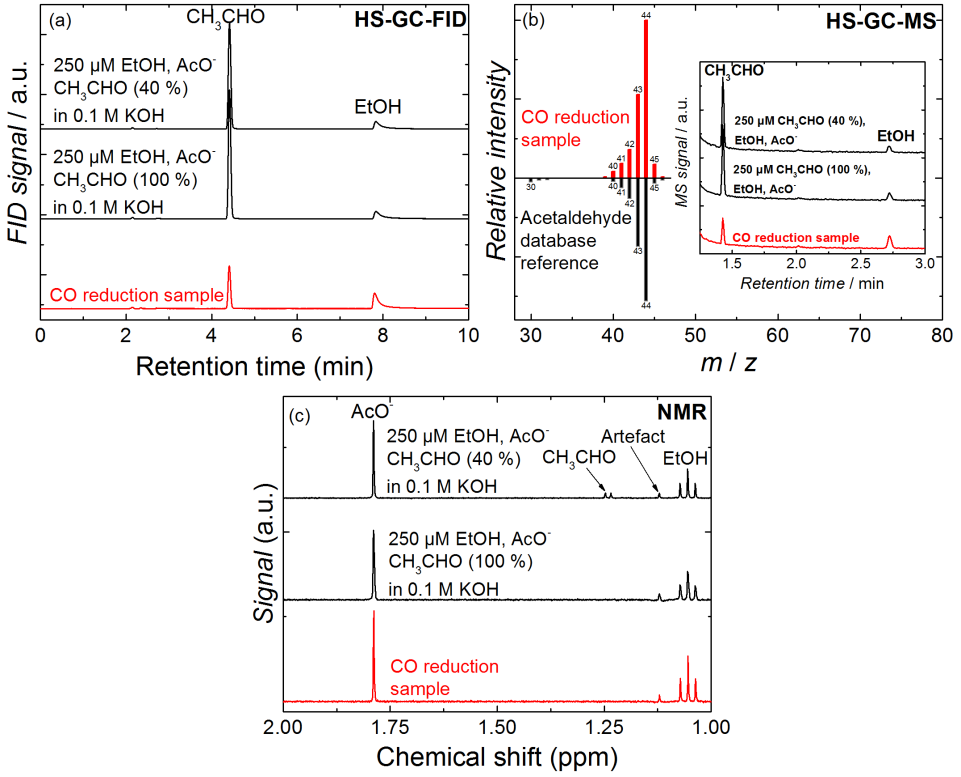

Figure 4.11: Analysis of liquid products from CO reduction on oxide-derived Cu, using (a) HS-GC coupled to an FID, (b) HS-GC coupled to an MS and (c) NMR spectroscopy. The red data are measured on CO reduction samples, while the black data are measured on solutions with known concentrations of ethanol, acetate and acetaldehyde. Reprinted from Bertheussen et al.[202]

could have been added to the 40% solution by since it was dissolved in water. However, very little information was given about this solution from the supplier.

The more significant point in relation to CO reduction product analysis, was that acetaldehyde in our CO reduction samples and certain solutions could not be detected by NMR spectroscopy. For the remainder of this section, our efforts to figure out why this was the case will be described, with three main hypotheses (i-iii). Our first ideas were that acetaldehyde was either (i) evaporating or (ii) undergoing disproportionation through the Cannizzaro reaction during storage. HS-GC is carried out in-house, while NMR spectroscopy is performed at a centralised facility at the university.

Thus, product analysis by HS-GC is normally carried out immediately after CO reduction experiments, while there is some waiting time for NMR spectroscopy. Another hypothesis that we formulated afterwards was that (iii) acetaldehyde could be polymerising in the alkaline electrolyte.

(i) Our first concern for what could be occurring during the extended storage period before NMR spectroscopy was evaporation. CH_3CHO has a high volatility in dilute solutions, as seen from its low Henry's law constant (14 M atm^{-1}). Thus, it could be that most of it evaporated before it was measured. To test this, we prepared a sample containing 250 μM CH_3CHO (from the 100% precursor) in 0.1 M KOH, a concentration similar to that observed from CO reduction measurements, and performed NMR spectroscopy on it. As was the case for CO reduction samples, no CH_3CHO could be observed in the resulting spectrum (not shown, identical to middle spectrum in Figure 4.11c). Afterwards, the sample was stored overnight in the NMR tube, and the 500 μL sample was transferred to a HS-GC vial and diluted to 5 mL with 0.1 M KOH. The resulting HS-GC chromatogram can be seen in Figure 4.12a. A clear CH_3CHO peak was visible, indicating that evaporation could not be the explanation for the observed discrepancies. The small peaks at lower retention times in the chromatogram in the figure were caused by short-chained hydrocarbons that dissolved in the samples during air exposure.

(ii) Our next hypothesis was related to the Cannizzaro reaction, a base-catalysed disproportionation of aldehydes into the corresponding carboxylic acid and alchohol.[219–221] For these samples, CH_3CHO would be converted to C_2H_5OH and CH_3COOH/CH_3COO^-, which were indeed the other liquid products we observed. It could be that the Cannizzaro reaction was occurring spontaneously in the 0.1 M KOH electrolyte. Because of the longer duration of storage for the samples measured by NMR spectroscopy, this could mean that all the acetaldehyde produced was converted to C_2H_5OH and CH_3COO^-. To check if this reaction could be occurring spontaneously at a significant rate at pH 13, we prepared a solution of 10 mM CH_3CHO in 0.1 M KOH and measured it using HS-GC immediately after preparation, and after storage overnight. The resulting chromatograms are shown in Figure 4.12. The sample that was kept overnight did show slightly lower intensity. However, no measurable amount of C_2H_5OH (retention time ~7.8 min) could be observed, indicating that this reaction did not occur to a

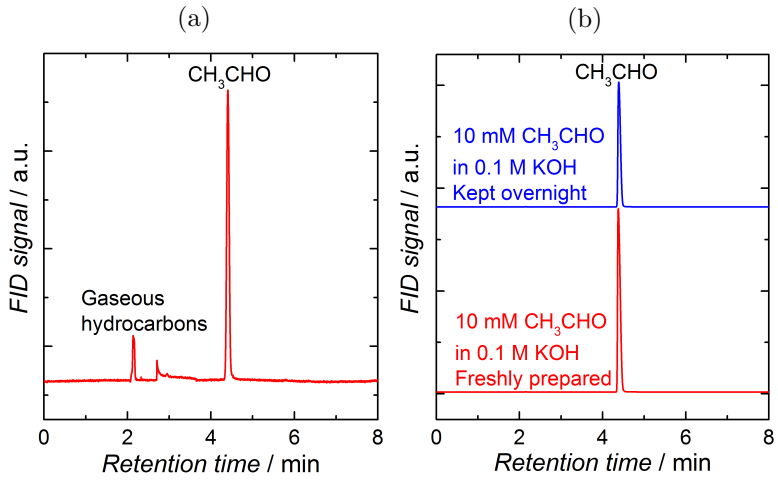

Figure 4.12: HS-GC chromatograms of (a) a sampled stored in an NMR tube overnight and subsequently measured by HS-GC to check for evaporation of acetaldehyde and (b) as-prepared and stored acetaldehyde samples to check whether the Cannizzaro reaction was occurring in bulk solution. Adapted from Bertheussen et al.[202]

significant extent in the bulk solution. Birdja et al. have suggested that the locally enhanced concentration of OH^- in the diffusion layer during CO_2 reduction in neutral electrolyte could facilitate this reaction.[221] However, the local pH is not likely to increase significantly during CO reduction at pH 13 because the bulk concentration of OH^- is already high. These experiments also show that this reaction does not occur spontaneously in bulk solution under these conditions. Thus, it is not clear if this reaction is relevant for CO reduction in 0.1 M KOH.

(iii) The measurements presented in the previous paragraphs indicated that evaporation or Cannizzaro disproportionation as a result of the longer storage was not the main reason for CH_3CHO not being detectable by NMR spectroscopy. When working with higher concentrations of CH_3CHO in 0.1 M KOH, the solution started turning yellowish and unclear after 1-2 hours of storage in room temperature, exhibiting more intense colouring with higher concentrations and/or longer storage time. In figure Figure 4.13a, a picture of a 0.1 M CH_3CHO solution in 0.1 M KOH that had been stored in room temperature for a few days in an NMR tube is shown. At this concentra-

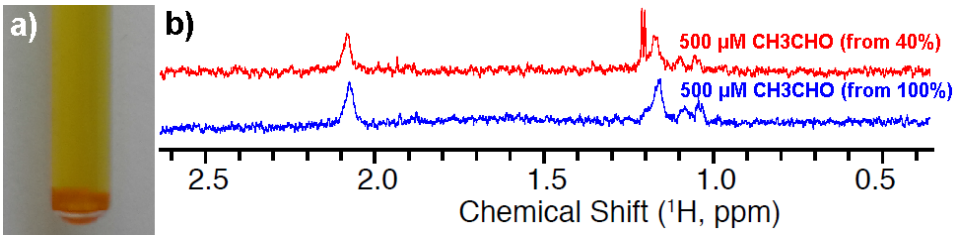

Figure 4.13: (a) Picture of a 0.1 M CH_3CHO solution in 0.1 M KOH in an NMR tube after storage in room temperature for around 2 days. (b) NMR spectra of 500 µM CH_3CHO in 0.1 KOH, prepared from two different precursor. The NMR spectra were acquired and plotted by Sebastian Meier. Reprinted from Bertheussen et al.[202]

tion, the solution turned completely yellow, and an orange precipitate was formed at the bottom. This led us to the hypothesis that the acetaldehyde is unstable in alkaline solution, polymerising into larger, insoluble chains. Since the analyte needs to be dissolved to be detected by NMR spectroscopy, this could explain why we were not able to detect acetaldehyde in CO reduction samples. HS-GC, on the other hand, relies on heating the sample to evaporate the analyte. This pushes the equilibrium of the polymerisation reaction towards the state with higher entropy, favouring individual CH_3CHO molecules, explaining why it can be detected using this technique.

In Figure 4.13b, the region of interest in NMR spectra of the two solutions containing CH_3CHO are studied in more detail. Broad peaks are present in both samples, supporting the polymerisation hypothesis. We measured similarly detailed NMR spectra on a CO reduction sample and a CH_3CHO solution before and after ageing, as shown in Figure 4.14. The top (green) spectrum was measured on the CO reduction sample, while the middle (red) and bottom (blue) spectra were from the same 0.1 M CH_3CHO in 0.1 M KOH sample immediately after preparation and after ageing for 10 hours in room temperature, respectively. When measured right after preparation (red spectrum), the 0.1 M CH_3CHO sample exhibited clear features. After ageing (blue spectrum), however, the original features were almost completely diminished. Instead, they were replaced by multiple smaller peaks, as well as a number of very broad features, a picture that fits well with the hypothesis that CH_3CHO polymerises. A significant increase in the size of the molecules present can lead to line broadening in NMR spectra.[222]

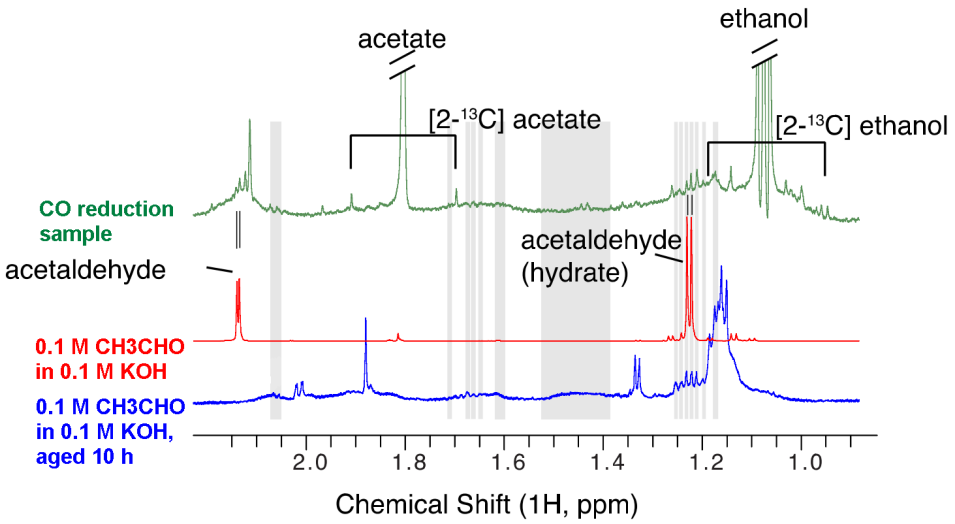

Figure 4.14: Detailed NMR spectra of various samples containing acetaldehyde. Green: Sample from CO reduction on oxide-derived Cu in 0.1 M KOH. Red: Solution containing 0.1 M CH_3CHO in 0.1 M KOH, measured shortly after preparation. Blue: Solution containing 0.1 M CH_3CHO in 0.1 M KOH, measured after ageing for 10 hours. Measurements carried out and figure prepared by Sebastian Meier. Reprinted from Bertheussen et al.[202]

Furthermore, the appearance of several smaller peaks could be explained by different protons in a long chain experiencing slightly different chemical environments, resulting in small changes in chemical shifts. The same features could also be observed for the CO reduction sample (green spectrum) as for the CH_3CHO solution. This confirmed that polymerisation was also taking place in CO reduction samples.

The sum of the factors mentioned above explains why we were not able to identify CH_3CHO from CO reduction measurements in alkaline solution using NMR spectroscopy. Line broadening led to a decrease in peak intensity, and thus increased the detection limit. Distribution of the signal from one peak into several smaller ones gave the same effect. In addition, a significant amount of the polymerised CH_3CHO seems to have precipitate out of solution, probably not contributing to the NMR signal at all.

Table 4.3: Summary of approximate detection limits for liquid products relevant to CO reduction, as measured by NMR spectroscopy and HS-GC in this study.

Product	Chem. formula	Approx. Detection limit (μM)	
		NMR	HS-GC
Methanol	CH_3OH	< 5	> 20
Acetate	CH_3COO^-	< 5	--
Acetaldehyde	CH_3CHO	> 200	< 0.5
Ethanol	C_2H_5OH	10	5
Propionaldehyde	C_2H_5CHO	100	< 0.5
1-Propanol	C_3H_7OH	10	10

4.2.5 Summary liquid product calibration

In this section, the performance of HS-GC and NMR spectroscopy were benchmarked for liquid product analysis from CO reduction in alkaline solution. This was done by comparing the detection limits for relevant products as measured by the two techniques. The results are summarised in Table 4.3. We found that as applied in our measurements, these two techniques have a similar performance for analysis of ethanol and 1-propanol. This is not, however, the case for acetaldehyde and propionaldehyde. These are products that cannot be analysed adequatly using NMR spectroscopy, due to polymerisation and subsequent precipitation. HS-GC, on the other hand, can detect these compounds with high selectivity. Finally, acetate and methanol are products that are difficult to detect using HS-GC. The case of methanol could possibly be related to the GC parameters used in this case. Acetate exists as an ion in solution, and exhibits no vapour pressure. However, these compounds can be detected with high sensitivity using NMR spectroscopy.

4.3 Conclusions

In this chapter, my approach to *ex-situ* product analysis has been described in detail. I showed the calibrations I carried out in order to be able to accurately quantify the gaseous products. In general, the gas products from CO_2 reduction and CO reduction can be quantified in a straightforward manner using GC. H_2 can be measured with relatively high sensitivity in the TCD when using Ar as a carrier gas because of the large difference

in thermal conductivity between the two compounds. Any hydrocarbons produced can be detected with excellent sensitivity using the FID. When carrying out CO_2 reduction, a methaniser can be installed so that CO can also be measured with the FID.

Liquid product quantification, on the other hand, is more challenging. There does not exist a unique technique for the detection of liquid products with figures of merits equivalent to GC for the detection of gas products, in terms of versatility and sensitivity. NMR spectroscopy and HPLC are the techniques of choice in the literature, because they should, in principle, be able to detect all relevant products. HS-GC is an excellent alternative for analysis of volatile products. It is a simple add-on to conventional GCs, and thus easily applicable in most labs where CO_2/CO reduction is performed. However, HS-GC does not exhibit satisfactory sensitivity to compounds with little or no volatility, and needs to be coupled with one or more complementary techniques.

Another challenge regarding liquid product analysis is the possibility for spontaneous organic reactions occurring when products accumulate in the electrolyte. I have described how acetaldehyde (and to a lesser extent propionaldehyde) polymerise and form a precipitate in alkaline solution. This makes these compounds very difficult to detect using NMR spectroscopy, while HS-GC detects them with high sensitivity. As a general note, I advice other researchers in the field to use more than one technique for liquid product analysis, in order to make sure that no products are overlooked. This seems to be particularly important when performing measurements in an alkaline electrolyte.

5

CO reduction on oxide-derived Cu

As described in section 2.5, nanostructured Cu is a promising electrocatalyst for CO reduction. Kanan and coworkers reported an experimental approach involving oxidation of Cu foils by annealing in air, and subsequent rapid reduction, as a simple and efficient means for obtaining nanostructured electrodes.[105,165] They later showed that this type of electrode exhibits high selectivity and geometric activity for CO reduction to C_2H_5OH and CH_3COO^- at low overpotentials (-0.25 to -0.35 V). The origin of this high performance is, however, still unclear. Aiming to obtain more insight, I reproduced this system and studied it further.

The work presented in this section is entirely based on a peer-reviewed article published in Angewandte Chemie in 2016, which is included in this thesis (number 1 in the list of publications).[202] Note that I already presented parts of this article that concern the chemistry of acetaldehyde in alkaline solution in section 4.2.4. I was the first author of the study, and carried out most of the experimental work myself, along with the writing of the first draft. Joseph H. Montoya, who was a PhD student in the Nørskov group at Stanford University at the time, carried out DFT calculations to create the free energy diagram described in section 5.4, and was supervised by Jens K. Nørskov. Ifan E.L. Stephens and Ib Chorkendorff played a central role in planning and analysis. All the authors participated in revision of the manuscript. I performed some preliminary measurements for this study during my Master's project.[209] However, all the measurements presented in this chapter were obtained during my PhD, with the exception of the SEM images (measured by Søren B. Scott, a PhD student in my group) presented

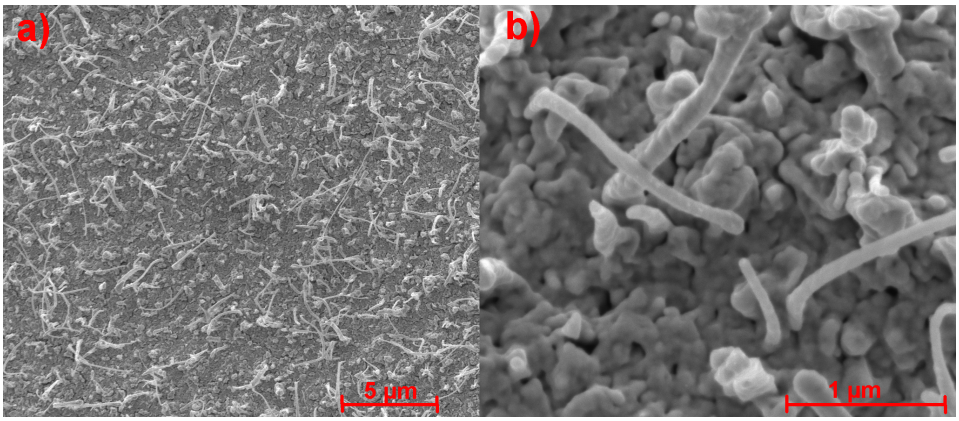

Figure 5.1: (a) Overview and (b) higher magnification SEM images of an oxide-derived Cu electrode. Images measured by Søren B. Scott

in section 5.1. For experiments that I have not carried out myself, this is specified in the respective figure captions.

5.1 Characterisation of the oxide-derived Cu electrodes

We prepared oxide-derived copper (OD Cu) electrodes using the procedure outlined by Li et al.,[105,165] as described in detail in section 3.2.4. The roughness factor of the electrodes was determined from the double layer capacitance in the potential region of -0.2 to 0.2 V of CVs recorded in 0.1 M KOH (details in section 3.2.5). An average roughness factor 87 ± 10 was determined from 7 electrodes prepared in different batches, but at identical conditions. The resulting surface structure can be seen in the SEM images in Figure 5.1. In panel (a), an overview image is shown , where a large number of fibre-like structures can be observed. Panel (b) shows a more detailed image , where holes are observed in the substrate in addition to the fibre-like structures, indicating a porous structure of the substrate. These structures combined are likely to be responsible for the large ECSA of these electrodes, in addition to further structuring on the nanoscale. The surface clearly resembles that obtained by Kanan and coworkers,[165] both in terms of ECSA and visible surface structure.

5.2 CO reduction on oxide-derived Cu

The product distribution and partial current densities measured from CO reduction on these electrodes are shown in Figure 5.2. The Faradaic efficiencies for the individual products were similar to those reported by Kanan and coworkers.[165] At -0.33 V, ethanol and acetate were each produced with ~25% Faradaic efficiency. We observed around 1% Faradaic efficiency towards ethylene and ethane combined, and ~40% towards H_2 evolution. As discussed in section 4.2.4, an additional product showed up in our HS-GC measurements. By coupling HS-GC with mass spectrometry, we identified the product as acetaldehyde, which was not reported by Kanan and coworkers. In our measurements, it was produced with 5% Faradaic efficiency at -0.33 V. The reasons for why it was previously overlooked are discussed in detail in section 4.2.4. It turns out that acetaldehyde is unstable in alkaline solutions, polymerising and precipitating out of solution. This makes detection by NMR spectroscopy difficult, since this technique relies on products being dissolved in the sample matrix. Since we used a combination of NMR spectroscopy and HS-GC for liquid product analysis, we were able to overcome these limitations.

Some irregularity in the total Faradaic efficiency was observed, as shown in Figure 5.2. At -0.39 V, the product quantification gave only ~80% total Faradaic efficiency. We hypothesised that this was mainly caused by H_2 leaks in the experimental setup. These measurements were carried out before I optimised the leak tightness of the setup (details about measures taken can be found in section 3.3.2). At -0.39 V, the H_2 selectivity was significantly higher than at the other potentials, which means that gas leaks would have a higher impact on the overall Faradaic efficiency. Furthermore, the higher H_2 production at this potential would result in a higher H_2 partial pressure (note that these were batch measurements), which could also be causing an accelerated leakage of H_2 under these conditions. At -0.28 V, on the other hand, the total Faradaic efficiency is 109%. This is most likely caused by a larger uncertainty in product analysis at this low overpotential, due to the low geometric activity resulting in product concentrations closer to the detection limits. This is reflected in the larger error bars in Figure 5.2a at this potential.

A closer inspection of the partial current densities displayed in Fig-

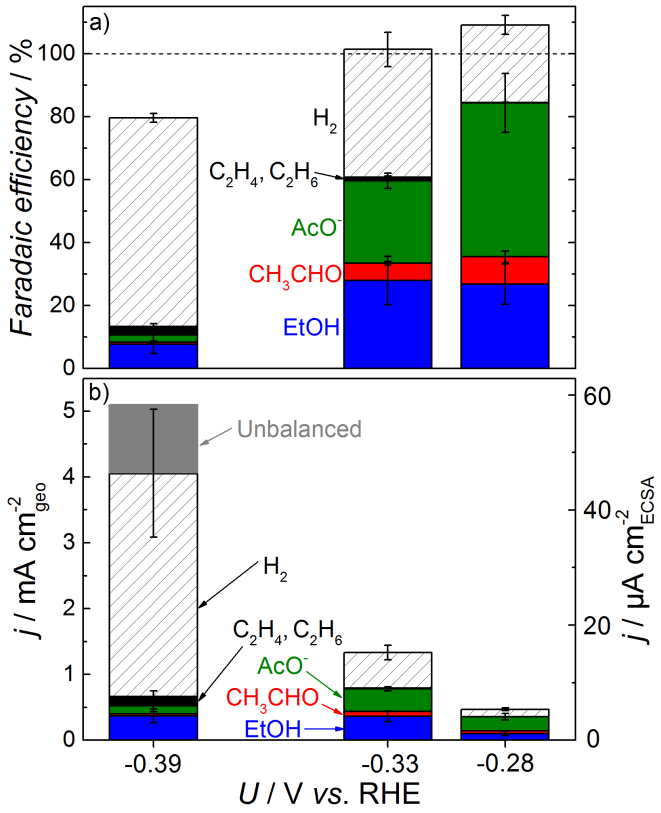

Figure 5.2: (a) Faradaic efficiency and (b) partial current density from CO reduction on oxide-derived Cu in 0.1 M KOH. Measurements at -0.28 V were carried out until a total charge of 5 C was passed, while measurements at -0.33 and -0.39 were carried out until a total charge of 10 C was passed. The data shown are the average of at least 3 individual measurements. Error bars represent ±σ. Reprinted from Bertheussen et al.[202]

ure 5.2, shows that a similar CO reduction activity was measured at -0.33 V and -0.39 V. The increased total activity at -0.39 V is directly related to an increase in H_2 evolution, indicating that mass transport limitated CO reduction activity has been reached. The solubility of CO in aqueous electrolyte is around 50 times lower than that of CO_2, meaning that the mass transport is even worse for CO reduction than CO_2 reduction. As a result, only the measurements at -0.28 and -0.33 V are likely to reflect the intrinsic activity of OD Cu towards CO reduction.

The identification of CH_3CHO as an additional product has various implications for the understanding of CO reduction on OD Cu. It is a valuable

chemical in its own, e.g. as a precursor for various industrial chemicals.[223] Thus, any new insight about how it can be produced efficiently could be commercially relevant. Furthermore, its presence can give important insight about the fundamentals of the reaction, as will be discussed later in this chapter. We observed a maximum Faradaic efficiency of 9% towards CH_3CHO at -0.28 V. This represents a low overpotential of 460 mV ($U_{CO/CH3CHO} = 0.18$ V, as shown in Table 2.2).

In the broader picture, the fact that this product was not observed in previous studies underlines the importance of conducting thorough product analysis. In principle, one should be able to assess whether a product is overlooked by studying the total Faradaic efficiency of a measurement. However, due to the inherent uncertainty of analytical techniques, this is not always the case, in particular for minor products such as acetaldehyde in this case.

5.3 Acetaldehyde as an intermediate in ethanol formation

We also studied the behaviour of OD Cu during longer measurements. In Figure 5.3, the concentration of acetaldehyde and ethanol are plotted as a function of the total charge passed for CO reduction at -0.33 V. The concentration of C_2H_5OH was rising more or less linearly with increasing measurement duration. This would be expected for a steady-state reaction where the Faradaic efficiency related to a certain product is constant. CH_3CHO formation, however, plateaued when reaching ~100 μM concentration, giving us the idea that CH_3CHO could be an intermediate in the formation of C_2H_5OH from CO reduction. It is possible that when a certain concentration is reached, the rate of CH_3CHO formation and further conversion to ethanol are similar, leading to a steady-state situation.

CH_3CHO has previously been determined as an intermediate in the ethanol formation from CO reduction on polycrystalline Cu by Hori et al.[127] The authors added CH_3CHO to the electrolyte and carried out electroreduction without introducing CO, observing formation of C_2H_5OH. In order to confirm that this is also the case on OD Cu, we performed a similar measurement. We added 10 mM CH_3CHO to our 0.1 M KOH electrolyte while sparging with Ar instead of CO. The resulting Faradaic ef-

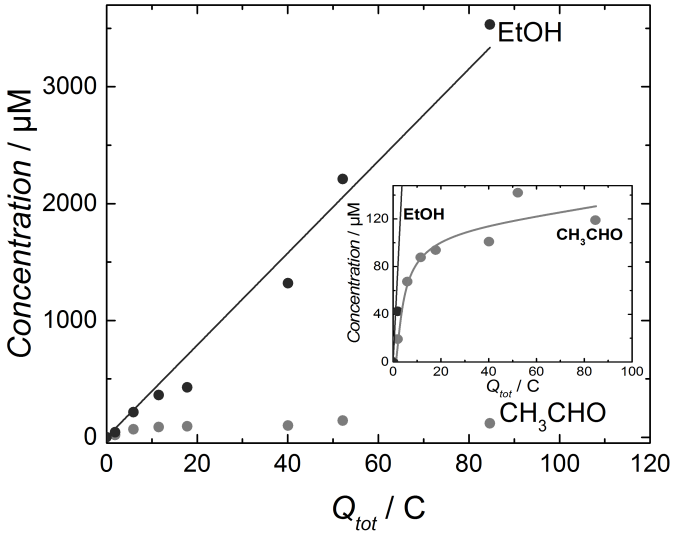

Figure 5.3: Electrolyte concentration of ethanol (EtOH) and acetaldehyde (CH_3CHO) as a function of the total charge passed during CO reduction on oxide-derived Cu at -0.33 V in 0.1 M KOH. Inset: The same data shown with higher resolution on the y-axis. Reprinted from Bertheussen et al.[202]

ficiencies from electroreduction of CH_3CHO are shown in Figure 5.4. A significant amount of C_2H_5OH is formed at all potentials, showing that CH_3CHO is indeed an intermediate in this reaction. In addition, small amounts of butyraldehyde (C_3H_7CHO) are formed. It is unclear whether this is a CH_3CHO reduction product, or if it is just formed in a chemical reaction in the solution without the involvement of the catalyst due to the high concentration of CH_3CHOin the electrolyte. Experimental and computational studies show that C-C coupling occurs at an early stage of the CO reduction pathway, before significant hydrogenation takes place.[224–226] Thus, it is unlikely that this C_4 aldehyde can be formed from electroreduction of its C_2 counterpart. Even so, the bulk concentration of CH_3CHO was significantly higher for the measurements shown in Figure 5.4 (10 mM) than what is the case after CO reduction (~100 µM was measured in the present study). Thus, it is possible that the different conditions could lead to changes in the reaction dynamics. However, the fact that we could not observe C_3H_7CHO during CO reduction, indicates that it is not relevant for this reaction.

None of the measurements in Figure 5.4 exhibit 100% total Faradaic

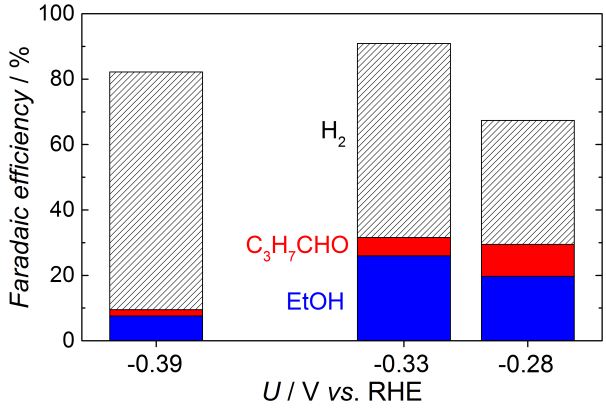

Figure 5.4: Electroreduction of acetaldehyde (10 mM) on oxide-derived Cu in Ar saturated 0.1 M KOH. Reprinted from Bertheussen et al.[202]

efficiency. As described above, making the setup completely gas tight is challenging. Thus, it is likely that H_2 leaks contributed to the missing Faradaic efficiency in this case. Additionally, our analytical techniques were not set up to measure larger molecules than C_4 compounds, and thus, any products with a longer carbon backbone would be overlooked.

5.4 Reaction mechanism for ethanol production

In order to study the reaction pathway in more detail, we performed DFT calculations for the reduction of *OCCHO on a Cu(211) slab and created a free energy diagram of different possible intermediates. *OCCHO is proposed as a likely C-C coupled intermediate,[224,225] and starting at this point can give insight about the reaction pathway from the C-C coupling step. The results are shown in Figure 5.5.

The lowest free energy pathway (marked in red) goes directly through aqueous acetaldehyde. This product is located in a thermodynamic minimum, which could explain why it accumulates in the electrolyte in measurable amounts. Between CH_3CHO and C_2H_5OH the $*OCH_2CH_3$ intermediate is located thermodynamically uphill. Ledezma-Yanez et al. studied the final reduction from CH_3CHO to C_2H_5OH on various single crystals, both by computational and experimental approaches.[227] They found that undercoordinated surfaces stabilise the $*OCH_2CH_3$ intermediate, making this step thermodynamically more favourable. The nanostructured surface

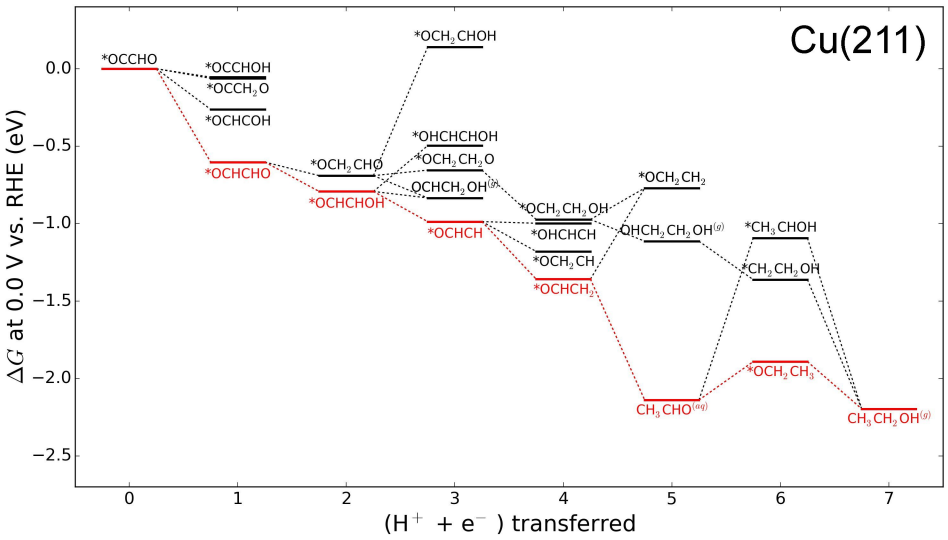

Figure 5.5: Free energy diagram for reduction of the C-C coupled intermediate *OCCHO on a Cu(211) surface, calculated using DFT. Intermediates marked in red represent the thermodynamically preferred pathway. Other intermediates of higher energy are shown in black. The DFT calculations were carried out by Joseph H. Montoya. Reprinted from Bertheussen et al.[202]

of OD Cu electrodes is likely to exhibit a large number of undercoordinated sites, as evidenced by CO temperature programmed desorption measurements performed in our group in a previous study.[170] This could be a possible explanation for the high selectivity towards C_2H_5OH observed on these electrodes. The high abundance of undercoordinated sites is also the reason why the calculations leading to the free energy diagram in Figure 5.5 were carried out on a Cu(211) surface.

5.5 Conclusions

The aim of this study was to obtain a better understanding of the reasons for the high performance of OD Cu for CO reduction, in particular the high ethanol selectivity. Using HS-GC for liquid product analysis, we identified acetaldehyde as an additional product, which had not been reported in former studies reporting CO reduction on OD Cu. Furthermore, we discovered that CH_3CHO is a reaction intermediate in the formation of C_2H_5OH from CO, which is a more reduced product. We used DFT calculations to ob-

tain a free energy diagram for C_2H_5OH formation, where aqueous CH_3CHO is on the lowest free energy pathway. A single intermediate was identified between CH_3CHO and C_2H_5OH, representing a thermodynamically uphill step. The reduction of CH_3CHO to C_2H_5CHO has been studied in detail in another report, where it was shown that undercoordinated sites stabilise this intermediate,[227] favouring C_2H_5OH formation. This could be an explanation for the high C_2H_5OH selectivity.

We achieved better understanding of the behaviour of OD Cu for CO reduction in the present study. However, much is yet to be understood about the general behaviour of Cu electrodes towards this reaction. This will be discussed further in the next chapter.

6

CO reduction on polycrystalline Cu

OD Cu electrodes exhibit high selectivity and geometric activity for CO reduction to ethanol and acetate at potentials anodic of -0.4 V.[165,166] There is, however, a lack of benchmark studies that these high-surface-area electrodes can be compared to. Polycrystalline foils represent a robust benchmark for CO_2 reduction on Cu electrodes,[45,48] and should in principle also be able to play the same role for CO reduction. Three studies exist, to the best of my knowledge, that report CO reduction on polycrystalline Cu in 0.1 M KOH.[79,170,228] However, only two of them carry out quantitative product analysis.[79,170] Furthermore, only one of the studies perform measurements in a wide potential range.[170] I therefore chose to study CO reduction on polycrystalline Cu foils, in order to obtain a benchmark for this reaction on Cu electrodes.

This chapter is based on work contained in a manuscript that is submitted for peer-review and is currently in the editorial process.[229] The current version of the manuscript is attached as an appendix to this thesis (number 3 in the list of appended articles). I was the shared first author of the study, together with Thomas Vagn Hogg, who is a fellow PhD student at DTU Physics. I was involved in all the measurements, either carrying them out myself or planning them. Albert K. Engstfeld, who held a postdoctoral position in our group at the time, contributed to the planning and analysis, and carried out some measurements. Younes Abghoui was a visiting PhD student in our group when this project was started, and carried out preliminary measurements. Ifan E.L. Stephens and Ib Chorkendorff were supervising the project, and were involved in the planning and analysis.

I wrote the manuscript draft together with Thomas, while the rest of the authors revised the manuscript. For the measurements I did not carry out myself, this is specified in the figure caption.

6.1 Performance of polycrystalline Cu for CO reduction

We carried out CO reduction on polycrystalline Cu foils in 0.1 M KOH at -0.40, -0.50 and -0.59 V vs. RHE. Gaseous products were analysed using GC, while a combination of HS-GC and NMR spectroscopy was used for the detection of liquid products. The resulting Faradaic efficiencies and partial current densities to the individual products are shown in Figure 6.1. We observed moderate CO reduction selectivity at all potentials, and significant activity at -0.5 and -0.59 V. The highest CO reduction Faradaic efficiency we measured was 56% at -0.59 V, with 30% going to ethylene (C_2H_4). The other products formed were acetaldehyde (CH_3CHO), ethanol (C_2H_5OH), propionaldehyde (C_2H_5CHO), 1-propanol (C_3H_7OH) and acetate (CH_3COO^-), along with H_2 from water splitting. Representative examples of chronoamperometry traces from short term (~30 min) measurements are shown in the inset in Figure 6.1b. Some deactivation could be observed at -0.40 and -0.50 V (up to 25% loss of activity at -0.40 V), while the measurements at -0.59 V were completely stable on this time scale. The chronoamperometry trace at -0.59 V exhibited significantly more noise than the other two. A likely reason for this is that the higher reaction rate led to bubble formation at the electrode surface, from H_2 formation in particular.

Only C_{2+} products were formed at the measured potentials, in line with previous results showing that C_1 selectivity is suppressed and C_{2+} selectivity is enhanced in alkaline electrolyte.[79,123,127] Interestingly, C_2H_5CHO was a major product at -0.40 and -0.50 V, produced with 18% Faradaic efficiency at the latter potential. The fact that a C_3 oxygenated compound was formed with such a selectivity at relatively low overpotentials ($\eta = 690$ mV, $U_{CO/C2H5CHO} = 0.19$ V) is remarkable. C_{2+} compounds exhibit high energy density, in particular liquid ones.[22] Furthermore, C_2H_5CHO has several industrial uses, e.g. in the production of plastics and the synthesis of rubber chemicals.[230] As discussed in chapter 5, we previously showed that CH_3CHO is an intermediate in C_2H_5OH formation on OD Cu.[202] This was

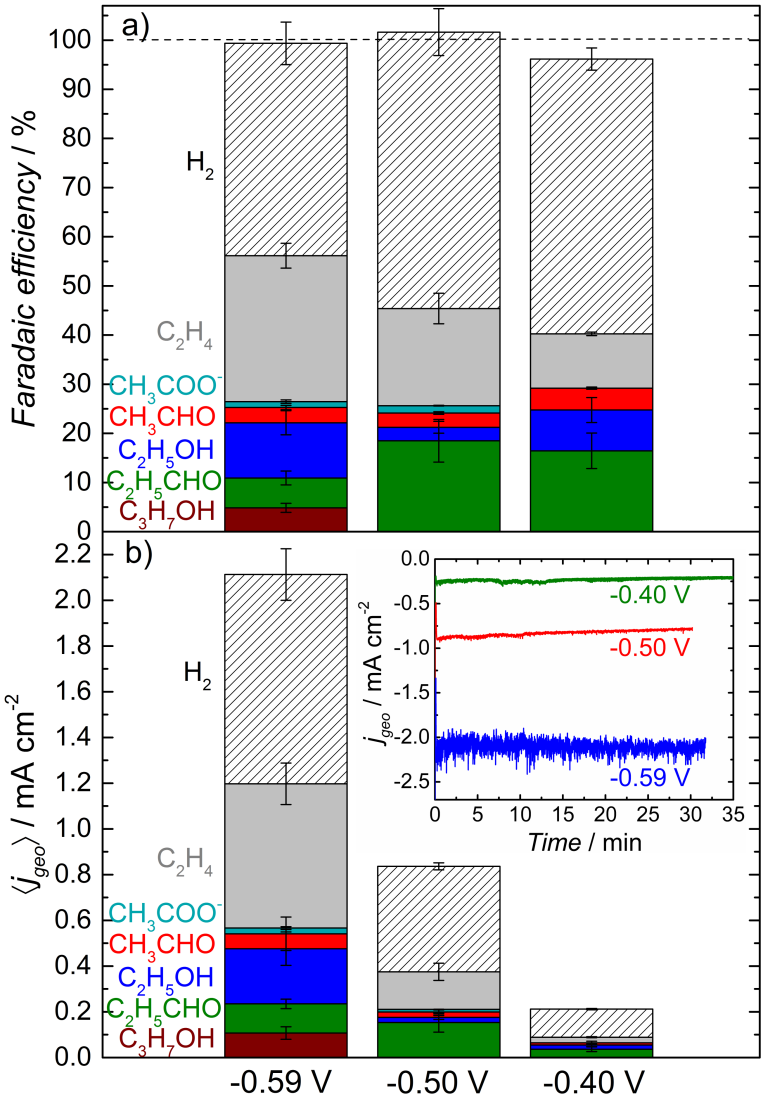

Figure 6.1: CO reduction on polycrystalline Cu in 0.1 M KOH. (a) Faradaic efficiency for individual products. (b) Mean partial current density for individual products. Inset: Representative examples of chronoamperometry traces from CO reduction at each potential. The data shown are the average of three individual measurements at each potential. Error bars represent ±σ for the individual products.

also shown by Hori et al for C_2H_5CHO reduction to 1-PrOH on polycrystalline Cu,[127] indicating that C_2H_5CHO is an intermediate in C_3H_7OH formation as well.

At the most cathodic potential (-0.59 V), we could measure C_3H_7OH in amounts above the detection limits of our analytical equipment. At the same potential, the selectivity towards C_2H_5CHO decreased significantly compared to the less cathodic conditions. This could be an indication that at this potential, the polarisation of the electrode is strong enough to convert significant amounts of C_2H_5CHO into C_3H_7OH. At -0.59 V, C_2H_5OH selectivity seems to increase as well, possibly due to the same effect. It is also clear that going from less to more cathodic potentials led to a significant increase in the hydrocarbon to oxygenate ratio. A similar trend was previously observed for CO_2 reduction.[48] This can possibly be explained by hydrocarbons requiring a higher overpotential for efficient production. Since hydrocarbons are more reduced than oxygenates with the same number of carbons (reaction equations shown in Table 2.2 on page 44), their reaction pathways are more complex, resulting in less efficient catalysis.

It should be mentioned here that polycrystalline Cu is not a viable catalyst for future industrial applications of CO reduction, due to its low ECSA. In order to obtain high geometric current densities, which is necessary to make the production of chemicals from CO reduction economically feasible, nanostructured electrodes will be needed. However, as previously stated, the main goal of this study was to investigate polycrystalline Cu as a benchmark for CO reduction on Cu electrodes.

6.2 Comparison with literature data

In the previous section, I presented results that showed significant CO reduction activity and selectivity for polycrystalline Cu foils at -0.40 to -0.59 V. Since the motivation for this work was to study these electrodes as a benchmark, it is instructive to compare the results shown in Figure 6.1 with literature data from this reaction on nanostructured and polycrystalline Cu electrodes. In Figure 6.2, the total CO reduction current density obtained in this study is displayed together with those of two studies on nanostructured Cu from Kanan and coworkers,[165,167] and two other studies on polycrystalline Cu foils.[79,170]

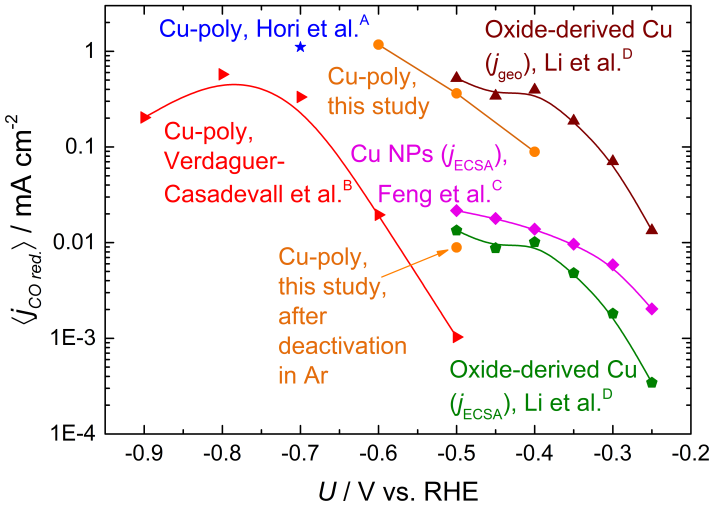

Figure 6.2: Mean CO reduction current densities measured on various Cu electrodes in 0.1 M KOH. The results obtained in this study are compared with data from polycrystalline Cu (A) reported by Hori et al.[79] and (B) Verdaguer-Casadevall et al.[170], as well as (C) Cu nanoparticles reported by Feng et al.[167] and (D) Oxide-derived Cu reported by Li et al.[165]

When comparing the CO reduction current density measured in this study with the geometric current density obtained from OD Cu foils, the nanostructured electrodes showed significantly enhanced activity at low overpotentials. This was expected because of the higher ECSA of the nanostructured materials; these electrodes exhibited roughness factors up to 66, as shown in Table 6.1. Note that the roughness factors of the polycrystalline Cu foils were assumed to be 1. This was consistent with the fact that these electrodes were used as a reference point when determining the ECSA of the nanostructured Cu by measuring double-layer capacitance. The ECSA determination method used for the two studies on nanostructured electrodes shown in Figure 6.2 is discussed in further detail in section 3.2.5.

When normalising the nanostructured electrodes by ECSA, however, the picture looked very different. These data were hard to compare accurately with the data from the present study, because the CO reduction activity start plateauing at relatively mildly cathodic potentials (around -0.35 V). A Faradaic reaction normally exhibits an exponential increase in current with higher overpotential, which would give a linear curve on this logarithmic plot. However, only the 2-3 data points at the least cathodic potentials

Table 6.1: Roughness factors for the different electrode materials discussed in this work. The ECSA of the nanostructured electrodes was estimated using double layer capacitance measurements.[105,165,167] Roughness factors were calculated by normalising to the capacitance of polycrystalline Cu. As a result, the roughness factor of polycrystalline Cu is assumed to be 1.

Electrode material	Roughness factor
Polycrystalline Cu[79,170]	1
Oxide-derived Cu[165]	39
Cu nanoparticles[167]	66

were relatively linear for the nanostructured electrodes. A likely reason for this behaviour is that these catalysts appeared to reach mass transport limitations at potentials cathodic of -0.35 V. The solubility of CO in aqueous solution is approximately 50 times lower than that of CO_2 (2.8×10^{-2} vs. 1.5 g L^{-1}).[22] Thus, mass transport is an even bigger issue for CO reduction than for CO_2 reduction. This is reflected in the significantly lower limiting current for CO reduction, ~1 mA cm^{-2} compared to around 20 mA cm^{-2} for CO_2 reduction.[152] The fact that the CO reduction activity of OD Cu electrodes reaches mass transport limitation at potentials cathodic of -0.35 V is also evident from a significant increase in Faradaic efficiency to H_2 evolution (product distribution from Li et al.[165] shown in Figure 2.11 on page 45).

OD Cu electrodes reach the limiting geometric current density at lower overpotentials than polycrystalline Cu due to higher ECSA. At the same time, nanostructured electrodes exhibit higher geometric CO reduction current density, and thus reach detectable concentrations of product more readily, even at potentials where low specific activity is taking place. This means that the practical potential range where the intrinsic activity can be measured without influence of mass transport limitations, while still accumulating sufficient product concentrations to facilitate adequate quantification, does not overlap for nanostructured and planar electrodes. As a result, the measurements on polycrystalline Cu presented here cannot be directly compared to the ECSA-normalised current density of the nanostructured electrodes. However, extrapolating the region where the nanostructured electrodes are not mass transport limited (i.e. the 2-3 most anodic points), can give an impression of the behaviour of the CO reduction activity in a hy-

pothetical situation where mass transport does not play a role. When doing this for the data included in Figure 6.2, it can be seen that the two nanostructured electrodes would reach a similar activity as what was measured for polycrystalline Cu in the present study.

These data indicate that planar, polycrystalline Cu yield comparable CO reduction activity to nanostructured Cu electrodes. The enhanced activity observed from nanostructured Cu is mainly a result of the high ECSA these electrodes exhibit, and the resulting increase in number of active sites per geometric area. A similar behaviour was observed when comparing literature data for the CO_2 reduction activity of various nanostructured Cu electrodes with that obtained from polycrystalline foils. These data were presented in Figure 2.8 on page 38 and discussed further there. However, Verdaguer-Casadevall et al. measured little to no CO reduction activity on polycrystalline Cu at -0.4 V. They used these measurements to correlate the CO reduction activity of OD Cu to the occurrence of a special strong binding site that was measured by CO TPD, which is not present on polycrystalline Cu. On the other hand, our data from the present study show that if a particular type of site is responsible for the CO reduction activity of Cu, it is also present on polycrystalline electrodes. While it has previously been assumed that nanostructuring enhances the intrinsic activity of Cu towards this reaction, the results presented here suggest otherwise. This is important to take into account when trying to design future catalyst materials for this reaction.

There were, however, differences in the product distribution observed from CO reduction on planar and nanostructured electrodes. While we observed significant hydrocarbon formation on polycrystalline Cu foils, mainly oxygenates were produced from the nanostructured electrodes presented here. This can be explained by the different potential windows accessed, since hydrocarbon formation occurs at higher overpotentials than oxygenate production.[48] Nanostructured Cu electrodes can give appreciable geometric activity from CO reduction already at mildly cathodic potentials, but is mass transport limited in the region where higher hydrocarbon selectivity is occurring. Likewise, polycrystalline Cu does not exhibit sufficient geometric activity at the potentials where particularly high oxygenate selectivity is occurring.

Another difference between the product distribution from CO reduction

on planar and nanostructured Cu is the type of oxygenates produced. For OD Cu, ethanol is the main product along with acetate, while small amounts of acetaldehyde can be observed as well.[165,202] On polycrystalline Cu, on the other hand, significantly higher aldehyde selectivity can be observed, towards C_2H_5CHO and CH_3CHO, and lower alcohol and acetate selectivity. Alcohols are more highly reduced than aldehydes (see Table 2.2), and thus contradict the argument about different potential windows from the previous paragraph. Thus, this cannot be the only explanation for the differences in product distribution. More complex reaction pathways lead to less efficient catalysis, meaning that higher overpotentials would be needed to drive the reaction(s). This could be observed to some extent in our data presented in Figure 6.1a, where aldehyde formation was more prominent at -0.40 and -0.50 V, while alcohol formation started dominating the product distribution at -0.59 V.

There are two likely explanations for the higher ethanol selectivity of OD Cu: (i) nanostructuring results in more undercoordinated surface sites, which have been shown to catalyse acetaldehyde reduction to ethanol more efficiently;[227] The porous structure of OD Cu gives increased probability for readsorption and further reduction of products in the three-dimensional electrode. Thus, acetaldehyde that is released from the electrode surface has a higher probability of becoming reduced to ethanol on OD Cu.

Another interesting point of discussion from the data presented in Figure 6.2 is the difference between the studies on polycrystalline Cu. As described previously, only a few groups have reported work on polycrystalline Cu in 0.1 M KOH.[79,170,228] Herein, we showed significant selectivity and activity towards CO reduction between -0.40 and -0.59 V for this electrode material. Verdaguer-Casadevall et al., on the other hand, reported little to no activity in the same potential region.[170] In another study by Hori et al.,[79] only a single potential was measured in 0.1 M KOH, showing similar CO reduction activity to the present work, albeit at higher overpotentials. The last relevant study on polycrystalline Cu (to the best of my knowledge) was performed by Schouten et al.[228] The authors reported ethylene formation at -0.35 to -0.60 V, but at insignificant total current densities. This work was not included in Figure 6.2 since they used online electrochemical mass spectrometry for product analysis. This technique normally does not yield quantitative data. As a result, the CO reduction reaction rate cannot

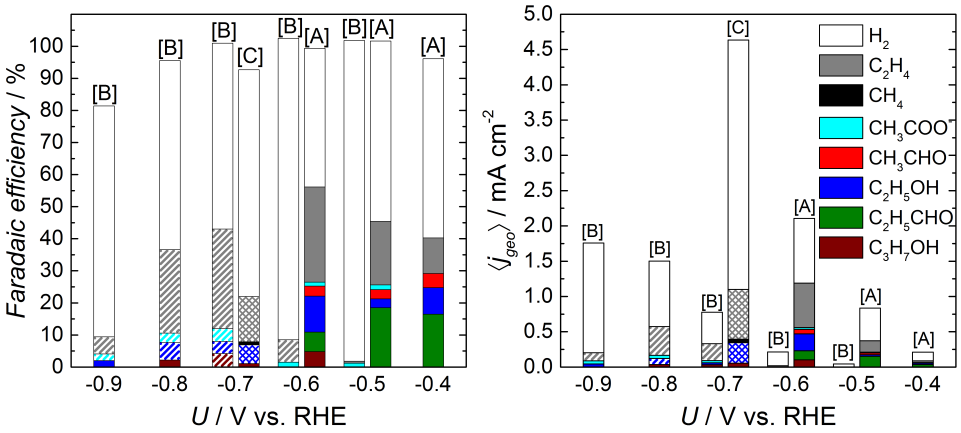

Figure 6.3: Comparison of (a) Faradaic efficiencies and (b) partial current densities to the individual products for CO reduction on polycrystalline Cu in 0.1 M KOH. The data included are from [A] the present work, [B] Verdaguer-Casadevall et al.[170] and [C] Hori et al.[79]

be determined. In Figure 6.3, the two studies by Hori et al. and Verdaguer et al. are compared in more detail, together with data from the present study.

Interestingly, the study by Verdaguer-Casadevall et al. reported almost exclusive selectivity towards H_2 evolution at -0.5 and -0.6 V, while significant CO reduction activity was measured at the same potentials in the present study. Furthermore, the total activity observed in our case was significantly higher. Taken together these factors lead to the large discrepancy in CO reduction activity that can be observed in Figure 6.2. Hori et al. reported lower CO reduction selectivity at -0.7 V than we observed at -0.59 V. However, it is clear from the partial current densities in Figure 6.3b that the CO reduction activity is similar at the two different potentials. However, the H_2 evolution current density increases significantly at the more cathodic potential. This indicates that polycrystalline Cu reaches mass transport limited CO reduction activity somewhere between -0.59 and -0.70 V. The fact that methane starts to emerge as a product at -0.70 V corroborates this, since this products first emerges for CO_2 reduction on polycrystalline Cu when the electrode starts reaching mass transport limitations.[48] It is important to keep in mind that this observation for the data in Figure 6.3 is based on studies from two different groups. As a result, they might have been acquired at different mass transport conditions, or with other variations in

Table 6.2: Summary of experimental conditions used for CO reduction on polycrystalline Cu in this study and for the studies by Hori et al.[79] and Verdaguer-Casadevall et al.[170].

Experimental conditions	**This study**	**Hori et al.[79]**	**Verdaguer-Casadevall et al.[170]**
Cell material	Glass	Not reported, glass used in previous publication.[47]	Glass
Electrode	Cu foil (99.9999%, Alfa Aesar Supratronic)	Cu foil (99.999%, electrodep., donated from Sumitomo Metal Mining Co.)	Cu foil (99.9999%, Alfa Aesar Supratronic)
Electrode preparation	Electropolishing at 2.1 V vs. Cu for 2 × 90 s in 30% H_3PO_4.	Electropolishing for 2 min in 85% H_3PO_4, potential and CE material not stated.	Electropolishing at 5 V vs. Ti for 5 min in 85% H_3PO_4.
Electrolyte	0.1 M KOH (Merck Suprapur, >99.995%)	0.1 M KOH (Reagent grade, pre-electrolysed)	0.1 M KOH (semiconductor grade, >99.99%)
CO gas purity	99.95%	>99.95%	99.5%
CO flow rate	~30 sccm	~70 sccm	5 sccm
CO reduction measurement	Chronoamperometric, ~30 min at specified potential	Chronopotentiometric, ~30 min at 5 mA cm^{-2}	Chronoamperometric, 2-3 h at specified potential

experimental conditions.

The significant discrepancy between the study by Verdaguer-Casadevall et al., as compared to present work and the study by Hori et al. is somewhat discouraging, since the aim of this study was to obtain a robust benchmark CO reduction on Cu electrodes by measuring polycrystalline Cu. The similarity of the data obtained in the present study and by Hori et al. indicate that reproducable measurements should be possible to achieve. The differences could be related to the experimental conditions used. In Table 6.2, various experimental parameters from the three studies are listed. An important difference between the studies is the duration of the CO reduction measurements. While our and Hori et al.'s studies performed chronoamperometry for ~30 minutes, Verdaguer-Casadevall et al. measured for 2-3 hours. As will be discussed in detail in section 6.3, we observed significant deactivation and a shift in product distribution for measurements carried out longer than half an hour. We mainly attributed this behaviour to poisoning by Si dissolved from the glass cell. It is likely that the other studies were encountering the same issues as us, since they were also conducted in glass H-cells. This indicates that the low activity measured by Verdaguer-Casadevall et al. might have been obtained from measurements on samples that were already deactivated. Meanwhile, the 30 minute measurements by Hori et al. were most likely still probing the original activity of Cu. In Figure 6.2, we included a point where we measured the CO reduction activity of polycrystalline Cu after deactivation in Ar-purged electrolyte. This data point is placed much closer to the data from Verdaguer-Casadevall et al., indicating that impurity poisoning could at least be part of the explanation for the low activity measured in that study. The chronoamperometry trace and Faradaic efficiency for the CO reduction measurement on the deactivated electrode are shown in Figure 6.6b in the following section, where the deactivation discussed in detail.

6.3 Deactivation

As shown in the inset of Figure 6.1b, the CO reduction activity of polycrystalline Cu could be maintained over the course of ~30 minutes. On a longer timescale, however, we observed significant deactivation. Figure 6.4 shows total activity and CO reduction current density (excluding CH_3COO^-), and

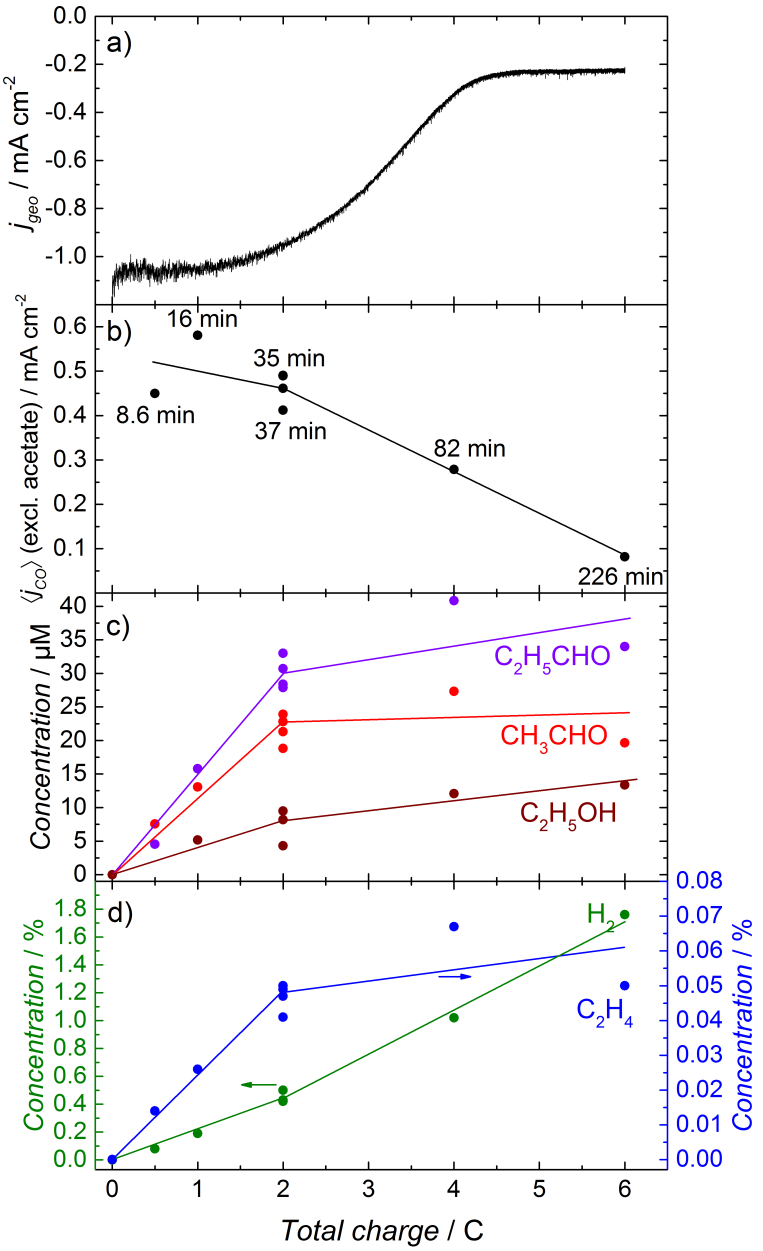

Figure 6.4: CO reduction on polycrystalline Cu at -0.5 V in 0.1 M KOH. (a) Representative chronoamperometry trace for a 225 minute measurement. (b) Mean CO reduction activity, excluding acetate that is a minor product, for individual measurements with varying total charge passed. (c-d) Concentration of (c) liquid and (d) gaseous products after individual measurements with varying total charge passed.

the concentration of liquid and gaseous products from CO reduction at -0.52 V as a function of total measurement charge. Note that the chronoamperometry trace in Figure 6.4a is a representative example from a single measurement. The deactivation profile was not exactly identical for all measurements, but the deactivation process always started after approximately the same measurement time. In Figure 6.4b-d, each data point represents an individual measurement.

As displayed in Figure 6.4a, deactivation started at around 2 C total measurement charge, equivalent to ~30 minutes. The CO reduction current density also decreased in line with the total activity (shown in Figure 6.4b). At the same time, the accumulative concentration of all the CO reduction products plateaued, as shown in Figure 6.4c and d. The H_2 evolution Faradaic efficiency increased slightly when deactivation started. This is expected, since the Faradaic efficiency to H_2 increased when the electrode deactivated. These observations indicate that two phenomena were occurring; a general deactivation of the electrodes and selective suppression of CO reduction.

One possible reason for the deactivation can be poisoning of the active sites by deposition of impurities. For CO_2/CO reduction, where the electrode is negatively biased, cations can be deposited on the electrode surface, blocking the active sites. Dissolved metal ions are particularly likely to deposit, since their thermodynamic equilibrium potentials typically are significantly anodic of the CO_2 /CO reduction operating potentials.[22] Previous studies have reported artefacts in electrocatalysis measurements as a result of impurities from the electrolyte precursor salt[210,231,232] and/or the glassware used for measurements[233,234]. In principle, artefacts from deposited metals can lead to either improved or degraded electrocatalytic performance. For instance, Subbaraman et al. discovered that certain metal impurities present in alkaline electrolyte salts lead to enhanced H_2 evolution on Pt electrodes.[231] For CO reduction, however, Cu is the only known catalyst material that can faciliate the reaction with significant activity and selectivity.[127] Thus, deposition of any foreign metal on the Cu electrode is likely to lead to a decrease in activity and selectivity.

Such a deactivation is exactly what we observed, indicating that poisoning could be taking place. This led us to perform post-electrolysis characterisation of the Cu electrodes using XPS, which would reveal whether

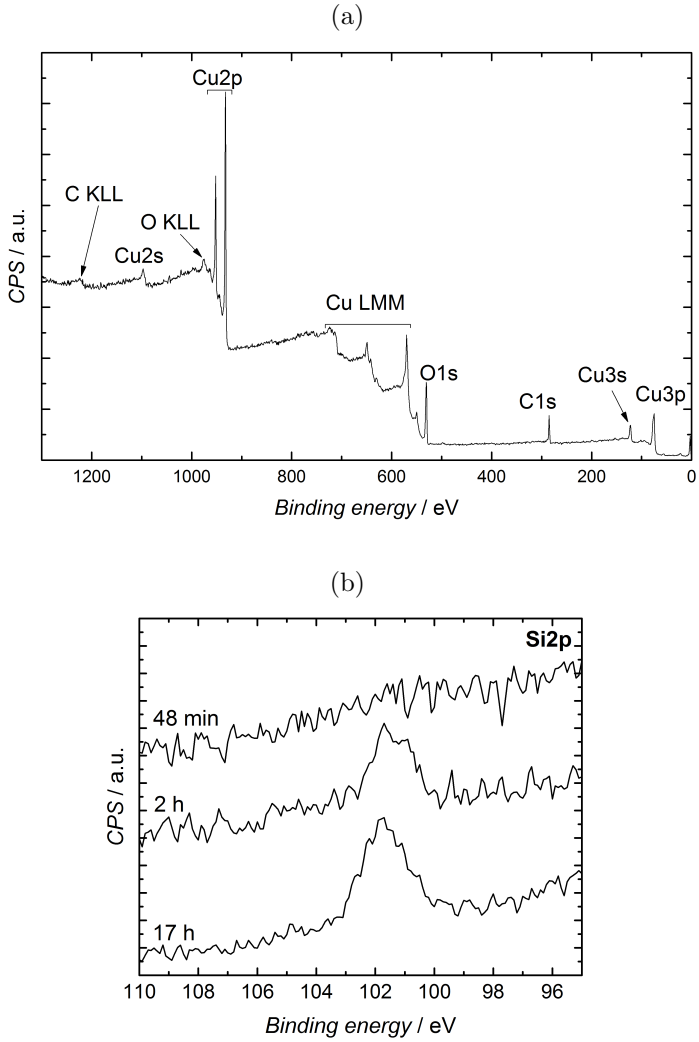

Figure 6.5: X-ray photoelectron spectroscopy of polycrystalline Cu electrodes after CO reduction at -0.5 V in 0.1 M KOH. (a) Survey spectrum of an electrode after a 17 h measurement. (b) Detailed spectra of Si2p region after measurements of varying duration.

detectable amounts of metal impurities were present on the electrodes after CO reduction. In order to minimise the removal of any impurities during the transfer from electrolyte to characterisation chamber, caution must be taken, as discussed in detail in section 3.5.2. The electrodes were removed from the electrolyte under potential control and rinsed briefly with Ar-saturated MilliQ water. They were stored in a closed Petri dish until XPS was performed, normally within 48 hours after removal of the sample from the CO reduction cell.

In Figure 6.5, XPS spectra of Cu electrodes after CO reduction measurements of different duration are shown. A survey spectrum measured after ~17 hours (Figure 6.5a) only revealed the presence of Cu, as well as adventitious oxygen and carbon from the atmosphere. However, when scanning the Si2p binding energy region in closer detail (Figure 6.5b), Si could be identified on the electrode surface. Glass is known to corrode in alkaline solutions.[233–235] Since we used a glass cell, it seems plausible that Si species accumulated in the electrolyte with longer measurement duration and deposited on the electrodes.

Other effects than impurity poisoning could be causing the deactivation observed. Poisoning of the electrode surface from reaction products and/or intermediates has been reported for other reactions, such as the electrooxidation of ethanol on Pt surfaces.[236] In these measurements, aldehydes were produced with relatively high selectivity. They polymerise in solution, a process that could also be happening in the electrode boundary layer, possibly leading to insoluble species blocking the surface. To investigate whether such a poisoning by aldehydes was occurring, we performed extended aldehyde reduction measurements. CH_3CHO and C_2H_5CHO were added to the electrolyte, which was saturated with Ar instead of CO. The resulting chronoamperometry trace from such a measurement is shown in Figure 6.6a. Deactivation can be observed after a similar amount of time as for CO reduction. This indicates that the deactivation was not related to the presence of CO.

In addition, we investigated the behaviour of polycrystalline Cu in Ar-saturated electrolyte. The chronoamperometry trace for such a measurement is shown in red in Figure 6.6b. The activity increased slightly at the beginning of the measurement, before it started deactivating. After 255 minutes of chronoamperometry, the sparging gas was changed to CO and

(a)

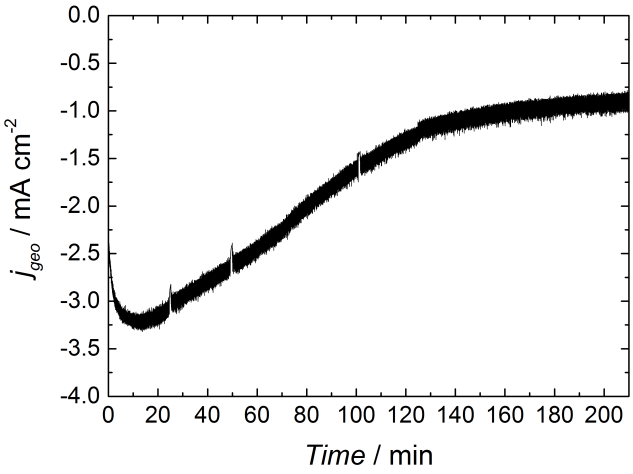

(b)

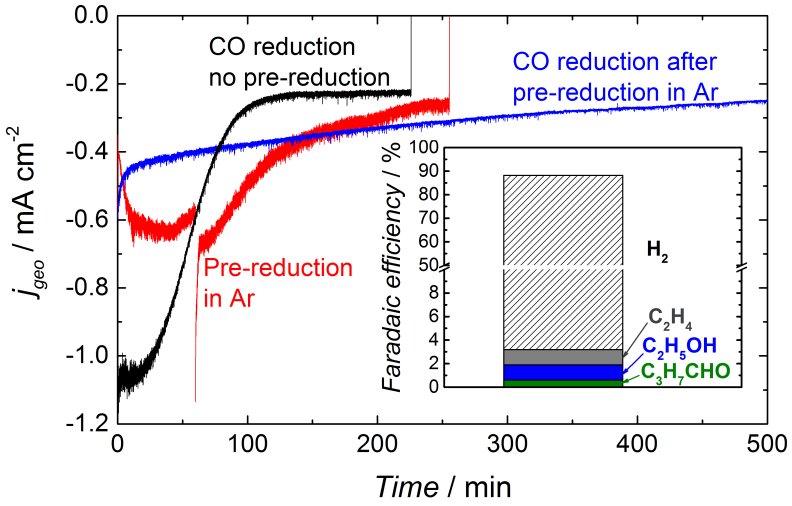

Figure 6.6: (a) Reduction of 200 µM acetaldehyde and 200 µM propionaldehyde at -0.5 V in 0.1 M KOH. (b) CO reduction (blue) after pre-reduction in Ar-sparged electrolyte (red) at -0.5 V in 0.1 M KOH. A representative CO reduction measurement performed with no pre-reduction (black) is shown for comparison. Inset: Faradaic efficiency to different products from CO reduction at -0.5 V in 0.1 M KOH after pre-reduction in Ar-saturated electrolyte.

the measurement was repeated (shown in blue). We observed significantly lower activity compared to CO reduction on a freshly electropolished sample (shown in black). Furthermore, we measured very little CO reduction selectivity, as shown by the Faradaic efficiencies in the inset (45% CO selectivity was measured on freshly electropolished electrodes). It seems that a similar deactivation occurs when only H_2 evolution is taking place, as when CO is present. This indicates that poisoning by reaction intermediates does not play a significant role in the deactivation.

Surface restructuring could be another phenomenon occurring during these measurements. Soriaga and coworkers showed that polycrystalline Cu changes its preferential faceting during CO_2 and CO reduction. [237–239] At the same time, certain Cu facets exhibit different selectivity, and to some extent activity, for these reactions than others.[71,72,128] Thus, restructuring of polycrystalline Cu during CO reduction could influence the resulting performance. Schouten et al. previously observed deactivation during CO reduction on polycrystalline Cu, and they hypothesised that it could be caused by such a restructuring of the electrode surface.[228]

CO is a reactive gas known to promote restructuring of different surfaces. [240–243] Thus, its presence in these measurements could be inducing this phenomenon. However, the electrodes also exhibit deactivation during H_2 evolution in Ar-saturated electrolyte (Figure 6.6b). It is hard to draw conclusions about restructuring based on these measurements. Phenomena that occur under operating conditions, including the examples of poisoning by intermediates and surface restructuring, are particularly challenging to study using conventional, *ex-situ* techniques. *In-situ*, or preferably *operando*, measurements would be highly useful in order to obtain more conclusive knowledge about whether these processes actually occur and to which extent they influence CO reduction activity.

As a general note, we advise keeping measurements intended as activity benchmarks as short as possible. This is important to minimise the influence of impurity poisoning, restructuring, corrosion and similar phenomena that can lead to activity artefacts. Short measurements are common for other electrocatalytic systems, such as the hydrogen fuel cell and water splitting reactions where the first few cycles (<1 minute) are normally used to evaluate the intrinsic activity of the materials.[244–248] For CO_2 reduction and CO reduction, however, the minimum measurement time is limited by

the detection limits of the analytical technique. For longer measuremens, a higher product concentration in the electrolyte can be achieved. As a result, the chance of overlooking products is lower. Thus, a compromise between minimising artefacts from impurity poisoning, restructuring and similar phenomena, and product analysis sensitivity needs to be found when conducting CO_2 and CO reduction measurements. When developing novel catalyst materials, it is also important to carry out extended measurements to study long-term stability. However, short experiments should also be used in such cases in order to obtain robust activity measurements.

6.4 Conclusions

In this project, we studied CO reduction on polycrystalline Cu foils in 0.1 M KOH at -0.40 V to -0.59 V. By accounting for all products through comprehensive analysis, we obtained robust data that can be used as a benchmark for copper catalysts for this reaction in the future. Such a benchmark is useful for nanostructured electrodes in particular, which show promising behaviour in terms of high oxygenate selectivity and activity. We observed high CO reduction activity from polycrystalline Cu under these conditions, in contrast to some of the previously reported studies on such electrodes. This indicates that the performance of polycrystalline Cu for CO reduction was previously underestimated.

Upon comparing our results to literature data, we observed that planar (polycrystalline) Cu exhibits similar specific CO reduction activity (i.e. normalised to ECSA) as nanostructured Cu electrodes. This indicates that the main effect of nanostructuring is increased geometric activity, and no significant changes in intrinsic activity compared to polycrystalline Cu. However, variations in product distribution were observed when comparing polycrystalline and nanostructured Cu electrodes. Higher oxygenate selectivity in general, and ethanol selectivity in particular, was observed from OD Cu. Likely reasons for this are (i) the different potential windows accessible for nanostructured and planar electrodes, (ii) readsorption and further reduction of products in the three-dimensional surface of nanostructured electrodes and (iii) the higher occurrence of undercoordinated sites on nanostructured electrodes. Since nanostructuring does not appear to affect the specific activity of Cu to a significant extent, different approaches need to

be developed in the pursuit of more intrinsically active electrocatalysts for this reaction.

We observed significant deactivation of the Cu foils when running CO reduction for longer than ~30 minutes. We used glass, which is known to corrode under alkaline conditions, as the cell material. Si impurities could be detected on the surface after CO reduction measurements, indicating that Si poisoning could be causing the deactivation. Poisoning by glass constituents has been reported previously for other electrocatalytic reactions,[233,234] but not for CO reduction. Different other groups use glass cells when studying CO reduction in alkaline electrolyte, which is a likely explanation for the discrepancies between individual studies on planar Cu electrodes for this reaction. Surface restructuring and poisoning by reaction intermediates/products could also play a role in relation to the deactivation. However, it is difficult to conclude whether these phenomena are occurring by using the *ex situ* techniques applied in this study. *In-situ* or *operando* measurements, e.g. IR spectroscopy and/or synchrotron-based techniques, are likely to give better understanding of phenomena that occur during CO reduction conditions. Such measurements will also be important in the quest to identify a relationship between surface structure and activity, a crucial next step in designing catalysts with improved intrinsic activity.

7

GIXRD of polycrystalline Cu during CO reduction

As described in the previous chapter, various phenomena such as restructuring [237–239,249] and poisoning by reaction intermediates[236] have been suggested to take place under during CO_2 and/or CO reduction. We thus consider them possible causes for the deactivation we observed for CO reduction on polycrystalline Cu. Surface structure is reported to influence the selectivity of Cu,[71–73,227,238,239] which means that restructuring could also lead to changes in product distribution. However, since restructuring and intermediate poisoning only occur under specific conditions applied during the electrochemical reaction, any evidence that these phenomena took place might disappear if removed from the electrolyte and transferred through air. Because of this, their occurrence is difficult to study using *ex-situ* techniques. Finally, insight about the surface structure of Cu during reaction conditions is important to develop structure-activity relationships.

At the same time, *in-situ* and *operando* studies of CO_2/CO reduction are inherently challenging to conduct. As outlined throughout this thesis, CO_2/CO reduction are complicated reactions that require careful planning and analysis. For instance, the electrochemical cell needs to be designed after certain principles, as described in section 3.3.2. Application of *operando* techniques involves added complexity, and give additional, often different, requirements of the cell and setup. In spite of the added complexity, an increasing number of *operando* studies of CO_2 reduction have been reported in the literature.[115,122,129,141,238,239]

Grazing incidence X-ray diffraction (GIXRD) can be used to determine the average structure of the topmost tens of atomic layers of solid samples,

and seems an ideal technique to give insight about the surface structure of polycrystalline Cu. However, absorption and scattering occurs when X-rays are passed through an electrolyte, resulting in significant loss of signal. Thus, the measurements need to be carried out using sources with a particularly high flux of X-rays, such as synchrotron facilities.

In this chapter, I discuss *operando* GIXRD measurements on polycrystalline Cu under CO reduction conditions carried out on beamline 2-1 at the Stanford Synchrotron Radiation Lightsource (SSRL) at the SLAC National Accelerator Laboratory. We started this project recently, and have thus only performed preliminary measurements to this date. However, the resulting data illustrate well the capabilities of this technique and give some initial insight about the system. As is normally the case for synchrotron measurements, a lot of people have been involved in planning and conducting the *operando* GIXRD measurements included in this thesis. I wrote the beamtime proposal together with my supervisors, Ifan E. L. Stephens and Ib Chorkendorff. I organised the planning of the beamtime, aided by the supervisors, colleagues at DTU and members of the Jaramillo group at Stanford University. The beamtime itself, I carried out together with Thomas Vagn Hogg and Søren B. Scott who are fellow PhD students at DTU, and John C. Lin and Alan T. Landers who are PhD students in the Jaramillo group. Other people involved in planning and conducting the beamtime were Associate Professor Brian Seger from my group at DTU, the staff scientists Christopher Hahn and Drew C. Higgins from the Jaramillo group, and Apurva Mehta and Ryan Davis, who are beamline scientists at SSRL. Søren, Thomas and I carried out data analysis. All the data analysis and plotting of results was done using a Python package written by Søren called "EC_Xray", from which the relevant modules can be found on GitHub.[250]

7.1 Two-theta scans

A detailed description of the setup that we used to perform *operando* GIXRD can be found in section 3.6. We prepared polycrystalline Cu films by physical vapour deposition on a Si(100) substrate with a Cr sticking layer. The samples were first characterised in a dry environment, in order to determine their initial structure. This would allow us to determine if any changes occured when introducing the electrolyte. Examples of GIXRD spectra from

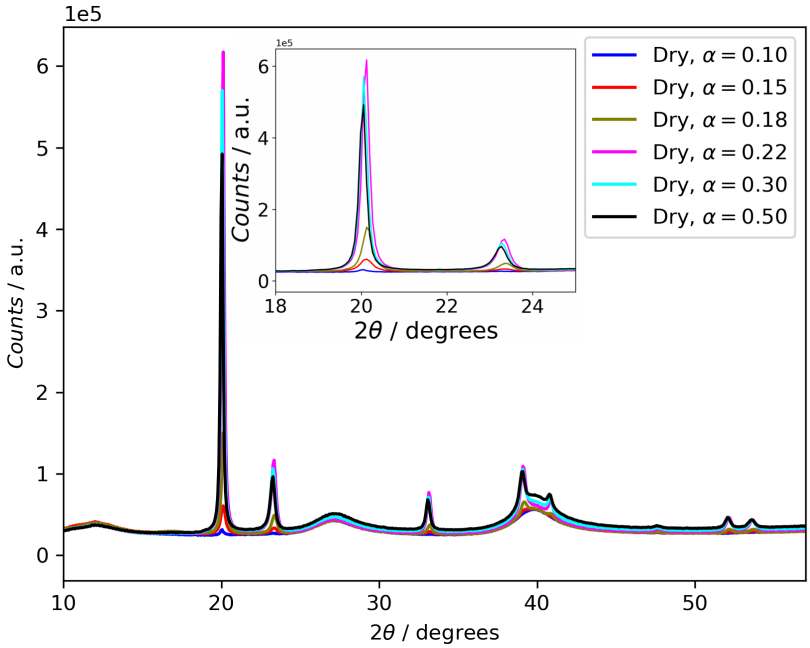

Figure 7.1: Dry GIXRD spectra from a polycrystalline Cu film at different X-ray incidence angles (α). Inset: The same data with better x-axis resolution around the Cu(111) and (100) peaks.

a representative sample that were measured at different incidence angles are shown in Figure 7.1. Several observations could be made from these data. Firstly, the Cu(111) peak at $2\theta = 20.1°$ was significantly more intense than the Cu(200) diffraction peak at $2\theta = 23.3°$. We thus conluded that the Cu films deposited by PVD were preferentially oriented in the Cu(111) direction. However, there were also signals from the other allowed diffraction peaks. These peaks and their 2θ values, as calculated by Bragg's law, are listed in Table 7.1. All the allowed peaks in the 2θ range measured were present in the dry spectra, confirming the polycrystalline nature of the samples. From Figure 7.1, it could be seen that the Cu peak intensities changed with the incidence angle of the X-ray beam (α). For the shallowest angle ($\alpha = 0.10°$; shown in blue), hardly any signal from metallic Cu was observed. This is well below the critical angle of total reflection ($\alpha = 0.18°$), and corresponds to a sampling depth of ~2 nm, as shown in Figure 3.14 on page 74. A possible reason for the lack of peaks is growth of an amorphous native oxide layer on Cu upon exposure to air.[148,149] Due to the

lack of long-range order, such a layer would yield no signal when measured by XRD. Our samples were stored for 1-2 weeks between preparation and characterisation.

When α was increased, the peak intensities rised as the X-rays probed more of the crystalline metallic Cu film below the native oxide, until a maximum peak intensity is reached at $\alpha = 0.22°$ (shown in magenta in Figure 7.1). For incidence angles from $\alpha = 0.30°$ (cyan) to $\alpha = 1.0°$ (black), the peak intensities decreased again. This can be explained, again, by studying the calculated attenuation length of the X-rays shown in Figure 3.14 on page 74. At $\alpha = 0.24°$, the radiation penetrates ~50 nm into the sample, corresponding to its entire thickness. Thus, when probing deeper, part of the substrate was sampled as well, lowering the signal from the Cu film. As a result, the rest of the 2θ scans presented in the rest of this thesis were measured at $\alpha < 0.24°$.

In addition to the Cu peaks, two broad features were present in the spectra around $2\theta = 27°$ and $2\theta = 40°$, respectively. These were also present when we measured at $\alpha = 0°$, thus not sampling the Cu surface. It is unclear what was causing the peaks, since we only observed them for some samples. One reason could be presence of foreign object(s) on the sample surfaces, e.g. specks of dust from the storage.

Once the samples were characterised in air, we introduced the electrolyte. Our aim was to characterise Cu at different conditions in both Ar and CO-saturated electrolyte. This way, any changes to the surface structure observed could be attributed to the application of a potential, and/or to the introduction of CO. Unfortunately, we encountered severe technical issues with the electrochemical cell (the setup is discussed in section 3.6). We attributed this to (i) blocking of the reference port by bubble(s) and/or (ii) shorting of the working electrode with the counter electrode for unknown reasons. As a result, we were only able to obtain reliable data in both Ar and CO atmosphere at three potentials; OCV, 0.0 and -0.2 V.

GIXRD spectra measured at OCV in Ar-saturated 0.1 M KOH with varying α are shown in Figure 7.2. The sample characterised in these measurements was kept at OCV for an extended period of time (~5 hours) because we experienced issues with getting contact to the reference electrode. Interestingly, this led to the appearance of two crystalline Cu oxide phases, Cu_2O and CuO, as opposed to the amorphous native oxide layer

Table 7.1: Expected XRD peaks from Cu and its oxide and hydroxide phases, along with 2θ values calculated from Bragg's law. For the Cu oxide and hydroxide phases, only one peak is shown, representing the most intense peak with $2\theta > 16°$ (since this is the region we normally monitored with the timescans).

Phase	**(hkl)**	**2θ / degrees**
Cu	(111)	20.1
	(200)	23.3
	(220)	33.2
	(311)	39.1
	(222)	40.9
	(400)	47.6
	(331)	52.2
	(420)	53.6
	(422)	59.2
Cu_2O	(111)	16.9
CuO	(111)	18.1
$Cu(OH)_2$	(021)	16.0

that was present under dry conditions. The 2θ values for the most intense peaks from these two phases are shown in Table 7.1. The appearance of surface oxides with long-range order was most likely related to the positive OCV we measured for Cu in Ar-saturated 0.1 M KOH (~0.6 V), which allows for oxidation of the surface by O_2. At $\alpha = 0.05°$, only peaks from the two oxide phases were visible. This indicated that the oxidised layer surface layer was thicker than 2 nm in this case. For the scans at $\alpha = 0.15°$and 0.22°, the metallic Cu peaks appeared. Interestingly, the peak intensities were lower at 0.22° than at 0.15°, while the opposite was the case for the dry measurements in Figure 7.1. This indicates that the Cu film might have corroded at OCV, resulting in it being thinner than the initial 50 nm.

When applying a potential of 0 V, the oxide peaks disappeared, and only the metallic Cu diffraction peaks were present, similarly to the dry spectra discussed above. This is discussed further in appendix C, where spectra at 0.0 V and -0.2 V in Ar and CO-saturated electrolyte are shown.

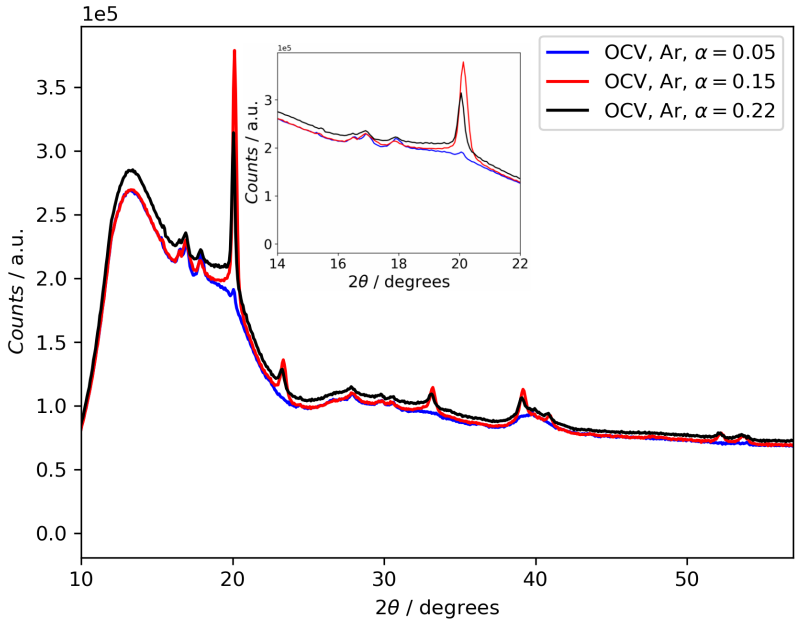

Figure 7.2: GIXRD spectra from a polycrystalline Cu film kept at OCV for ~5 h in Ar, measured at different X-ray incidence angles (α). Inset: The same data with better x-axis resolution around the Cu(111), CuO(111) and Cu_2O peaks.

No changes in the surface structure of the sample could be observed in these measurements, indicating that the surface of these films did not reconstruct to a significant extent once reduced.

7.2 Timescans

In the previous section, I discussed GIXRD spectra obtained at steady conditions, where each measurement took around 10 minutes. However, in order to be able to gain detailed understanding of dynamic phenomena, a significantly higher time resolution is necessary. As described in section 3.6.5, a detector with spatial resolution in two dimensions was used for these measurements. It sampled ~5 degrees of the 2θ spectrum, enabling us to monitor part of the XRD spectrum without moving the detector. As a result, a time resolution of 2-3 seconds could be achieved.

An example of a dynamic phenomenon that that the timescan approach allowed us to study, is the behaviour of the oxide that appeared as the sample was being kept at OCV. Only metallic peaks could be observed after the

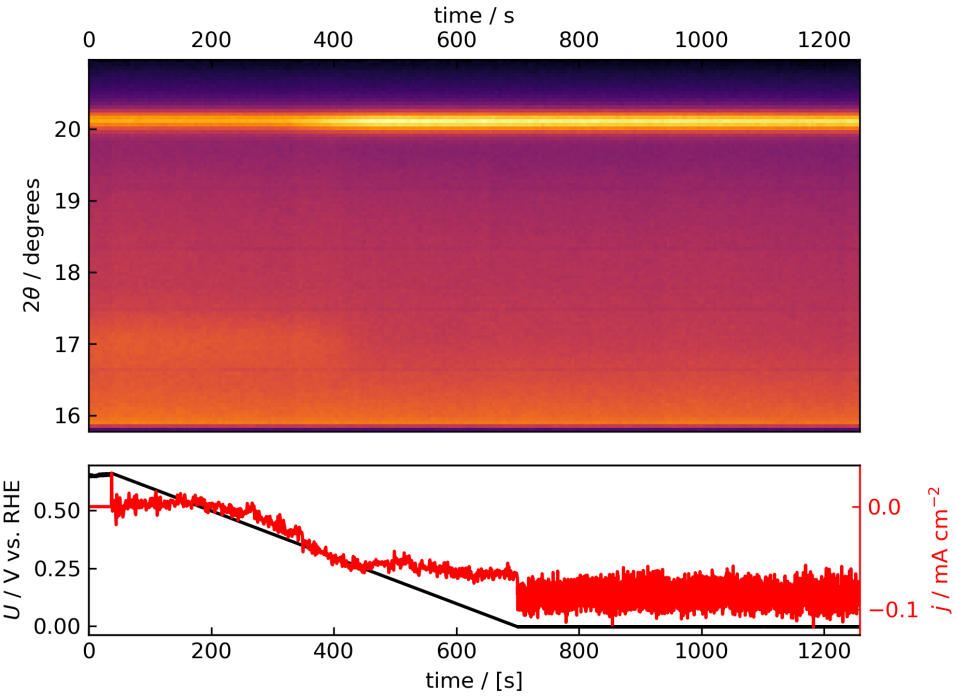

Figure 7.3: Timescan during a linear potential sweep from the open-circuit voltage to 0 V for polycrystalline Cu in Ar-saturated 0.1 M KOH. Top: X-ray data. Bottom: EC data.

potential was changed to 0 V, meaning that surface reduction occurs in that potential range. With the timescans, we were able to study the reduction of the electrode in closer detail. The resulting XRD and electrochemistry data from a sample in Ar-saturated 0.1 M KOH are shown in the top and bottom panel of Figure 7.3, respectively. The measurement started at OCV (~0.6 V), where the electrode had been kept for around 3 hours. At this potential, the Cu(111) peak was clearly discernable at 20.1°. A weak signal from the Cu_2O phase could be observed at 16.9°. The potential was then swept linearly to 0 V at a scan rate of 1 mV s^{-1}, and subsequently kept at this potential for ~10 minutes. Based on the current response, it appeared that reduction began at ~0.4 V, indicated by a cathodic current. The current plateaued around -0.25 V, suggesting that the sample was reduced. At the same time, the Cu_2O peak vanished from the XRD spectrum and the Cu peak became more intense, confirming the reduction of the sample. The current remained constant at ~60-90 µA cm^{-2}, even after reduction of the

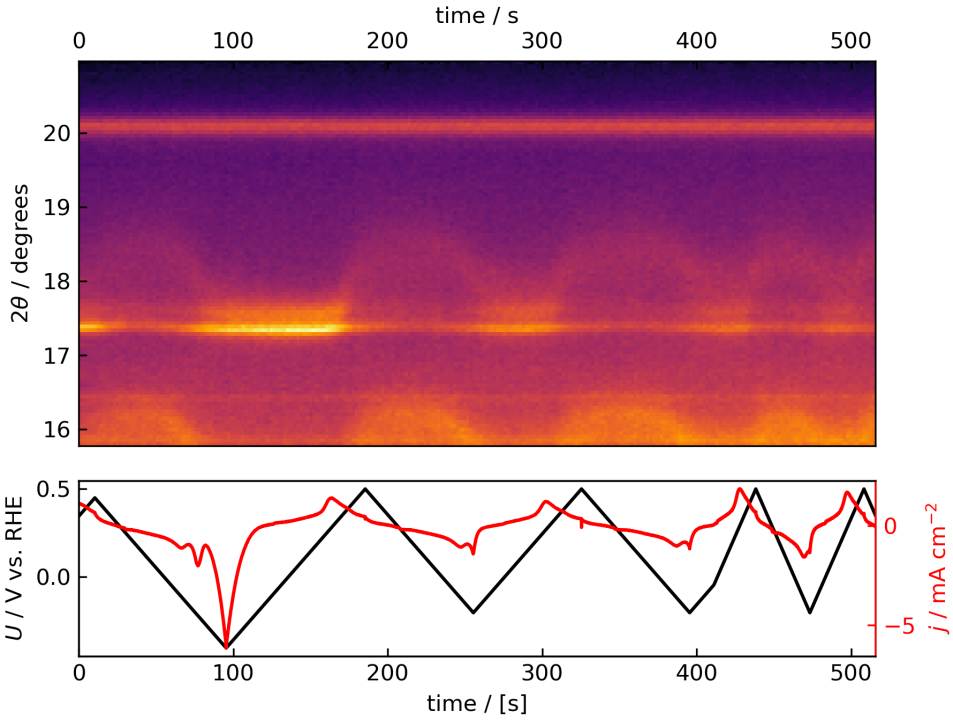

Figure 7.4: Timescan during CVs between cathodic and anodic potentials for polycrystalline Cu in Ar-saturated 0.1 M KOH, in the presence of Ni. Top: X-ray data. Bottom: EC data.

electrode. This could be caused by presence of small amounts of O_2 causing ORR current. In addition, a particularly high current range (100 mA) was set on the potentiostat to avoid loss of potential control in the case of an unexpected jump in current. The high current range gives poor sensitivity to currents in the µA range, and the cathodic current that we measured could be an artefact from this. For some reason, the noise increased significantly after 600 s. Incidentally, the potentiostat switched from linear sweep voltammetry to chronoamperometry at that exact time. Thus, it was most likely caused by the potentiostat settings. The reduction of the oxide when scanning the potential cathodic from OCV behaved similarly in CO atmosphere, as shown in Figure C.3 in appendix C.

Another example of a dynamic phenomenon that is interesting to study using the timescan approach are non-Cu peaks that we observed for certain samples. From their 2θ values, we attributed them to Ni deposition on our

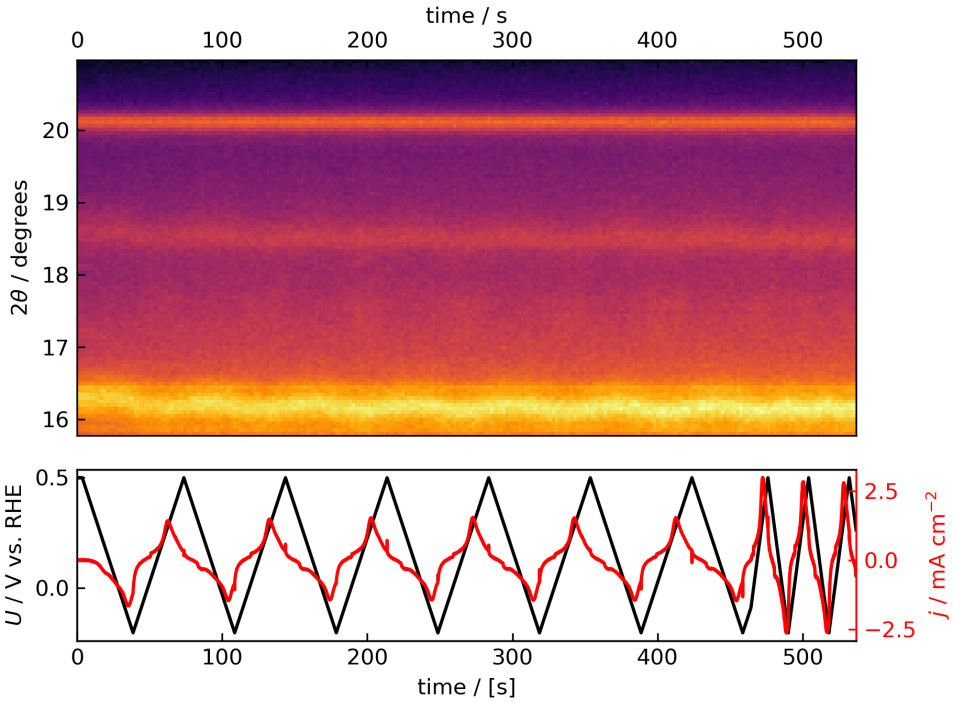

Figure 7.5: Timescan during CVs between cathodic and anodic potentials for polycrystalline Cu in Ar-saturated 0.1 M KOH. The sample has been roughened from repeated cycling. Top: X-ray data. Bottom: EC data.

Cu films, caused by carbonyls from the CO gas cylinder and/or the Ni mesh that was present in the electrolyte loop. In order to confirm our hypothesis that the peaks were related to a species adsorbing rather than a structural change of the Cu, we decided to carry out cyclic voltammetry between cathodic and anodic potentials. The resulting X-ray and electrochemical data are shown in the top and bottom panel of Figure 7.4. The Cu(111) peak remained constant at 20.1°. However, the Ni peak at 17° disappeared and reappeared at anodic and cathodic potentials, respectively, indicating that the Ni was stripped and redeposited. The Ni peaks shifted to higher 2θ values as the Ni overlayer was stripped off the surface, indicating an expansion of the lattice.

After repeated cycling of the the electrode to anodic potentials, the Ni peaks disappeared, and Cu oxide peaks appeared instead. The desorbed Ni most likely left the cell with the electrolyte flow, and adsorbed to the Chelex that was present in the electrolyte loop. The timescan resulting from CVs

between cathodic and anodic potentials on the (presumably) Ni-free sample is shown in Figure 7.5. A strong signal could be observed at 16.1-16.2°. The closest peak amongst the different Cu phases in Table 7.1 is the $Cu(OH)_2$ at 16.0°. We hypothesised that the peak originated from a hydroxide layer that is somewhat strained on the roughened sample. The peak position shifted by ~0.1° between anodic and cathodic potentials. Interestingly, the signal did not disappear when the electrode was cycled to -0.2 V. If this peak represented a hydroxide layer, it was resilient to reduction at mildly cathodic potentials on this particular samples. Note that the history of this sample was complex, since it had previously been contaminated with Ni. It is for instance possible that some Ni was still present during these measurements, which could affect the behaviour of the electrode. In addition, because of repeated cycling, it appeared to be roughened, as confirmed by performing X-ray reflectivity measurements. This could indicate that roughening of Cu electrodes have a stabilising effect on surface and/or near-surface hydroxides under cathodic potentials. To substantiate this observation, however, similar measurements would have to be performed on a sample that has not experienced contamination.

In the measurements discussed in the previous paragraphs, we obtained detailed information about oxidation and reduction processes on the electrode by monitoring part of the XRD spectrum with high time resolution. However, one of the main aims of carrying out *operando* GIXRD was studying whether restructuring occurred under CO reduction conditions. The time resolution of the timescan approach, could help reveal any dynamic changes occurring when the experimental conditions were changed. As a result, we performed timescans during a linear potential sweeps from 0 to -0.2 V in Ar and a change from Ar to CO sparge while keeping the potential at -0.2 V. However, no changes could be observed during these timescans (data shown in appendix C). This indicates that no major changes to the average surface structure of polycrystalline Cu films take place at -0.2 V and more anodic, in either Ar or CO on a time span of < 1 hour. Note that no product analysis was applied for these measurements. As a result, we were not able to distinguish current going to CO reduction from other processes. CO reduction products have been reported as anodic as -0.15 V from nanostructured electrodes,[166] indicating that some CO reduction could be occurring at -0.20 V. However, the deactivation discussed in the

previous chapter was studied in detail at -0.5 V, where significant CO reduction with activity on the order of ~1 mA cm^{-2} was occurring. Based on the GIXRD measurements presented here, we were not able to conclude whether restructuring is occurring at more relevant potentials.

7.3 Conclusions

In this chapter, I have presented GIXRD measured on polycrystalline Cu under CO reduction conditions. One of the main aims of this study was to elucidate whether changes to the surface structure of polycrystalline Cu occurs under reaction conditions. By using a detector with spatial resolution in the 2θ dimension, we could monitor ~5 degrees of the 2θ spectrum without moving the detector. This enabled us to study relevant peaks with a time resolution of 2-3 seconds. As a result, we could investigate the reduction of the electrodes in real-time during a potential sweep from OCV to 0 V. Furthermore, we studied the deposition and stripping of foreign metal species on the surface as we performed CVs between cathodic and anodic potentials. Interestingly, we observed oxides present as cathodic as -0.2 V on a roughened sample. This could indicate that surface roughening stabilises oxide species. However, this sample had a complex pre-history, meaning that these measurements should be repeated before any conclusions can be drawn.

Using the timescan approach, we monitored the surface structure of Cu when sweeping the potential cathodically to -0.2 V. Subsequently, while keeping this potential, we changed the gas sparge from Ar to CO. No significant changes in the Cu(111) peak intensity could be observed during any of these procedures, indicating that no observable restructuring of the surface was taking place. We cannot, however, draw general conclusions about this system, since our measurements were limited to relatively mildly cathodic potentials. In future studies, we aim to study the system at potentials where higher CO reduction activity was observed from polycrystalline Cu in *ex-situ* studies. Another aim for future studies will be to perform product analysis during these *operando* GIXRD measurements. This is important in order to confirm that CO reduction is indeed taking place to a significant extent. *Operando* GIXRD measurements were performed with electrolyte flow, while the *ex-situ* CO reduction that was reported in previous chapters

was carried out using batch measurements. It is likely that the convection achieved from the electrolyte flow in the *operando cell* is stronger than that from the electrolyte sparging and the magnetic stir bar in the *ex-situ* cell, resulting in different mass transport conditions.

8

General conclusions and outlook

In this thesis, I have discussed various aspects regarding CO reduction on Cu electrodes.

Product analysis is an important factor for obtaining robust results from CO_2 and CO reduction measurements. Therefore, I spent a significant part of my PhD benchmarking and optimising analytical techniques, in particular for quantification of liquid products. Static headspace-gas chromatography (HS-GC) and NMR spectroscopy were used for liquid product analysis in the present work. The results from benchmarking of these techniques indicate that the use of alkaline electrolytes leads to more complicated liquid product analysis. Acetaldehyde and propionaldehyde polymerise and form a precipitate in alkaline solution, which makes analysis by NMR spectroscopy difficult. HS-GC, on the other hand, exhibits excellent sensitivity towards these compounds. This case underlines the importance of performing comprehensive product analysis, in particular when alkaline electrolytes are being used. Application of multiple, complementary techniques is preferable.

On the basis of thorough product analysis, we identified acetaldehyde as an additional, previously overlooked product from CO reduction on oxide-derived Cu. Using a combination of experiments and DFT calculations, we identified it as a key intermediate in the formation of ethanol from CO. This allowed us to propose the following hypotheses to explain the high ethanol selectivity of oxide-derived Cu: (i) due to the porous electrode structure, acetaldehyde produced at the electrode surface has a relatively high probability for readsorption and further reduction; (ii) undercoordinated sites have been shown to catalyse conversion of acetaldehyde to ethanol more

efficiently,[227] and a higher abundance of such sites on the nanostructured surface of oxide-derived Cu is likely.

Based on the high performance that has been reported for oxide-derived Cu towards CO reduction, we identified the need for a robust benchmark for this reaction on Cu electrodes. Polycrystalline Cu foils are successfully used as a benchmark for CO_2 reduction,[45,48,79] inspiring us to perform CO reduction experiments on polycrystalline Cu. Based on the data from these measurements, no significant difference in CO reduction activity between planar, polycrystalline Cu foils and nanostructured electrodes could be observed, when normalised by the electrochemically active surface area. The same trend can be seen for CO_2 reduction when comparing data from a number of previous studies on nanostructured and polycrystalline electrodes. A common perception in the field has been that nanostructuring can be applied as a means of modifying the intrinsic activity of Cu. This is reflected in the large amount of studies that exists in the literature studying CO_2 and CO reduction on nanostructured electrodes. However, these measurements suggest that the main effect of nanostructuring is increased geometric activity and altered product distribution.

Above, I discussed our hypotheses for why oxide-derived Cu exhibits such a high selectivity to ethanol. The proposed effects of the three-dimensional structure and high occurrence of undercoordinated sites on these nanostructured surfaces are supported by the observation that aldehydes are produced with higher selectivity than alcohols from CO reduction on polycrystalline Cu at low overpotentials. Another interesting difference in product distribution between polycrystalline and oxide-derived Cu is that the former exhibits significant hydrocarbon selectivity, while the latter almost exclusively facilitates oxygenate formation. The fact that oxide-derived Cu reaches mass transport limitations at potentials cathodic of -0.35 V could possibly explain this. Meanwhile, polycrystalline Cu starts to exhibit appreciable current density from CO reduction around -0.40 V. As a result, the potential windows where oxide-derived and polycrystalline Cu exhibit sufficient activity for quantification of any CO reduction products, but have not yet reached mass transport limitations, do not overlap. From CO_2 reduction, we know that oxygenates are produced at more anodic potentials than hydrocarbons. Thus, a reason for the higher oxygenate selectivity of oxide-derived Cu could be that these electrodes are generally measured at lower overpotentials.

Despite the significant progress made in recent years, further improvements are needed before CO_2 reduction can become a technological reality. Importantly, catalysts that exhibit high activity, energy efficiency and selectivity towards valuable products at the same time are yet to be developed. The observation that nanostructuring mainly seems to influence product distribution and geometric activity, but not specific activity, calls for novel approaches to catalyst development. An example of an important focus point for future work is the design of different strategies for breaking the scaling relations between the different reaction intermediates toward $>2e^-$ products. This scaling is currently a major limiting factor to the energy efficiency of CO_2 and CO reduction.[32,64] One promising approach is engineering of the catalyst surface. Moving beyond these limitations can, in theory, be achieved by doping/alloying, where different metal sites are present next to each other on the surface.[64,65,67] Alternatively, three-dimensional engineering of surfaces to produce binding sites where the different intermediates are sterically forced to bind to different site geometries.[68] Finally, promoters/ligands could be added to the electrolyte that modulate the binding of certain intermediates to the surface. A few studies on bimetallic electrodes with Cu have shown promising results, in terms of improved $>2e^-$ selectivity and/or activity, as discussed in section 2.3.1.[102,103] This seems like a promising approach moving forward. However, efforts will have to be made in several different directions to reach the improvements that are necessary.

Bibliography

[1] A. Goeppert, M. Czaun, J.-P. Jones, G. K. Surya Prakash, and G. A. Olah, "Recycling of carbon dioxide to methanol and derived products - closing the loop.," *Chem. Soc. Rev.*, vol. 43, no. 23, pp. 7995–8048, 2014.

[2] Central Intelligence Agency, "The World Factbook," 2016.

[3] P. Crompton and Y. Wu, "Energy consumption in China: Past trends and future directions," *Energy Econ.*, vol. 27, no. 1, pp. 195–208, 2005.

[4] United Nations, "World population prospects 2017," tech. rep., 2017.

[5] B. plc., "BP Statistical Review of World Energy: June 2017," tech. rep., 2017.

[6] Enerdata, "Global Energy Statistics Yearbook 2017," tech. rep., 2017.

[7] N. S. Lewis and D. G. Nocera, "Powering the planet: chemical challenges in solar energy utilization," *Proc. Natl. Acad. Sci. U. S. A.*, vol. 103, no. 43, pp. 15729–15735, 2006.

[8] German Federal Institute of Geosciences and Natural Resources, "Energy Study 2016. Reserves, Resources and Availability of Energy Resources," 2016.

[9] E. Boeker and R. van Grondelle, *Environmental Physics - Sustainable Energy and Climate Change*. Wiley-VCH, 3rd ed., 2011.

[10] Intergovernmental Panel On Climate Change, *Climate Change 2014: The Physical Science Basis*. Cambridge University Press, 2014.

[11] E. Roston and B. Migliozzi, "What's Really Warming the World?," 2015.

[12] Intergovernmental Panel On Climate Change, *Climate Change 2007 - The Physical Science Basis*. 2007.

[13] M. I. Hoffert, K. Caldeira, A. K. Jain, E. F. Haites, L. D. D. Harvey, S. D. Potter, M. E. Schlesinger, S. H. Schneider, R. G. Watts, T. M. L. Wigley, and D. J. Wuebbles, "Energy implications of future stabilization of atmospheric CO2 content," *Nature*, vol. 395, no. 6705, pp. 881–884, 1998.

[14] United Nations Framework Convention on Climate Change, "Report of the Conference of the Parties on its twenty-first session," tech. rep., 2015.

[15] C. McGlade and P. Ekins, "The geographical distribution of fossil fuels unused when limiting global warming to 2 C," *Nature*, vol. 517, no. 7533, pp. 187–190, 2015.

[16] A. A. Fawcett, G. C. Iyer, L. E. Clarke, J. A. Edmonds, N. E. Hultman, H. C. McJeon, J. Rogelj, R. Schuler, J. Alsalam, G. R. Asrar, J. Creason, M. Jeong, J. McFarland, A. Mundra, and W. Shi, "Can Paris pledges avert severe climate change?," *Science*, vol. 350, no. 6265, pp. 1168–1169, 2015.

[17] M. Meinshausen, N. Meinshausen, W. Hare, S. C. Raper, K. Frieler, R. Knutti, D. J. Frame, and M. R. Allen, "Greenhouse-gas emission targets for limiting global warming to 2 C," *Nature*, vol. 458, no. 7242, pp. 1158–1162, 2009.

[18] K. Zickfeld, M. Eby, H. D. Matthews, and A. J. Weaver, "Setting cumulative emissions targets to reduce the risk of dangerous climate change," *Proc. Natl. Acad. Sci.*, vol. 106, no. 38, pp. 16129–16134, 2009.

[19] K. Zickfeld, A. H. MacDougall, and H. D. Matthews, "On the proportionality between global temperature change and cumulative CO

2 emissions during periods of net negative CO 2 emissions," *Environ. Res. Lett.*, vol. 11, no. 5, p. 055006, 2016.

[20] U.S. National Oceanic and Atmospheric Administration, "Trends in Atmospheric CO2 Concentrations," 2017.

[21] N. Nakicenovic and R. Swart, "Special Report on Emission Scenarios," tech. rep., International Panel on Climate Change, 2000.

[22] W. M. Haynes, ed., *CRC Handbook of Chemistry and Physics*. Boca Raton, FL: CRC Press/Taylor & Francis, 97th ed., 2016.

[23] B. Obama, "The irreversible momentum of clean energy," *Science*, vol. 355, no. 6321, pp. 126–129, 2017.

[24] M. Burke, S. M. Hsiang, and E. Miguel, "Global non-linear effect of temperature on economic production," *Nature*, vol. 527, no. 7577, pp. 235–239, 2015.

[25] R. Fu, D. Feldman, R. Margolis, M. Woodhouse, and K. Ardani, "U.S. Solar Photovoltaic System Cost Benchmark: Q1 2017," tech. rep., 2017.

[26] N. S. Lewis, "Toward Cost-Effective Solar Energy Use," *Science*, vol. 315, no. 5813, pp. 798–801, 2007.

[27] R. Wiser and M. Bolinger, "U.S. Department of Energy Wind Technologies Market Report 2015," tech. rep., 2016.

[28] H. Lund, "Large-scale integration of wind power into different energy systems," *Energy*, vol. 30, no. 13, pp. 2402–2412, 2005.

[29] H. Chen, T. N. Cong, W. Yang, C. Tan, Y. Li, and Y. Ding, "Progress in electrical energy storage system: A critical review," *Prog. Nat. Sci.*, vol. 19, pp. 291–312, mar 2009.

[30] F. Díaz-González, A. Sumper, O. Gomis-Bellmunt, and R. Villafáfila-Robles, "A review of energy storage technologies for wind power applications," *Renew. Sust. Energ. Rev.*, vol. 16, pp. 2154–2171, may 2012.

[31] I. Chorkendorff and J. W. Niemantsverdriet, *Concepts of Modern Catalysis and Kinetics*. Weinheim: Wiley-VCH, 2nd ed., 2007.

[32] Z. W. Seh, J. Kibsgaard, C. F. Dickens, I. Chorkendorff, J. K. Nørskov, and T. F. Jaramillo, "Combining theory and experiment in electrocatalysis: Insights into materials design," *Science*, vol. 355, no. 6321, pp. 1–12, 2017.

[33] Intergovernmental Panel on Climate Change, *Special Report on Carbon Dioxide Capture and Storage*. Cambridge University Press, 2005.

[34] J. C. Abanades, E. S. Rubin, M. Mazzotti, and H. J. Herzog, "On the climate change mitigation potential of CO2 conversion to fuels," *Energy Environ. Sci.*, vol. 10, no. 12, pp. 2491–2499, 2017.

[35] R. Kothari, D. Buddhi, and R. L. Sawhney, "Comparison of environmental and economic aspects of various hydrogen production methods," *Renew. Sustain. Energy Rev.*, vol. 12, no. 2, pp. 553–563, 2008.

[36] United Nations Department of Economic and Social Affairs, "World Population Prospects: The 2017 Revision," 2017.

[37] A. Mittasch and W. Frankenburg, "Early Studies of Multicomponent Catalysts," *Adv. Catal.*, vol. 2, pp. 81–104, 1950.

[38] J. R. Jennings, ed., *Catalytic Ammonia Syntesis - Fundamentals and Practice*. Springer, 1991.

[39] K. Waugh, "Methanol Synthesis," *Catal. Today*, vol. 15, no. 1, pp. 51–75, 1992.

[40] E. Bertheussen, S. A. Nitopi, S. B. Scott, A. K. Engstfeld, X. Liu, K. Chan, C. Hahn, J. K. Nørskov, T. F. Jaramillo, I. E. L. Stephens, and I. Chorkendorff, "Electroreduction of CO2 on Copper Electrodes." in preparation, 2018.

[41] S. Verma, B. Kim, H. R. M. Jhong, S. Ma, and P. J. A. Kenis, "A Gross-Margin Model for Defining Technoeconomic Benchmarks in the Electroreduction of CO2," *ChemSusChem*, vol. 9, no. 15, pp. 1972–1979, 2016.

[42] M. J. Roberts, "Low Temperature Hydrocarbon Gas Separation Process," 2001.

[43] K. G. Gallagher, S. Goebel, T. Greszler, M. Mathias, W. Oelerich, D. Eroglu, and V. Srinivasan, "Quantifying the promise of lithium–air batteries for electric vehicles," *Energy Environ. Sci.*, vol. 7, no. 5, p. 1555, 2014.

[44] S. Dial, "Wikimedia Commons." https://commons.wikimedia.org/wiki/File:Energy_d 2008.

[45] Y. Hori, H. Wakebe, T. Tsukamoto, and O. Koga, "Electrocatalytic process of CO selectivity in electrochemical reduction of CO2 at metal electrodes in aqueous media," *Electrochim. Acta*, vol. 39, no. 11-12, pp. 1833–1839, 1994.

[46] A. Bagger, W. Ju, A. S. Varela, P. Strasser, and J. Rossmeisl, "Electrochemical CO2 Reduction: A Classification Problem," *ChemPhysChem*, vol. 18, no. 22, pp. 3266–3273, 2017.

[47] Y. Hori, K. Kikuchi, and S. Suzuki, "Production of CO and CH4 in electrochemical reduction of CO2 at metal electrodes in aqueous hydrogencarbonate solution," *Chem. Lett.*, no. 11, pp. 1695–1698, 1985.

[48] K. P. Kuhl, E. R. Cave, D. N. Abram, and T. F. Jaramillo, "New insights into the electrochemical reduction of carbon dioxide on metallic copper surfaces," *Energy Environ. Sci.*, vol. 5, no. 2012, pp. 7050–7059, 2012.

[49] D. D. Zhu, J. L. Liu, and S. Z. Qiao, "Recent Advances in Inorganic Heterogeneous Electrocatalysts for Reduction of Carbon Dioxide," *Adv. Mater.*, vol. 28, no. 18, pp. 3423–3452, 2016.

[50] M. R. Singh and A. T. Bell, "Design of an artificial photosynthetic system for production of alcohols in high concentration from CO2," *Energy Environ. Sci.*, vol. 9, no. 1, pp. 193–199, 2016.

[51] Y. Hori, "Electrochemical CO2 Reduction on Metal Electrodes," in *Mod. Asp. Electrochem.* (C. Vayenas, R. White, and M. Gamboa-Aldeco, eds.), vol. 42, ch. 3, pp. 89–189, Springer, 2008.

[52] K. Krischer and E. R. Savinova, "Fundamentals of Electrocatalysis," in *Handb. Heterog. Catal.*, 2008.

[53] K. P. Kuhl, T. Hatsukade, E. R. Cave, D. N. Abram, J. Kibsgaard, and T. F. Jaramillo, "Electrocatalytic Conversion of Carbon Dioxide to Methane and Methanol on Transition Metal Surfaces," *J. Am. Chem. Soc.*, vol. 136, pp. 14107–14113, sep 2014.

[54] J. K. Nørskov, T. Bligaard, A. Logadottir, J. R. Kitchin, J. G. Chen, S. Pandelov, and U. Stimming, "Trends in the Exchange Current for Hydrogen Evolution," *J. Electrochem. Soc.*, vol. 152, no. 3, pp. J23–J26, 2005.

[55] R. Parsons, "The rate of electrolytic hydrogen evolution and the heat of adsorption of hydrogen," *Trans. Faraday Soc.*, vol. 54, pp. 1053–1063, 1958.

[56] B. Hinnemann, P. G. Moses, J. Bonde, K. P. Jørgensen, J. H. Nielsen, S. Horch, I. Chorkendorff, and J. K. Nørskov, "Biomimetic hydrogen evolution: MoS2 nanoparticles as catalyst for hydrogen evolution," *J. Am. Chem. Soc.*, vol. 127, no. 15, pp. 5308–5309, 2005.

[57] P. Sabatier, "Hydrogenations et deshydrogenations par catalyse," *Berichte der Dtsch. Chem. Gesellschaft*, vol. 44, no. 3, pp. 1984–2001, 1911.

[58] M. T. M. Koper, "Thermodynamic theory of multi-electron transfer reactions: Implications for electrocatalysis," *J. Electroanal. Chem.*, vol. 660, no. 2, p. 254, 2011.

[59] M. T. M. Koper, "Theory of multiple proton–electron transfer reactions and its implications for electrocatalysis," *Chem. Sci.*, vol. 4, no. 7, pp. 2710–2723, 2013.

[60] I. E. L. Stephens, A. S. Bondarenko, U. Grønbjerg, J. Rossmeisl, and I. Chorkendorff, "Understanding the electrocatalysis of oxygen reduction on platinum and its alloys," *Energy Environ. Sci.*, vol. 5, no. 5, p. 6744, 2012.

[61] P. Hernandez-Fernandez, F. Masini, D. N. McCarthy, C. E. Strebel, D. Friebel, D. Deiana, P. Malacrida, A. Nierhoff, A. Bodin, A. M.

Wise, J. H. Nielsen, T. W. Hansen, A. Nilsson, I. E. L. Stephens, and I. Chorkendorff, "Mass-selected nanoparticles of PtxY as model catalysts for oxygen electroreduction," *Nat. Chem.*, vol. 6, no. 8, pp. 732–738, 2014.

[62] M. Escudero-Escribano, P. Malacrida, M. H. Hansen, U. G. Vej-Hansen, A. Velazquez-Palenzuela, V. Tripkovic, J. Schiøtz, J. Rossmeisl, I. E. L. Stephens, and I. Chorkendorff, "Tuning the activity of Pt alloy electrocatalysts by means of the lanthanide contraction," *Science*, vol. 352, no. 6281, pp. 73–76, 2016.

[63] A. A. Peterson, F. Abild-Pedersen, F. Studt, J. Rossmeisl, and J. K. Nørskov, "How copper catalyzes the electroreduction of carbon dioxide into hydrocarbon fuels," *Energ. Environ. Sci.*, vol. 3, no. 9, pp. 1311–1315, 2010.

[64] A. A. Peterson and J. K. Nørskov, "Activity descriptors for CO 2 electroreduction to methane on transition-metal catalysts," *J. Phys. Chem. Lett.*, vol. 3, no. 2, pp. 251–258, 2012.

[65] N. B. Halck, V. Petrykin, P. Krtil, and J. Rossmeisl, "Beyond the volcano limitations in electrocatalysis – oxygen evolution reaction," *Phys. Chem. Chem. Phys.*, vol. 16, no. 27, pp. 13682–13688, 2014.

[66] M. Busch, N. B. Halck, U. I. Kramm, S. Siahrostami, P. Krtil, and J. Rossmeisl, "Beyond the top of the volcano? A unified approach to electrocatalytic oxygen reduction and oxygen evolution," *Nano Energy*, vol. 29, pp. 126–135, 2016.

[67] X. Hong, K. Chan, C. Tsai, and J. K. Nørskov, "How Doped MoS2 Breaks Transition-Metal Scaling Relations for CO2 Electrochemical Reduction," *ACS Catal.*, vol. 6, no. 7, pp. 4428–4437, 2016.

[68] A. D. Doyle, J. H. Montoya, and A. Vojvodic, "Improving oxygen electrochemistry through nanoscopic confinement," *ChemCatChem*, vol. 7, no. 5, pp. 738–742, 2015.

[69] W. J. Durand, A. A. Peterson, F. Studt, F. Abild-Pedersen, and J. K. Nørskov, "Structure effects on the energetics of the electrochemical

reduction of CO2 by copper surfaces," *Surf. Sci.*, vol. 605, no. 15-16, pp. 1354–1359, 2011.

[70] X. Liu, J. Xiao, H. Peng, X. Hong, K. Chan, and J. K. Nørskov, "Understanding trends in electrochemical carbon dioxide reduction rates," *Nat. Commun.*, vol. 8, p. 15438, may 2017.

[71] Y. Hori, I. Takahashi, O. Koga, and N. Hoshi, "Selective formation of C2 compounds from electrochemical reduction of CO2 at a series of copper single crystal electrodes," *J. Phys. Chem. B*, vol. 106, no. 1, pp. 15–17, 2002.

[72] Y. Hori, I. Takahashi, O. Koga, and N. Hoshi, "Electrochemical reduction of carbon dioxide at various series of copper single crystal electrodes," *J. Mol. Catal. A Chem.*, vol. 199, pp. 39–47, may 2003.

[73] C. Hahn, T. Hatsukade, Y. G. Kim, A. Vailionis, J. H. Baricuatro, D. C. Higgins, S. A. Nitopi, M. P. Soriaga, and T. F. Jaramillo, "Engineering Cu surfaces for the electrocatalytic conversion of CO2: Controlling selectivity toward oxygenates and hydrocarbons," *Proc. Natl. Acad. Sci. U. S. A.*, vol. 114, no. 23, pp. 5918–5923, 2017.

[74] P. N. Ross, "Structure Sensitivity in the Electrocatalytic Properties of Pt I . Hydrogen Adsorption on Low Index Single Crystals and the Role of Steps," *J. Electrochem. Soc.*, vol. 126, no. 1, pp. 67–77, 1979.

[75] N. M. Markovic, R. R. Adzic, and V. B. Vesovic, "Structural effects in electrocatalysis - Oxygen reduction on the gold single crystal electrodes with (110) and (111) orientations," *J. Electroanal. Chem.*, vol. 165, no. 1-2, pp. 121–133, 1984.

[76] J. A. Rodriguez, "Physical and chemical properties of bimetallic surfaces," *Surf. Sci. Rep.*, vol. 24, pp. 223–287, 1996.

[77] V. Ponec, "Alloy catalysts: The concepts," *Appl. Catal. A Gen.*, vol. 222, no. 1-2, pp. 31–45, 2001.

[78] J. H. Sinfelt, J. L. Carter, and D. J. Yates, "Catalytic hydrogenolysis and dehydrogenation over copper-nickel alloys," *J. Catal.*, vol. 24, no. 2, pp. 283–296, 1972.

[79] Y. Hori, A. Murata, R. Takahashi, and S. Suzuki, "Electroreduction of CO To CH4 and C2H4 At a Copper Electrode in Aqueous-Solutions At Ambient-Temperature and Pressure," *J. Am. Chem. Soc.*, vol. 109, no. 16, pp. 5022–5023, 1987.

[80] N. Todoroki, N. Yokota, S. Nakahata, H. Nakamura, and T. Wadayama, "Electrochemical Reduction of CO2 on Ni- and Pt-Epitaxially Grown Cu(111) Surfaces," *Electrocatalysis*, vol. 7, no. 1, pp. 97–103, 2016.

[81] X. Zhao, B. Luo, R. Long, C. Wang, and Y. Xiong, "Composition-dependent activity of Cu–Pt alloy nanocubes for electrocatalytic CO2 reduction," *J. Mater. Chem. A*, vol. 3, no. 8, pp. 4134–4138, 2015.

[82] X. Guo, Y. Zhang, C. Deng, X. Li, Y. Xue, Y.-M. Yan, and K. Sun, "Composition dependent activity of Cu–Pt nanocrystals for electrochemical reduction of CO2," *Chem. Commun.*, vol. 51, no. 7, p. 1345, 2015.

[83] A. S. Varela, C. Schlaup, Z. P. Jovanov, P. Malacrida, S. Horch, I. E. L. Stephens, and I. Chorkendorff, "CO2 electroreduction on well-defined bimetallic surfaces: Cu overlayers on Pt(111) and Pt(211)," *J. Phys. Chem. C*, vol. 117, no. 40, pp. 20500–20508, 2013.

[84] R. Reske, M. Duca, M. Oezaslan, K. J. P. Schouten, M. T. M. Koper, and P. Strasser, "Controlling catalytic selectivities during CO2 electroreduction on thin Cu metal overlayers," *J. Phys. Chem. Lett.*, vol. 4, no. 15, pp. 2410–2413, 2013.

[85] Q. Li, J. Fu, W. Zhu, Z. Chen, B. Shen, L. Wu, Z. Xi, T. Wang, G. Lu, J.-j. Zhu, and S. Sun, "Tuning Sn-Catalysis for Electrochemical Reduction of CO2 to CO via the Core/Shell Cu/SnO2 Structure," *J. Am. Chem. Soc.*, vol. 139, no. 12, pp. 4290–4293, 2017.

[86] Z. B. Hoffman, T. S. Gray, K. B. Moraveck, T. B. Gunnoe, and G. Zangari, "The Electrochemical Reduction of Carbon Dioxide to Syngas and Formate at Dendritic Copper-Indium Electrocatalysts," *ACS Catal.*, vol. 7, no. 8, pp. 5381–5390, 2017.

[87] Y. Zhao, C. Wang, and G. G. Wallace, "Tin nanoparticles decorated copper oxide nanowires for selective electrochemical reduction of aqueous CO2 to CO," *J. Mater. Chem. A*, vol. 4, no. 27, pp. 10710–10718, 2016.

[88] S. Sarfraz, A. T. Garcia-Esparza, A. Jedidi, L. Cavallo, and K. Takanabe, "Cu-Sn Bimetallic Catalyst for Selective Aqueous Electroreduction of CO2 to CO," *ACS Catal.*, vol. 6, no. 5, pp. 2842–2851, 2016.

[89] S. Rasul, D. H. Anjum, A. Jedidi, Y. Minenkov, L. Cavallo, and K. Takanabe, "A highly selective copper-indium bimetallic electrocatalyst for the electrochemical reduction of aqueous CO2 to CO," *Angew. Chem. Int. Ed.*, vol. 54, no. 7, pp. 2146–2150, 2015.

[90] G. O. Larrazábal, A. J. Martín, S. Mitchell, R. Hauert, and J. Pérez-Ramírez, "Enhanced Reduction of CO2 to CO over Cu–In Electrocatalysts: Catalyst Evolution Is the Key," *ACS Catal.*, vol. 6, no. 9, pp. 6265–6274, 2016.

[91] J. He, K. E. Dettelbach, D. A. Salvatore, T. Li, and C. P. Berlinguette, "High-Throughput Synthesis of Mixed-Metal Electrocatalysts for CO2 Reduction," *Angew. Chem. Int. Ed.*, vol. 56, no. 22, pp. 6068–6072, 2017.

[92] W. Lv, J. Zhou, F. Kong, H. Fang, and W. Wang, "Porous tin-based film deposited on copper foil for electrochemical reduction of carbon dioxide to formate," *Int. J. Hydrogen Energy*, vol. 41, no. 3, pp. 1585–1591, 2016.

[93] Y. Wang, J. Zhou, W. Lv, H. Fang, and W. Wang, "Electrochemical reduction of CO2 to formate catalyzed by electroplated tin coating on copper foam," *Appl. Surf. Sci.*, vol. 362, pp. 394–398, 2016.

[94] J. Choi, M. J. Kim, S. H. Ahn, I. Choi, J. H. Jang, Y. S. Ham, J. J. Kim, and S. K. Kim, "Electrochemical CO2 reduction to CO on dendritic Ag-Cu electrocatalysts prepared by electrodeposition," *Chem. Eng. J.*, vol. 299, pp. 37–44, 2016.

[95] G. Kyriacou and A. Anagnostopoulos, "Electrochemical reduction of CO2 at Cu + Au electrodes," *J. Electroanal. Chem.*, vol. 328, no. 1-2, pp. 233–243, 1992.

[96] C. Roy, J. Galipaud, L. Fréchette-Viens, S. Garbarino, J. Qiao, and D. Guay, "CO 2 electroreduction at AuxCu1-x obtained by pulsed laser deposition in O2 atmosphere," *Electrochim. Acta*, vol. 246, pp. 115–122, 2017.

[97] J. Christophe, T. Doneux, and C. Buess-Herman, "Electroreduction of Carbon Dioxide on Copper-Based Electrodes: Activity of Copper Single Crystals and Copper-Gold Alloys," *Electrocatalysis*, vol. 3, no. 2, pp. 139–146, 2012.

[98] D. Kim, J. Resasco, Y. Yu, A. M. Asiri, and P. Yang, "Synergistic geometric and electronic effects for electrochemical reduction of carbon dioxide using gold-copper bimetallic nanoparticles," *Nat. Commun.*, vol. 5, pp. 1–8, 2014.

[99] D. Kim, C. Xie, N. Becknell, Y. Yu, M. Karamad, K. Chan, E. J. Crumlin, J. K. Nørskov, and P. Yang, "Electrochemical Activation of CO2 through Atomic Ordering Transformations of AuCu Nanoparticles," *J. Am. Chem. Soc.*, vol. 139, no. 24, pp. 8329–8336, 2017.

[100] S. Ishimaru, R. Shiratsuchi, and G. Nogami, "Pulsed Electroreduction of CO2 on Cu-Ag Alloy Electrodes," *J. Electrochem. Soc.*, vol. 147, no. 5, p. 1864, 2000.

[101] F. Jia, X. Yu, and L. Zhang, "Enhanced selectivity for the electrochemical reduction of CO2 to alcohols in aqueous solution with nanostructured Cu-Au alloy as catalyst," *J. Power Sources*, vol. 252, pp. 85–89, 2014.

[102] D. Ren, B. S.-H. Ang, and B. S. Yeo, "Tuning the Selectivity of Carbon Dioxide Electroreduction toward Ethanol on Oxide-Derived CuxZn Catalysts," *ACS Catal.*, vol. 6, no. 12, pp. 8239–8247, 2016.

[103] E. L. Clark, C. Hahn, T. F. Jaramillo, and A. T. Bell, "Electrochemical CO2 Reduction over Compressively Strained CuAg Surface Alloys with Enhanced Multi-Carbon Oxygenate Selectivity," *J. Am. Chem. Soc.*, vol. 139, no. 44, pp. 15848–15857, 2017.

[104] J. Monzó, Y. Malewski, R. Kortlever, F. J. Vidal-Iglesias, J. Solla-Gullón, M. T. M. Koper, and P. Rodriguez, "Enhanced electrocat-

alytic activity of Au@Cu core@shell nanoparticles towards CO2 reduction," *J. Mater. Chem. A*, vol. 3, no. 47, pp. 23690–23698, 2015.

[105] C. W. Li and M. W. Kanan, "CO2 reduction at low overpotential on Cu electrodes resulting from the reduction of thick Cu2O films," *J. Am. Chem. Soc.*, vol. 134, pp. 7231–7234, may 2012.

[106] D. Raciti, K. J. T. Livi, and C. Wang, "Highly Dense Cu Nanowires for Low-Overpotential CO2 Reduction," *Nano Lett.*, vol. 15, no. 10, pp. 6829–6835, 2015.

[107] S. Min, X. Yang, A. Y. Lu, C. C. Tseng, M. N. Hedhili, L. J. Li, and K. W. Huang, "Low overpotential and high current CO2 reduction with surface reconstructed Cu foam electrodes," *Nano Energy*, vol. 27, pp. 121–129, 2016.

[108] M. Ma, K. Djanashvili, and W. A. Smith, "Selective Electrochemical Reduction of CO2 to CO on CuO-derived Cu Nanowires," *Phys. Chem. Chem. Phys.*, vol. 17, no. 32, pp. 20861–20867, 2015.

[109] M. Ma, K. Djanashvili, and W. A. Smith, "Controllable Hydrocarbon Formation from the Electrochemical Reduction of CO2 over Cu Nanowire Arrays," *Angew. Chem. Int. Ed.*, vol. 55, no. 23, pp. 6680–6684, 2016.

[110] W. Tang, A. A. Peterson, A. S. Varela, Z. P. Jovanov, L. Bech, W. J. Durand, S. Dahl, J. K. Nørskov, and I. Chorkendorff, "The importance of surface morphology in controlling the selectivity of polycrystalline copper for CO2 electroreduction," *Phys. Chem. Chem. Phys.*, vol. 14, pp. 76–81, jan 2012.

[111] F. S. Roberts, K. P. Kuhl, and A. Nilsson, "High selectivity for ethylene from carbon dioxide reduction over copper nanocube electrocatalysts," *Angew. Chem. Int. Ed.*, vol. 54, no. 17, pp. 5179–5182, 2015.

[112] C. S. Chen, A. D. Handoko, J. H. Wan, L. Ma, D. Ren, and B. S. Yeo, "Stable and selective electrochemical reduction of carbon dioxide to ethylene on copper mesocrystals," *Catal. Sci. Technol.*, vol. 5, no. 1, pp. 161–168, 2015.

[113] Y. Kwon, Y. Lum, E. L. Clark, J. W. Ager, and A. T. Bell, "CO2 Electroreduction with Enhanced Ethylene and Ethanol Selectivity by Nanostructuring Polycrystalline Copper," *ChemElectroChem*, vol. 3, no. 6, pp. 1012–1019, 2016.

[114] D. Ren, N. T. Wong, A. D. Handoko, Y. Huang, and B. S. Yeo, "Mechanistic Insights into the Enhanced Activity and Stability of Agglomerated Cu Nanocrystals for the Electrochemical Reduction of Carbon Dioxide to n-Propanol," *J. Phys. Chem. Lett.*, vol. 7, no. 1, pp. 20–24, 2016.

[115] H. Mistry, A. S. Varela, C. S. Bonifacio, I. Zegkinoglou, I. Sinev, Y.-W. Choi, K. Kisslinger, E. A. Stach, J. C. Yang, P. Strasser, and B. R. Cuenya, "Highly selective plasma-activated copper catalysts for Carbon Dioxide Reduction To Ethylene," *Nat. Commun.*, vol. 7, pp. 1–8, 2016.

[116] D. Gao, I. Zegkinoglou, N. J. Divins, F. Scholten, I. Sinev, P. Grosse, and B. Roldan Cuenya, "Plasma-Activated Copper Nanocube Catalysts for Efficient Carbon Dioxide Electroreduction to Hydrocarbons and Alcohols," *ACS Nano*, vol. 11, no. 5, pp. 4825–4831, 2017.

[117] D. Gao, F. Scholten, and B. Roldan Cuenya, "Improved CO2 Electroreduction Performance on Plasma-Activated Cu Catalysts via Electrolyte Design: Halide Effect," *ACS Catal.*, vol. 7, no. 8, pp. 5112–5120, 2017.

[118] R. Kas, R. Kortlever, A. Milbrat, M. T. M. Koper, G. Mul, and J. Baltrusaitis, "Electrochemical CO2 reduction on Cu2O-derived copper nanoparticles: controlling the catalytic selectivity of hydrocarbons," *Phys. Chem. Chem. Phys.*, vol. 16, no. 24, pp. 12194–201, 2014.

[119] D. Kim, S. Lee, J. D. Ocon, B. Jeong, J. K. Lee, and J. Lee, "Insights into autonomously formed oxygen-evacuated Cu2O electrode for the selective production of C2H4 from CO2," *Phys. Chem. Chem. Phys.*, vol. 17, no. 2, pp. 824–830, 2014.

[120] D. Ren, Y. Deng, A. D. Handoko, C. S. Chen, S. Malkhandi, and B. S. Yeo, "Selective Electrochemical Reduction of Carbon Dioxide

to Ethylene and Ethanol on Copper(I) Oxide Catalysts," *ACS Catal.*, vol. 5, no. 5, pp. 2814–2821, 2015.

[121] A. D. Handoko, C. W. Ong, Y. Huang, Z. G. Lee, L. Lin, G. B. Panetti, and B. S. Yeo, "Mechanistic insights into the selective electroreduction of carbon dioxide to ethylene on Cu2O-derived copper catalysts," *J. Phys. Chem. C*, vol. 120, no. 36, pp. 20058–20067, 2016.

[122] P. De Luna, R. Quintero-Bermudez, C.-T. Dinh, M. B. Ross, O. S. Bushuyev, P. Todorovic, T. Regier, S. O. Kelley, P. Yang, and E. H. Sargent, "Catalyst electro-redeposition controls morphology and oxidation state for selective carbon dioxide reduction," *Nat. Catal.*, 2018.

[123] F. S. Roberts, K. P. Kuhl, and A. Nilsson, "Electroreduction of Carbon Monoxide over a Copper Nanocube Catalyst: Surface Structure and pH Dependence on Selectivity," *ChemCatChem*, vol. 8, no. 6, pp. 1119–1124, 2016.

[124] Y. Lum, B. Yue, P. Lobaccaro, A. T. Bell, and J. W. Ager, "Optimizing C-C Coupling on Oxide-Derived Copper Catalysts for Electrochemical CO2 Reduction," *J. Phys. Chem. C*, vol. 121, no. 26, pp. 14191–14203, 2017.

[125] D. Raciti, M. Mao, and C. Wang, "Mass Transport Modeling for the Electroreduction of CO2 on Cu Nanowires," *Nanotechnology*, 2017.

[126] Y. Hori, A. Murata, S.-y. Ito, Y. Yoshinami, and O. Koga, "Nickel and iron modified copper electrode for electroreduction of CO2 by in-situ electrodeposition," *Chem. Lett.*, no. 9, pp. 1567–1570, 1989.

[127] Y. Hori, R. Takahashi, Y. Yoshinami, and A. Murata, "Electrochemical Reduction of CO at a Copper Electrode," *J. Phys. Chem. B*, vol. 101, no. 36, pp. 7075–7081, 1997.

[128] K. J. P. Schouten, E. Pérez Gallent, and M. T. M. Koper, "Structure sensitivity of the electrochemical reduction of carbon monoxide on copper single crystals," *ACS Catal.*, vol. 3, no. 6, pp. 1292–1295, 2013.

[129] A. Eilert, F. S. Roberts, D. Friebel, and A. Nilsson, "Formation of Copper Catalysts for CO2 Reduction with High Ethylene/Methane

Product Ratio Investigated with in Situ X-ray Absorption Spectroscopy," *J. Phys. Chem. Lett.*, vol. 7, no. 8, pp. 1466–1470, 2016.

[130] K. D. Yang, W. R. Ko, J. H. Lee, S. J. Kim, H. Lee, M. H. Lee, and K. T. Nam, "Morphology-Directed Selective Production of Ethylene or Ethane from CO2 on a Cu Mesopore Electrode," *Angew. Chem. Int. Ed.*, vol. 56, no. 3, pp. 796–800, 2016.

[131] A. Dutta, M. Rahaman, N. C. Luedi, M. Mohos, and P. Broekmann, "Morphology Matters: Tuning the Product Distribution of CO2 Electroreduction on Oxide-Derived Cu Foam Catalysts," *ACS Catal.*, vol. 6, no. 6, pp. 3804–3814, 2016.

[132] A. Dutta, M. Rahaman, M. Mohos, A. Zanetti, and P. Broekmann, "Electrochemical CO2 conversion using skeleton (sponge) type of Cu catalysts," *ACS Catal.*, vol. 7, pp. 5431–5437, 2017.

[133] C. Reller, R. Krause, E. Volkova, B. Schmid, S. Neubauer, A. Rucki, M. Schuster, and G. Schmid, "Selective Electroreduction of CO2 toward Ethylene on Nano Dendritic Copper Catalysts at High Current Density," *Adv. Energy Mater.*, vol. 7, no. 12, p. 1602114, 2017.

[134] M. R. Gonçalves, A. Gomes, J. Condeço, T. R. C. Fernandes, T. Pardal, C. A. C. Sequeira, and J. B. Branco, "Electrochemical conversion of CO2 to C2 hydrocarbons using different ex situ copper electrodeposits," *Electrochim. Acta*, vol. 102, pp. 388–392, 2013.

[135] H. S. Jeon, S. Kunze, F. Scholten, and B. Roldan Cuenya, "Prism-shaped Cu nanocatalysts for electrochemical CO2 reduction to ethylene," *ACS Catal.*, p. acscatal.7b02959, 2017.

[136] T. T. H. Hoang, S. Ma, J. I. Gold, P. J. A. Kenis, and A. A. Gewirth, "Nanoporous Copper Films by Additive-Controlled Electrodeposition: CO2 Reduction Catalysis," *ACS Catal.*, vol. 7, pp. 3313–3321, 2017.

[137] Y. Peng, T. Wu, L. Sun, J. M. V. Nsanzimana, A. C. Fisher, and X. Wang, "Selective Electrochemical Reduction of CO2 to Ethylene on Nanopores Modified Copper Electrodes in Aqueous Solution," *ACS Appl. Mater. Interfaces*, vol. 9, no. 38, pp. 32782–32789, 2017.

[138] K. W. Frese, "Electrochemical Reduction of CO2 at Intentionally Oxidized Copper Electrodes," *J. Electrochem. Soc.*, vol. 138, no. 11, p. 3338, 1991.

[139] C. S. Le Duff, M. J. Lawrence, and P. Rodriguez, "Role of the adsorbed oxygen species in the selective electrochemical reduction of CO2 to alcohols and carbonyls on copper electrodes," *Angew. Chem. Int. Ed.*, vol. 56, no. 42, pp. 12919–12924, 2017.

[140] H. Mistry, F. Behafarid, R. Reske, A. S. Varela, P. Strasser, and B. Roldan Cuenya, "Tuning Catalytic Selectivity at the Mesoscale via Interparticle Interactions," *ACS Catal.*, vol. 6, no. 2, pp. 1075–1080, 2016.

[141] A. Eilert, F. Cavalca, F. S. Roberts, J. Osterwalder, C. Liu, M. Favaro, E. J. Crumlin, H. Ogasawara, D. Friebel, L. G. M. Pettersson, and A. Nilsson, "Subsurface Oxygen in Oxide-Derived Copper Electrocatalysts for Carbon Dioxide Reduction," *J. Phys. Chem. Lett.*, vol. 8, no. 1, pp. 285–290, 2017.

[142] F. Cavalca, R. Ferragut, S. Aghion, A. Eilert, O. Diaz-Morales, C. Liu, A. L. Koh, T. W. Hansen, L. G. M. Pettersson, and A. Nilsson, "Nature and Distribution of Stable Subsurface Oxygen in Copper Electrodes During Electrochemical CO2 Reduction," *J. Phys. Chem. C*, 2017.

[143] C. Liu, M. P. Lourenço, S. Hedström, F. Cavalca, O. Diaz-Morales, H. A. Duarte, A. Nilsson, and L. G. M. Pettersson, "Stability and Effects of Subsurface Oxygen in Oxide-Derived Cu Catalyst for CO2 Reduction," *J. Phys. Chem. C*, 2017.

[144] M. Favaro, H. Xiao, T. Cheng, W. A. Goddard III, J. Yano, and E. J. Crumlin, "Subsurface oxide plays a critical role in CO2 activation by Cu (111) surfaces to form chemisorbed CO2 , the first step in reduction of CO2," *Proc. Natl. Acad. Sci. U. S. A.*, vol. 114, no. 26, pp. 6706–6711, 2017.

[145] S. Lee, D. Kim, and J. Lee, "Electrocatalytic production of C3-C4 compounds by conversion of CO2 on a chloride-induced Bi-phasic

Cu2O-Cu catalyst," *Angew. Chem. Int. Ed.*, vol. 54, no. 49, pp. 14701–14705, 2015.

[146] Y. Terunuma, A. Saitoh, and Y. Momose, "Relationship between hydrocarbon production in the electrochemical reduction of CO2 and the characteristics of the Cu electrode," *J. Electroanal. Chem.*, vol. 434, no. 1-2, pp. 69–75, 1997.

[147] M. Le, M. Ren, Z. Zhang, P. T. Sprunger, R. L. Kurtz, and J. C. Flake, "Electrochemical Reduction of CO2 to CH3OH at Copper Oxide Surfaces," *J. Electrochem. Soc.*, vol. 158, no. 5, pp. E45–E49, 2011.

[148] I. Platzman, R. Brener, H. Haick, and R. Tannenbaum, "Oxidation of Polycrystalline Copper Thin Films at Ambient Conditions," *J. Phys. Chem. C*, vol. 112, no. 4, pp. 1101–1108, 2008.

[149] J. W. Lim, J. Iijima, Y. Zhu, J. H. Yoo, G. S. Choi, K. Mimura, and M. Isshiki, "Nanoscale investigation of long-term native oxidation of Cu films," *Thin Solid Films*, vol. 516, no. 12, pp. 4040–4046, 2008.

[150] Y. Lum and J. W. Ager, "Stability of residual oxides in oxide-derived Cu catalysts for electrochemical CO2 reduction investigated with 18O labeling," *Angew. Chem. Int. Ed.*, 2017.

[151] A. Garza, A. T. Bell, and M. Head-Gordon, "Is Subsurface Oxygen Necessary for the Electrochemical Reduction of CO2 on Copper?," *J. Phys. Chem. Lett.*, vol. 9, pp. 601–606, 2018.

[152] M. R. Singh, E. L. Clark, and A. T. Bell, "Effects of electrolyte, catalyst, and membrane composition and operating conditions on the performance of solar-driven electrochemical reduction of carbon dioxide," *Phys. Chem. Chem. Phys.*, vol. 17, no. 29, pp. 18924–18936, 2015.

[153] S. Ma, M. Sadakiyo, R. Luo, M. Heima, M. Yamauchi, and P. J. A. Kenis, "One-step electrosynthesis of ethylene and ethanol from CO2 in an alkaline electrolyzer," *J. Power Sources*, vol. 301, 2016.

[154] J. T. Feaster, C. Shi, E. R. Cave, T. Hatsukade, D. N. Abram, K. P. Kuhl, C. Hahn, J. K. Nørskov, and T. F. Jaramillo, "Understanding

Selectivity for the Electrochemical Reduction of Carbon Dioxide to Formic Acid and Carbon Monoxide on Sn Electrodes," *ACS Catal.*, vol. 7, pp. 4822–4827, 2016.

[155] Z. P. Jovanov, H. A. Hansen, A. S. Varela, P. Malacrida, A. A. Peterson, J. K. Nørskov, I. E. L. Stephens, and I. Chorkendorff, "Opportunities and challenges in the electrocatalysis of CO2 and CO reduction using bifunctional surfaces: A theoretical and experimental study of Au–Cd alloys," *J. Catal.*, vol. 343, pp. 215–231, 2016.

[156] Y. Chen, C. W. Li, and M. W. Kanan, "Aqueous CO2 reduction at very low overpotential on oxide-derived Au nanoparticles," *J. Am. Chem. Soc.*, vol. 134, no. 49, pp. 19969–19972, 2012.

[157] W. Zhu, R. Michalsky, Ö. Metin, H. Lv, S. Guo, C. J. Wright, X. Sun, A. A. Peterson, and S. Sun, "Monodisperse Au nanoparticles for selective electrocatalytic reduction of CO2 to CO.," *J. Am. Chem. Soc.*, vol. 135, pp. 16833–16836, nov 2013.

[158] E. R. Cave, J. H. Montoya, K. P. Kuhl, D. N. Abram, T. Hatsukade, C. Shi, C. Hahn, J. K. Nørskov, and T. F. Jaramillo, "Electrochemical CO2 reduction on Au surfaces: mechanistic aspects regarding the formation of major and minor products," *Phys. Chem. Chem. Phys*, vol. 19, no. 24, pp. 15856–15863, 2017.

[159] W. Zhu, Y.-J. Zhang, H. Zhang, H. Lv, Q. Li, R. Michalsky, A. A. Peterson, and S. Sun, "Active and Selective Conversion of CO2 to CO on Ultrathin Au Nanowires," *J. Am. Chem. Soc.*, vol. 136, pp. 16132–16135, 2014.

[160] H. Mistry, Y.-W. Choi, A. Bagger, F. Scholten, C. S. Bonifacio, I. Sinev, N. J. Divins, I. Zegkinoglou, H. S. Jeon, K. Kisslinger, E. A. Stach, J. C. Yang, J. Rossmeisl, and B. Roldan Cuenya, "Enhanced Carbon Dioxide Electroreduction to Carbon Monoxide over Defect-Rich Plasma-Activated Silver Catalysts," *Angew. Chem. Int. Ed.*, vol. 56, no. 38, pp. 11394–11398, 2017.

[161] A. S. Varela, N. Ranjbar Sahraie, J. Steinberg, W. Ju, H. S. Oh, and P. Strasser, "Metal-Doped Nitrogenated Carbon as an Efficient

Catalyst for Direct CO2 Electroreduction to CO and Hydrocarbons," *Angew. Chem. Int. Ed.*, vol. 54, no. 37, pp. 10758–10762, 2015.

[162] A. Bagger, W. Ju, A. S. Varela, P. Strasser, and J. Rossmeisl, "Single site porphyrine-like structures advantages over metals for selective electrochemical CO2reduction," *Catal. Today*, vol. 288, pp. 74–78, 2017.

[163] W. Ju, A. Bagger, G. P. Hao, A. S. Varela, I. Sinev, V. Bon, B. Roldan Cuenya, S. Kaskel, J. Rossmeisl, and P. Strasser, "Understanding activity and selectivity of metal-nitrogen-doped carbon catalysts for electrochemical reduction of CO2," *Nat. Commun.*, vol. 8, p. 944, 2017.

[164] K. J. P. Schouten, Y. Kwon, C. J. M. van der Ham, Z. Qin, and M. T. M. Koper, "A new mechanism for the selectivity to C1 and C2 species in the electrochemical reduction of carbon dioxide on copper electrodes," *Chem. Sci.*, vol. 2, no. 10, p. 1902, 2011.

[165] C. W. Li, J. Ciston, and M. W. Kanan, "Electroreduction of carbon monoxide to liquid fuel on oxide-derived nanocrystalline copper," *Nature*, vol. 508, pp. 504–507, apr 2014.

[166] D. Raciti, L. Cao, K. J. T. Livi, P. F. Rottmann, X. Tang, C. Li, Z. Hicks, K. H. Bowen, K. J. Hemker, T. Mueller, and C. Wang, "Low-Overpotential Electroreduction of Carbon Monoxide Using Copper Nanowires," *ACS Catal.*, 2017.

[167] X. Feng, K. Jiang, S. Fan, and M. W. Kanan, "A Direct Grain-Boundary-Activity Correlation for CO Electroreduction on Cu Nanoparticles," *ACS Cent. Sci.*, vol. 2, no. 3, pp. 169–174, 2016.

[168] R. G. Mariano, K. Mckelvey, H. S. White, and M. W. Kanan, "Selective increase in CO2 electroreduction activity at grain-boundary surface terminations," *Science*, vol. 358, no. 6367, pp. 1187–1192, 2017.

[169] X. Feng, K. Jiang, S. Fan, and M. W. Kanan, "Grain-Boundary-Dependent CO 2 Electroreduction Activity," *J. Am. Chem. Soc.*, vol. 137, no. 14, pp. 4606–4609, 2015.

[170] A. Verdaguer-Casadevall, C. W. Li, T. P. Johansson, S. B. Scott, J. T. McKeown, M. Kumar, I. E. L. Stephens, M. W. Kanan, and I. Chorkendorff, "Probing the active surface sites for CO reduction on oxide-derived copper electrocatalysts," *J. Am. Chem. Soc.*, vol. 137, no. 31, pp. 9808–9811, 2015.

[171] Metrohm Autolab B.V., "Basic overview of the working principle of a potentiostat/galvanostat (PGSTAT) – Electrochemical cell setup," 2011.

[172] A. J. Bard and L. R. Faulkner, *Electrochemical Methods: Fundamentals and Applications*. Wiley-VCH, 2nd ed., 2001.

[173] G. Yang, B. Wang, K. Tawfiq, H. Wei, S. Zhou, and G. Chen, "Electropolishing of surfaces: theory and applications," *Surf. Eng.*, vol. 33, no. 2, pp. 149–166, 2017.

[174] S. Van Gils, C. Le Pen, A. Hubin, H. Terryn, and E. Stijns, "Electropolishing of Copper in H3PO4," *J. Electrochem. Soc.*, vol. 154, no. 3, p. C175, 2007.

[175] Z. P. Jovanov, *Towards synthetic fuels via electrocatalysis*. Ph.d. thesis, Technical University of Denmark, 2014.

[176] P. Lobaccaro, M. R. Singh, E. L. Clark, Y. Kwon, A. T. Bell, and J. W. Ager, "Effects of temperature and gas-liquid mass transfer on the operation of small electrochemical cells for the quantitative evaluation of CO2 reduction electrocatalysts," *Phys. Chem. Chem. Phys.*, vol. 18, no. 38, pp. 26777–26785, 2016.

[177] R. Sander, "Compilation of Henry's Law Constants for Inorganic and Organic Species of Potential Importance in Environmental Chemistry," *Database*, 1999.

[178] O. M. Morgan and O. Maass, "An investigation of the equilibria existing in gas-water systems forming electrolytes," *Can. J. Res.*, vol. 5, no. 2, pp. 162–199, 1931.

[179] D.-Q. Zheng, T.-M. Guo, and H. Knapp, "Experimental and modeling studies on the solubility of CO2, CHC1F2, CHF3, C2H2F4 and

C2H4F2 in water and aqueous NaCl solutions under low pressures," *Fluid Phase Equilib.*, vol. 129, no. 1-2, pp. 197–209, 1997.

[180] R. W. Meadows and D. J. Spedding, "The solubility of very low concentrations of carbon monoxide in aqueous solution," *Tellus A*, vol. 26, no. 1-2, pp. 143–150, 1974.

[181] J. Servant, G. Kouadio, B. Cros, and R. Delmas, "Carboxylic monoacids in the air of mayombe forest (Congo): Role of the forest as a source or sink," *J. Atmos. Chem.*, vol. 12, no. 4, pp. 367–380, 1991.

[182] I. Khan, P. Brimblecombe, and S. L. Clegg, "Solubilities of pyruvic acid and the lower (C1-C6) carboxylic acids. Experimental determination of equilibrium vapour pressures above pure aqueous and salt solutions," *J. Atmos. Chem.*, vol. 22, no. 3, pp. 285–302, 1995.

[183] B. J. Johnson, E. A. Betterton, and D. Craig, "Henry's law coefficient of formic and acetic acids," *J. Atmos. Chem.*, vol. 24, no. 1, pp. 113–119, 1996.

[184] J. A. V. Butler, C. N. Ramchandani, and D. W. Thomson, "The solubility of non-electrolytes. Part I. The free energy of hydration of some aliphatic alcohols," *J. Chem. Soc.*, pp. 280–285, 1935.

[185] M. G. Burnett, "Determination of Partition Coefficients at Infinite Dilution by the Gas Chromatographic Analysis of the Vapor above Dilute Solutions.," *Anal. Chem.*, vol. 35, no. 11, pp. 1567–1570, 1963.

[186] J. Timmermans, *The Physico-Chemical Constants of Binary Systems in Concentrated Solutions, Vol. 4.* New York, NY: Interscience Publisher Inc., 1960.

[187] J. R. Snider and G. A. Dawson, "Tropospheric light alcohols, carbonyls, and acetonitrile: Concentrations in the southwestern United States and Henry's law data," *J. Geophys. Res.*, vol. 90, no. D2, pp. 3797–3805, 1985.

[188] E. A. Betterton and M. R. Hoffmann, "Henry's law constants of some environmentally important aldehydes," *Environ. Sci. Technol.*, vol. 22, no. 1, pp. 1415–1418, 1988.

[189] X. Zhou and K. Mopper, "Apparent Partition-Coefficients of 15 Carbonyl-Compounds between Air and Seawater and between Air and Fresh-Water - Implications for Air Sea Exchange," *Environ. Sci. Technol.*, vol. 24, no. 12, pp. 1864–1869file:///M:/Documents/Ph.D/Literature/Mend, 1990.

[190] J. A. V. Butler and C. N. Ramchandani, "The solubility of non-electrolytes. Part II. The influence of the polar group on the free energy of hydration of aliphatic compounds," *J. Chem. Soc.*, pp. 952–955, 1935.

[191] R. Bone, P. Cullis, and R. Wolfenden, "Solvent Effects on Equilibria of Addition of Nucleophiles to Acetaldehyde and the Hydrophilic Character of Diols," *J. Am. Chem. Soc.*, vol. 105, no. 5, pp. 1339–1343, 1983.

[192] R. G. Buttery, L. C. Ling, and D. G. Guadagni, "Food Volatiles: Volatilities of Aldehydes, Ketones. and Esters in Dilute Water Solution," *J. Agric. Food Chem.*, vol. 17, no. 2, pp. 385–389, 1969.

[193] H. J. Benkelberg, S. Hamm, and P. Warneck, "Henry's law coefficients for aqueous solutions of acetone, acetaldehyde and acetonitrile, and equilibrium constants for the addition compounds of acetone and acetaldehyde with bisulfite," *J. Atmos. Chem.*, vol. 20, no. 1, pp. 17–34, 1995.

[194] L. Rohrschneider, "Solvent characterization by gas-liquid partition coefficients of selected solutes," *Anal. Chem.*, vol. 45, no. 7, pp. 1241–1247, 1973.

[195] Y.-N. Lee and X. Zhou, "Method for the determination of some soluble atmospheric carbonyl compounds," *Environ. Sci. Technol.*, pp. 749–756, 1993.

[196] E. A. Betterton, "The partitioning of ketones between the gas and aqueous phases," *Atmos. Environ. Part A, Gen. Top.*, vol. 25, no. 8, pp. 1473–1477, 1991.

[197] A. G. Vitenberg, B. V. Ioffea, Z. S. Dimitrova, and I. L. Butaeva, "Determinatlon of gas-liquid means of gas chromatographic," *J. Chromatogr. A*, vol. 112, pp. 319–327, 1975.

[198] J. T. Hoff, D. Mackay, R. Gillham, and W. Y. Shiu, "Partitioning of organic chemicals at the air-water interface in environmental systems," *Environ. Sci. Technol.*, vol. 27, no. 10, pp. 2174–2180, 1993.

[199] G. J. Pierotti, C. H. Deal, and E. L. Derr, "Activity Coefficients and Molecular Structure," *Ind. Eng. Chem.*, vol. 51, no. 1, pp. 95–102, 1959.

[200] W. M. Meylan and P. H. Howard, "Bond contribution method for estimating Henry's law constants," *Environ. Toxicol. Chem.*, vol. 10, no. 10, pp. 1283–1293, 1991.

[201] USEPA, "Air and steam stripping of toxic pollutants. Tech. rep. EPA-68-03-002," tech. rep., Industrial Environmental Research Laboratory, Cincinnati, OH, USA, 1982.

[202] E. Bertheussen, A. Verdaguer-Casadevall, D. Ravasio, J. H. Montoya, D. B. Trimarco, C. Roy, S. Meier, J. Wendland, J. K. Nørskov, I. E. L. Stephens, and I. Chorkendorff, "Acetaldehyde as an Intermediate in the Electroreduction of Carbon Monoxide to Ethanol on Oxide-Derived Copper," *Angew. Chem. Int. Ed.*, vol. 55, no. 4, pp. 1450–1454, 2016.

[203] E. Bertheussen, Y. Abghoui, Z. P. Jovanov, A. S. Varela, I. E. L. Stephens, and I. Chorkendorff, "Quantification of Liquid Products from the Electroreduction of CO2 and CO using Static Headspace-Gas Chromatography and Nuclear Magnetic Resonance Spectroscopy," *Catal. Today*, vol. 288, pp. 54–62, 2017.

[204] J. H. Gross, *Mass Spectrometry.* Springer, 2017.

[205] M. Balci, *Basic 1H- and 13C-NMR Spectroscopy.* Elsevier, 2005.

[206] J. I. Goldstein, D. E. Newbury, J. R. Michael, N. W. M. Ritchie, J. H. J. Scott, and D. C. Joy, *Scanning Electron Microscopy and X-Ray Microanalysis.* New York: Springer, 2017.

[207] G. A. Somorjai, *Chemistry in two dimensions: surfaces.* Cornell University Press, 1981.

[208] B. L. Henke, E. M. Gullikson, and J. C. Davis, "X-ray interactions: Photoabsorption, scattering, transmission, and reflection at E = 50-30000 eV, Z = 1-92," 1993.

[209] E. Bertheussen, *Aspects of CO2 Reduction Electrocatalysis*. Master's thesis, Technical University of Denmark, 2014.

[210] A. Wuttig and Y. Surendranath, "Impurity Ion Complexation Enhances Carbon Dioxide Reduction Catalysis," *ACS Catal.*, vol. 5, no. 7, pp. 4479–4484, 2015.

[211] O. A. Baturina, Q. Lu, M. A. Padilla, L. Xin, W. Li, A. Serov, K. Artyushkova, P. Atanassov, F. Xu, A. Epshteyn, T. Brintlinger, M. Schuette, and G. E. Collins, "CO2 electroreduction to hydrocarbons on carbon-supported Cu nanoparticles," *ACS Catal.*, vol. 4, no. 10, pp. 3682–3695, 2014.

[212] R. Reske, H. Mistry, F. Behafarid, B. Roldan Cuenya, and P. Strasser, "Particle size effects in the catalytic electroreduction of CO2 on Cu nanoparticles," *J. Am. Chem. Soc.*, vol. 136, no. 19, pp. 6978–6986, 2014.

[213] M. Asadi, B. Kumar, A. Behranginia, B. A. Rosen, A. Baskin, N. Repnin, D. Pisasale, P. Phillips, W. Zhu, R. Haasch, R. F. Klie, P. Král, J. Abiade, and A. Salehi-Khojin, "Robust carbon dioxide reduction on molybdenum disulphide edges.," *Nat. Commun.*, vol. 5, p. 4470, jan 2014.

[214] Q. Kong, D. Kim, C. Liu, Y. Yu, Y. Su, Y. Li, and P. Yang, "Directed Assembly of Nanoparticle Catalysts on Nanowire Photoelectrodes for Photoelectrochemical CO 2 Reduction," *Nano Lett.*, vol. 16, no. 9, pp. 5675–5680, 2016.

[215] J. E. Pander, M. F. Baruch, and A. B. Bocarsly, "Probing the Mechanism of Aqueous CO2 Reduction on Post-Transition-Metal Electrodes using ATR-IR Spectroelectrochemistry," *ACS Catal.*, vol. 6, no. 11, pp. 7824–7833, 2016.

[216] Y. Lum, Y. Kwon, P. Lobaccaro, L. Chen, E. L. Clark, A. T. Bell, and J. W. Ager, "Trace Levels of Copper in Carbon Materials Show

Significant Electrochemical CO2 Reduction Activity," *ACS Catal.*, vol. 6, no. 1, pp. 202–209, 2016.

[217] A. Loiudice, P. Lobaccaro, E. A. Kamali, T. Thao, B. H. Huang, J. W. Ager, and R. Buonsanti, "Tailoring Copper Nanocrystals towards C2 Products in Electrochemical CO2 Reduction," *Angew. Chem. Int. Ed.*, vol. 55, no. 19, pp. 5789–5792, 2016.

[218] J. Hong, W. Zhang, J. Ren, and R. Xu, "Photocatalytic reduction of CO2: a brief review on product analysis and systematic methods," *Anal. Methods*, vol. 5, no. 5, pp. 1086–1097, 2013.

[219] S. Cannizzaro, "Ueber den der Benzoësäure entsprechenden Alkohol," *Justus Liebigs Ann. Chem.*, vol. 88, no. 1, pp. 129–130, 1853.

[220] T. A. Geissman, "The Cannizzaro Reaction," in *Org. React.*, ch. 3, pp. 94–113, Wiley-VCH, 2nd ed., 2011.

[221] Y. Y. Birdja and M. T. M. Koper, "The Importance of Cannizzaro-Type Reactions during Electrocatalytic Reduction of Carbon Dioxide," *J. Am. Chem. Soc.*, vol. 139, no. 5, pp. 2030–2034, 2017.

[222] M. P. Foster, C. A. McElroy, and C. D. Amero, "Solution NMR of large molecules and assemblies," *Biochemistry*, vol. 46, no. 2, pp. 331–340, 2007.

[223] M. Eckert, G. Fleischmann, R. Jira, H. M. Bolt, and K. Golka, "Acetaldehyde," *Ullman's Encycl. Ind. Chem.*, p. 191, 2006.

[224] E. Pérez Gallent, M. C. Figueiredo, F. Calle-Vallejo, and M. T. M. Koper, "Spectroscopic Observation of a Hydrogenated CO Dimer Intermediate During CO Reduction on Cu(100) Electrodes," *Angew. Chem. Int. Ed.*, vol. 56, no. 13, pp. 3621–3624, 2017.

[225] J. H. Montoya, C. Shi, K. Chan, and J. K. Nørskov, "Theoretical Insights into a CO Dimerization Mechanism in CO2 Electroreduction," *J. Phys. Chem. Lett.*, vol. 6, no. 11, pp. 2032–2037, 2015.

[226] F. Calle-Vallejo and M. T. M. Koper, "Theoretical considerations on the electroreduction of CO to C2 Species on Cu(100) electrodes," *Angew. Chem. Int. Ed.*, vol. 52, no. 28, pp. 7282–7285, 2013.

[227] I. Ledezma-Yanez, E. P. Gallent, M. T. M. Koper, and F. Calle-Vallejo, "Structure-sensitive electroreduction of acetaldehyde to ethanol on copper and its mechanistic implications for CO and CO2 reduction," *Catal. Today*, vol. 262, pp. 90–94, 2016.

[228] K. J. P. Schouten, Z. Qin, E. Pérez Gallent, and M. T. M. Koper, "Two pathways for the formation of ethylene in CO reduction on single-crystal copper electrodes," *J. Am. Chem. Soc.*, vol. 134, no. 24, pp. 9864–9867, 2012.

[229] E. Bertheussen, T. Vagn Hogg, Y. Abghoui, A. K. Engstfeld, I. Chorkendorff, and I. E. L. Stephens, "Electroreduction of CO on Polycrystalline Copper at Low Overpotentials." submitted, 2018.

[230] United States Environmental Protection Agency, "Propionaldehyde," 2000.

[231] R. Subbaraman, N. Danilovic, P. P. Lopes, D. Tripkovic, D. Strmcnik, V. R. Stamenkovic, and N. M. Markovic, "Origin of anomalous activities for electrocatalysts in alkaline electrolytes," *J. Phys. Chem. C*, vol. 116, no. 42, pp. 22231–22237, 2012.

[232] Y. Hori, H. Konishi, T. Futamura, A. Murata, O. Koga, H. Sakurai, and K. Oguma, "Deactivation of copper electrode in electrochemical reduction of CO2," *Electrochim. Acta*, vol. 50, no. 27, pp. 5354–5369, 2005.

[233] K. J. J. Mayrhofer, A. S. Crampton, G. K. H. Wiberg, and M. Arenz, "Analysis of the Impact of Individual Glass Constituents on Electrocatalysis on Pt Electrodes in Alkaline Solution," *J. Electrochem. Soc.*, vol. 155, no. 6, pp. P78–P81, 2008.

[234] K. J. J. Mayrhofer, G. K. H. Wiberg, and M. Arenz, "Impact of Glass Corrosion on the Electrocatalysis on Pt Electrodes in Alkaline Electrolyte," *J. Electrochem. Soc.*, vol. 155, no. 1, pp. P1–P5, 2008.

[235] V. S. Molchanov and N. E. Prikhidko, "Corrosion of Silicate Glasses By Alkaline Solutions," *Bull. Acad. Sci. USSR, Div. Chem. Sci.*, vol. 6, no. 10, pp. 1179–1184, 1957.

[236] M. Heinen, Z. Jusys, and R. J. Behm, "Ethanol, acetaldehyde and acetic acid adsorption/electrooxidation on a Pt thin film electrode: An in-situ ATR-IR spectroscopy flow-cell study," *J. Phys. Chem. C*, vol. 114, no. 21, pp. 9850–9864, 2010.

[237] Y. G. Kim, J. H. Baricuatro, A. Javier, J. M. Gregoire, and M. P. Soriaga, "The evolution of the polycrystalline copper surface, first to Cu(111) and then to Cu(100), at a fixed CO2RR potential: A study by operando EC-STM," *Langmuir*, vol. 30, no. 50, pp. 15053–15056, 2014.

[238] Y. G. Kim, A. Javier, J. H. Baricuatro, D. A. Torelli, K. D. Cummins, C. F. Tsang, J. C. Hemminger, and M. P. Soriaga, "Surface reconstruction of pure-Cu single-crystal electrodes under CO-reduction potentials in alkaline solutions: A study by seriatim ECSTM-DEMS," *J. Electroanal. Chem.*, vol. 780, pp. 290–295, 2016.

[239] Y. G. Kim, A. Javier, J. H. Baricuatro, and M. P. Soriaga, "Regulating the Product Distribution of CO Reduction by the Atomic-Level Structural Modification of the Cu Electrode Surface," *Electrocatalysis*, vol. 7, no. 5, pp. 391–399, 2016.

[240] A. Hopkinson, J. M. Bradley, X.-C. Guo, and D. A. King, "Nonlinear Island Growth Dynamics in Adsorbate-Induced Restructuring of Quasihexagonal Reconstructed Pt(100) by CO," *Phys. Rev. Lett.*, vol. 71, no. 10, pp. 1597–1600, 1993.

[241] H. J. Venvik, A. Borg, and C. Berg, "Formation of the CO-induced (3x1) surface structure on Co (1120) studied by STM," *Surf. Sci.*, vol. 397, pp. 322–332, 1998.

[242] R. Raval, S. Haq, M. A. Harrison, G. Blyholder, and D. A. King, "Molecular adsorbate-induced surface reconstruction: CO/Pd(110)," *Chem. Phys. Lett.*, vol. 167, no. 5, pp. 391–398, 1990.

[243] N. Kruse and A. Gaussmann, "CO-Induced Morphological Changes of Rh Crystallites: Mechanisms, Kinetics and Real-Space Imaging on the Atomic Scale," *J. Catal.*, vol. 144, no. 2, pp. 525–543, 1993.

[244] V. R. Stamenkovic, B. Fowler, B. S. Mun, G. Wang, P. N. Ross, C. A. Lucas, and N. M. Markovic, "Improved oxygen reduction activity on Pt3Ni (111) via increased surface site availability," *Science*, vol. 315, no. 5811, pp. 493–498, 2007.

[245] J. Suntivich, K. J. May, H. A. Gasteiger, J. B. Goodenough, and Y. Shao-Horn, "A Perovskite Oxide Optimized for Molecular Orbital Principles," *Science*, vol. 334, no. 6061, pp. 1383–1385, 2011.

[246] D. Strmcnik, M. Uchimura, C. Wang, R. Subbaraman, N. Danilovic, D. Van Der Vliet, A. P. Paulikas, V. R. Stamenkovic, and N. M. Markovic, "Improving the hydrogen oxidation reaction rate by promotion of hydroxyl adsorption," *Nat. Chem.*, vol. 5, no. 4, pp. 300–306, 2013.

[247] A. Grimaud, O. Diaz-Morales, B. Han, W. T. Hong, Y. L. Lee, L. Giordano, K. A. Stoerzinger, M. T. M. Koper, and Y. Shao-Horn, "Activating lattice oxygen redox reactions in metal oxides to catalyse oxygen evolution," *Nat. Chem.*, vol. 9, no. 5, pp. 457–465, 2017.

[248] J. Kibsgaard, Z. Chen, B. N. Reinecke, and T. F. Jaramillo, "Engineering the surface structure of MoS 2 to preferentially expose active edge sites for electrocatalysis," *Nat. Mater.*, vol. 11, no. 11, pp. 963–969, 2012.

[249] H. Matsushima, A. Taranovskyy, C. Haak, Y. Gründer, and O. M. Magnussen, "Reconstruction of Cu (100) Electrode Surfaces during Hydrogen Evolution," *J. Am. Chem. Soc.*, vol. 131, no. 30, pp. 10362–10363, 2009.

[250] S. B. Scott, "GitHub." https://github.com/ScottSoren, 2018.

Appendices

A

Materials

Here appendix, details are given for the important chemicals that have been used for measurements in this thesis.

MilliQ water from a Millipore MilliQ Integral purification system was used for all cleaning, rinsing, mixing of electrolyte and other processes requiring the use of water. 0.1 M KOH (potassium hydroxide hydrate, Merck Suprapur, $> 99.995\%$) was used as electrolyte for all measurements. Carbon monoxide (AGA, 99.95%) and argon (AGA, 99.999%) were used to sparge the electrolyte. Cu samples for all *ex-situ* measurements were cut from a 100×100 mm sheet (Alfa Aesar Supratronic, $> 99.9999\%$, 0.1 mm thickness) and attached to a Cu wire (Goodfellow, $> 99.999\%$, 0.5 mm diameter). Electropolishing was performed in 30% H_3PO_4 (Merck EMSURE, 85% diluted in MilliQ water). Nafion 117 (Fuel Cell Store) was used to separate the working electrode and counter electrode compartments. Standard solutions of methanol (Sigma-Aldrich CHROMASOLV, $> 99.9\%$), acetic acid (Sigma-Aldrich, $> 99.99\%$) acetaldehyde (Fluka, $> 99.5\%$, anhydrous), ethanol (Merck EMSURE, $> 99.9\%$), propionaldehyde (Sigma-Aldrich, $> 97\%$) and 1-propanol (Sigma-Aldrich CHROMASOLV, $> 99.9\%$) were used for preparation of standard solutions for calibration. Note that an additional acetaldehyde solution (Sigma-Aldrich, 40 wt. % in H_2O) was used for the experiments regarding acetaldehyde chemistry in chapter 4.

B

Detection limits of liquid products

In section 4.2, I presented calibration data for ethanol (EtOH), 1-propanol (1-PrOH), methanol (MeOH), acetate (AcO^--), acetaldehyde (MeCHO) and propionaldehyde (EtCHO), as measured by HS-GC and NMR spectroscopy. The aim was to benchmark the two techniques for liquid product analysis in alkaline electrolyte. An important metric for the performance of a technique is its detection limits. In figures B.1-B.5, I present the NMR spectra and HS-GC chromatograms that were used to estimate the detection limits of the various compounds.

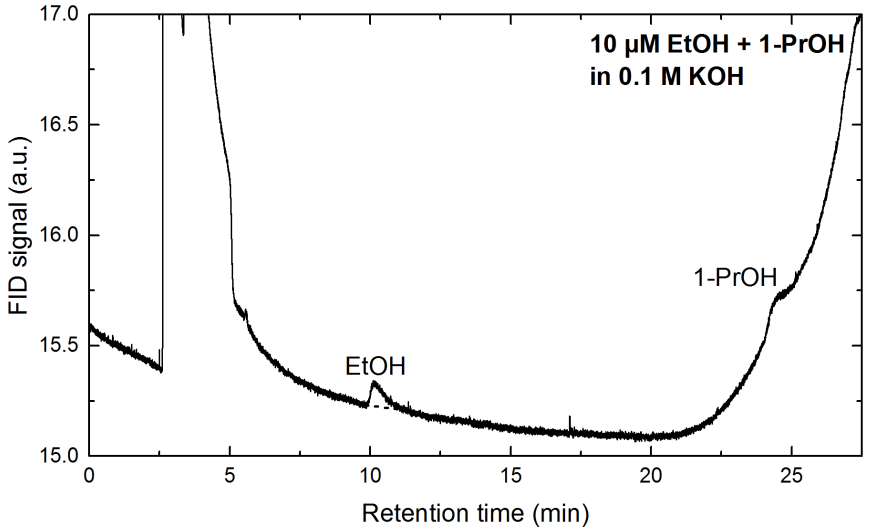

Figure B.1: HS-GC chromatogram of 10 µM ethanol (EtOH) and 1-propanol (1-PrOH) in 0.1 M KOH. This was used to estimate their approximate detection limits.

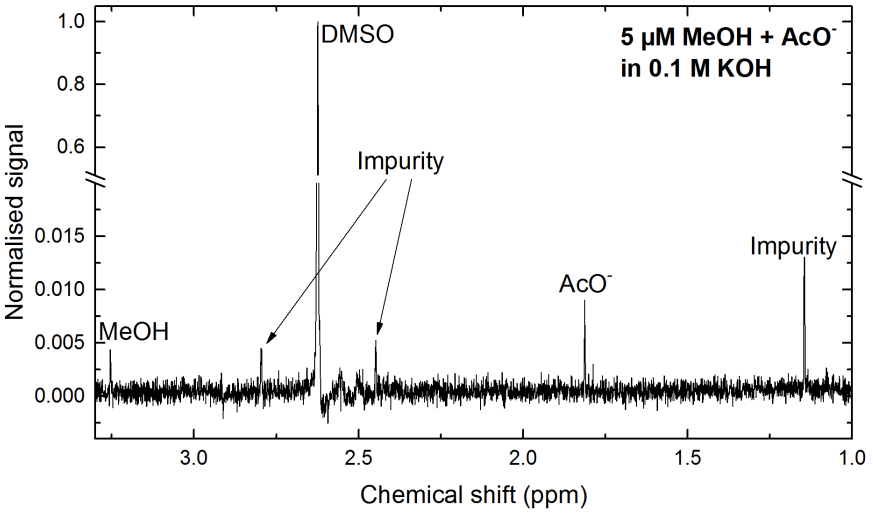

Figure B.2: NMR spectrum of 5 µM methanol (MeOH) and acetate (AcO^-) in 0.1 M KOH. This was used to estimate their approximate detection limits.

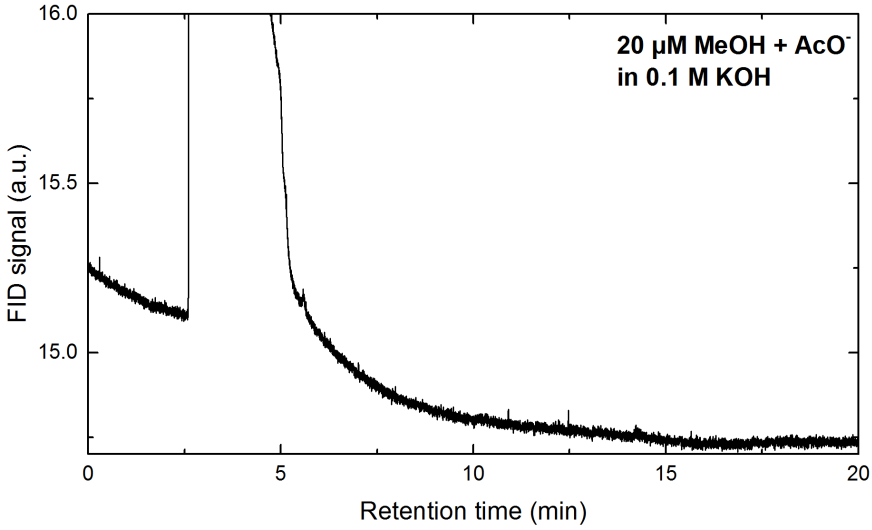

Figure B.3: HS-GC chromatogram of 20 µM methanol (MeOH) and acetate (AcO^-) in 0.1 M KOH. This was used to estimate the approximate detection limit of methanol.

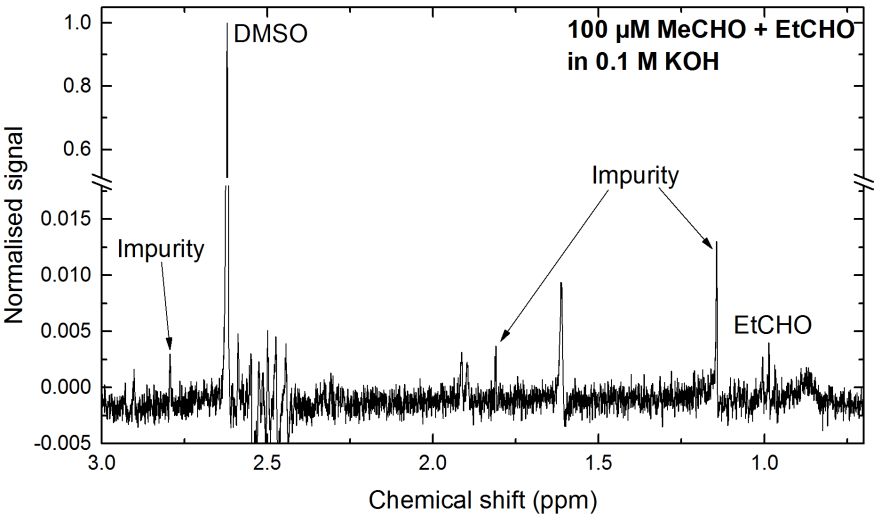

Figure B.4: NMR spectrum of 100 µM acetaldehyde (MeCHO) and propionaldehyde (EtCHO) in 0.1 M KOH. This was used to estimate the approximate detection limit of propionaldehyde.

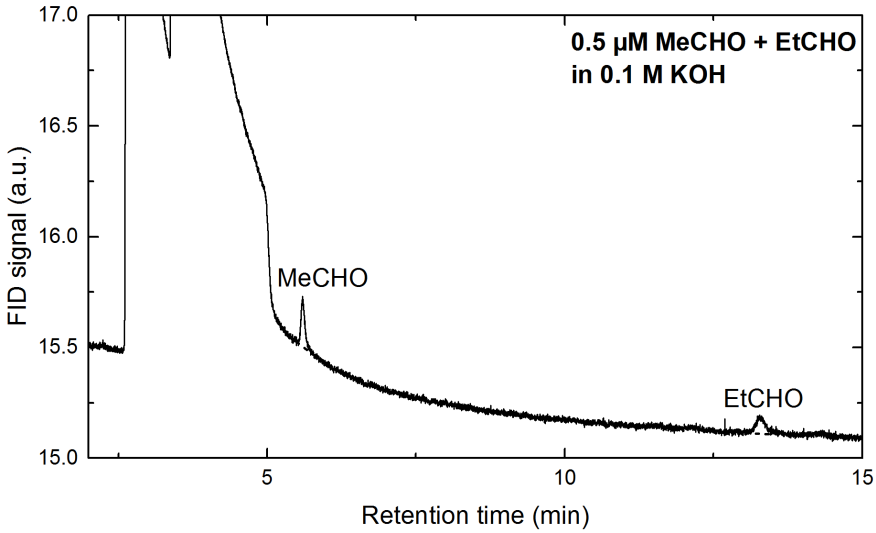

Figure B.5: HS-GC chromatogram of 0.5 µM acetaldehyde (MeCHO) and propionaldehyde (EtCHO) in 0.1 M KOH. This was used to estimate their approximate detection limits.

C

Operando GIXRD spectra

As discussed in chapter 7, we measured GIXRD spectra of polycrystalline Cu films at 0.0 V and -0.2 V in both Ar and CO atmosphere. Representative 2θ scans from such measurements are shown in Figure C.1. Note that the spectra are all measured at an incidence angle (α) of 0.15°. This is slightly below the critical angle of total reflection, and ensures a high degree of surface sensitivity. According to the attenuation length calculations shown in Figure 3.14 on page 74, this corresponds to a sampling depth of around 2.5 nm. At both 0.0 V and -0.2 V in Ar and CO, mainly metallic Cu peaks can be observed, when comparing to the calculated diffraction peaks listed in Table 7.1. A tiny peak is present at $2\theta = 15.8°$ in all the spectra. This does not fit with any of the expected Cu or Cu oxide peaks. There is a (200) reflection from $Cu(OH)_2$ that is expected at $2\theta = 16.0°$ from Bragg's law, which is the closest realistic peak. Alternatively, it could be a metallic contaminant that is strained because of its interaction with the Cu surface. The higher baseline observed for the Ar measurement in Figure C.1a compared to the CO sample is most likely because these spectra were measured on different samples. Slight differences in the X-ray beam calibriation relative to the sample could cause significant variations in signal.

We used the timescan approach in order to obtain better time resolution of these measurements. First, we followed the 2θ range between 15.8° and 20.8° during a linear potential sweep from OCV to 0 V to study the reduction of the oxide appearing while the electrode was being kept at OCV. The resulting GIXRD and electrochemistry data are shown in Figure C.2. Reduction of the oxide occurred at around -0.3 V, which was also the case

(a)

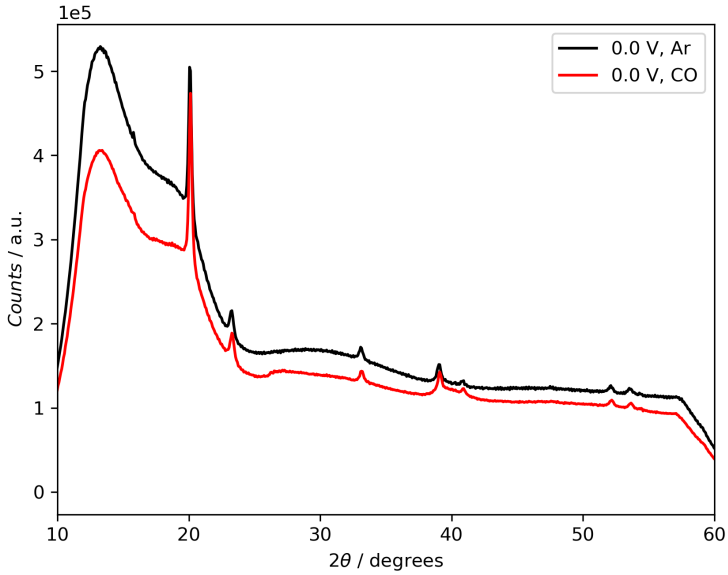

(b)

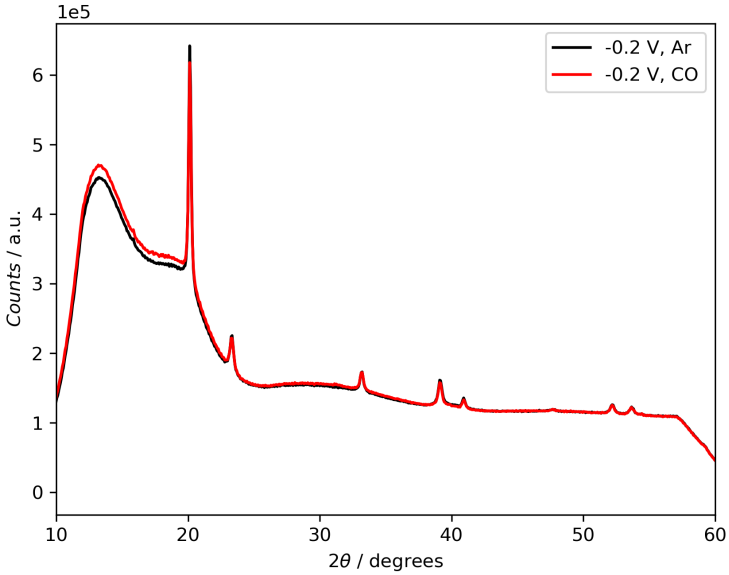

Figure C.1: GIXRD spectra of polycrystalline Cu measured at (a) 0.0 V and (b) -0.2 V in Ar and CO-saturated 0.1 M KOH. $\alpha = 0.15^{\circ}$.

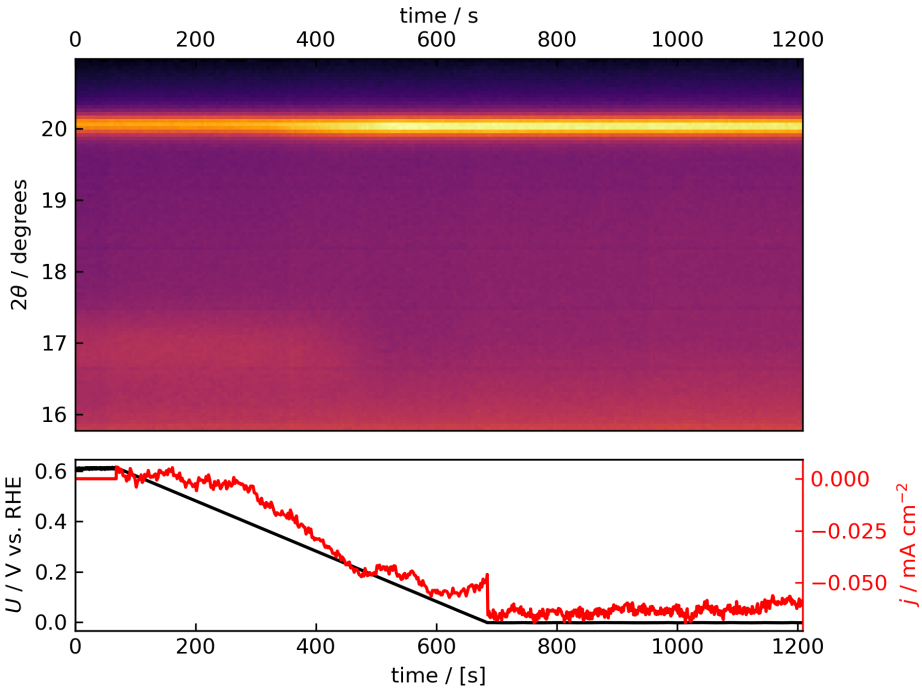

Figure C.2: Timescan during a linear potential sweep from OCV to 0.0 V at 1 mV s^{-1} scan rate for polycrystalline Cu in Ar-saturated 0.1 M KOH. $\alpha = 0.15°$. Top: X-ray data. Bottom: EC data.

in Ar, as discussed in chapter 7

For another sample we tried going more cathodic (to -0.2 V) to study whether applying cathodic potentials affect the structure of the electrodes. The resulting timescan is shown in Figure C.3. Note that this electrode was only kept briefly (< 30 minutes) at OCV before starting the timescan. As a result, no visible Cu oxide could be observed in this case. The sample underwent no significant changes in to the 2θ range between 15.8° and 20.8°. Note that only the (111) diffraction peak of metallic Cu is within this range. The reason for choosing this region of the 2θ spectrum was that both Cu oxide peaks and the peaks we attributed to Ni contamination would show up here. In hindsight, however, it would have been instructive to study the Cu(200) peak at 23.3° when studying whether any restructuring of the metallic Cu phase occurred. Still, significant restructuring would lead to a change in Cu(111) intensity, which we would be able to observe with the present measurements.

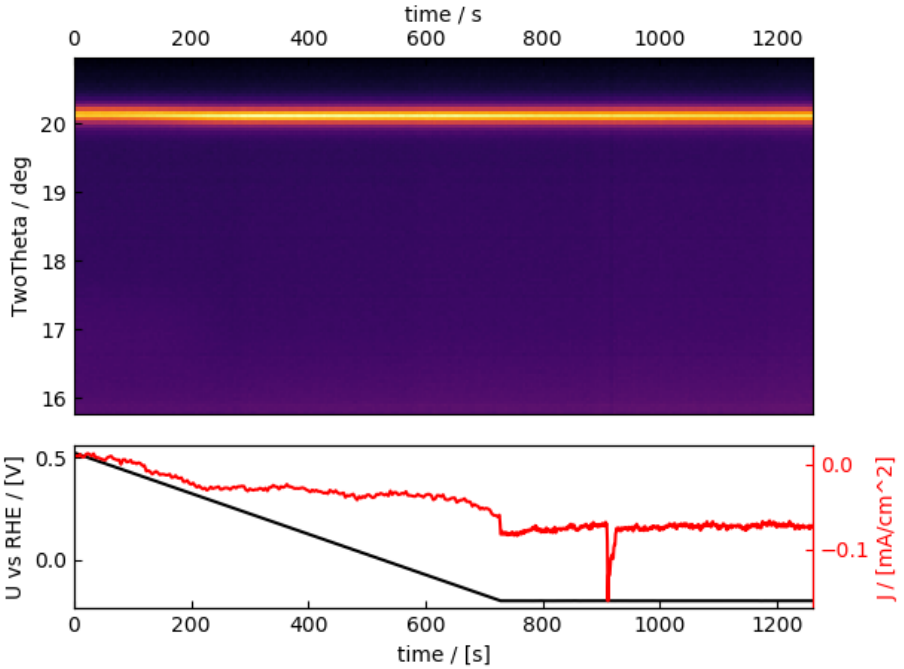

Figure C.3: Timescan during a linear potential sweep from OCV to -0.2 V at 1 mV s^{-1} scan rate for polycrystalline Cu in Ar-saturated 0.1 M KOH. $\alpha = 0.15°$. Top: X-ray data. Bottom: EC data.

It is also instructive to study whether introducing CO in the electrolyte induces changes in the surface structure of the Cu electrodes. As mentioned in the chapter 6, this has been shown for various other metallic electrocatalysts.[240–243] To study this, we decided to do a timescan of an electrode that was kept at -0.2 V while switching from Ar to CO sparge of the electrolyte. The resulting timescan is shown in Figure C.4. We started the timescan while the electrolyte was still saturated with Ar. Then we entered the beamline hutch to switch the gases, which resulted in the shutters blocking the beam, which is the reason that there was no signal between 80 s and 270 s. The CO purge was started at 300 s. A small dip in the current could be observed right at the time when we stopped the flow of Ar and started the flow of CO. This could be due to small amounts of O_2 entering the setup at this moment, which would lead to some current going to ORR. When studying the XRD, though, no changes can be observed at

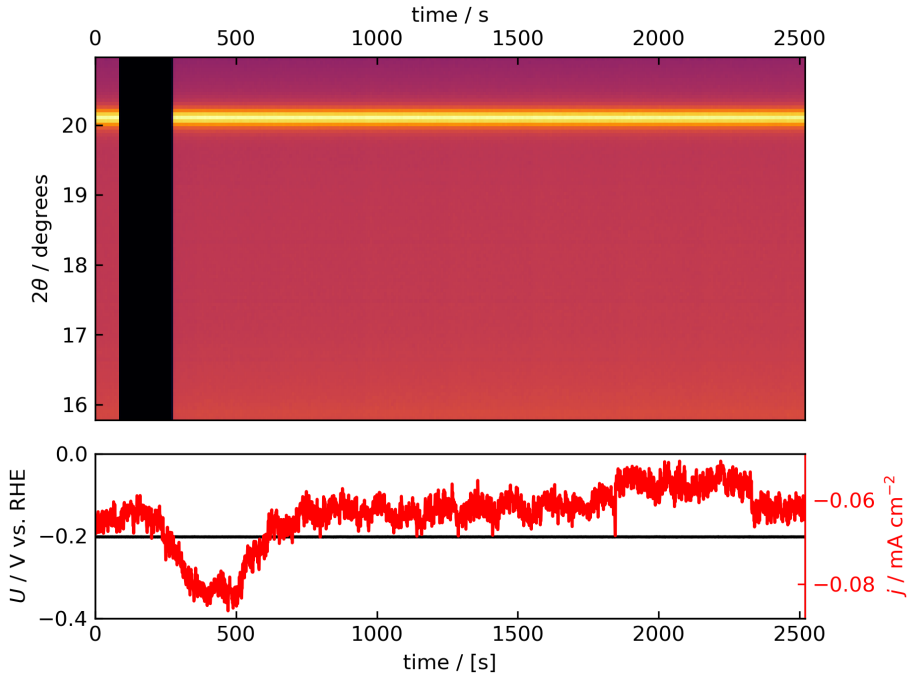

Figure C.4: Timescan during switch from Ar to CO sparge for polycrystalline Cu at -0.2 V vs. RHE in 0.1 M KOH. Top: X-ray data. $\alpha = 0.15^{\circ}$. Bottom: EC data.

all, over a period of ~2000 s/30 min from when the CO sparge was started. After approximately the same measurement duration, our Cu foils started deactivating during the measurements I discussed in the previous chapter. However, as discussed in the previous paragraph, only the Cu(111) peak is observable in this 2θ region. In future studies, a slightly different detector position should be applied, so that the Cu(200) peak can be studied as well.

Appended articles

Paper I

Acetaldehyde as an intermediate in the electroreduction of carbon monoxide on oxide-derived copper

Erlend Bertheussen, Arnau Verdaguer-Casadevall, Davide Ravasio, Joseph H. Montoya, Daniel B. Trimarco, Claudie Roy, Sebastian Meier, Jürgen Wendland, Jens K. Nørskov, Ifan E.L. Stephens, Ib Chorkendorff.

Angewandte Chemie International Edition, 2016, volume **55**, pages 1450-1454.

Electrochemistry

International Edition: DOI: 10.1002/anie.201508851
German Edition: DOI: 10.1002/ange.201508851

Acetaldehyde as an Intermediate in the Electroreduction of Carbon Monoxide to Ethanol on Oxide-Derived Copper

Erlend Bertheussen, Arnau Verdaguer-Casadevall, Davide Ravasio, Joseph H. Montoya, Daniel B. Trimarco, Claudie Roy, Sebastian Meier, Jürgen Wendland, Jens K. Nørskov, Ifan E. L. Stephens, and Ib Chorkendorff**

Abstract: *Oxide-derived copper (OD-Cu) electrodes exhibit unprecedented CO reduction performance towards liquid fuels, producing ethanol and acetate with >50% Faradaic efficiency at −0.3 V (vs. RHE). By using static headspace-gas chromatography for liquid phase analysis, we identify acetaldehyde as a minor product and key intermediate in the electroreduction of CO to ethanol on OD-Cu electrodes. Acetaldehyde is produced with a Faradaic efficiency of ≈5% at −0.33 V (vs. RHE). We show that acetaldehyde forms at low steady-state concentrations, and that free acetaldehyde is difficult to detect in alkaline solutions using NMR spectroscopy, requiring alternative methods for detection and quantification. Our results represent an important step towards understanding the CO reduction mechanism on OD-Cu electrodes.*

Utilization of CO_2 as a feedstock for producing fuels and commodity chemicals is a highly promising technology for reducing the anthropogenic carbon footprint. Capture of CO_2 from point sources or ambient air, followed by reduction, gives an opportunity to close the carbon cycle.[1] Electrochemical technology provides a means of achieving this, as electrochemical devices can operate at ambient conditions, with minimal capital investment, and with fast start–stop cycles enabling coupling to intermittent energy sources. To date, implementation of this technology is hindered by a lack of electrocatalysts capable of converting CO_2 into energy-rich products in an efficient and selective manner. Copper is the only pure metal that is active for CO_2 reduction towards hydrocarbons and alcohols.[2] However, high overpotentials are needed and a variety of products are formed. Measurements on planar extended surfaces of Cu electrodes showed that potentials of −1 V (vs. RHE), or overpotentials, $\eta > \approx 1.0$ V, are needed to produce significant amounts of C2 products, that is, above 5% Faradaic efficiency with a current density of 1 mA cm^{-2} or higher.[2–6]

A viable route forward is to split the reaction into two sequences; reducing CO_2 to CO at first, and then reducing CO to the desired product in a second step. Since CO is a key intermediate in the reduction of CO_2 to alcohols and hydrocarbons, CO reduction can be used as a proxy for understanding trends in CO_2 reduction.[2,4] Several catalysts have been reported to reduce CO_2 to CO efficiently and selectively,[7–11] but the second step remains a challenge owing to multi-electron transfer involving several reaction intermediates.[12] This calls for development of new catalysts with improved energy efficiency and selectivity for CO reduction towards valuable compounds. Kanan and co-workers recently achieved a breakthrough in this area; they showed that oxidation and subsequent reduction of polycrystalline copper yields a high surface area metallic copper electrode with unprecedented CO electroreduction performance.[13,14] Oxide-derived copper (OD-Cu) has a Faradaic efficiency towards ethanol as high as 43% at −0.3 V, $\eta \approx 500$ mV ($U^0_{CO/CH3CH2OH} = 0.18$ V), and a total Faradaic efficiency towards CO reduction products of 57%, with a total geometric current density of ≈0.3 mA cm^{-2}.

The underlying reasons for the high performance of OD-Cu electrodes remain unknown. Our own temperature programmed desorption (TPD) experiments show that the activity correlates with the presence of strong binding sites, which in turn correlates with the presence of grain boundaries.[15] Importantly, the mechanism for ethanol production

[*] E. Bertheussen, Dr. A. Verdaguer-Casadevall, D. B. Trimarco, C. Roy, Prof. Dr. I. E. L. Stephens, Prof. Dr. I. Chorkendorff
Department of Physics, Technical University of Denmark
2800 Kgs. Lyngby (Denmark)
E-mail: ifan@fysik.dtu.dk
ibchork@fysik.dtu.dk

Dr. D. Ravasio, Prof. Dr. J. Wendland
Carlsberg Laboratory
Gamle Carlsberg vej 4, 1799 København V (Denmark)

Dr. J. H. Montoya
SUNCAT Center for Catalysis and Interface Science
Department of Chemical Engineering, Stanford University
443 Via Ortega, Stanford, CA 94305 (USA)

Dr. S. Meier
Department of Chemistry, Technical University of Denmark
2800 Kongens Lyngby (Denmark)

Prof. Dr. J. K. Nørskov
SUNCAT Center for Catalysis and Interface Science
SLAC National Accelerator Laboratory
2675 Sand Hill Road, Menlo Park, CA 94025 (USA)

Prof. Dr. I. E. L. Stephens
Department of Mechanical Engineering
Massachusetts Institute of Technology (MIT)
77 Massachusetts Avenue, Cambridge, MA 02319 (USA)

Supporting information and ORCID(s) from the author(s) for this article are available on the WWW under http://dx.doi.org/10.1002/anie.201508851.

has not been determined yet. In this work, we reveal the role of acetaldehyde as a likely reaction intermediate and product of CO reduction on OD-Cu electrodes.

Oxide-derived Cu electrodes were produced following the procedure outlined by Li et al. (Supporting Information, section S.1).[14] The resulting electrodes had a roughness factor of 87 ± 10 (section S.2). Electrochemical CO reduction was carried out in CO-saturated 0.1 M KOH electrolyte. We used three approaches to analyze the reaction products. The gas phase composition over the electrolyte was measured by gas chromatography (GC). The liquid phase products were analyzed by extracting liquid samples and using a combination of nuclear magnetic resonance (NMR) spectroscopy and static headspace gas chromatography (HS-GC), the latter coupled with either a flame ionization detector (FID) or a mass spectrometer (MS). Figure 1 a shows the Faradaic

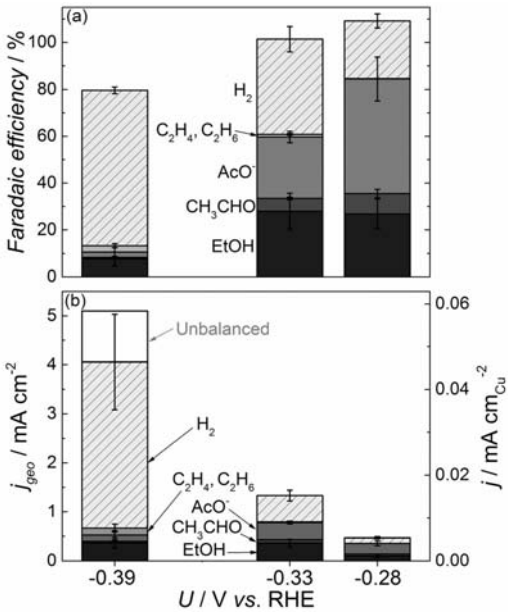

Figure 1. CO reduction on oxide-derived Cu electrodes. (a) Faradaic efficiency and (b) current density normalized to geometric and specific surface area for the individual products. Measurements were carried out in CO saturated (1.1 bar) 0.1 M KOH. Note: The unbalanced contribution to the current is only added at −0.39 V, since the total Faradaic efficiency at the other two potentials are ≈100% within the experimental error. The data are based on at least three independent measurements for each potential. At −0.28 V, electrolysis was carried out until the accumulated charge reached ≈5 C, and at −0.33 and −0.39 V until ≈10 C.

efficiency for CO reduction on oxide-derived Cu electrodes. Results resemble those reported by Kanan and co-workers.[14] At −0.33 V (vs. RHE; unless otherwise stated, all potentials in this work are given against the RHE scale), the current efficiency to ethanol and acetate is 25% for each, and 1% of the charge results in ethylene and ethane. Our observation that C_2H_4 and C_2H_6 is formed on OD-Cu is consistent with earlier works.[14,16] The parasitic evolution of hydrogen accounts for the remaining ≈40%. Interestingly, we observed that acetaldehyde, which is previously unreported on OD-Cu, is produced with a current efficiency of 5% at −0.33 V, or $\eta \approx 400$ mV ($U^0_{CO/CH3CHO} = 0.10$ V). The fact that we can only observe C2 products corresponds well with the previous observations that such products are favored on Cu-based electrodes at low overpotentials under alkaline conditions.[14,17] The total Faradaic efficiency at −0.28 and −0.33 V comes, within the experimental error, to ≈100%; we attribute the error to uncertainties in the calibration as well as minor leaks. At −0.39 V, ≈20% of the charge is not accounted for; this is likely to be caused by the high current density towards hydrogen evolution, where some of the H_2 escapes the cell. Figure 1 b shows the partial current densities to the various products, normalized to the geometrical and specific electrode surface area. The overall current densities are two to three times higher than those reported by Li et al. at all potentials.[14] This discrepancy could be caused by differences in mass transport, which is a function of the cell design. Alternatively, the greater capacitance observed for the electrodes produced in the current study could indicate that they have a higher surface area (section S.2).

Earlier studies on extended surfaces of Cu have suggested that acetylaldehyde is an intermediate for ethanol production from CO_2 or CO reduction;[3,18] Hori et al. reported that on polycrystalline Cu, acetaldehyde is formed from CO at potentials negative of −0.83 V RHE, albeit with a low selectivity of 0.5%. They also showed that acetaldehyde can be reduced to ethanol,[16] suggesting it is a soluble intermediate in the reaction (incidentally acetaldehyde is a key intermediate in ethanol oxidation, the reverse reaction[19]).

To investigate the possibility that acetaldehyde is an intermediate during CO reduction on OD-Cu, we tested its hydrogenation by introducing 10 mM CH_3CHO in Ar-saturated 0.1 M KOH. As shown in Figure 2, ethanol is produced

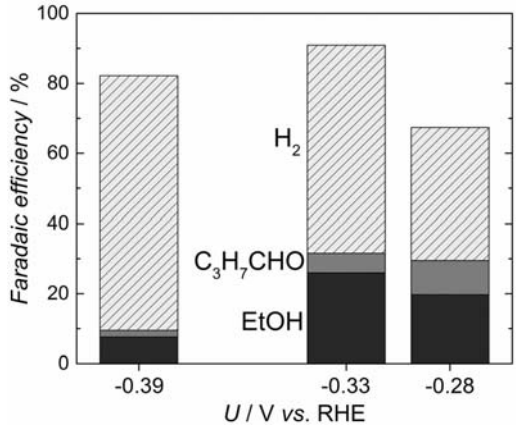

Figure 2. Faradaic efficiency for CH_3CHO hydrogenation at different potentials. Measurements were carried out in Ar saturated (1.1 bar) 0.1 M KOH with 10 mM of acetaldehyde. Note: The charge not accounted for is attributed to higher carbon oxygenates that have not been quantified.

with a Faradaic efficiency of ≈30% at −0.33 V. Significant production of C_3H_7CHO also occurred. We did not observe this compound during our CO reduction experiments, possibly because of the lower acetaldehyde concentrations. However, we cannot discard the possibility that C_3H_7CHO is produced in concentrations below the detection limit from CO reduction. For lower added concentrations of acetaldehyde, much less ethanol and butanal were produced, possibly because of poorer mass transport of acetaldehyde to the electrode. This makes measurements at the concentrations observed for CO reduction (≈120 μM) difficult. Interestingly, performing the same experiment with acetate did not yield any detectable CO reduction products; this suggests that acetate cannot be reduced further when it is formed at the electrode. Figure 3 shows the concentration of acetaldehyde and ethanol from CO reduction at −0.33 V as a function of total electrolysis charge. Whereas ethanol concentration scales linearly with charge, the acetaldehyde concentration quickly saturates at ≈120 μM. We hypothesize that this is caused by the formation of aqueous acetaldehyde and its further reduction to ethanol reaching equilibrium.

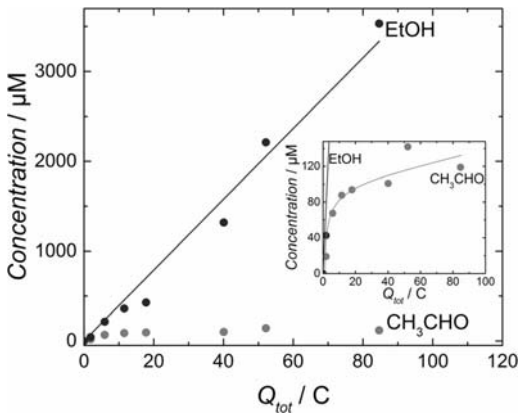

Figure 3. Acetaldehyde and ethanol concentration from CO reduction at −0.33 V showed as a function of the charge involved in each measurement. Measurements were carried out in 0.1 M KOH.

In Figure 4, we provide the results of density functional theory (DFT) calculations of intermediates proceeding from adsorbed *OCCHO, a likely intermediate in the C–C coupling pathway.[17,20] The most favorable thermodynamic pathway towards ethanol on Cu(211), highlighted in black proceeds directly through this intermediate. Using other copper facets could alter the reactivity of the surface, but is unlikely to change the overall shape of the reaction pathway.[12] Aqueous acetaldehyde can be seen as an intermediate, as previously reported.[21] The step following the formation of CH_3CHO, a proton-coupled electron transfer producing adsorbed $*OCH_2CH_3$, is uphill at 0.0 V vs. RHE. However, it is downhill at −0.3 V, and will be even more exergonic with increasing concentrations of CH_3CHO. The lower free energy found for aqueous acetaldehyde compared to its adsorbed counterpart (≈0.7 eV) yields a thermodynamic sink, supporting the experimental observation that it is released from the electrode and is present in the electrolyte in detectable concentrations.

Typically, NMR spectroscopy is used for detection of liquid products.[3,14,22] Liquid state NMR spectroscopy requires analytes to be dissolved in a liquid phase for adequate detection. Alternative techniques can overcome this limitation. For instance, HS-GC heats up the liquid samples, in this case to 70 °C, and relies on the volatility of compounds for identification.[22] This is particularly useful for products that evaporate readily, or that decompose into such compounds upon heating. Acetaldehyde has a boiling point of

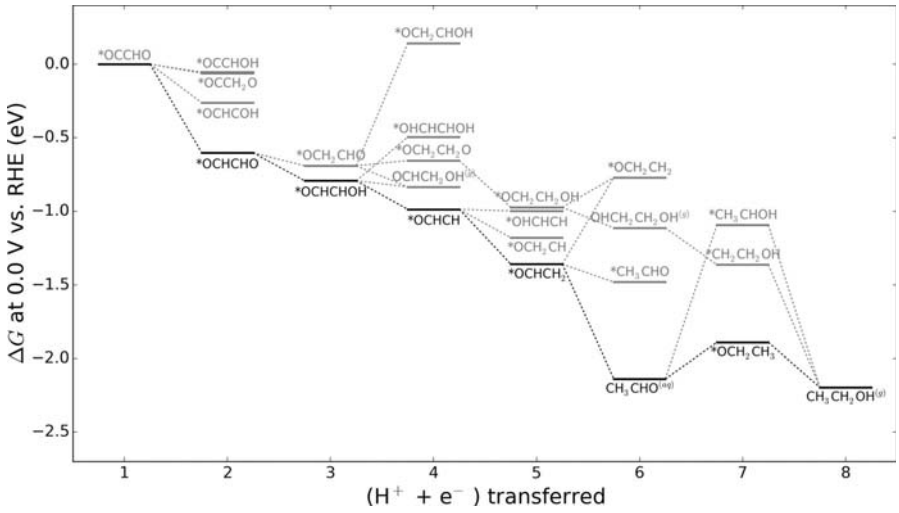

Figure 4. Free energy diagram for reduction of C–C coupled intermediate *OCCHO on Cu(211). The free energy for $CH_3CH_2OH^{(g)}$ was calculated at 1 bar and the free energy of $CH_3CHO^{(aq)}$ was calculated at a concentration of 100 μM. The steps marked with black represent the thermodynamically most favorable pathway. The gray represent other potential intermediates of higher energy.

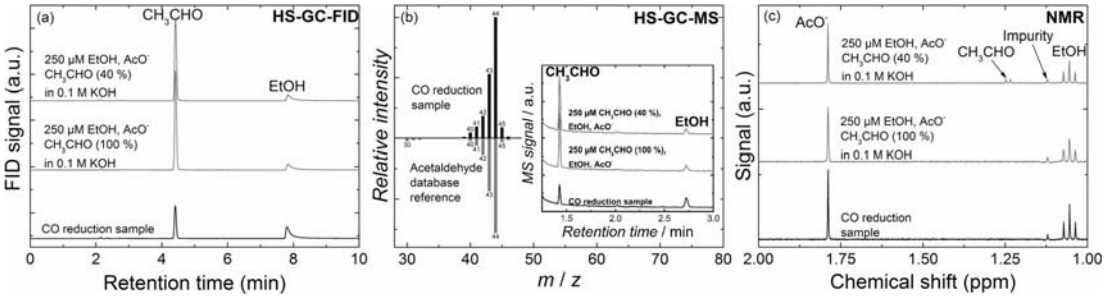

Figure 5. Liquid product analysis for a representative CO reduction sample from electrolysis at −0.33 V (black) as well as two solutions containing 250 µM CH_3CHO, EtOH and AcO^- in 0.1 M KOH (gray), one made from a 40%, and the other from a 100% acetaldehyde precursor. (a) HS-GC-FID chromatograms. (b) HS-GC-MS mass spectrum obtained from the acetaldehyde peak (at ≈1.5 min) of a CO reduction measurement, compared to a database reference mass spectrum for acetaldehyde. Inset: HS-GC-MS chromatograms (c) NMR spectra.

20.9 °C under standard conditions.[23] However, no trace of acetaldehyde was observed in the gas phase, which might be due to deviations from standard conditions and low concentrations. In Figure 5, a typical sample from CO reduction at −0.33 V is compared with two different solutions containing the same liquid products as the sample, analyzed with HS-GC-FID, HS-GC-MS, and NMR spectroscopy. For the two GC techniques, acetaldehyde can be clearly identified, both for the sample and the two prepared solutions. HS-GC-MS enables positive identification of acetaldehyde at mass 44. In contrast, acetaldehyde only appears in NMR through its diol form in the solution made from 40% acetaldehyde, observed as a doublet at ≈1.25 ppm. Neither the solution made from a 100% acetaldehyde precursor, nor the CO reduction sample shows any major signals that could be attributed to this compound, implying that routine NMR spectroscopy is not a reliable technique to identify acetaldehyde under basic conditions.

The organic chemistry of acetaldehyde, particularly in alkaline solutions, is complex.[24] Acetaldehyde occurs in various hydrated, aggregated, and polymerized states in solution (see section S.3 for further discussion). We hypothesize that the main difficulty in detecting acetaldehyde with NMR spectroscopy is polymerization, possibly caused by a high local concentration at the electrode. This could yield insoluble compounds invisible to NMR and/or significant signal broadening. Three key observations support this hypothesis: a) For concentrated solutions in alkaline media, a yellow precipitate can be observed (Supporting Information, Figure S.6 b), which could be attributed to an aggregated or polymerized form. b) Acetaldehyde standards aged in 0.1 M KOH and extensive NMR signal accumulation in high-field NMR yield spectra consistent with the presence of acetaldehyde and its condensation products formed upon aging (Figure S.5). Since acetaldehyde occurs as a minor steady-state intermediate (Figure 3), the detection of acetaldehyde by more routine NMR methods, on the other hand, remains difficult. c) Upon acidification of the 0.1 M KOH solution from pH 13 to pH 1, visible but broadened signals appear in the NMR spectra (Figure S.6 a). We attribute their presence to ethyl acetate, an acetaldehyde dimer, which could result from an acid-catalyzed depolymerization process. Acetaldehyde chemistry is discussed further in section S.3, but is beyond the scope of this study.

The appearance of an additional product should, in principle, be observable through the Faradaic efficiency not reaching 100%. However, the uncertainty in the analysis techniques could lead to minor products being overlooked.

In summary, we present evidence that acetaldehyde is a product and key intermediate in the electroreduction of carbon monoxide on oxide-derived copper. Detection of acetaldehyde in alkaline solutions using NMR spectroscopy is challenging, and thus, identification is performed using HS-GC. Our results highlight the importance of using complementary methods for product detection from electrochemical reactions. Identification of acetaldehyde represents a first step in elucidating the CO reduction mechanism on OD-Cu electrodes and paves the way for the design of improved catalysts.

Experimental Section

Rectangular electrodes of 5 × 10 mm were cut and electropolished. They were annealed in air at 500 °C for an hour and cooled to room temperature, before being mounted in the electrochemical cell where the Cu_2O surface layer was reduced chronopotentiometrically at 7 mA cm^{-2}. Electrode capacitance measured by cyclic voltammetry was used to determine the roughness of the electrodes.

The working electrode (WE) and counter electrode (CE) compartments were separated by a Nafion 117 membrane and the WE and reference electrode (RE) compartments were separated by an ion-conducting ceramic frit. A gold mesh was used as CE, while an $Hg/HgSO_4$ electrode was used as reference, calibrated to the reversible hydrogen electrode (RHE) in the same electrolyte. CO reduction was carried out potentiostatically at the desired potential. 85% of the uncompensated ohmic drop was corrected for in the software, as measured through electrochemical impedance spectroscopy.[25] If significant, the remaining 15% was corrected for after the experiment. The ohmic drop typically ranged from 20 to 50 Ω, depending on the WE position relative to the RE.

During measurements, CO reduction products accumulate in the electrolyte and headspace of the WE compartment. The gaseous product composition was analyzed by a GC mounted with a flame ionization detector (FID) and a thermal conductivity detector (TCD).

Liquid products were analyzed through HS-GC and NMR spectroscopy.

DFT calculations were performed on a $4\times3\times3$-atom periodic computational cell corresponding to the (211) facet of fcc Cu, with a 4-atom long step edge. The (211) facet was chosen based on the presence of step edge, four-fold, and three-fold terrace sites that may occur on OD-Cu. Electronic energies were determined with the Dacapo DFT calculator as implemented in the open-source Atomic Simulation Environment (ASE),[26] and the revised Perdew–Burke–Ernzerhof (RPBE) exchange correlation functional was chosen for its relative accuracy in describing chemisorption energies.[27] The geometries of multiple configurations of each adsorbate corresponding to placement on each available binding site were optimized into local energy minima, and the most stable configuration selected for the energies presented with a free energy correction corresponding to vibrational contributions determined in the harmonic approximation. Static solvation corrections based on the presence of aldehyde and hydroxyl groups on adsorbates similar to previous work[12,28] are also included.

More details can be found in the Supporting Information.

Acknowledgements

We acknowledge funding from Danish Council for Strategic Research's NACORR project. I.E.L. Stephens is the recipient of the Peabody Visiting Associate Professorship from the Department of Mechanical Engineering at MIT. We also acknowledge the assistance of Casper Hoeck and Charlotte H. Gotfredsen in setting up and carrying out NMR spectroscopy measurements, as well as Zarko Jovanov and Ana Sofia Varela in setting up the HS-GC equipment.

Keywords: analytical chemistry · catalysis · electrochemistry · energy conversion · materials science

How to cite: *Angew. Chem. Int. Ed.* **2016**, *55*, 1450–1454
Angew. Chem. **2016**, *128*, 1472–1476

[1] A. Goeppert, M. Czaun, J. P. Jones, G. K. Surya Prakash, G. A. Olah, *Chem. Soc. Rev.* **2014**, *43*, 7995–8048.
[2] Y. Hori, in *Mod. Asp. Electrochem.* (Eds.: C. G. Vayenas, R. E. White, M. E. Gamboa-Aldeco), Springer, Berlin, **2008**, pp. 89–189.
[3] K. P. Kuhl, E. R. Cave, D. N. Abram, T. F. Jaramillo, *Energy Environ. Sci.* **2012**, *5*, 7050–7059.
[4] K. J. P. Schouten, Y. Kwon, C. J. M. van der Ham, Z. Qin, M. T. M. Koper, *Chem. Sci.* **2011**, *2*, 1902–1909.
[5] A. Wuttig, Y. Surendranath, *ACS Catal.* **2015**, *5*, 4479–4484.
[6] W. Tang, A. A. Peterson, A. S. Varela, Z. P. Jovanov, L. Bech, W. J. Durand, S. Dahl, J. K. Nørskov, I. Chorkendorff, *Phys. Chem. Chem. Phys.* **2012**, *14*, 76–81.
[7] Y. Chen, C. W. Li, M. W. Kanan, *J. Am. Chem. Soc.* **2012**, *134*, 19969–19972.
[8] J. Medina-Ramos, J. L. Dimeglio, J. Rosenthal, *J. Am. Chem. Soc.* **2014**, *136*, 8361–8367.
[9] W. Zhu, Y. J. Zhang, H. Zhang, H. Lv, Q. Li, R. Michalsky, A. A. Peterson, S. Sun, *J. Am. Chem. Soc.* **2014**, *136*, 16132–16135.
[10] M. Asadi, B. Kumar, A. Behranginia, B. A. Rosen, A. Baskin, N. Repnin, D. Pisasale, P. Phillips, W. Zhu, R. Haasch, et al., *Nat. Commun.* **2014**, *5*, 4470.
[11] A. S. Varela, N. R. Sahraie, J. Steinberg, W. Ju, H. S. Oh, P. Strasser, *Angew. Chem. Int. Ed.* **2015**, *54*, 10758–10762; *Angew. Chem.* **2015**, *127*, 10908–10912.
[12] A. A. Peterson, J. K. Nørskov, *J. Phys. Chem. Lett.* **2012**, *3*, 251–258.
[13] C. W. Li, M. W. Kanan, *J. Am. Chem. Soc.* **2012**, *134*, 7231–7234.
[14] C. W. Li, J. Ciston, M. W. Kanan, *Nature* **2014**, *508*, 504–507.
[15] A. Verdaguer-Casadevall, C. W. Li, T. P. Johansson, S. B. Scott, J. T. McKeown, M. Kumar, I. E. L. Stephens, M. W. Kanan, I. Chorkendorff, *J. Am. Chem. Soc.* **2015**, *137*, 9808–9811.
[16] Y. Hori, R. Takahashi, Y. Yoshinami, A. Murata, *J. Phys. Chem. B* **1997**, *101*, 7075–7081.
[17] J. H. Montoya, C. Shi, K. Chan, J. K. Nørskov, *J. Phys. Chem. Lett.* **2015**, *6*, 2032–2037.
[18] Y. Hori, I. Takahashi, O. Koga, N. Hoshi, *J. Phys. Chem. B* **2002**, *106*, 15–17.
[19] M. Heinen, Z. Jusys, Y. X. Chen, R. J. Behm, *J. Phys. Chem. C* **2010**, *114*, 9850–9864.
[20] J. K. Nørskov, A. A. Peterson, J. H. Montoya, *ChemCatChem* **2013**, *5*, 737–742.
[21] F. Calle-Vallejo, M. T. M. Koper, *Angew. Chem. Int. Ed.* **2013**, *52*, 7282–7285; *Angew. Chem.* **2013**, *125*, 7423–7426.
[22] J. Hong, W. Zhang, J. Ren, R. Xu, *Anal. Methods* **2013**, *5*, 1086–1097.
[23] R. D. Harrison, *Revised Nuffield Advanced Science Book of Data*, Longman, Harlow, **1984**.
[24] Y. Kwon, S. C. S. Lai, P. Rodriguez, M. T. M. Koper, *J. Am. Chem. Soc.* **2011**, *133*, 6914–6917.
[25] V. Čolić, A. S. Bandarenka, J. Tymoczko, A. Maljusch, A. Ganassin, W. Schuhmann, *ChemElectroChem* **2015**, *2*, 143–149.
[26] S. R. Bahn, K. W. Jacobsen, *Comput. Sci. Eng.* **2002**, *4*, 56–66.
[27] B. Hammer, L. Hansen, J. Nørskov, *Phys. Rev. B* **1999**, *59*, 7413–7421.
[28] A. A. Peterson, F. Abild-Pedersen, F. Studt, J. Rossmeisl, J. K. Nørskov, *Energy Environ. Sci.* **2010**, *3*, 1311–1315.

Received: September 21, 2015
Revised: October 22, 2015
Published online: December 21, 2015

Paper II

Quantification of liquid products from the electroreduction of CO_2 and CO using static headspace-gas chromatography and nuclear magnetic resonance spectroscopy

Erlend Bertheussen, Younes Abghoui, Zarko P. Jovanov, Ana-Sofia Varela, Ifan E.L. Stephens, Ib Chorkendorff.

Catalysis Today, 2017, volume **288**, pages 54-62.

Catalysis Today 288 (2017) 54–62

Contents lists available at ScienceDirect

Catalysis Today

journal homepage: www.elsevier.com/locate/cattod

Quantification of liquid products from the electroreduction of CO_2 and CO using static headspace-gas chromatography and nuclear magnetic resonance spectroscopy

Erlend Bertheussen[a], Younes Abghoui[a,b], Zarko P. Jovanov[a,c], Ana-Sofia Varela[a,d], Ifan E.L. Stephens[a,*], Ib Chorkendorff[a,*]

[a] Department of Physics, Technical University of Denmark, 2800 Kgs. Lyngby, Denmark
[b] Science Institute and Faculty of Physical Sciences, VR-III, University of Iceland, IS-107 Reykjavik, Iceland
[c] Department of Chemistry, Chemical Engineering Division, Technical University Berlin, 10623 Berlin, Germany
[d] Institute of Chemistry, National Autonomous University of Mexico, 04510 Mexico City, Mexico

ARTICLE INFO

Article history:
Received 20 October 2016
Received in revised form 11 February 2017
Accepted 22 February 2017
Available online 31 March 2017

Keywords:
CO_2 reduction
Electrocatalysis
Product analysis
Static headspace-gas chromatography
NMR spectroscopy

1. Introduction

The electroreduction of carbon dioxide is emerging as a promising way of converting waste CO_2 and excess renewable energy into valuable chemicals, chemical feedstock and/or fuels [1,2]. Hence, waste carbon dioxide captured from point sources or ambient air could represent a sustainable carbon source, and the anthropogenic carbon cycle could be closed [1]. There are, however, several limitations that need to be overcome before the technology is viable for large-scale application. Due to complex reaction pathways with multiple proton and electron transfers and low aqueous solubility of CO_2, high overpotentials and low current densities are generally obtained [3–5]. One way to overcome this is to separate the overall reduction process into two reactions. The reduction of CO_2 to CO is a two-electron process that can be catalyzed relatively easily. By focusing on the further reduction of CO, the demands on the catalyst can be reduced, with a lower number of intermediates. Furthermore, CO has been shown to be an intermediate in the reduction of CO_2 to fuels and other useful chemicals [6–9]. Another challenge that electrochemical CO_2/CO reduction is facing, is that the thermodynamic equilibrium potentials for most products have similar values. Taking the mentioned overpotentials into account, they can also be found in a similar potential region as the hydrogen evolution reaction. As a result, a mixture of products is often formed, making thorough product detection vital when testing potential electrocatalysts for CO_2/CO reduction [2].

Detection and quantification of all reaction products is needed, both to determine the selectivity for the catalyst of interest, and to get potential mechanistic information yielding deeper understanding. There are many different approaches to product analysis in the field. The most conventional choice for ex-situ product detection is gas chromatography for detection and quantification of any gaseous products formed [10–20]. For liquid products, nuclear magnetic resonance (NMR) spectroscopy [10,11,15,19], high-performance liquid chromatography (HPLC) [15,20–22], and/or static headspace-gas chromatography (HS-GC) [14,15,23] can be applied.

The chromatography-based techniques GC, HPLC and HS-GC all rely on separation of the different compounds in the sample mixture by a capillary column. For conventional GC, the samples are

* Corresponding authors.
E-mail addresses: ifan.stephens@fysik.dtu.dk (I.E.L. Stephens), ibchork@fysik.dtu.dk (I. Chorkendorff).

http://dx.doi.org/10.1016/j.cattod.2017.02.029

injected directly in their gaseous form. A temperature conductivity detector (TCD) and a flame ionization detector (FID) are typically applied after separation. The FID exhibits excellent sensitivity towards hydrocarbons, as well as CO and CO_2 if a methanizer is applied, making quantification straightforward. The TCD is mainly used for quantification of H_2. Alternatively, GC could be coupled with mass spectrometry (MS) to analyze the products, making identification of unknown compounds more facile. HS-GC is based on conventional GC, in which liquid samples can be analysed by vaporizing them before injection. By heating a liquid sample in a gas-tight vial, a mixture of the sample matrix and any other volatile compounds present will accumulate in the headspace. This gas can then be analysed using FID as described for gas chromatography. Injection can be done manually with a syringe, or using dedicated add-on equipment that is offered by most GC equipment retailers. Because of the sampling technique, only products that are volatile at temperatures below the boiling point of the sample matrix can be probed. This is one of the main limitations of the technique, since non-volatiles such as formate and acetate are major products from CO_2 and CO reduction on some surfaces [10,24–26]. Hence, HS-GC needs to be combined with one or more alternative method(s), such as NMR spectroscopy and/or HPLC, to achieve complete product detection.

As opposed to the separation of compounds in the chromatography-based techniques, NMR spectroscopy relies on the spin magnetic moment of certain nuclei. Their chemical environment can change depending on the structure they are part of, and thus, different compounds can be distinguished. Because of the size and cost of the equipment, NMR spectrometers are often located in specialized laboratories. Hence, measurements are typically performed off-site. As a result, product analysis is often taking place hours or longer after electrolysis. Since many relevant organic compounds are unstable in certain alkaline or acidic environments, the product distribution might not stay constant over the course of this time span. Hence, immediate product analysis will in some cases be important to determine the actual performance of the electrocatalyst. In addition, water suppression is necessary for aqueous samples in order to resolve the much smaller product signals.

Another approach to product detection is to utilize differential electrochemical mass spectrometry (DEMS) to probe the formation of compounds close to the electrode surface. This can enable fast time response, practically yielding real-time information about reaction products. As a result, DEMS is widely applied for CO_2 electroreduction [6,27,28]. Recently, another method to maintain the fast time response without using differential pumping has been developed in our group [29], showing improved sensitivity. In general, however, when dealing with mixtures of hydrocarbons, mass spectrometry may be tedious and require high mass resolution to identify and quantify the various compounds. Another limitation of this technique has previously been to achieve reliable product quantification. However, Bell et al. recently reported improvements to the quantification by DEMS techniques [28].

Recently [14], we showed that acetaldehyde is a product from CO reduction on oxide-derived copper. Conversely, the earlier study of this catalyst, where NMR was employed for product detection, did not report acetaldehyde. We found that the reason for this discrepancy is that acetaldehyde is undetectable at low concentrations using routine NMR spectroscopy. Aldehydes can undergo a number of spontaneous reactions, in particular in alkaline solutions [30]. We hypothesized that the acetaldehyde molecules polymerize and precipitate out of solution. Since NMR spectroscopy relies on analytes to be dissolved, this could explain why it was previously undetected. Applying HS-GC, however, allowed for facile detection. The case of acetaldehyde in alkaline solution is a rather specific example, but we believe that it emphasizes the importance of using complementary techniques for liquid product analysis. As a general note, also emphasized by Hori [25], it is important to monitor and report the total Faradaic efficiency obtained from electrolysis. This way, one could check if any major product remains undetected due to incomplete product analysis, by determining whether or not a complete balance of charge is obtained. Nonetheless, this is not possible for minor products, such as acetaldehyde in the example mentioned above, because of the uncertainty inherent to experimental product analysis.

2. Experimental details

2.1. Materials

All calibration solutions were made in 0.1 M KOH (Sigma-Aldrich, semiconductor grade, 99.99%). Methanol (MeOH – Sigma-Aldrich, CHROMASOLV®, HPLC grade, 99.9%), acetic acid (AcOH – Sigma-Aldrich, ≥99.99%), acetaldehyde (MeCHO – Fluka, anhydrous, GC grade, ≥99.5%), ethanol (EtOH–), propionaldehyde (EtCHO – Sigma-Aldrich, reagent grade, 97%) and 1-propanol (1-PrOH – Sigma-Aldrich, CHROMASOLV®, HPLC grade, 99,9%) were used as precursors for the calibration solutions.

2.2. Product analysis by HS-GC

HS-GC measurements were carried out using an Agilent 7694E Headspace sampler with an Agilent 7890A GC. Specialized 10 mL vials were filled with 5 mL of sample and sealed. They were heated to 70 °C over 15 min in the headspace sampler and 250 μL of the headspace gas composition was automatically injected into the GC. The sample loop (110 °C) and transfer line (120 °C) were both heated to avoid condensation. Argon (AGA, 5.0) was used as carrier gas. An HP-PLOT Q column (Length: 45 m; ID: 0.53 mm; Film: 40.0 μm) was used to separate the compounds in the sample. It was kept at 130 °C for 20 min, then heated to 230 °C at a rate of 10 °C min^{-1}, and finally kept at 230 °C for 5 min. Subsequently, a 15 min post-run at 230 °C was carried out. The temperature increase and post-run were applied to make sure that larger compounds would not get trapped in the column. The separated products were analysed with an FID. Usually, 12 samples were measured in series, the maximum capacity of the headspace sampler. If further data points were needed, they had to be obtained through additional measurements.

2.3. Product analysis by NMR spectroscopy

NMR data were acquired at a Bruker Ascend 400 MHz spectrometer with a Prodigy CryoProbe. A standard 1D NOESY experiment with pre-saturation during relaxation delay and mixing time (noesypr1d) was used to acquire the 1D ^1H spectra, in order to obtain sufficient water suppression. Standard acquisition parameters were as follows; number of scans = 64, relaxation delay = 5 s, acquisition time = 4 s (i.e. a total recycle delay of 9 s) t_m = 20 ms, pre-saturation power level = 43 dB, spectral width = 20 ppm, and number of time domain points = 65 k. 17% D_2O and 0.5 mM of dimethyl sulfoxide (DMSO) was added, the latter as an internal standard.

3. Results and discussion

In the following, we will illustrate the use of HS-GC for liquid product analysis. This is done by comparison with NMR spectroscopy, since it is not a chromatography-based technique. However, HS-GC can of course be coupled with other methods, e.g. HPLC. In Table 1, a number of liquid CO(2) reduction products

Table 1
Henry's law constant values for a number of possible liquid CO(2) reduction products. All products have been detected from CO_2 reduction on polycrystalline copper by Kuhl et al. [11]. Henry's law constants have been retrieved from a number of references, via the compilation made by Sander [31]. When possible, only references stating an actual measured value has been taken into account, marked by 'M' in the compilation document. This is the case unless otherwise stated. For compounds with several references, the average is calculated. The uncertainty stated corresponds to the standard deviation. *We have chosen to show the individual values from the two references for ethylene glycol, due to the discrepancy between them. **This reference was marked with 'C' in the compilation by Sander, meaning that the paper cited refers to another reference that could not be obtained. ***These references were marked with 'X' in the compilation by Sander. This means that he has not actually seen the reference, but has found it cited by another paper or knows about it through others.

Product	Chemical formula	k_H (M atm^{-1})	References
Formate	$HCOO^-$	–	–
Methanol	CH_3OH	$(2.2 \pm 0.1) \times 10^2$	[32–35]
Acetate	CH_3COO^-	–	–
Glyoxal	OCHCHO	$(3.3 \pm 0.4) \times 10^5$	[36,37]
Glycolaldehyde	$HOCH_2CHO$	4.1×10^4	[36]
Ethylene glycol	$(CH_2OH)_2$	$1.7 \times 10^{4*}$, $4.0 \times 10^{6*}$	[38] [39]
Acetaldehyde	CH_3CHO	$(1.4 \pm 0.2) \times 10^1$	[35–37,40,41]
Ethanol	C_2H_5OH	$(2.0 \pm 0.3) \times 10^2$	[32–35,42]
Hydroxyacetone	CH_3COCH_2OH	$7.8 \times 10^{3**}$	[43]
Acetone	$(CH_3)_2CO$	$(2.8 \pm 0.4) \times 10^1$	[33,35,37,40,41,44–46]
Allyl alcohol	C_3H_5OH	$(2.8 \pm 1.4) \times 10^{2***}$	[47–49]
Propionaldehyde	C_2H_5CHO	1.3×10^1	[37,40]
1-Propanol	C_3H_7OH	$(1.4 \pm 0.2) \times 10^2$	[32,33,35]

Table 2
Summary of approximate detection limits for typical liquid CO reduction products when analysed by NMR spectroscopy and static headspace-gas chromatography (HS-GC).

Product	Approximate detection limits (μM)	
	NMR	HS-GC
MeOH	<5	>20
AcO^-	<5	–
MeCHO	>200	<0.5
EtOH	10	5
EtCHO	100	<0.5
1-PrOH	10	10

Table 3
Solubility and Henry's law constants for the two relevant reactant gases, carbon dioxide and carbon monoxide.

Reactant gas	Solubility (g L^{-1})	k_H (M atm^{-1})
Carbon dioxide	1.50×10^0 [50]	3.5×10^{-2} [51,52]
Carbon monoxide	2.76×10^{-2} [50]	7.5×10^{-3} [53]

reported in literature are listed, along with their Henry's law constants. In the following, we will focus the analysis on the probable CO reduction products listed in Table 2, because it is the type of measurements we have the most experience with. However, the conclusions drawn should be valid for the other products as well. In Table 3, the solubility and Henry's law constant for the two relevant reactant gases, CO_2 and CO, are listed.

The calibrations are carried out with mixtures of two products at a time. One could suspect that the choice of pairing of products here could affect results if organic reactions were induced. This could particularly the case for HS-GC, where the sample is heated before analysis. In the supporting information of our previous work [14], we showed that acetaldehyde, acetate and ethanol gave consistent results when calibrated together. At no point could we find any indication that mixing the products could give discrepancies. Thus, we are confident that the results presented in this work are independent of pairing in the calibration mixtures. Since CO reduction is normally carried out in an alkaline electrolyte, we chose 0.1 M KOH as the sample matrix. The concentrations chosen range from 0.5 to 200 μM. For CO reduction, product concentrations are expected to be in this range, as exemplified in Table 4. The tabulated data are obtained from oxide-derived copper, and comprises an upper limit because of the high activity and selectivity of this material. CO_2 reduction currents are typically significantly higher, partly caused by the difference in solubility as shown in Table 3. This would again lead to higher product concentrations in the electrolyte. In this work, the detection limit will be defined as the concentration where a peak is no longer discernable, since this is the practical limit to the application of the technique. We give an example of this in Fig. S1, showing a spectrum obtained for 10 μM ethanol and 1-propanol in 0.1 M KOH. The most intense signal from both compounds is just about visible, but the baseline noise makes integration impossible. We do not aim to provide a highly accurate value of the detection limit, but rather to give an indication of the lowest concentrations where the method can be practically applied.

Table 4
Faradaic efficiency, partial current density and electrolyte concentration for liquid CO reduction products from oxide-derived copper at −0.33 V vs. RHE. The data are obtained from our previous study [14], where potentiostatic CO electrolysis was carried out until approximately 10 C of total charge had been passed. The electrolyte volume was 12 mL.

Product	Faradaic efficiency (%)	j_{geo} (mA cm)	Concentration (μM)
Acetate	26	0.34	280
Acetaldehyde	5.5	0.072	300
Ethanol	28	0.36	59

3.1. EtOH and 1-PrOH

In Figs. 1 and 2, NMR spectroscopy and HS-GC data for ethanol (EtOH) and 1-propanol (1-PrOH) are shown, respectively. We measured solutions containing 200, 100, 50, 20, 10 and 5 μM EtOH and 1-PrOH in 0.1 M KOH. In Fig. 1a), a part of the NMR spectrum for the solution containing 200 μM EtOH and 1-PrOH in 0.1 M KOH is shown. Two distinct signals can be seen for ethanol and three for 1-propanol, as expected. The noise around 2.5 ppm is caused by resonance from the water suppression pulse. The singlets at 1.14, 1.81 and 2.80 ppm are caused by impurities that are also present in the blank measurements (Fig. S2). They are most likely caused by trace amounts of organic compounds that can be present in containers and pipette tips used for sample preparation. The presence of impurities could affect the overall analysis, for instance if mistaken for products. Thus, it is important to carry out blank measurements and/or thorough cleaning of sample preparation equipment. From the slope of the calibration curves in Fig. 1b) and c), it can be seen that both these compounds give a similar signal intensity response in NMR spectra, 7.4×10^{-4} μM^{-1} and 8.3×10^{-4} μM^{-1},

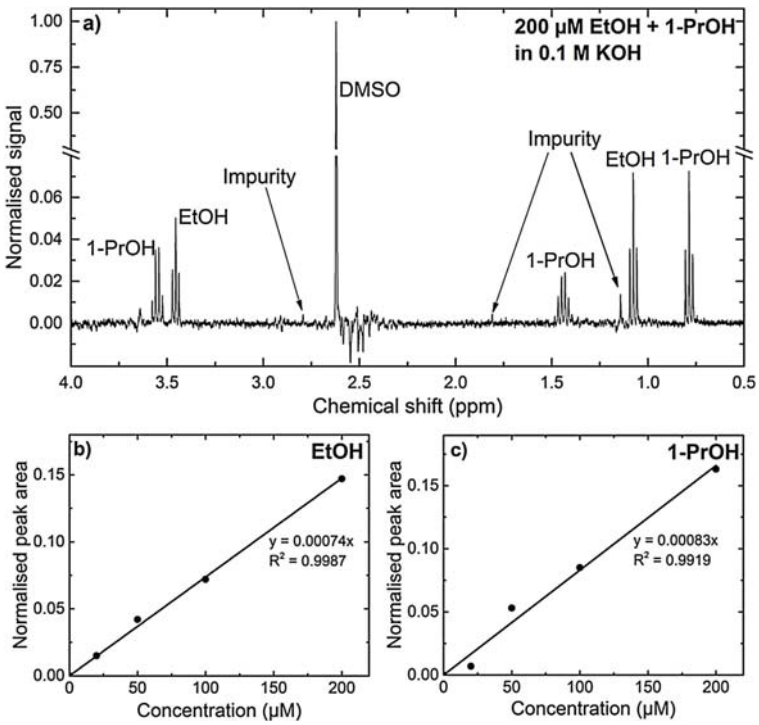

Fig. 1. NMR spectroscopy data for ethanol and 1-propanol. Solutions containing 200, 100, 50, 20, 10 and 5 μM EtOH and 1-PrOH in 0.1 M KOH were analysed. a) NMR spectrum of 200 μM EtOH and 1-PrOH in 0.1 M KOH, cut to show the relevant region. The y-axis is normalized to the intensity of the DMSO peak. The noise around 2.5 ppm is caused by resonance from the water suppression pulse. The singlets at 1.14, 1.81 and 2.80 ppm are impurities also present in blank measurements (Fig. S2). b) Calibration curve for EtOH. The signals are obtained from the peak with the lowest chemical shift, the triplet at 1.07 ppm. The entire peak area is taken into account, and the integrated signal is normalized to that of the DMSO peak. The y-axis intercept of the linear fit is fixed to 0. No EtOH peak was adequately quantifiable below 20 μM, and data points for these measurements are hence not shown. c) Calibration curve for 1-PrOH. The signals are obtained from the peak with the lowest chemical shift, the triplet at 0.79 ppm. The entire peak area is taken into account, and the integrated signal is normalized to that of the DMSO peak. The y-axis intercept of the linear fit is fixed to 0. No 1-PrOH peak was adequately quantifiable below 20 μM, and data points for these measurements are hence not shown.

respectively. The intensity of a peak scales with the number of chemically equal protons that constitute it, and the most intense signal for the two compounds originate from the methyl group at the end of the molecules. Hence, these peaks were used to make the calibration curves. No data points for the measurements at 10 and 5 μM concentration are shown in these curves, because the signals were so low that the peaks could not be adequately integrated. In Fig. S1, a spectrum obtained from the solution with 10 μM EtOH and 1-PrOH is shown. The signals of the two compounds can be seen, but they are in the same intensity range as the baseline noise, and cannot be accurately integrated.

In Fig. 2a), a chromatogram from a 200 μM solution of EtOH and 1-PrOH is displayed. The peaks present at low retention times (<5 min) are caused by CO_2 and hydrocarbons dissolved in the solution, originating from the atmosphere. The increase in signal towards the end of the measurement is caused by bleeding from the column due to the temperature ramp. The calibration curves in Fig. 2b) and c) shows that EtOH and 1-PrOH give different responses when analysed by HS-GC, as opposed to what was the case for NMR spectroscopy. The slope of the calibration curves for the two are 0.232 and 0.449, respectively. Hence, the technique is close to twice as sensitive towards 1-propanol than ethanol using with the parameters we used. One of the reasons for this is that the FID signal is proportional to the number of carbon atoms in the molecule. In addition, 1-propanol has a higher vapor pressure compared to ethanol, as seen from their Henry's law constants listed in Table 1. This leads to a higher amount of the compound being vaporized and injected. Although 1-propanol gives a stronger signal, it actually yields a higher practical detection limit compared to ethanol. This is mainly due to its greater peak width, making integration difficult at low intensities. In Fig. S3, we show a chromatogram obtained for 10 μM EtOH and 1-PrOH in 0.1 M KOH. At this concentration, ethanol can still be integrated, whereas the 1-propanol peak is much wider, giving a significant integration error. The fact that the 1-propanol peak coincides with the baseline rise from the temperature increase also affects the quantification negatively at these low concentrations. These challenges could be mitigated by further optimization of the GC method. We have, however, refrained from that in the current study, in order to run the samples under identical conditions.

3.2. MeOH and AcO

Next, we investigated the response of the two techniques towards methanol and acetate. Again, 200, 100, 50, 20, 10 and 5 μM standard solutions of the two compounds in 0.1 M KOH were measured. In this case, only one signal from each of them is produced in NMR spectra, as seen in Fig. 3a). They originate from the methyl groups of the respective molecules, and give rise to a similar response as for ethanol and 1-propanol. From the calibration curves in Fig. 3b) and c), a slope of 6.6×10^{-4} and 8.7×10^{-4} μM^{-1} can be determined for MeOH and AcO^-, respectively. Even though their

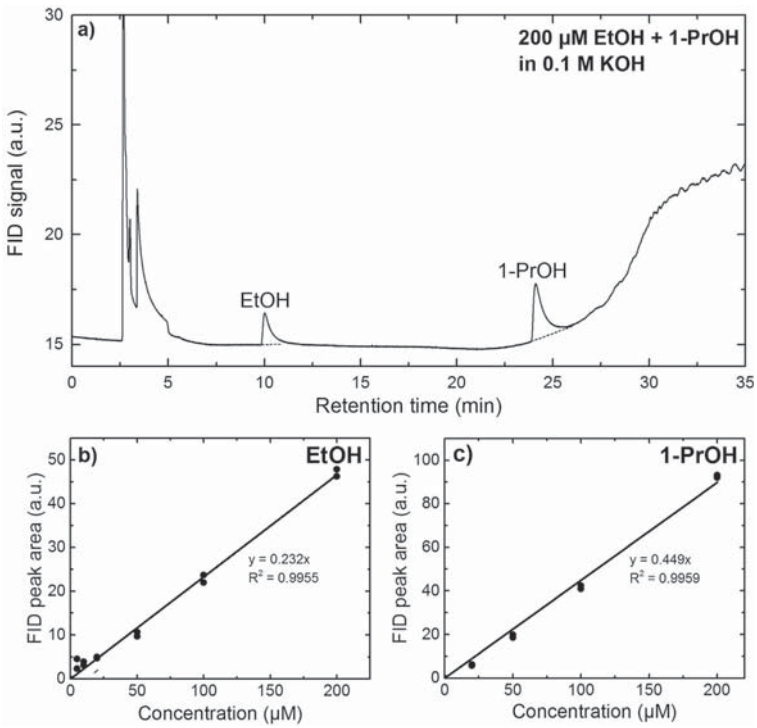

Fig. 2. HS-GC data for ethanol and 1-propanol. Solutions containing 200, 100, 50, 20, 10 and 5 μM EtOH and 1-PrOH in 0.1 M KOH were analysed. c) Chromatogram of 200 μM EtOH and 1-PrOH in 0.1 M KOH. Integration baselines are indicated with stapled lines. The peaks at low retention times (<5 min) are CO_2 and gaseous hydrocarbons absorbed from the air. The features at high retention times are most likely caused by impurities from the column that are released when the temperature is increased. a) Calibration curve for EtOH. The y-axis intercept of the linear fit is fixed to 0. b) Calibration curve for 1-PrOH. The intercept of the linear fit is fixed to 0. No peak could be adequately quantified below 20 μM, and data points for these measurements are hence not shown.

response is similar to that of the two larger alcohols, the detection limit is lower for methanol and acetate in NMR spectroscopy. This is mainly due to the fact that both signals appear as sharp singlets, while the EtOH and 1-PrOH signals are either triplets or quartets. From Fig. S4 it can be seen that even at concentrations of 5 μM, the peaks can be integrated relatively accurately. This makes NMR spectroscopy an ideal method for detection of these compounds. Another singlet peak is present at 1.14 ppm. This is attributed to an impurity, as was the case for the EtOH and 1-PrOH spectrum.

In Fig. 4a), the chromatogram for 200 μM methanol and acetate in 0.1 M KOH is shown. It is clearly seen that acetate cannot be detected with HS-GC, since it has no vapor pressure in the deprotonated form. From the calibration curve in Fig. 4b), a very low slope of 0.068 was found for MeOH. Furthermore, we observed a significant scatter for samples of identical concentration throughout the calibration series. This is likely to be partly due to the fact that the methanol peak falls right on top of the tail from CO_2 and the gaseous hydrocarbons, giving challenges when integrating. However, there also seems to be some correlation with the amount of time from the preparation of the samples, with the first few samples in the series giving significantly higher signals than the samples measured afterwards, pointing to the importance of fast analysis of samples containing volatile products. In our experimental set up we observe that MeOH could not be detected at 20 μM or lower, giving a relatively high detection limit. The chromatogram for this concentration can be seen in Fig. S5.

HS-GC seems to be particularly unsuited for detection and quantification of acetate and methanol. In fact, acetate and similar deprotonated species cannot be detected at all, as they are not expected to vaporize. This is one of the main disadvantages of the technique, and one of the reasons it should only be used together with a complementary method. On the other hand, NMR spectroscopy works excellently for these compounds, with detection limits below 5 μM for both of them.

3.3. MeCHO and EtCHO

Finally, we studied the behavior of acetaldehyde and propionaldehyde when examined with the two techniques. As expected from the results of our previous investigation [14], these aldehydes are not easily detected using NMR spectroscopy. A region of the NMR spectrum of 200 μM MeCHO and EtCHO in 0.1 M KOH can be seen in Fig. 5. None of the expected acetaldehyde signals can be observed, as we reported in that work. A triplet at 0.98 ppm can be attributed to the propionaldehyde methyl group. Compared to the signals from methyl groups of the other compounds shown above, however, this peak is relatively small. Already at 100 μM, it cannot be properly integrated, as can be seen in Fig. S6. The explanation is likely to be the same as for acetaldehyde, that the molecules are unstable in alkaline solution and polymerize. The broad singlet at 1.61 ppm and the presence of several other small signals also point towards this hypothesis. As for the previous measurements, the singlets at 1.14, 1.81 and 2.80 ppm are likely to be impurities, since it is also present in the blank measurement (Fig. S2), as previously discussed. The features around 2.5 ppm are caused by resonance from the water suppression pulse, as previously described.

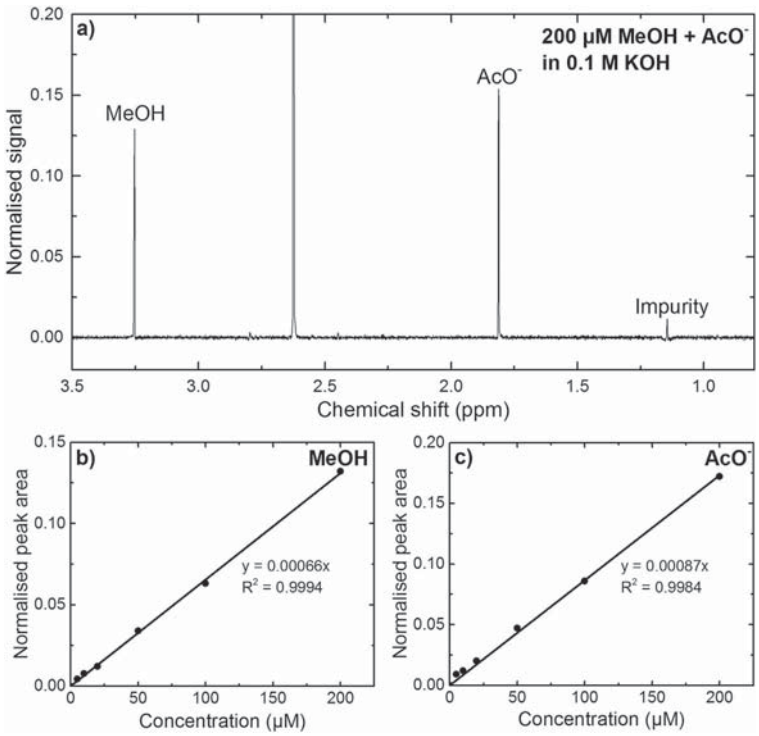

Fig. 3. NMR spectroscopy data for methanol and acetate. Solutions containing 200, 100, 50, 20, 10 and 5 μM MeOH and AcO^- in 0.1 M KOH were analysed. a) NMR spectrum of 200 μM MeOH and AcO^- in 0.1 M KOH, cut to show the relevant region. The y-axis is normalized to the intensity of the DMSO peak. The singlet at 1.14 ppm is an impurity also present in blank measurements (Fig. S2). b) Calibration curve for MeOH. The integrated signal is normalized to that of the DMSO peak. The y-axis intercept for the linear fit was fixed at 0. b) Calibration curve for AcO^-. The integrated signal is normalized to that of the DMSO peak. The y-axis intercept for the linear fit was fixed at 0.

HS-GC exhibits a dramatically different response to the two aldehydes in comparison to NMR spectroscopy. As can be seen from Fig. 6a), the chromatogram signal for both are sharp and intense compared to other compounds reported in this work. This gives very high sensitivity; even at 0.5 μM both MeCHO and EtCHO have visible peaks (Fig. S7). The most important reason for the large peak areas is the high volatility of these compounds in aqueous solution [31]. EtCHO gives an even larger area than MeCHO due to its higher volatility, as well as the presence of an additional carbon atom, as seen from the calibration curves in Fig. 6b) and c). The slopes for these curves are 0.71 and 1.35 for acetaldehyde and propionaldehyde, respectively, which is much higher than any of the other compounds measured in this work.

It is important to note that this investigation is carried out in alkaline solution, making NMR particularly unfavorable for detection of aldehydes. However, the high sensitivity of HS-GC to the aldehydes is universal, with the exception of formaldehyde, and is a great strength for the technique. Formaldehyde has a high Henry's law constant [36,37], giving low vapor pressure for dilute solutions. We thus predict a low sensitivity for this compound with HS-GC. The relatively small scatter in the calibration results for acetaldehyde and propionaldehyde might seem counter-intuitive with the hypothesis that these compounds polymerize at alkaline conditions. It is likely, however, that the polymerized species exist in equilibrium with the aldehyde molecules. Heating the mixture would push this equilibrium towards free aldehydes, the state with the higher entropy. Because of the equilibrium, the gas-phase aldehyde concentration, and thus the amount that is sampled, would still scale with the amount of aldehydes on aggregated form. Detection of aldehydes is challenging in general. When using HPLC, high sensitivity towards aldehydes can only be achieved after derivatization with 2,4-dinitrophenylhydrazine, a time-consuming process [54]. DEMS or other MS based techniques are likely to be applicable for detection of MeCHO and higher aldehydes, due to the high vapor pressure of these compounds. This is, however, yet to be shown experimentally.

3.4. Summary

The two techniques have different strengths and weaknesses, as summarized in Table 2. A clear strength for HS-GC is the detection of aldehydes, with detection limits below 0.5 μM for acetaldehyde and propionaldehyde. This is mainly caused by the high volatility of aldehydes, with the exception of formaldehyde, in alkaline solution. On the other hand, the technique exhibits relatively high detection limits for compounds with low volatility, such as methanol, and is unable to detect deprotonated compounds, such as acetate. For methanol, we determined the detection limit to be above 20 μM for HS-GC with our configuration. Two other alcohols, ethanol and 1-propanol, were investigated, showing detection limits of around 5 μM and 10 μM, respectively. Based on these conclusions, the response for the technique towards other possible CO_2 reduction products listed in Table 1 should be possible to predict qualitatively, based on their Henry's law constant and the number of carbon atoms in the molecule.

NMR spectroscopy, however, has difficulties detecting aldehydes in alkaline solution. At 200 μM, we observed none of the expected peaks for acetaldehyde, while propionaldehyde gave a

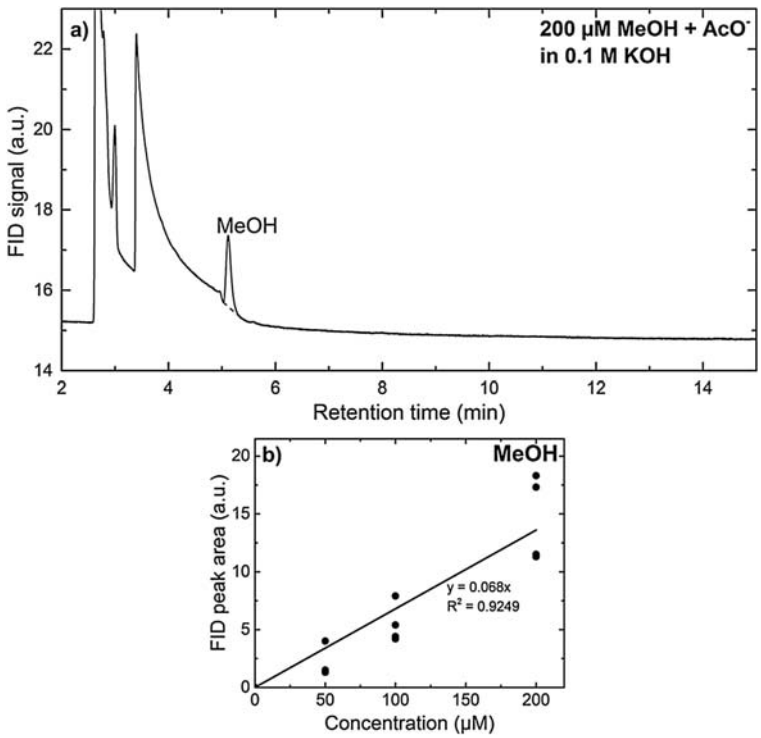

Fig. 4. HS-GC data for methanol and acetate. Solutions containing 200, 100, 50, 20, 10 and 5 µM MeOH and AcO^- in 0.1 M KOH were analysed. a) Chromatogram of 200 µM MeOH and AcO^- in 0.1 M KOH. The integration baseline is indicated with stapled lines. The peaks at low retention times (<5 min) are CO_2 and gaseous hydrocarbons absorbed from the air. Note that the methanol peak is positioned right at the tail of the CO_2/hydrocarbon peaks, giving errors when integrating. b) Calibration curve for MeOH. The y-axis intercept of the linear fit is fixed to 0.

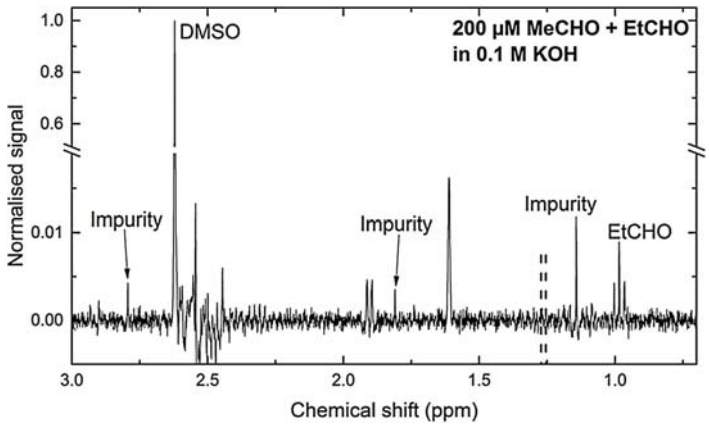

Fig. 5. NMR spectrum of 200 µM MeCHO and EtCHO in 0.1 M KOH, cut to show the relevant region. The noise around 2.5 ppm is caused by resonance from the water suppression pulse. The singlets at 1.14, 1.81 and 2.80 ppm are impurities also present in blank measurements (Fig. S2). The other signals could not be clearly identified, but are most likely related to polymerized forms of acetaldehyde and/or propionaldehyde. The two dashed lines illustrate where the acetaldehyde signal is typically found as doublet, originating from the methyl group at the end of the hydrated molecule.

signal significantly weaker than expected. This is likely to be caused by polymerization of the compounds, giving rise to line broadening and chemical shift changes, as well as precipitation. Furthermore, Cannizzarro disproportionation of an aldehyde into the corresponding alcohol and carboxylic acid could take place at strongly alkaline conditions [55], but was not found to occur to a significant degree for dilute (250 µM) acetaldehyde at pH 13 [14]. All these factors affect the detection limit in a negative manner. On the other hand, NMR spectroscopy is highly suited for analysis of acetate and methanol, with detection limits below 5 µM for both species. For

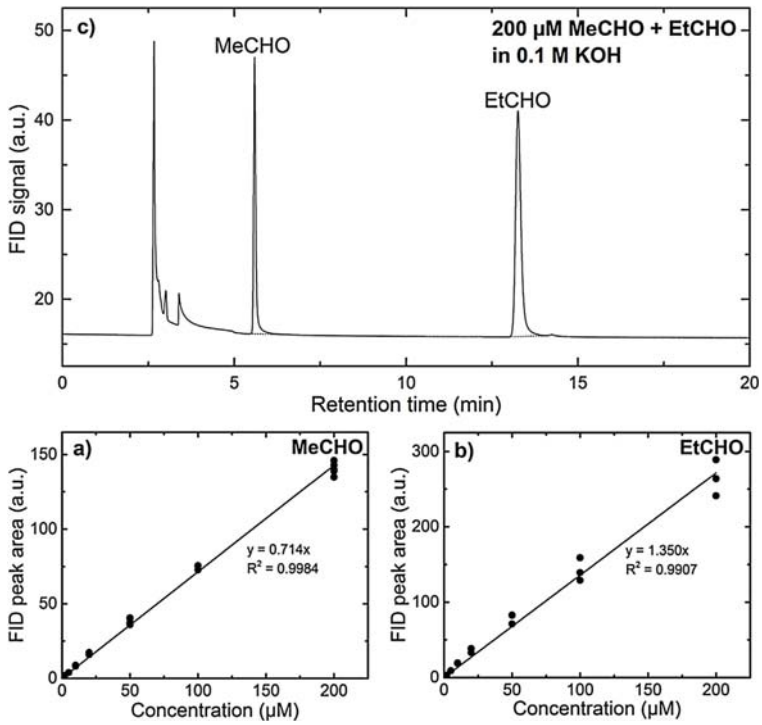

Fig. 6. HS-GC data for acetaldehyde and propionaldehyde. Solutions containing 200, 100, 50, 20, 10, 5, 2, 1 and 0.5 µM MeCHO and EtCHO in 0.1 M KOH were analysed. a) Chromatogram of 200 µM MeCHO and EtCHO in 0.1 M KOH. Integration baselines are indicated with stapled lines. The peaks at low retention times (<5 min) are CO_2 and gaseous hydrocarbons absorbed from the air. b) Calibration curve for MeCHO. The y-axis intercept of the linear fit is fixed to 0. c) Calibration curve for EtCHO. The y-axis intercept of the linear fit is fixed to 0.

ethanol and 1-propanol, NMR spectroscopy gives similar detection limits as HS-GC, around 10 µM. In general, an advantage for this technique is that it can be used to determine the structure of unknown compounds. When using GC based methods, mass spectrometry needs to be applied for identification of previously unknown products.

It is also interesting to consider the difference in size and cost for the two techniques. HS-GC can be carried out with a simple headspace sampler add-on to a conventional GC, while NMR is a large and expensive piece of equipment. Another advantage of HS-GC, is that the chromatography, for instance separation and peak width, can be easily manipulated by changing the temperature of the GC oven. If drastic changes to the chromatography are needed, the columns can be readily replaced by another type more suitable for the user's needs. Since the sensitivity depends significantly on the peak width, the detection limit can be enhanced this way. For NMR, on the other hand, the line broadening depends mostly on parameters that are not tunable on a specific instrument, such as the magnetic field strength.

4. Conclusion

In this work, we have summarized product analysis in the field of CO2 electroreduction, with particular emphasis on static headspace-gas chromatography by comparison with NMR spectroscopy. We have focused on the detection of liquid products relevant for CO reduction, in alkaline solution. It is clear that both techniques have their strengths and weaknesses. For instance, HS-GC cannot detect products present as ions, such as formate or acetate. On the other hand, detection of aldehydes in alkaline solution is challenging with NMR spectroscopy. This emphasizes the importance of having a complete overview of the Faradaic efficiencies and applying a complementary set of product detection methods. In failing to do this, one could risk overlooking products. That way, one could miss potentially important information, and in the case of aldehydes, valuable chemicals.

Acknowledgements

This work was supported by a research grant (9455) from VILLUM FONDEN. Furthermore, we would like to acknowledge support from Icelandic Research Fund and Research Fund of the University of Iceland.

Appendix A. Supplementary data

Supplementary data associated with this article can be found, in the online version, at http://dx.doi.org/10.1016/j.cattod.2017.02.029.

References

[1] A. Goeppert, M. Czaun, J.-P. Jones, G.K. Surya Prakash, G.A. Olah, Recycling of carbon dioxide to methanol and derived products – closing the loop, Chem. Soc. Rev. 43 (2014) 7995–8048, http://dx.doi.org/10.1039/c4cs00122b.
[2] Y. Hori, CO2 reduction using electrochemical approach, in: M. Sugiyama, K. Fujii, S. Nakamura (Eds.), Solar to Chemical Energy Conversion, Springer, 2016, pp. 191–211, http://dx.doi.org/10.1007/978-3-319-25400-5.
[3] A.A. Peterson, J.K. Nørskov, Activity descriptors for CO 2 electroreduction to methane on transition-metal catalysts, J. Phys. Chem. Lett. 3 (2012) 251–258, http://dx.doi.org/10.1021/jz201461p.

[4] J. Durst, A. Rudnev, A. Dutta, Y. Fu, J. Herranz, V. Kaliginedi, A. Kuzume, A.A. Permyakova, Y. Paratcha, P. Broekmann, T.J. Schmidt, Electrochemical CO2 reduction – a critical view on fundamentals, materials and applications, Chim. Int. J. Chem. 69 (2015) 769–776, http://dx.doi.org/10.2533/chimia.2015.769.

[5] Y. Oh, X. Hu, Organic molecules as mediators and catalysts for photocatalytic and electrocatalytic CO2 reduction, Chem. Soc. Rev. 42 (2013) 2253–2261, http://dx.doi.org/10.1039/c2cs35276a.

[6] K.J.P. Schouten, Y. Kwon, C.J.M. van der Ham, Z. Qin, M.T.M. Koper, A new mechanism for the selectivity to C1 and C2 species in the electrochemical reduction of carbon dioxide on copper electrodes, Chem. Sci. 2 (2011) 1902, http://dx.doi.org/10.1039/c1sc00277e.

[7] A.A. Peterson, F. Abild-Pedersen, F. Studt, J. Rossmeisl, J.K. Nørskov, How copper catalyzes the electroreduction of carbon dioxide into hydrocarbon fuels, Energy Environ. Sci. 3 (2010) 1311–1315, http://dx.doi.org/10.1039/c0ee00071j.

[8] J.K. Nørskov, A.A. Peterson, J.H. Montoya, Insights into CC coupling in CO2 electroreduction on copper electrodes, ChemCatChem 5 (2013) 737–742.

[9] A. Wuttig, C. Liu, Q. Peng, M. Yaguchi, C.H. Hendon, K. Motobayashi, S. Ye, M. Osawa, Y. Surendranath, Tracking a common surface-bound intermediate during CO2-to-fuels catalysis, ACS Cent. Sci. 2 (2016) 522–528, http://dx.doi.org/10.1021/acscentsci.6b00155.

[10] C.W. Li, M.W. Kanan, CO2 reduction at low overpotential on Cu electrodes resulting from the reduction of thick Cu2O films, J. Am. Chem. Soc. 134 (2012) 7231–7234, http://dx.doi.org/10.1021/ja3010978.

[11] K.P. Kuhl, E.R. Cave, D.N. Abram, T.F. Jaramillo, New insights into the electrochemical reduction of carbon dioxide on metallic copper surfaces, Energy Environ. Sci. 5 (2012) 7050–7059, http://dx.doi.org/10.1039/c2ee21234j.

[12] Y. Hori, K. Kikuchi, S. Suzuki, Production of CO and CH4 in electrochemical reduction of CO2 at metal electrodes in aqueous hydrogencarbonate solution, Chem. Lett. (1985) 1695–1698, http://dx.doi.org/10.1246/cl.1985.1695.

[13] A. Wuttig, Y. Surendranath, Impurity ion complexation enhances carbon dioxide reduction catalysis, ACS Catal. 5 (2015) 4479–4484, http://dx.doi.org/10.1021/acscatal.5b00808.

[14] E. Bertheussen, A. Verdaguer-Casadevall, D. Ravasio, J.H. Montoya, D.B. Trimarco, C. Roy, S. Meier, J. Wendland, J.K. Nørskov, I.E.L. Stephens, I. Chorkendorff, Acetaldehyde as an intermediate in the electroreduction of carbon monoxide to ethanol on oxide-derived copper, Angew. Chem. Int. Ed. 55 (2016) 1450–1454, http://dx.doi.org/10.1002/anie.201508851.

[15] Z.P. Jovanov, H.A. Hansen, A.S. Varela, P. Malacrida, A.A. Peterson, J.K. Nørskov, I.E.L. Stephens, I. Chorkendorff, Opportunities and challenges in the electrocatalysis of CO2 and CO reduction using bifunctional surfaces: a theoretical and experimental study of Au-Cd alloys, J. Catal. (2016), http://dx.doi.org/10.1016/j.jcat.2016.04.008.

[16] O.A. Baturina, Q. Lu, M.A. Padilla, L. Xin, W. Li, A. Serov, K. Artyushkova, P. Atanassov, F. Xu, A. Epshteyn, T. Brintlinger, M. Schuette, G.E. Collins, CO2 electroreduction to hydrocarbons on carbon-supported Cu nanoparticles, ACS Catal. 4 (2014) 3682–3695, http://dx.doi.org/10.1021/cs500537y.

[17] R. Reske, H. Mistry, F. Behafarid, B. Roldan Cuenya, P. Strasser, Particle size effects in the catalytic electroreduction of CO2 on Cu nanoparticles, J. Am. Chem. Soc. 136 (2014) 6978–6986, http://dx.doi.org/10.1021/ja500328k.

[18] M. Asadi, B. Kumar, A. Behranginia, B.A. Rosen, A. Baskin, N. Repnin, D. Pisasale, P. Phillips, W. Zhu, R. Haasch, R.F. Klie, P. Král, J. Abiade, A. Salehi-Khojin, Robust carbon dioxide reduction on molybdenum disulphide edges, Nat. Commun. 5 (2014) 4470, http://dx.doi.org/10.1038/ncomms5470.

[19] Q. Kong, D. Kim, C. Liu, Y. Yu, Y. Su, Y. Li, P. Yang, Directed assembly of nanoparticle catalysts on nanowire photoelectrodes for photoelectrochemical CO 2 reduction, Nano Lett. 16 (2016) 5675–5680, http://dx.doi.org/10.1021/acs.nanolett.6b02321.

[20] W. Tang, A.A. Peterson, A.S. Varela, Z.P. Jovanov, L. Bech, W.J. Durand, S. Dahl, J.K. Nørskov, I. Chorkendorff, The importance of surface morphology in controlling the selectivity of polycrystalline copper for CO2 electroreduction, Phys. Chem. Chem. Phys. 14 (2012) 76–81, http://dx.doi.org/10.1039/C1CP22700A.

[21] Y. Lum, Y. Kwon, P. Lobaccaro, L. Chen, E.L. Clark, A.T. Bell, J.W. Ager, Trace levels of copper in carbon materials show significant electrochemical CO2 reduction activity, ACS Catal. 6 (2016) 202–209, http://dx.doi.org/10.1021/acscatal.5b02399.

[22] A.S. Varela, N. Ranjbar Sahraie, J. Steinberg, W. Ju, H.S. Oh, P. Strasser, Metal-doped nitrogenated carbon as an efficient catalyst for direct CO2 electroreduction to CO and hydrocarbons, Angew. Chem. Int. Ed. 54 (2015) 10758–10762, http://dx.doi.org/10.1002/anie.201502099.

[23] Z.P. Jovanov, Towards Synthetic Fuels via Electrocatalysis, Technical University of Denmark, 2014.

[24] H. Li, Y. Li, M.T.M. Koper, F. Calle-Vallejo, Bond-making and breaking between carbon, nitrogen, and oxygen in electrocatalysis, J. Am. Chem. Soc. 136 (2014) 15694–15701, http://dx.doi.org/10.1021/ja508649p.

[25] Y. Hori, Electrochemical CO2 reduction on metal electrodes, in: C.G. Vayenas, R.E. White, M.E. Gamboa-Aldeco (Eds.), Modern Aspects of Electrochemistry, Springer, 2008, pp. 89–189, http://dx.doi.org/10.1007/978-0-387-49489-0_3.

[26] R. Kortlever, I. Peters, S. Koper, M.T.M. Koper, Electrochemical CO2 reduction to formic acid at low overpotential and with high faradaic efficiency on carbon-supported bimetallic Pd-Pt nanoparticles, ACS Catal. 5 (2015) 3916–3923, http://dx.doi.org/10.1021/acscatal.5b00602.

[27] F.S. Roberts, K.P. Kuhl, A. Nilsson, High selectivity for ethylene from carbon dioxide reduction over copper nanocube electrocatalysts, Angew. Chem. Int. Ed. 54 (2015) 5179–5182, http://dx.doi.org/10.1002/anie.201412214.

[28] E.L. Clark, M.R. Singh, Y. Kwon, A.T. Bell, Differential electrochemical mass spectrometer cell design for online quantification of products produced during electrochemical reduction of CO2, Anal. Chem. 87 (2015), http://dx.doi.org/10.1021/acs.analchem.5b02080.

[29] D.B. Trimarco, T. Pedersen, O. Hansen, I. Chorkendorff, P.C.K. Vesborg, Fast and sensitive method for detecting volatile species in liquids, Rev. Sci. Instrum. 86 (2015), http://dx.doi.org/10.1063/1.4923453.

[30] J. McMurry, Organic Chemistry, 6th ed., Thomson-Brooks/Cole, 2004.

[31] R. Sander, Compilation of Henry's Law constants for inorganic and organic species of potential importance in environmental chemistry, Database (1999), http://dx.doi.org/10.1017/CBO9781107415324.004.

[32] J.A.V. Butler, C.N. Ramchandani, D.W. Thomson, The solubility of non-electrolytes. Part I. The free energy of hydration of some aliphatic alcohols, J. Chem. Soc. (1935) 280–285.

[33] M.G. Burnett, Determination of partition coefficients at infinite dilution by the gas chromatographic analysis of the vapor above dilute solutions, Anal. Chem. 35 (1963) 1567–1570, http://dx.doi.org/10.1021/ac60204a007.

[34] J. Timmermans, The Physico-Chemical Constants of Binary Systems in Concentrated Solutions, vol. 4, Interscience Publisher Inc., New York, NY, 1960.

[35] J.R. Snider, G.A. Dawson, Tropospheric light alcohols, carbonyls, and acetonitrile: concentrations in the southwestern United States and Henry's law data, J. Geophys. Res. 90 (1985) 3797–3805.

[36] E.A. Betterton, M.R. Hoffmann, Henry's law constants of some environmentally important aldehydes, Environ. Sci. Technol. 22 (1988) 1415–1418, http://dx.doi.org/10.1021/es00177a004.

[37] X. Zhou, K. Mopper, Apparent partition-coefficients of 15 carbonyl-compounds between air and seawater and between air and fresh-water – implications for air sea exchange, Environ. Sci. Technol. 24 (1990) 1864–1869, http://dx.doi.org/10.1021/es00082a013 file:///M:/Documents/Ph.D/Literature/Mend.

[38] J.A.V. Butler, C.N. Ramchandani, The solubility of non-electrolytes. Part II. The influence of the polar group on the free energy of hydration of aliphatic compounds, J. Chem. Soc. (1935) 952–955.

[39] R. Bone, P. Cullis, R. Wolfenden, Solvent effects on equilibria of addition of nucleophiles to acetaldehyde and the hydrophilic character of diols, J. Am. Chem. Soc. 105 (1983) 1339–1343, http://dx.doi.org/10.1021/ja00343a044.

[40] R.G. Buttery, L.C. Ling, D.G. Guadagni, Food volatiles: volatilities of aldehydes, ketones and esters in dilute water solution, J. Agric. Food Chem. 17 (1969) 385–389, http://dx.doi.org/10.1021/jf60162a025.

[41] H.J. Benkelberg, S. Hamm, P. Warneck, Henry's law coefficients for aqueous solutions of acetone, acetaldehyde and acetonitrile, and equilibrium constants for the addition compounds of acetone and acetaldehyde with bisulfite, J. Atmos. Chem. 20 (1995) 17–34, http://dx.doi.org/10.1007/BF01099916.

[42] L. Rohrschneider, Solvent characterization by gas-liquid partition coefficients of selected solutes, Anal. Chem. 45 (1973) 1241–1247, http://dx.doi.org/10.1021/ac60329a023.

[43] Y.-N. Lee, X. Zhou, Method for the determination of some soluble atmospheric carbonyl compounds, Environ. Sci. Technol. (1993) 749–756, http://dx.doi.org/10.1021/es00041a020.

[44] E.A. Betterton, The partitioning of ketones between the gas and aqueous phases, Atmos. Environ. Part A Gen. Top. 25 (1991) 1473–1477, http://dx.doi.org/10.1016/0960-1686(91)90006-S.

[45] A.G. Vitenberg, B.V. Ioffea, Z.S. Dimitrova, I.L. Butaeva, Determinatlon of gas-liquid means of gas chromatographic, J. Chromatogr. A 112 (1975) 319–327, http://dx.doi.org/10.1016/S0021-9673(00)99964-3.

[46] J.T. Hoff, D. Mackay, R. Gillham, W.Y. Shiu, Partitioning of organic chemicals at the air-water interface in environmental systems, Environ. Sci. Technol. 27 (1993) 2174–2180, http://dx.doi.org/10.1021/es00047a026.

[47] G.J. Pierotti, C.H. Deal, E.L. Derr, Activity coefficients and molecular structure, Ind. Eng. Chem. 51 (1959) 95–102, http://dx.doi.org/10.1021/ie50589a048.

[48] W.M. Meylan, P.H. Howard, Bond contribution method for estimating Henry's law constants, Environ. Toxicol. Chem. 10 (1991) 1283–1293, http://dx.doi.org/10.1002/etc.5620101007.

[49] USEPA, Air and Steam Stripping of Toxic Pollutants. Tech. Rep. EPA-68-03-002, Industrial Environmental Research Laboratory, Cincinnati, OH, USA, 1982.

[50] CRC Handbook of Chemistry and Physics, in: W.M. Haynes (Ed.), 97th ed., CRC Press/Taylor & Francis, Boca Raton, FL, 2016.

[51] O.M. Morgan, O. Maass, An investigation of the equilibria existing in gas-water systems forming electrolytes, Can. J. Res. 5 (1931) 162–199.

[52] D.-Q. Zheng, T.-M. Guo, H. Knapp, Experimental and modeling studies on the solubility of CO2, CHC1F2, CHF3, C2H2F4 and C2H4F2 in water and aqueous NaCl solutions under low pressures, Fluid Phase Equilib. 129 (1997) 197–209, http://dx.doi.org/10.1016/S0378-3812(96)03177-9.

[53] R.W. Meadows, D.J. Spedding, The solubility of very low concentratiions of carbon monoxide in aqueous solution, Tellus A 26 (1974) 143–150, http://dx.doi.org/10.3402/tellusa.v26i1-2.9745.

[54] J. Hong, W. Zhang, J. Ren, R. Xu, Photocatalytic reduction of CO2: a brief review on product analysis and systematic methods, Anal. Methods 5 (2013) 1086–1097, http://dx.doi.org/10.1039/c2ay26270c.

[55] T.A. Geissman, The Cannizzaro reaction, in: Organic Reactions, 2nd ed., Wiley-VCH, 2011, pp. 94–113.

Paper III

Electroreduction of CO on polycrystalline copper at low overpotentials

Erlend Bertheussen, Thomas V. Hogg, Albert K. Engstfeld, Younes Abghoui, Ib Chorkendorff, Ifan E.L. Stephens.

Submitted, 2018.

Electroreduction of CO on Polycrystalline Copper at Low Overpotentials

Erlend Bertheussen[¶,†], *Thomas V. Hogg*[¶,†], *Younes Abghoui*[†,‡], *Albert K. Engstfeldt*[†,§], *Ib Chorkendorff*[*,†], *Ifan E. L. Stephens*[*,†,||]

[†]Section for Surface Physics and Catalysis, Department of Physics, Technical University of Denmark, DK-2800 Kgs. Lyngby, Denmark;

[‡]Science Institute and Faculty of Physical Sciences, VR-III, University of Iceland, IS-107 Reykjavik, Iceland;

[§]Institute of Surface Chemistry and Catalysis, Ulm University, D-89069 Ulm, Germany

[||]Department of Materials, Imperial College London, Royal School of Mines, London, SW7 2AZ, UK.

Corresponding Authors

* E-mail: ibchork@fysik.dtu.dk (I.C.)

E-mail: i.stephens@imperial.ac.uk (I.E.L.S.)

KEYWORDS. Carbon monoxide, electroreduction, electrocatalysis, copper, alkaline, C2+ products.

ABSTRACT: Cu is the only monometallic electrocatalyst to produce highly reduced products from CO_2 selectively due to its intermediate binding of CO. We investigate the performance of polycrystalline Cu for the electroreduction of CO in alkaline media (0.1 M KOH) at low overpotentials (-0.4 to -0.6 V vs RHE). We find that polycrystalline Cu is highly active at these potentials. The overall CO reduction rates are comparable to nanostructured forms of the material, albeit with a distinct product distribution. While nanostructured forms of Cu favor alcohols, polycrystalline Cu produces greater amounts of C_2 and C_3 aldehydes, as well as ethylene.

TOC GRAPHICS

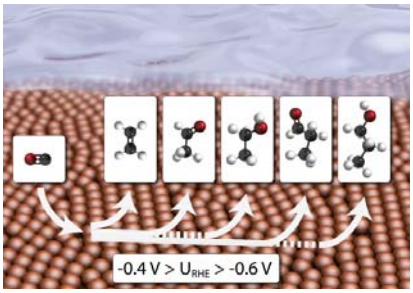

Electrochemical reduction using renewable energy is emerging as a promising mean of recycling carbon dioxide (CO_2) from point sources or ambient air into useful chemicals.[1–3] This way, the anthropogenic carbon cycle can be closed and our dependence on fossil energy sources to produce fuels and commodity chemicals can be reduced. The successful implementation of this technology requires development of electrocatalysts that can produce the desired product(s) efficiently and selectively.[1,2] Examples of useful products are energy-rich compounds such as hydrocarbons and oxygenates that can be used either as fuels or commodity chemicals.[1] Multi-carbon (C_{2+}) products are of special interest, due to their high energy density.[4] Moreover, unlike C_1 products such as methanol, they are particularly challenging to synthesize via thermally activated CO or CO_2 reduction methods.[5]

Copper is the only pure metal that can convert CO_2 into highly reduced and C-C coupled products in significant amounts.[6,7] This process, however, requires large overpotentials, and a large number of compounds are produced. In order to make this process suitable for large scale energy conversion, significant improvements are necessary. One approach is to use a tandem system whereby CO_2 is reduced in two stages: (i) reduce CO_2 to CO followed by (ii) further reduction of CO to more energy-rich products.[8] Several catalysts, including nanostructured Au,[9–11] Ag[12] and transition metal doped, nitrogenated carbon,[13–15] are highly selective and moderately active for the first step. For the second step, Cu based materials are the only catalysts to reduce CO at significant rates and with reasonable selectivity.[16] In particular, works led by Hori[16] and Koper[17] showed that C_2 products are favored under more alkaline conditions; subsequent theoretical works suggested that C-C coupling barriers are lower at high pH.[18,19] Moreover, increased surface roughness generally seems to favor the production of C_2 products, such as ethylene from CO_2.[20–24] Here, it is worth pointing out the significant difference in performance between aqueous half-cell measurements and experiments performed in real devices.[1] In aqueous electrolytes, CO_2 and CO reduction is limited by the low solubility of the reactant gas.[4] One

means of dealing with this issue is to conduct experiments on gas diffusion electrodes, which are not completely submerged in the electrolyte.[25,26]

Building upon the earlier findings regarding CO reduction on Cu electrodes, Kanan and co-workers showed that oxide-derived, nanostructured copper has a high (geometrically normalized) activity towards CO reduction at low overpotentials in 0.1 M KOH.[8] It exhibited high selectivity towards ethanol, with a maximum Faradaic efficiency of 43% at -0.3 V vs. RHE. The authors attributed the activity to a high density of grain boundary surface terminations.[8,27] A study from our own laboratory showed that the CO evolution activity was strongly correlated to the presence of a site – presumably undercoordinated – with exceptionally strong interaction with CO.[28] Other groups have also reported that stepped or kinked surfaces yield higher proportions of oxygenates, relative to hydrocarbons, from CO_2 or CO reduction.[29–31] This phenomenon is likely related to the more favorable free energy pathway for aldehyde reduction to alcohols on high index Cu surfaces than on terraces.[32]

Oxide derived-Cu evidently has a complex surface chemistry;[27,28] moreover its porous morphology is likely to yield mesoscopic transport effects during CO reduction, especially given the involvement of soluble intermediates such as acetaldehyde.[33–35] On the other hand, the chemistry of CO reduction on polycrystalline Cu should be simpler; on that basis, it could be used as a robust benchmark for activity measurements. To the best of our knowledge, there are only two reports in the literature that quantify the activity and selectivity of planar polycrystalline Cu for CO reduction in 0.1 M KOH.[28,36] Even so, there is significant variability between those two reports, as described in more detail in the supporting information (Section S3 and Figure S1). This leads us to the focus of the current investigation, which is to establish the following: *What is the activity of polycrystalline Cu for CO reduction, a viable benchmark for this reaction on copper based electrodes? How does it compare in terms of activity and Faradaic efficiency to literature data on nanostructured copper materials?* On the basis of our current understanding, we aim to establish the reasons for the fundamental differences in

catalytic performance between polycrystalline and nanostructured Cu. Consequently, we investigate CO reduction on polycrystalline copper foils between -0.40 V and -0.59 V vs. RHE , i.e. at potentials more positive than previously reported for this material. We report appreciable activity and selectivity to CO reduction across this potential range. We also show that the total CO reduction current density of polycrystalline copper is comparable to that of oxide-derived copper, when normalized to electrochemical surface area (ECSA).

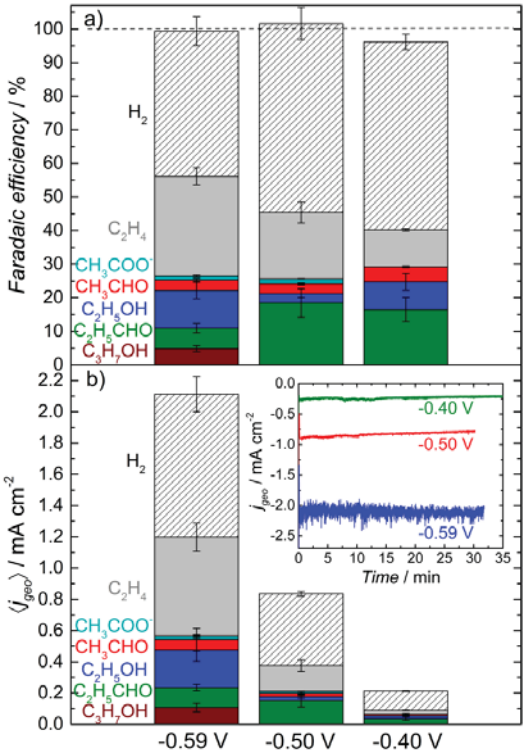

Figure 1. Faradaic efficiency (a) and mean partial current density (b) from chronoamperometric CO reduction performed in CO saturated 0.1 M KOH at -0.40, -0.50 and -0.59 V vs. RHE. Data represent the average of 3 individual measurements, and error bars indicate ±σ. Inset: Chronoamperometry traces from representative measurements at each potential. Measurements were carried out until a certain charge was reached (0.5 C at -0.40 V, 1.5 C at -0.50 V and 4.0 C at -0.59 V).

Acivity and product distribution from CO reduction on polycrystalline Cu. We carried out short-term (~30 minutes) chronoamperometric CO reduction measurements at three different potentials, i.e., -0.40, -0.50 and -0.59 V vs. RHE (all potentials are referred to this scale in the following) in CO-saturated 0.1 M KOH electrolyte using a glass H-cell. The resulting Faradaic efficiencies and partial current densities for the individual products are shown in Figure 1a and 1b, respectively. Within the uncertainty of our measurements, we could account for a 100% balance of charge with products detected, including both H_2 and compounds derived from CO reduction. We observed that the Faradaic efficiency towards CO reduction increases from 40% at -0.40 V to 56% at -0.59 V. Consistent with earlier reports on oxide-derived Cu,[8,27,28,33] only C_{2+} products are formed under these conditions. The two major CO reduction products are propionaldehyde (with a maximum of 18% Faradaic efficiency at -0.50 V) and ethylene (30% at -0.59 V). The other CO reduction products are ethanol, 1-propanol, acetaldehyde and acetate. The rates towards alcohol production are particularly high at the most negative potential, -0.59 V where the concentration of 1-propanol exceeds the detection limit of our analytical equipment. Notably, we measured significant CO reduction partial current densities, up to 1.2 mA cm^{-2} at -0.59 V.

Another important observation is how the product distribution changes with the applied potential. Among the oxygenated compounds, aldehydes are formed primarily at the more positive potentials, while alcohol formation becomes more prominent at -0.59 V. Several studies, including results from our group, show that acetaldehyde is an intermediate in the production of ethanol.[16,32,33] Hori et al. reported that propionaldehyde could be reduced to 1-propanol on polycrystalline copper strongly suggesting that also the C_3 aldehyde is an intermediate in alcohol formation.[16] It seems that applying -0.59 V instead of -0.50 V accelerates aldehyde conversion to alcohols. It is worth noting that aldehydes are challenging to

detect in alkaline solutions using routine NMR spectroscopy.[33,37] However, our use of static headspace-gas chromatography (HS-GC) enables us to measure these compounds with high sensitivity.

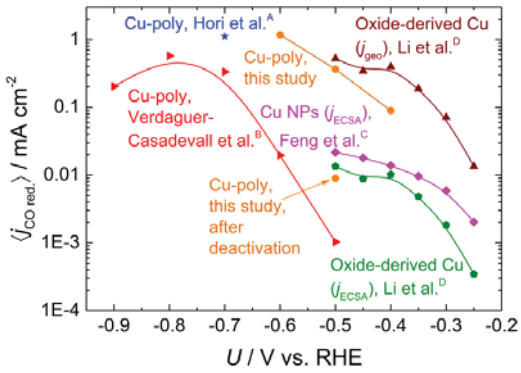

Figure 2. Comparison of mean partial current densities for CO reduction on polycrystalline Cu, oxide derived Cu and Cu nanoparticles. Oxide derived Cu is normalized with respect to both geometric and electrochemically active surface area. The results from the current study are the same that are shown in Figure 1, and are compared with data adapted from (A) Hori et al.,[36] (B) Verdaguer-Casadevall et al.,[28] (C) Feng et al.[27] and (D) Li et al.[8] The bottom orange point represents the result from a sample after deactivation, for which detailed data are shown in Figure S2. We have summarized the roughness factors we used for the ECSA normalization in Table S2, obtained from each of the relevant studies. We assume that the polycrystalline Cu electrodes have a roughness factor of 1.

Comparison with literature data for polycrystalline Cu and nanostructured Cu. Figure 2 compares the total CO reduction current densities of this work with some results from relevant studies reported in the literature. An interesting comparison can be drawn between the results from this work and previously published data from oxide-derived Cu and Cu nanoparticles. It seems that nanostructured electrodes reach mass transport limitations for CO reduction at potentials just cathodic of -0.30 V to -

0.35 V. By extrapolating the first two to three points of the data that are normalized to electrochemical surface area (ECSA) , it seems that these lines would roughly coincide with the polycrystalline data from the present work. This suggests that the activity towards CO reduction for nanostructured copper is actually similar to that of polycrystalline copper. Thus, according to our data, there is no significant difference between the CO reduction activity of planar polycrystalline Cu and nanostructured oxide derived Cu: the high current densities of the oxide derived Cu – when normalized to geometric surface area – are due to the exceptionally large roughness factors of 39 or higher. This important observation shows that nanostructuring is not a prerequisite for high CO reduction activity.

There are significant variations in product distribution between the two types of materials. An example of this is the difference in ethylene production. Polycrystalline copper shows significant selectivity to ethylene at all potentials measured in this study, in particular at -0.5 V and more cathodic. On nanostructured copper, on the other hand, ethylene is not produced in significant amounts, probably because these catalysts are mass transport limited in the region where hydrocarbons are normally produced.

At the same time, oxygenates are almost exclusively produced from CO reduction on nanostructured electrodes when not mass transport limited. It has been shown for CO_2 reduction that oxygenates are generally produced at lower overpotentials than hydrocarbons.[38] This points towards the different potential regions accessible on planar and nanostructured surfaces as a likely reason for the variation in oxygenate selectivity. The high ECSA of the nanostructured electrodes allows for measurements at lower overpotentials, since the larger geometric current density allows for adequate product analysis even though the ECSA-normalized current density is low. On the other hand, such electrodes reach mass transport limitations already around -0.35 V, as discussed above. As a result, the potential range accessible to measurements is distinct from planar electrodes. It is also evident that nanostructured oxide derived Cu yields higher selectivity to energy-rich alcohols than planar

polycrystalline Cu.[8,33] We attribute this phenomenon to two effects: (i) oxide-derived Cu has more strong-binding undercoordinated sites, which are more effective at reducing aldehydes to alcohols, as discussed in the introduction, and (ii) the porosity leads to enhanced retention of aldehydes, accelerating their reduction to alcohols. We would like to emphasise that the low ECSA of polycrystalline Cu makes it an unsuitable CO reduction catalyst for commercial purposes. However, we consider it provides an excellent, simple-to-reproduce benchmark. Moreover, it is of critical interest to establish the differences between it and nanostructured forms of Cu in order to design improved catalyst materials.

When comparing the individual studies on polycrystalline copper, it can be seen that they differ significantly from each other. For instance, our present results show significant CO reduction activity for polycrystalline copper between -0.40 V and -0.59 V, whereas the results of an earlier collaboration between our group and Kanan and coworkers showed little to no CO reduction activity at potentials between -0.50 and -0.90 V on similar electrodes.[28] We speculate that these differences could be caused, at least partly, by the longer duration of the measurements in that study. They were carried out for 2-3 hours, a period in which the electrodes in the current study experience significant deactivation. We mainly attribute this deactivation to poisoning by silicon from the glassware, as discussed in detail below. In Figure 2, we show a data point from a measurement carried out on an electrode that had already been deactivated in argon-purged electrolyte (chronoamperometry trace and Faradaic efficiency are shown in Figure S2). Its activity is much closer to the data from Verdaguer-Casadevall et al., suggesting that those data could have been affected by silicon poisoning. In addition to the studies mentioned above, Koper and coworkers also investigated CO reduction on polycrystalline Cu. They observe formation of ethylene between -0.35 and -0.60 V on polycrystalline Cu, but with insignificant overall current densities.4 The authors use online electrochemical mass spectrometry (OLEMS) for product analysis: this technique is highly sensitive to gas phase species; however, it is challenging to use

it to yield quantitative measurements of reaction rates. On that basis, we have not included it in Figure 2.

In general, the low ECSA of planar electrodes makes them far more susceptible to poisoning by impurities than their nanostructured counterparts with a more favorable electrode area/electrolyte volume ratio. When studying the intrinsic behavior of low surface area electrocatalysts, we recommend keeping the measurement time as short as possible, so that the effect of any impurities that might be present is minimized. For CO_2/CO reduction measurements, the measurement duration is normally limited by accumulation of liquid products above the detection limits of the analytical equipment used.

Another reason for the discrepancies could be differences in initial electrode surface structure. In Figure S3, we show that different batches of copper foils from the same supplier can give significantly different features in CVs under inert gas conditions. This is reflected in the CO reduction activity shown in Figure S4, where the foil that exhibits more (100)-like features shows higher CO reduction selectivity, in particular towards ethylene formation. Several groups have shown that the surface orientation of copper electrocatalysts can have a significant effect on CO reduction performance.[29–31,39–42] Thus, we conjecture that the surface orientation of different polycrystalline foils could also vary significantly, hence affecting the catalyst activity.

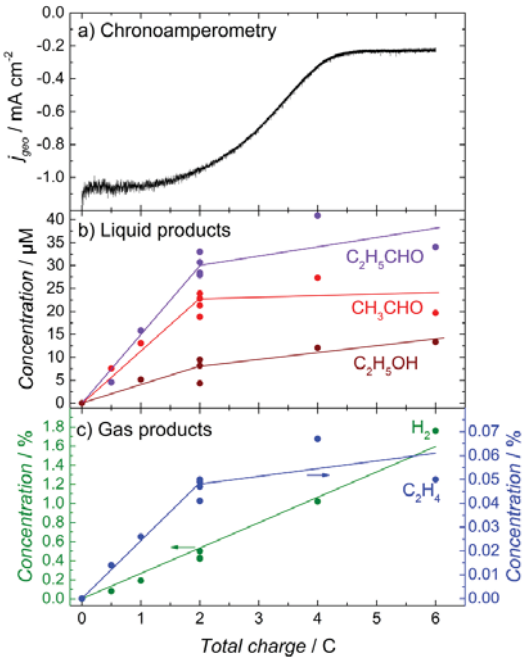

Figure 3. CO reduction measurements at -0.52 V in CO saturated 0.1 M KOH. (a) Chronoamperometry trace for measurement stopped at 6 C charge. (b) Concentration of the liquid products ethanol, acetaldehyde and propionaldehyde as a function of total measurement charge. (c) Concentration of the individual gaseous products as a function of total measurement charge. Note: 1-propanol and acetate are not shown in (b). 1-propanol was not produced in concentrations above our detection limits at this potential, and acetate was measured using NMR spectroscopy, which was not carried out for these measurements. Acetate is a minor product quantified to ~1% Faradaic efficiency in other measurements. Each data point in (b) and (c) represents data from an individual measurement. Lines have been added to guide the eye. The corresponding duration of each measurement is shown in Figure S6b in the Supporting Information.

Deactivation for extended measurements. Using our current experimental setup, it is challenging to maintain the activity of Cu for extended periods of time. Representative chronoamperometry traces

for short-term measurements are shown in the inset of Figure 1b. The high CO reduction activity that we described above is relatively stable over the course of ~30 minutes at all three potentials. A minor loss of activity can be observed at -0.40 V and -0.50 V, while the measurements at -0.59 V are completely stable. Significant deactivation occurs on a longer time scale, however (current density as a function of time for the same measurement is shown in Figure S5, total CO reduction partial current density for each point is shown in Figure S6b). For the measurement shown in Figure 3a, the initial current density decreases by almost 80%. At the same time, a strong shift in product distribution can be observed. In Figure 3b and c, the development of product concentration with total measurement charge is shown for liquid and gaseous products, respectively. The H_2 concentration increases linearly with accumulated measurement charge. On the other hand, at the point where the current density starts rapidly decreasing, the concentration of the CO reduction products ethylene, acetaldehyde, propionaldehyde and ethanol reaches a plateau. The slope of the H_2 concentration would, in principle, be expected to increase when deactivation starts, due to an increase in Faradaic efficiency. A minor leakage of H_2 for measurements longer than ~30 minutes could be the reason that this is not the case.

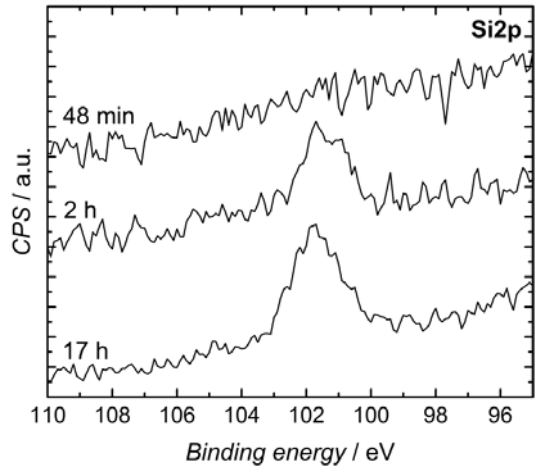

Figure 4. XPS spectra of the Si2p binding energy region on polycrystalline copper foils after CO reduction at -0.50 V for different times. Note: Each measurement is carried out on a new CO reduction sample.

The observed catalyst deactivation could be caused by several effects, including i) changes in the elemental composition of the surface due to accumulation of impurities,[43–47] ii) the electropolished Cu surface undergoing a structural transformation under reaction conditions,[30,39,48] and/or iii) self-poisoning of the surface by reaction products/intermediates, as shown previously for other reactions, e.g., by Heinen et al. for the electrooxidation of ethanol.[34] In order to investigate possible impurity deposition of the electrode, we performed X-ray photoelectron spectroscopy (XPS) studies after the CO reduction measurement. In Figure 4, we show XPS spectra of the Si2p region measured on copper electrodes after different electrolysis times. For short-term measurements, where significant deactivation has not yet occurred, little or no Si can be detected on the surface with this technique. For longer measurements, however, the Si2p line is clearly visible, suggesting that there might be a correlation between the presence of Si and the deactivation. Mayrhofer et al. showed that Pb and Si, derived from glass corrosion under alkaline conditions, can poison reactions such as O_2 reduction on Pt.[43,44] Since we are using glass cells for these measurements, it is a plausible reason for the deactivation we see. Figure S7 shows a survey spectrum of an electrode after long-term CO reduction. No clear lines of other possible metallic contaminants are present.

To investigate whether self-poisoning by aldehydes contribute to the observed deactivation, we added acetaldehyde and propionaldehyde to Ar-saturated 0.1 M KOH and carried out chronoamperometry measurements at -0.50 V. We chose aldehydes for this measurement as a result of our previous observation that acetaldehyde undergoes spontaneous organic reactions in alkaline solution, including polymerization.[33] The resulting trace is displayed in Figure S8. Initially, an increased current density can be observed, suggesting that the aldehydes do not immediately poison the surface.

The electrode does, however start losing activity after ~30 minutes, similarly to the long-term CO reduction measurement shown in Figure S5. In order to elucidate if restructuring of the electrode under reaction conditions occurs, and influences the activity, we also investigated the behavior of the electrode when kept at -0.50 V in Ar-purged electrolyte, before switching to CO. The resulting chronoamperometry trace and the respective product distribution are shown in Figure S2. After an initial activation, the H_2 evolution current starts to deactivate as well. After switching to CO, the initial activity is significantly lower than right after electropolishing. Furthermore, only small amounts of CO reduction products could be detected. These experiments together suggest that self-poisoning by reaction intermediates is not causing the deactivation. They do not, however, conclusively show if silicon poisoning or restructuring are causing it, or a combination of both effects.

In this study, we investigated the activity and product selectivity of polycrystalline Cu for the reduction of CO at low overpotentials in alkaline media. We measured more than 50% Faradaic efficiency for CO reduction, primarily due to the formation of C_2 and C_3 aldehydes and alcohols, as well as ethylene. A comparison of data from this study with results reported previously in the literature indicates that polycrystalline Cu can yield comparable CO reduction rates to oxide-derived, nanostructured Cu. Even so, oxide-derived Cu favors the production of highly-coveted energy-rich alcohols; we attribute this difference to a higher abundance of undercoordinated sites and decreased mass transport within the pores of oxide derived Cu. In summary, by performing bulk electrolysis measurements using three different analytical chemistry techniques, we demonstrate that planar polycrystalline copper exhibits equivalent activity for CO reduction to state-of-the-art nanostructured catalyst materials. The enhanced current densities afforded by nanostructured surfaces are only due to the large surface area. Future studies should focus on improving the *intrinsic activity* of Cu.

EXPERIMENTAL DETAILS

A more detailed description of materials used (Section S1) and experimental details (Section S2) can be found in the Supporting Information.

Polycrystalline copper electrodes were cut to a size of 5x10 mm, and a piece of copper wire was attached. The electrodes were electropolished in 30% phosphoric acid and rinsed thoroughly with MilliQ water. The procedure was carried out immediately before the electrode was mounted in the custom made H-cell. The electrolyte was purged with CO for 15 minutes at 30 sccm. The ohmic resistance was measured using electrochemical impedance spectroscopy. 85% of the Ohmic drop was compensated for in the EC-Lab software, with post-measurement correction applied to account for the final 15%. A Hg/Hg_2SO_4 reference electrode was used for all measurements, converted into the RHE scale by calibration against the onset of H_2 evolution/H_2 oxidation on a Pt electrode. CO reduction was carried out in batch measurements. Chronoamperometry was carried out until a certain amount of charge was passed. For short-term measurements the values for total measurement charge were 0.5 C at -0.40 V, 1.5 C at -0.50 V and 4.0 C at -0.59 V. The average current from a measurement was used in later analyses. After chronoamperometry, 250 μL of the gas mixture was injected in the GC. Liquid product analysis was performed using HS-GC and NMR spectroscopy following the protocols from a previous publication.[37] XPS was performed using an Al Kα X-ray source. An Ar flood gun was used for sample charge neutralization.

ASSOCIATED CONTENT

The Supporting Information is available free of charge on the ACS Publications website at DOI:

AUTHOR INFORMATION

Corresponding Authors

* E-mail: ibchork@fysik.dtu.dk (I.C.)

* E-mail: i.stephens@imperial.ac.uk (I.E.L.S.)

Author Contributions

[¶]E.B. and T.V.H. contributed equally to this work.

Present Addresses

[‡] Y.A.: Science Institute, Faculty of Physical Sciences, VR-III, University of Iceland, IS-107 Reykjavik, Iceland

[§] A.K.E.: Institute of Surface Chemistry and Catalysis, Ulm University, D-89069 Ulm, Germany

[||] I.E.L.S.: Department of Materials, Imperial College London, Royal School of Mines, London, SW7 2AZ, UK.

ACKNOWLEDGMENTS

This work was funded by the Villum Foundation V-SUSTAIN grant 9455 to the Villum Center for the Science of Sustainable Fuels and Chemicals.

Y.A received funding from The Icelandic Research Fund;

A.K.E. received funding from the People Program (Marie Curie Actions) of the European Union's Seventh Framework Program (FP7/2007-2013) under REA grant agreement n°609405 (COFUNDPostdocDTU).[*info on website]

We thank Jakob Kibsgaard for producing the table of content graphic.

REFERENCES

(1) Whipple, D. T.; Kenis, P. J. A. Prospects of CO2 Utilization via Direct Heterogeneous Electrochemical Reduction. *J. Phys. Chem. Lett.* **2010**, *1* (24), 3451–3458.

(2) Seh, Z. W.; Kibsgaard, J.; Dickens, C. F.; Chorkendorff, I.; Nørskov, J. K.; Jaramillo, T. F. Combining theory and experiment in electrocatalysis: Insights into materials design. *Science* **2017**, *355* (6321), 1–12.

(3) Hori, Y. Electrochemical CO2 Reduction on Metal Electrodes. In *Modern Aspects of*

Electrochemistry; Vayenas, C. G., White, R. E., Gamboa-Aldeco, M. E., Eds.; Springer, 2008; Vol. 42, pp 89–189.

(4) *CRC Handbook of Chemistry and Physics*, 97th ed.; Haynes, W. M., Ed.; CRC Press/Taylor & Francis: Boca Raton, FL, 2016.

(5) Medford, A. J.; Lausche, A. C.; Abild-Pedersen, F.; Temel, B.; Schjødt, N. C.; Nørskov, J. K.; Studt, F. Activity and selectivity trends in synthesis gas conversion to higher alcohols. *Top. Catal.* **2014**, *57* (1–4), 135–142.

(6) Hori, Y.; Wakebe, H.; Tsukamoto, T.; Koga, O. Electrocatalytic process of CO selectivity in electrochemical reduction of CO2 at metal electrodes in aqueous media. *Electrochim. Acta* **1994**, *39* (11–12), 1833–1839.

(7) Bagger, A.; Ju, W.; Varela, A. S.; Strasser, P.; Rossmeisl, J. Electrochemical CO2 Reduction: A Classification Problem. *ChemPhysChem* **2017**, *18* (22), 3266–3273.

(8) Li, C. W.; Ciston, J.; Kanan, M. W. Electroreduction of carbon monoxide to liquid fuel on oxide-derived nanocrystalline copper. *Nature* **2014**, *508* (7497), 504–507.

(9) Zhu, W.; Michalsky, R.; Metin, Ö.; Lv, H.; Guo, S.; Wright, C. J.; Sun, X.; Peterson, A. A.; Sun, S. Monodisperse Au nanoparticles for selective electrocatalytic reduction of CO2 to CO. *J. Am. Chem. Soc.* **2013**, *135* (45), 16833–16836.

(10) Zhu, W.; Zhang, Y.-J.; Zhang, H.; Lv, H.; Li, Q.; Michalsky, R.; Peterson, A. A.; Sun, S. Active and Selective Conversion of CO2 to CO on Ultrathin Au Nanowires. *J. Am. Chem. Soc.* **2014**, *136*, 16132–16135.

(11) Chen, Y.; Li, C. W.; Kanan, M. W. Aqueous CO2 reduction at very low overpotential on oxide-

derived Au nanoparticles. *J. Am. Chem. Soc.* **2012**, *134* (49), 19969–19972.

(12) Mistry, H.; Choi, Y.-W.; Bagger, A.; Scholten, F.; Bonifacio, C. S.; Sinev, I.; Divins, N. J.; Zegkinoglou, I.; Jeon, H. S.; Kisslinger, K.; Stach, E. A.; Yang, J. C.; Rossmeisl, J.; Roldan Cuenya, B. Enhanced Carbon Dioxide Electroreduction to Carbon Monoxide over Defect-Rich Plasma-Activated Silver Catalysts. *Angew. Chem. Int. Ed.* **2017**, *56* (38), 11394–11398.

(13) Varela, A. S.; Ranjbar Sahraie, N.; Steinberg, J.; Ju, W.; Oh, H. S.; Strasser, P. Metal-Doped Nitrogenated Carbon as an Efficient Catalyst for Direct CO2 Electroreduction to CO and Hydrocarbons. *Angew. Chem. Int. Ed.* **2015**, *54* (37), 10758–10762.

(14) Bagger, A.; Ju, W.; Varela, A. S.; Strasser, P.; Rossmeisl, J. Single site porphyrine-like structures advantages over metals for selective electrochemical CO2reduction. *Catal. Today* **2017**, *288*, 74–78.

(15) Ju, W.; Bagger, A.; Hao, G. P.; Varela, A. S.; Sinev, I.; Bon, V.; Roldan Cuenya, B.; Kaskel, S.; Rossmeisl, J.; Strasser, P. Understanding activity and selectivity of metal-nitrogen-doped carbon catalysts for electrochemical reduction of CO2. *Nat. Commun.* **2017**, *8*, 944.

(16) Hori, Y.; Takahashi, R.; Yoshinami, Y.; Murata, A. Electrochemical Reduction of CO at a Copper Electrode. *J. Phys. Chem. B* **1997**, *101* (36), 7075–7081.

(17) Schouten, K. J. P.; Kwon, Y.; van der Ham, C. J. M.; Qin, Z.; Koper, M. T. M. A new mechanism for the selectivity to C1 and C2 species in the electrochemical reduction of carbon dioxide on copper electrodes. *Chem. Sci.* **2011**, *2* (10), 1902.

(18) Calle-Vallejo, F.; Koper, M. T. M. Theoretical considerations on the electroreduction of CO to C2 Species on Cu(100) electrodes. *Angew. Chem. Int. Ed.* **2013**, *52* (28), 7282–7285.

(19) Montoya, J. H.; Shi, C.; Chan, K.; Nørskov, J. K. Theoretical Insights into a CO Dimerization Mechanism in CO2 Electroreduction. *J. Phys. Chem. Lett.* **2015**, *6* (11), 2032–2037.

(20) Tang, W.; Peterson, A. A.; Varela, A. S.; Jovanov, Z. P.; Bech, L.; Durand, W. J.; Dahl, S.; Nørskov, J. K.; Chorkendorff, I. The importance of surface morphology in controlling the selectivity of polycrystalline copper for CO2 electroreduction. *Phys. Chem. Chem. Phys.* **2012**, *14* (1), 76–81.

(21) Roberts, F. S.; Kuhl, K. P.; Nilsson, A. High selectivity for ethylene from carbon dioxide reduction over copper nanocube electrocatalysts. *Angew. Chem. Int. Ed.* **2015**, *54* (17), 5179–5182.

(22) Mistry, H.; Varela, A. S.; Bonifacio, C. S.; Zegkinoglou, I.; Sinev, I.; Choi, Y.-W.; Kisslinger, K.; Stach, E. A.; Yang, J. C.; Strasser, P.; Cuenya, B. R. Highly selective plasma-activated copper catalysts for Carbon Dioxide Reduction To Ethylene. *Nat. Commun.* **2016**, *7*, 1–8.

(23) Kim, D.; Lee, S.; Ocon, J. D.; Jeong, B.; Lee, J. K.; Lee, J. Insights into autonomously formed oxygen-evacuated Cu2O electrode for the selective production of C2H4 from CO2. *Phys. Chem. Chem. Phys.* **2014**, *17* (2), 824–830.

(24) Ren, D.; Deng, Y.; Handoko, A. D.; Chen, C. S.; Malkhandi, S.; Yeo, B. S. Selective Electrochemical Reduction of Carbon Dioxide to Ethylene and Ethanol on Copper(I) Oxide Catalysts. *ACS Catal.* **2015**, *5* (5), 2814–2821.

(25) Ma, S.; Sadakiyo, M.; Luo, R.; Heima, M.; Yamauchi, M.; Kenis, P. J. A. One-step electrosynthesis of ethylene and ethanol from CO2 in an alkaline electrolyzer. *J. Power Sources* **2016**, *301*.

(26) Reller, C.; Krause, R.; Volkova, E.; Schmid, B.; Neubauer, S.; Rucki, A.; Schuster, M.; Schmid,

G. Selective Electroreduction of CO2 toward Ethylene on Nano Dendritic Copper Catalysts at High Current Density. *Adv. Energy Mater.* **2017**, *7* (12), 1602114.

(27) Feng, X.; Jiang, K.; Fan, S.; Kanan, M. W. A Direct Grain-Boundary-Activity Correlation for CO Electroreduction on Cu Nanoparticles. *ACS Cent. Sci.* **2016**, *2* (3), 169–174.

(28) Verdaguer-Casadevall, A.; Li, C. W.; Johansson, T. P.; Scott, S. B.; McKeown, J. T.; Kumar, M.; Stephens, I. E. L.; Kanan, M. W.; Chorkendorff, I. Probing the active surface sites for CO reduction on oxide-derived copper electrocatalysts. *J. Am. Chem. Soc.* **2015**, *137* (31), 9808–9811.

(29) Hori, Y.; Takahashi, I.; Koga, O.; Hoshi, N. Electrochemical reduction of carbon dioxide at various series of copper single crystal electrodes. *J. Mol. Catal. A Chem.* **2003**, *199* (1–2), 39–47.

(30) Kim, Y. G.; Javier, A.; Baricuatro, J. H.; Soriaga, M. P. Regulating the Product Distribution of CO Reduction by the Atomic-Level Structural Modification of the Cu Electrode Surface. *Electrocatalysis* **2016**, *7* (5), 391–399.

(31) Hahn, C.; Hatsukade, T.; Kim, Y. G.; Vailionis, A.; Baricuatro, J. H.; Higgins, D. C.; Nitopi, S. A.; Soriaga, M. P.; Jaramillo, T. F. Engineering Cu surfaces for the electrocatalytic conversion of CO2: Controlling selectivity toward oxygenates and hydrocarbons. *Proc. Natl. Acad. Sci. U. S. A.* **2017**, *114* (23), 5918–5923.

(32) Ledezma-Yanez, I.; Gallent, E. P.; Koper, M. T. M.; Calle-Vallejo, F. Structure-sensitive electroreduction of acetaldehyde to ethanol on copper and its mechanistic implications for CO and CO2 reduction. *Catal. Today* **2016**, *262*, 90–94.

(33) Bertheussen, E.; Verdaguer-Casadevall, A.; Ravasio, D.; Montoya, J. H.; Trimarco, D. B.; Roy, C.; Meier, S.; Wendland, J.; Nørskov, J. K.; Stephens, I. E. L.; Chorkendorff, I. Acetaldehyde as

an Intermediate in the Electroreduction of Carbon Monoxide to Ethanol on Oxide-Derived Copper. *Angew. Chem. Int. Ed.* **2016**, *55* (4), 1450–1454.

(34) Heinen, M.; Jusys, Z.; Behm, R. J. Ethanol, acetaldehyde and acetic acid adsorption/electrooxidation on a Pt thin film electrode: An in-situ ATR-IR spectroscopy flow-cell study. *J. Phys. Chem. C* **2010**, *114* (21), 9850–9864.

(35) Hall, A. S.; Yoon, Y.; Wuttig, A.; Surendranath, Y. Mesostructure-Induced Selectivity in CO2 Reduction Catalysis. *J. Am. Chem. Soc.* **2015**, *137* (47), 14834–14837.

(36) Hori, Y.; Murata, A.; Takahashi, R.; Suzuki, S. Electroreduction of CO To CH4 and C2H4 At a Copper Electrode in Aqueous-Solutions At Ambient-Temperature and Pressure. *J. Am. Chem. Soc.* **1987**, *109* (16), 5022–5023.

(37) Bertheussen, E.; Abghoui, Y.; Jovanov, Z. P.; Varela, A. S.; Stephens, I. E. L.; Chorkendorff, I. Quantification of Liquid Products from the Electroreduction of CO2 and CO using Static Headspace-Gas Chromatography and Nuclear Magnetic Resonance Spectroscopy. *Catal. Today* **2017**, *288*, 54–62.

(38) Kuhl, K. P.; Cave, E. R.; Abram, D. N.; Jaramillo, T. F. New insights into the electrochemical reduction of carbon dioxide on metallic copper surfaces. *Energy Environ. Sci.* **2012**, *5* (2012), 7050–7059.

(39) Kim, Y. G.; Javier, A.; Baricuatro, J. H.; Torelli, D. A.; Cummins, K. D.; Tsang, C. F.; Hemminger, J. C.; Soriaga, M. P. Surface reconstruction of pure-Cu single-crystal electrodes under CO-reduction potentials in alkaline solutions: A study by seriatim ECSTM-DEMS. *J. Electroanal. Chem.* **2016**, *780*, 290–295.

(40) Schouten, K. J. P.; Qin, Z.; Pérez Gallent, E.; Koper, M. T. M. Two pathways for the formation

of ethylene in CO reduction on single-crystal copper electrodes. *J. Am. Chem. Soc.* **2012**, *134* (24), 9864–9867.

(41) Schouten, K. J. P.; Pérez Gallent, E.; Koper, M. T. M. Structure sensitivity of the electrochemical reduction of carbon monoxide on copper single crystals. *ACS Catal.* **2013**, *3* (6), 1292–1295.

(42) Roberts, F. S.; Kuhl, K. P.; Nilsson, A. Electroreduction of Carbon Monoxide over a Copper Nanocube Catalyst: Surface Structure and pH Dependence on Selectivity. *ChemCatChem* **2016**, *8* (6), 1119–1124.

(43) Mayrhofer, K. J. J.; Crampton, A. S.; Wiberg, G. K. H.; Arenz, M. Analysis of the Impact of Individual Glass Constituents on Electrocatalysis on Pt Electrodes in Alkaline Solution. *J. Electrochem. Soc.* **2008**, *155* (6), P78–P81.

(44) Mayrhofer, K. J. J.; Wiberg, G. K. H.; Arenz, M. Impact of Glass Corrosion on the Electrocatalysis on Pt Electrodes in Alkaline Electrolyte. *J. Electrochem. Soc.* **2008**, *155* (1), P1–P5.

(45) Hori, Y.; Konishi, H.; Futamura, T.; Murata, A.; Koga, O.; Sakurai, H.; Oguma, K. Deactivation of copper electrode in electrochemical reduction of CO2. *Electrochim. Acta* **2005**, *50* (27), 5354–5369.

(46) Wuttig, A.; Surendranath, Y. Impurity Ion Complexation Enhances Carbon Dioxide Reduction Catalysis. *ACS Catal.* **2015**, *5* (7), 4479–4484.

(47) Subbaraman, R.; Danilovic, N.; Lopes, P. P.; Tripkovic, D.; Strmcnik, D.; Stamenkovic, V. R.; Markovic, N. M. Origin of anomalous activities for electrocatalysts in alkaline electrolytes. *J. Phys. Chem. C* **2012**, *116* (42), 22231–22237.

(48) Kim, Y. G.; Baricuatro, J. H.; Javier, A.; Gregoire, J. M.; Soriaga, M. P. The evolution of the polycrystalline copper surface, first to Cu(111) and then to Cu(100), at a fixed CO2RR potential: A study by operando EC-STM. *Langmuir* **2014**, *30* (50), 15053–15056.

Paper IV

Electroreduction of CO_2 on copper electrodes

Erlend Bertheussen, Stephanie A. Nitopi, Søren B. Scott, Albert K. Engstfeld, Xinyan Liu, Karen Chan, Christopher Hahn, Jens K. Nørskov, Thomas F. Jaramillo, Ifan E.L. Stephens, Ib Chorkendorff.

In preparation, 2018.

Electroreduction of CO_2 on Copper Electrodes

Erlend Bertheussen[1¶], Stephanie A. Nitopi[2¶], Søren B. Scott[1], Albert K. Engstfeld[1,3], Xinyan Liu[2,4], Karen Chan[4], Christopher Hahn[2,4], Jens K. Nørskov[2,4], Thomas F. Jaramillo[2,4], Ifan E. L. Stephens[1,5], Ib Chorkendorff[1]

[1]Section for Surface Physics and Catalysis, Department of Physics, Technical University of Denmark, DK-2800 Kgs. Lyngby, Denmark;
[2]Department of Chemical Engineering, Stanford University, Stanford, CA 94305;
[3]Institute of Surface Chemistry and Catalysis, Ulm University, D-89069 Ulm, Germany;
[4]SUNCAT Center for Interface Science and Catalysis, SLAC National Laboratory, Menlo Park, CA 94025;
[5]Department of Materials, Imperial College London, Royal School of Mines, London, SW7 2AZ, UK.

[¶]E.B. and S.A.N. contributed equally.

Abstract:
Electrochemical conversion of CO_2 exhibits high potential, both as a means of energy storage for the fluctuating output from renewable electricity sources, and for carbon-neutral production of fuels and chemicals that are currently derived from fossil fuels. Copper is unique among the transition metals in the sense that it facilitates formation of highly reduced and energy-rich products with relatively high activity and selectivity. However, this occurs at high overpotentials, leading to significant energy losses. Furthermore, the selectivity to individual products is relatively low. In this review article, we give an overview of the literature that exists for CO_2 reduction on Cu. We describe different effects that control the fundamentals of the reaction, and which thus are responsible for the limitations observed. On this basis, we discuss bimetallic and nanostructured electrodes with Cu, which are common approaches used in the literature when aiming to improve the performance of Cu for CO_2 reduction towards highly reduced products. We compare the vast number of studies that have been performed and identify trends between the different types of materials. Two important conclusions were drawn from this comparison: (i) with a few exceptions, bimetallic electrodes with Cu exhibit lower selectivity towards highly reduced products, and increased selectivity towards two-electron products and/or H_2 compared to monometallic Cu; (ii) nanostructured Cu electrodes exhibit higher selectivity for CO_2 reduction towards multi-carbon products compared to polycrystalline Cu, while the ECSA-normalized activity of nanostructured and polycrystalline Cu are similar.

Outline:
- Introduction to electrochemical CO_2 reduction. What makes Cu unique?
- Overview of current mechanistic understanding in the field, as investigated by DFT.
- Mechanistic insight from experiments. Included measurements on single crystals, as well as discussions about pH and electrolyte effects.
- CO_2 reduction on nanostructured Cu electrodes. Qualitative and quantitative comparison between various studies.
- CO_2 reduction on bimetallic electrodes with Cu. Qualitative and quantitative comparison between various studies.
- Summary and outlook; what should the field focus on in future studies?